Functionalized Hydrogels for Controlled Nutrient Release

MAJED SALEM ALSAIAARI

Submitted in accordance with the requirements for the degree of Doctor of Philosophy

The University of Leeds

School of Chemistry

JULY 2025

Declaration

The candidate confirms that the work submitted is his/her own, except where work which has formed part of jointly authored publications has been included. The contribution of the candidate and the other authors to this work has been explicitly indicated below. The candidate confirms that appropriate credit has been given within the thesis where reference has been made to the work of others. *Further details of the jointly authored publications and the contributions of the candidate and the other authors to the work should be included below this statement.*

Table of Contents

List of Figures

1

List of Tables

List of Equations

List of Abbreviations

ASTM	American Society for Testing and Materials.
Avg	Average
BET	Brunauer, Emmett, Teller(Surface area measurements)
Chitosan-PAM	Chitosan-Polyacrylamide
CMC	Carboxymethyl Cellulose
E*	Complex Young module
EGDMA	Ethylene glycol dimethacrylate
eV	Electron volts
FDA	The Food and Drug Administration
g	Gram
G’	Storage module
G’’	Loss module
G*	Complex shear module
GG	Gellan Gum gellan gum (GG) 1- high acyl (H) and 2-low acyl (L)
GG	Guar Gum
HEC	Hydroxyethyl cellulose
HEC	Hydroxyethyl Cellulose
HEMA	2-hydroxyethyl methacrylate
ICP	Inductively Coupled Plasma
ICP-MS	Inductively Coupled Plasma Mass Spectrometry
ICP-OES	Inductively Coupled Plasma Optical Emission Spectrometry
ISO	International Organization for Standardisation
K	Kalvin
LCST	Lower critical solution temperature
LVE	Limit of Linear Viscoelastic
M	Moles Per Litre
Max	Maximum
mg	Milgram
Min	Minute
NaCMC	Sodium carboxymethyl cellulose)
nm	Nanometre
NPAM	N-Isopropylacrylamide

P HEMA	Poly-2-hydroxyethylmethacrylate
PAM	Polyacrylamide
PAM	Polyacrylamide
PE	Polyethylene
PEG	Polyethylene glycol
PEs	Primary Electrons
PVA	Polyvinyl alcohol
SEM	Scanning electron microscope
SEs	Secondary Electrons
ST.	Dev Stander Deviation
T max	Maximum temperature
TDS	Total dissolved solids
3D	Three dimensions
°C	Degrees Celsius
µM	Micrometre
µS/cm	micro-Siemens per centimetre
γ	Strain
$\dot{\gamma}$	Strain rate
η^*	Complex viscosity
κ	Ionic Conductivity
σ	Stress
ω	Frequency

Acknowledgements

All praise is due to Allah, the Most Gracious, the Most Merciful. I am deeply thankful to Him for bestowing upon me the knowledge, perseverance, and opportunities to complete this research. Truly, without His guidance, none of this would have been achieved. I would like to express my sincere gratitude to my supervisor, Dr. Terence P. Kee, for giving me the opportunity to work under his guidance and for selecting an excellent research topic. Throughout the project and during my first year of study, he provided invaluable support, encouragement, motivation, and expert guidance, for which I am truly grateful. I also extend my appreciation to Dr. Paul Thornton for facilitating my registration in key research-related modules such as Soft Materials, which introduced me to advanced topics in chemistry. His assistance in granting me access to course materials through the Chemistry Department's online resources was especially helpful. My thanks go to the University of Leeds and the School of Chemistry for providing a supportive academic environment. I particularly appreciated the numerous opportunities to enhance my academic and research skills through workshops and short courses focused on self-development and training—all offered free to students. I am deeply thankful to the Government of the Kingdom of Saudi Arabia for its unwavering moral, psychological, and financial support throughout my studies. I am especially grateful to both my workplace and the Saudi Cultural Office in London for their continued encouragement. I would also like to acknowledge the technical staff in the Chemistry Department. Special thanks to Mr. David Fogarty for his assistance with UV-Visible Spectrometry and light scattering measurements, and to Dr. Mark J. Howard, Experimental Officer in NMR Spectroscopy, for his comprehensive training in this field. I am equally grateful to Dr. Alex Kulak for helping with SEM imaging, BET analysis, and EDX measurements. My sincere thanks also go to Dr. Algy Kazlauciunas, who guided me in performing viscosity measurements, and to Dr. Ian Gorrell, whose support helped me navigate various aspects of the laboratory system. I am pleased to acknowledge Dr. Daniel Baker from the School of Physics and Astronomy for his assistance and support during my rheological measurements. I am also grateful to Dr. A.M. Cunliffe CSci MRSC, Analytical Laboratory Manager at the School of Chemical and Process Engineering, for his help with thermal analysis. Additionally, I would like to thank Mr. Stephen Reid from the School of Earth and Environment, who provided support with ICP measurements. I would also like to thank my fellow colleagues Seham Alanazi, Hind Alluqmani, and Mansour Alsarrani for their support, especially during training in the use of analytical instruments and essential software programs such as EndNote and Origin. And I

don’t forget to thank the master's student Jack Garnett for returning some of the rheological experiments to confirm their authenticity. Finally, I am deeply grateful to my wife, who has been a constant source of support and strength despite facing her own health challenges. I also extend heartfelt thanks to my sons, my father, my mother, and all my brothers and sisters for their continuous encouragement and love. I acknowledge the use of CoPilot https://m365.cloud.microsoft/chat to proofread my final draft and ChatGPT for proofreading and correct Grammarly.

Abstract

This study aims to develop hydrogel systems for potential future applications in sustainable agriculture. Whilst this application itself did not forma significant element of this study explicitly, we have focused more on integrating plant germination and growth nutrients within a composite hydrogel environment. Such composite hydrogels have been prepared, and aspects of their bulk behaviour and structural properties studied using analytical techniques including electron microscopy, thermal analysis and rheology. Subsequently, release or dissipation of nutrients from such composite gels *via* dialysis has been studied using ionic conductivity and inductively coupled plasma methods.

Three hydrogel formulations have been investigated: (1) gellan gum, (2) gellan gum composites with hydroxyethyl cellulose (HEC), and (3) composite gellan gum hydrogels with with carboxymethyl cellulose (CMC). Commercial Miracle-Gro fertiliser was incorporated as the nutrient source. Comprehensive characterisation was performed using scanning electron microscopy (SEM), energy-dispersive X-ray spectroscopy (EDX) with elemental mapping, Brunauer-Emmett-Teller (BET) surface area analysis, thermal analysis, conductivity measurements, inductively coupled plasma mass spectrometry (ICP-MS), inductively coupled plasma optical emission spectrometry (ICP-OES), and rheological analysis.

This thesis explores the development and characterisation of environmentally friendly polysaccharide-based hydrogel systems for agricultural applications. The hydrogels demonstrate potential as controlled-release nutrient carriers, capable of improving fertiliser efficiency, reducing nutrient loss through leaching, and mitigating environmental impacts—thereby contributing to more sustainable agricultural practices.

Chapter 1 provides the context and motivation for the research, highlighting global agricultural challenges and the urgent need for sustainable fertilisation strategies. It introduces hydrogels as promising candidates for nutrient delivery, detailing their classifications, fabrication methods, and the advantages of hybrid formulations. The chapter focuses on three biodegradable polysaccharides—gellan gum (GGH), hydroxyethyl cellulose (HEC), and carboxymethyl cellulose (CMC)—chosen for their environmental compatibility. It also outlines the analytical techniques used to assess the hydrogels' structural, thermal, mechanical, and nutrient-release properties. Proof reading provided by Dr Jamie Bailey.

Chapter 2 investigates three hydrogel formulations: (1) GGH alone, (2) GGH-HEC composites, and (3) GGH-CMC composites. These formulations were loaded with Miracle-Gro fertiliser as a model nutrient. The hydrogels were comprehensively characterised using

scanning electron microscopy (SEM), energy-dispersive X-ray spectroscopy (EDX) with elemental mapping, and Brunauer–Emmett–Teller (BET) surface area analysis.

Chapter 3 examines the thermal behaviour of both unmodified and modified hydrogel samples, with and without nutrient incorporation. Thermogravimetric analysis (TGA) and differential scanning calorimetry (DSC) were employed, using a fixed gellan gum concentration of 12 mg/cm³ to standardise comparisons and evaluate the effect of compositional modifications on thermal stability.

Chapter 4 presents ionic conductivity studies conducted on all hydrogel samples post-dialysis over six-time intervals to assess nutrient release dynamics. Inductively coupled plasma mass spectrometry (ICP-MS) and optical emission spectroscopy (ICP-OES) were used to quantify the release of key elements, including potassium (K), phosphorus (P), iron (Fe), copper (Cu), manganese (Mn), molybdenum (Mo), and zinc (Zn).

Chapter 5 details rheological investigations into the viscoelastic and flow behaviour of the GGH-based hydrogels. Oscillatory amplitude sweeps, frequency sweeps, and rotational flow tests were conducted to understand the mechanical properties and stability of the hydrogel networks under stress.

Chapter 6 outlines the experimental procedures, including materials, preparation methods, and analytical protocols used throughout Chapters 2 to 5.

Chapter 7 concludes the thesis by summarising the major findings, demonstrating how each objective was met, and underscoring the potential of these hydrogel systems to support more sustainable and efficient fertiliser use in agriculture.

Chapter 1: Introduction to Hydrogels and their Applications in Sustainable Agriculture

1.1 introduction

The agricultural sector faces a variety of difficulties, including sustainability, climate change, productivity, and resource accessibility (1). To tackle these issues, a comprehensive strategy is needed that includes sustainable habits, policy backing, technical advancements, and global collaboration.

The growing global population necessitates the cultivation of a variety of food sources. There is an annual increase of 1% in feeding demand, which requires a commensurate increase in food production to maintain a healthy population (2). One of the key global issues in today's world is access to clean water for drinking, irrigation, crop protection, and nutrient delivery, particularly in countries like India (3). Most of the world's population lives in primarily agricultural regions, with 18 % of the global population residing in India alone, and 19 % in African nations (4). Globally, agriculture faces many challenges that affect food security, sustainability and productivity. One such issue is the erosion of soil, which poses a threat to food production and causes a reduction in nutrient content, worsening malnutrition in regions that affect roughly two-thirds of the global population (5). To address the growing need for food, particularly in developing nations, it is estimated that a two-fold increase in food production will be required by 2100 (6).

Additionally, overpopulation, a growing elderly population, climate change and a scarcity of young labourers are exacerbating the difficulties in enhancing food production, which will require significant shifts in farming practices to manage (7, 8).

Food Production produces 21-37% of global greenhouse gasses and as such plays a substantial role in the amplification of climate change (9). In developing nations like India, where newer agricultural methods are unaffordable for many; there is a struggle to adopt sustainable practices (10). Issues such as low productivity, climate change vulnerabilities, and limited access to financial resources compound this challenge (11) Governments worldwide could alleviate this by providing more support for agricultural modernisation in developing nations (12). Agricultural incentives in numerous African countries are restricted, resulting in limitations in the development of value chains, disparities in quality, and low productivity, especially among small-scale farmers (13). Groundwater over-extraction in nations like India

presents significant sustainability problems for irrigation (14). While using smart farming technologies to industrialise and commercialise agriculture presents opportunities, it also brings up ethical issues. In developing countries, agriculture remains a vital occupation for many, especially the poor (14, 15).

In semi-arid and arid regions of the world, water management is quickly rising to the top of the list of urgent problems that nations must deal with. A severe water scarcity is expected to arise from a 50% increase in global water usage by 2030. In most parts of the world, agriculture uses more than 70% of freshwater, increasing the pressure on water scarcity (16).
Several arid and semi–arid regions around the world suffer from increased water shortages due to on-going climate change (Figure 1.1). This commonly leads to restrictions in water use in cities and industrial and agricultural regions, which are normally amongst the largest water-consuming sectors in most countries (17).

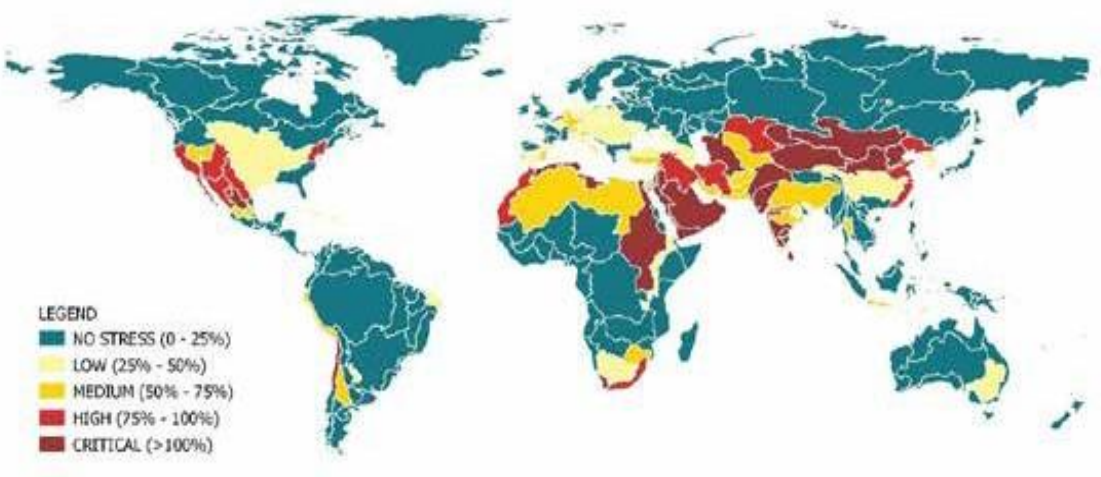

Figure 1.1: A global map depicting the level of water stress by country in 2018.

One of the most rapidly developing materials in the world are hydrogel polymers, because they have been demonstrated to impact in several areas, the most important of which are the agricultural, medical and pharmaceutical sectors (Figure 1.2) (18). Polymer hydrogels have the potential to play a key role in agricultural infrastructure development, as they have been shown to aid efficient water usage and can help to create appropriate environments for the cultivation of all plants (19). In the last decade, polymer hydrogels have been widely used in studies focused on soil water retention for plants and improving growth media by enhancing water availability and reducing moisture loss (20-22).

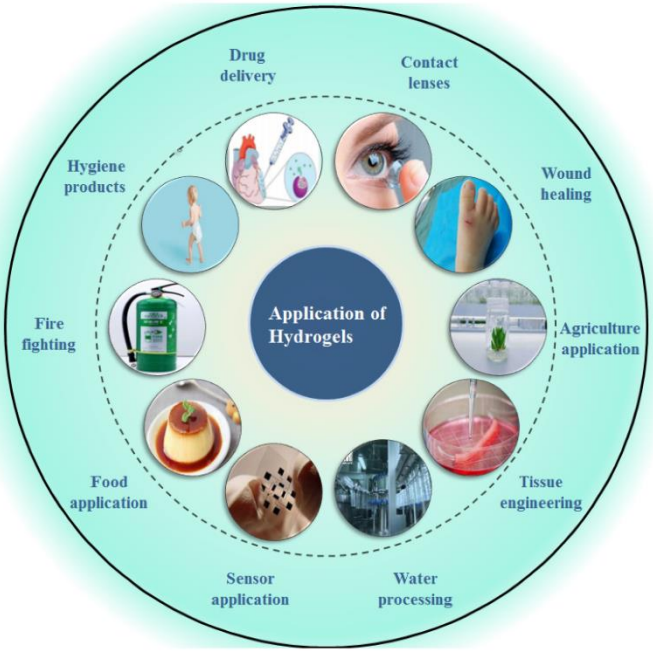

Figure 1.2: Some of applications for hydrogels (23).

Agriculture extensively uses hydrogels to enhance farming and crop growth, enhance plant cultivation under adverse weather conditions, and create more favourable conditions for plant development. Hydrogels improve the physical properties of soils and restore their biota as well as promoting seed germination and seedling emergence rates, which can improve root growth and plant density by optimizing moisture retention and nutrient storage/release, as well as reducing the impact of moisture stress. Hydrogels shorten the nursery establishment period by ensuring consistent hydration, improving nutrient efficiency, accelerating root development, and reducing environmental stress. This allows seedlings to mature faster and be transplanted earlier, improving productivity in commercial nurseries and agricultural systems. They reduce crop irrigation frequencies and fertilization requirements while increasing input use efficiency. Hydrogels can be applied in two ways: either as soil conditioners to stabilize the soil's surface, inhibit crust formation, and improve water-holding capacity, or to improve the poor structure at deeper depths through aggregation, thereby enhancing plant growth. Hydrogel polymers are critical compounds in solving water shortages and increasing crop yields (19). Hydrogels have demonstrated the capacity to function as artificial soils and soil enhancers, due to their ability to absorb and retain substantial amounts of water and nutrients (Figure 1.3) (16).

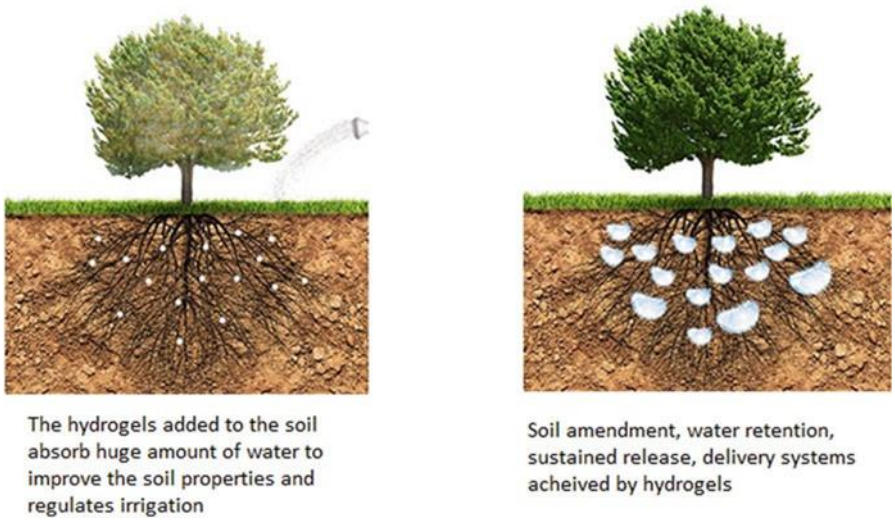

Figure 1.3: A depiction of the use of hydrogels in agriculture. The hydrogels retain water close to the root system, reducing water loss from drainage (23).

1.2 Introduction to hydrogels

1.2.1 History

Hydrogels are 3-dimensional, porous, polymeric materials, specifically used to adsorb and store water (24). Hydrogels are a type of polymeric material which has a hydrophilic structure that allows them to hold significant amounts of water inside their three-dimensional network (24). Hydrogels were first reported in the 19th century as colloidal gels made from inorganic salts (25). The first reported hydrogel-like materials were metal-hydroxide gels, which had a network structure that could retain water. Notable examples are aluminium hydroxide or ferric hydroxide, which form through precipitation when metal salt solutions are mixed with alkaline solutions. For instance, aqueous solutions of ferric chloride hexahydrate ($FeCl_3.6H_2O$) and ammonium molybdate tetrahydrate ($(NH_4)6Mo_7O_{24}.\ 6H_2O$) can be mixed under ambient conditions form a viscous yellow gel that traps a large volume of water (Figure 1.4) (26).

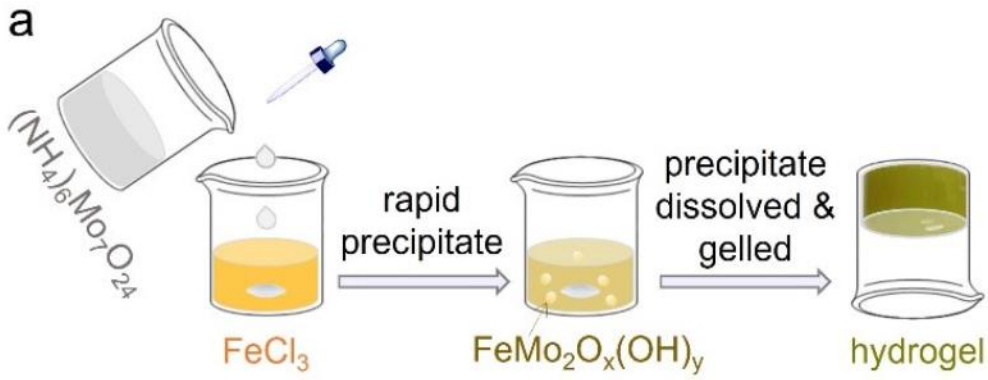

Figure 1.4: Schematic illustration of the synthetic route used to synthesise the mineral gels reported in just this study (26).

However, it wasn't until Wichterle and Lim discovered the first synthetic hydrogel on crosslinked poly-2-hydroxyethylmethacrylate (pHEMA) in 1954 that the application of gels first achieved real attention (Figure 1.5) (27).

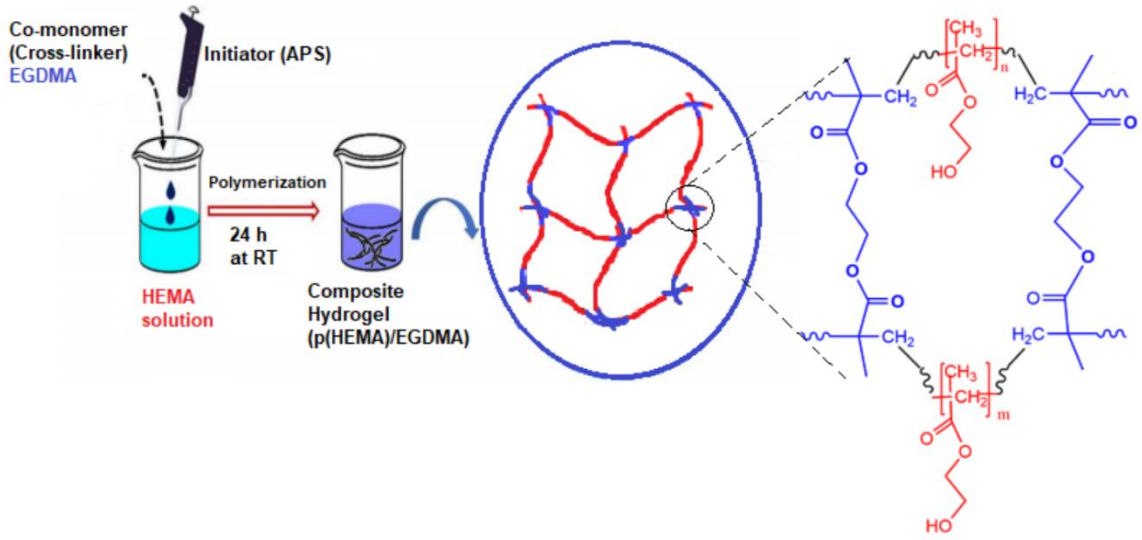

Figure 1.5: A schematic representing of the synthesis of pHEMA hydrogel from copolymerisation of HEMA with other co-monomers (EGDMA, ethylene glycol dimethacrylate) (28).

Since then, three-dimensional networks of hydrophilic polymers have been referred to as "hydrogels" (Figure 1.6). In Western Europe, soft contact lenses made using pHEMA's crosslinked macromolecular network became commercially available in the 1960s and the Food and Drug Administration (FDA) authorised the pHEMA-designed lenses in 1971 (29).

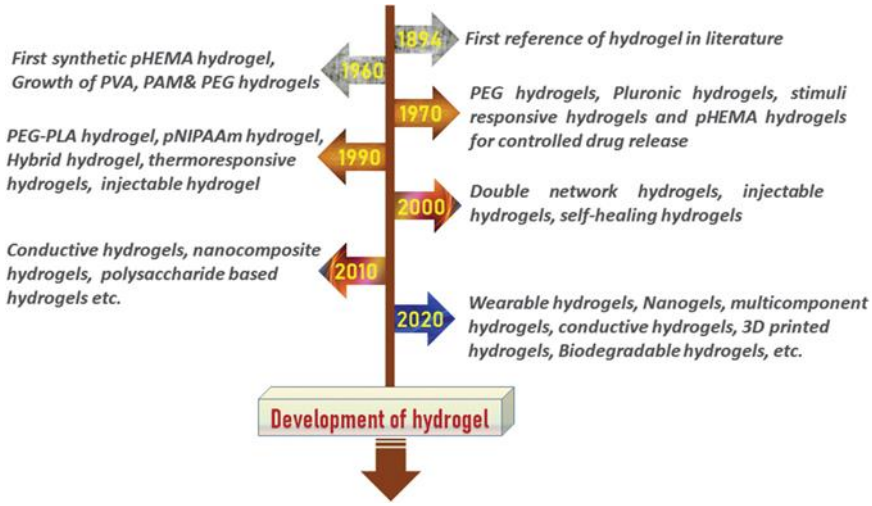

Figure 1.6: Hydrogels have developed over time (25).

Updike and Hicks developed medical sensors in 1967 by encasing enzyme glucose-oxidase in a hydrogel based on polyacrylamide (PAM) and pHEMA has been used extensively in drug delivery since (30). Since then, hydrogels have been used for drug delivery, tissue engineering, skincare, and food products. In the 1970s, new hydrogel concepts were explored (31), and Tanaka's experiments revealed gel collapse due to temperature or solvent composition changes (31). In the 1990s, research focused on developing thermo-responsive hydrogels using polymers like polyvinyl alcohol (PVA), poly-N-isopropylacrylamide, and polyethylene glycol (PEG). These hydrogels were used for one-off drug release below the lower critical solution temperature (LCST), with injectable hydrogels being investigated for biomedical applications (25).

In the 21st century, hydrogels have been improved through various methods and structural modifications. In 2003, Gong *et al*. created the first double-network hydrogels with high mechanical strength. This progress has led to the development of biocompatible hydrogels for critical biomedical applications like bone implants, biosensors, contact lenses, and tissue engineering. Recent research has focused on innovative hydrogels like wearable patches, conducting hydrogels, injectable hydrogels, self-healing hydrogels, multi-component hydrogels, and biodegradable hydrogels (25). Four generations of hydrogel formation have been envisaged (Figure 1.7).

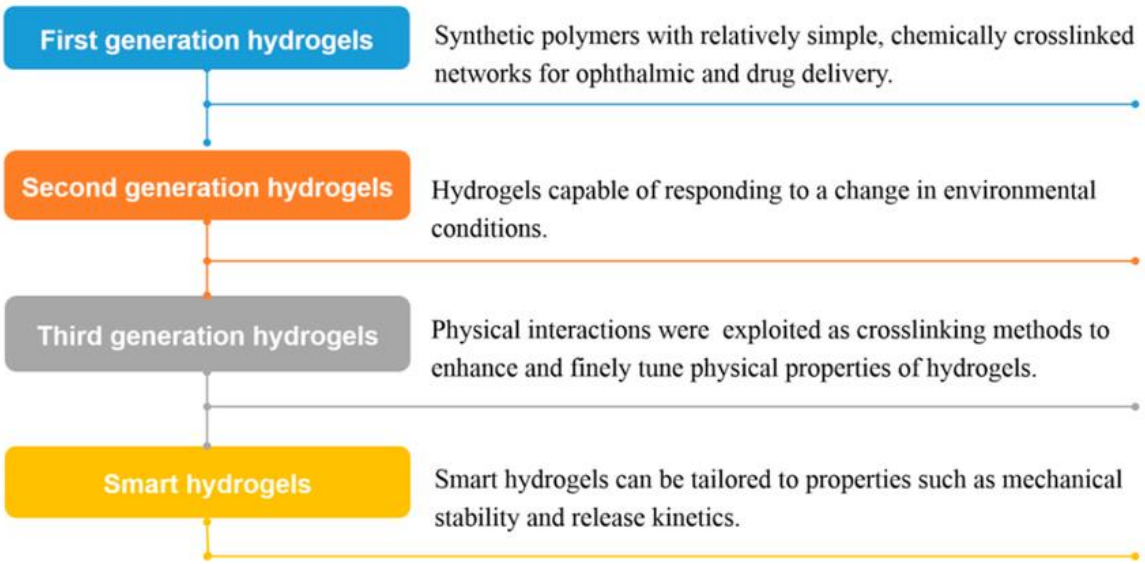

Figure 1.7: Hydrogels have been in their growth stage over the last few years (32).

1.2.2 Hydrogel definition

A material can only be classified as a hydrogel if water makes up a minimum of 10% of its entire weight or volume (Figure 1.8) (33). Their hydrophilic, three-dimensional structures have unique characteristics that enable them to retain a significant quantity of water and expand inside the polymeric network, while maintaining their overall structure (34, 35). These materials consist of hydrophilic polymer chains contained within a water-rich environment. This arrangement forms a network that holds water and allows the controlled release and protection of compounds contained within the hydrogel matrix in response to environmental conditions (36).

Hydrogel matrices exhibit useful characteristics such as low cost, flexbility, durability, biocompatibility,, and the capacity to imitate flexible human tissues (25, 37, 38).

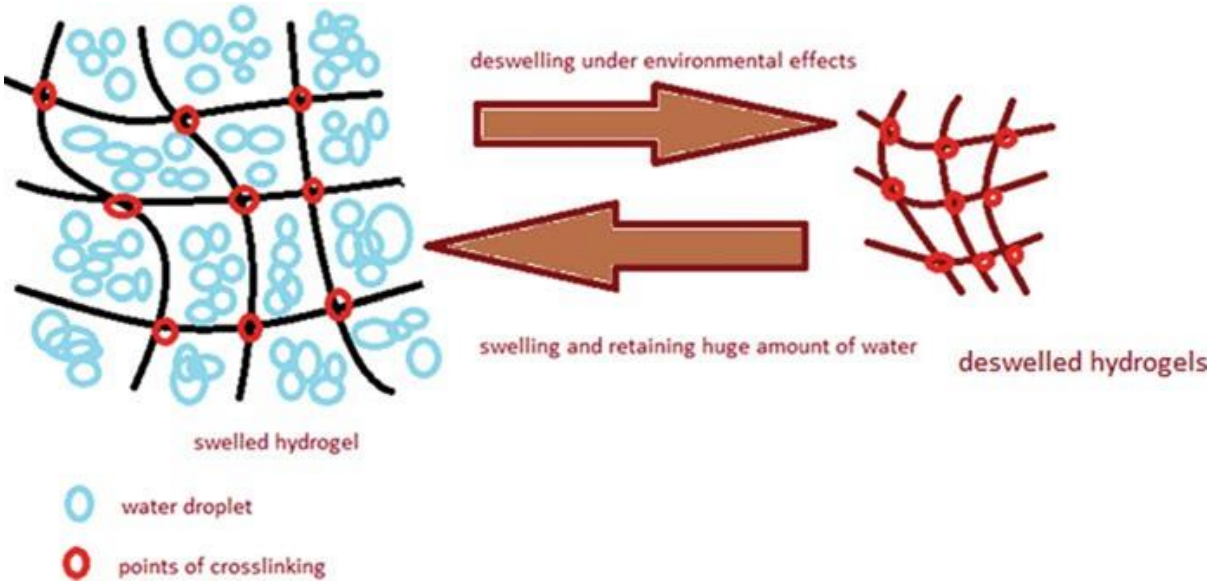

Figure 1.8: Water absorption of hydrogels (23).

The hydrogels exhibit a significant capacity for water absorption because they contain hydrophilic functionalities, including hydroxyl (–OH), carboxyl (-COOH), amide (-CONH), sulfonic acid (-SO_3H), and amine (-NH_2) groups. These facilitate hydrogen bonding, ionic forces, capillary action, and controlled polymer crosslinking. These properties make them ideal for biomedical applications because their water-rich structure mimics natural tissue, making them ideal for drug delivery, wound healing, or scaffolding. They are also well suited to use in agriculture due to their ability to retain water, which improves soil moisture, reduces irrigation needs, and protects against drought. Finally, they make excellent water retention materials, as hydrogels hold and slowly release water to plants or surfaces, which has clear benefits for use in arid climates. In addition, these functional groups serve as a foundation for undergoing functionalisation or chemical changes that enable crosslinking (39).

Additionally, hydrogels have remarkable physicochemical characteristics, such as permeability and swelling, biocompatibility and unique mechanical and optical qualities which have made them an adaptable tool for use in imaging, diagnosis, and medication (37, 38).

Hydrogels undergo a large volume phase transition, or gel-sol phase transition, in response to a variety of physical and chemical stimuli. While pH, ions, and particular chemical compositions are examples of chemical or biochemical stimuli, temperature, electric and magnetic fields, light intensity, and pressure are examples of physical stimuli (Figure 1.9) (33).

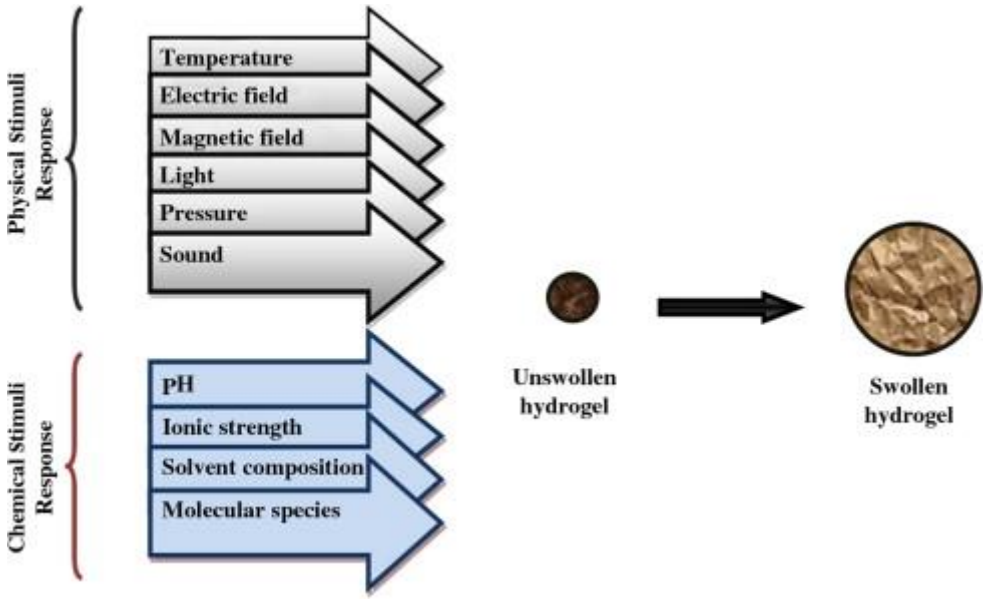

Figure 1.9: Extending hydrogel in reaction to stimuli (18).

The degree of crosslinking, polymer volume percentage, and network structure of hydrogels influence their mechanical strength and toughness, among other features (40). Hydrogels can be synthesised from both synthetic and natural sources, each having unique advantages and disadvantages (see Table 1.1).

Table 1.1: Advantages and Disadvantages of Natural vs Synthetic Hydrogel Sources.

Source	**Advantages**	**Disadvantages**
Synthetic	Strong, customizable, consistent properties	Less biocompatible, non-biodegradable, expensive
Natural	Biocompatible, biodegradable, non-toxic	Poor mechanical strength, variable purity

The diversity of synthetic routes makes hydrogels suitable for a wide range of applications. For instance, natural hydrogels are widely used in pharmaceuticals, biomaterials, biotechnology, and medical applications such as wound closure (41), due to their ability to mimic native tissue. Additionally, their biomimetic properties make them highly valuable in tissue engineering. They are also utilized in tissue engineering due to their biomimetic properties, providing porous microenvironments for cell infiltration and high permeability for essential nutrients (42). Moreover, hydrogels have been successfully employed in encapsulating different cell types using materials like alginate, which can be crosslinked with divalent cations such as (Ca^{2+}, Ba^{2+}, Sr^{2+}, Mg^{2+}, Zn^{2+}) (43). There are several innovative types of hydrogels, including double-network and composite hydrogels. Double-network hydrogels are made of two different polymer networks. One is stiff and breaks easily, helping to absorb and spread-out energy when

the material is stressed. The other is soft and flexible, which helps the hydrogel stay together and keep its shape even after the stiff part breaks. Composite hydrogels are made by adding strong materials like tiny particles, fibres, clay, or carbon-based substances. These added materials make the hydrogel stronger, more heat-resistant, and sometimes able to conduct electricity or interact with biological systems. These have been developed to enhance their mechanical properties, durability and functionalities (44). These advancements have led to the creation of hydrogels with unique characteristics and the ability to tune them to specific external stimuli. One example is poly(*N*-isopropylacrylamide-*co*-acrylic acid), which can be tuned to open or close depending on pH and temperature. This allows it to deliver therapeutic agents at targeted locations in the body (45). Furthermore, hydrogels have been combined with other materials like graphene and cellulose nanofibrils to improve drug loading efficiency, sustained release, and tissue differentiation capabilities (46). Hydrogels can be formed into thin films (47) or shaped into various forms, sizes, lengths, or structures, as needed (48). In many applications, most of the polymers used for hydrogel preparation are considered non-toxic and suitable for use in human beings. The toxicity of hydrogel materials is assessed through various biological, chemical, and physicochemical tests to ensure they are biocompatible and safe for use in humans (49-52). Regulators like the FDA (Food and Drug Administration), ISO (International Organization for Standardization), and ASTM (American Society for Testing and Materials) set the standards for these evaluations.

Hydrogel preparation is a critical aspect of ensuring their safety for various applications. The non-toxicity of hydrogels is a fundamental requirement, especially in biomedical and pharmaceutical fields. Several studies have highlighted the importance of using non-toxic materials in hydrogel preparation to ensure biocompatibility and safety. One study by Obara et al. focused on the synthesis of a non-toxic hydrogel composite using sodium carboxymethyl cellulose (NaCMC) and hydroxyethyl cellulose (HEC) with activated carbon as a filler. The study emphasized the non-toxic nature of the hydrogel composite, making it suitable for applications such as desalination of seawater (53). Hydrogels can desalinate seawater by absorbing water into their polymer network while leaving most salt ions behind. Then, when the hydrogel is heated or squeezed, it releases the absorbed fresh water, resulting in lower-salinity water.

Figure 1.10: An illustration showing the molecular structure of the hydrogel matrix composed of sodium carboxymethyl cellulose (NaCMC) and hydroxyethyl cellulose (HEC) with activated carbon as a filler (53).

Gong et al.'s study on pH-responsive core-shell composite hydrogel capsules demonstrated their potential for controlled, sustained drug delivery, reducing drug intake and maintaining stable blood-drug levels. The non-toxic capsules also demonstrated potential safety for biomedical use, indicating their potential for targeted and prolonged drug delivery. (Figure 1.11) (54).

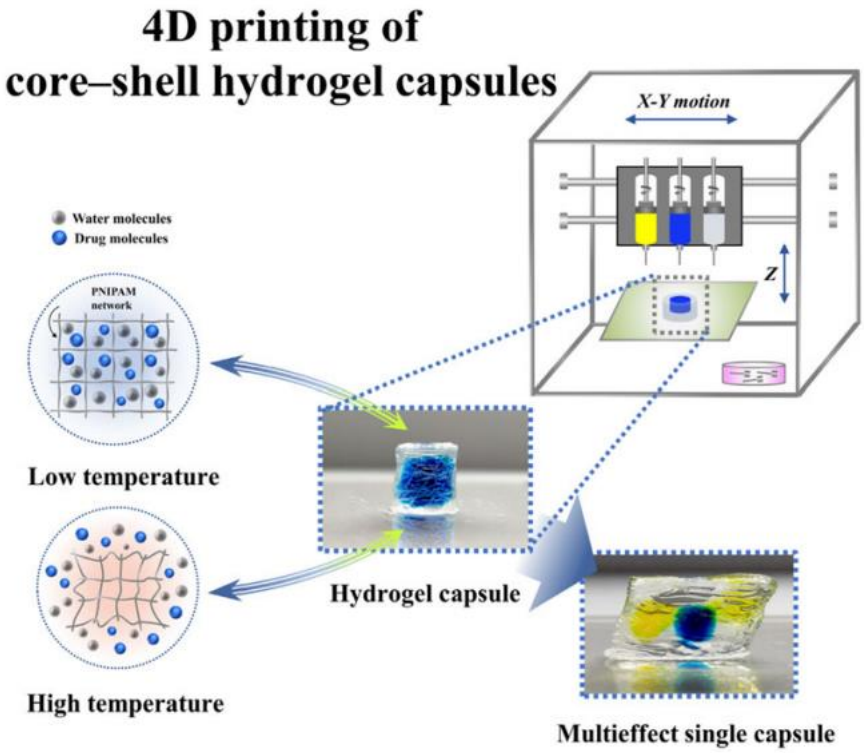

Figure 1.11: pH-Responsive polymer vesicles for controlled enzyme encapsulation and release (55).

Another study by Asy-Syifa *et al.* emphasized the non-toxic nature of polyvinyl alcohol (PVA) hydrogels and polypeptide/polysaccharide-based hydrogels, respectively (56). These hydrogels exhibited high biocompatibility, non-toxicity, and biodegradability, and have been applied in various biomedical applications including wound healing, drug delivery, tissue engineering, ophthalmic applications, and biosensing (56)

Hydrogels possess a biphasic structure consisting of a solid network that provides their unique properties of elasticity and viscosity. Hydrogels are known for their unique properties of elasticity and viscosity. Elasticity refers to the ability of a material to deform under stress and return to its original shape when the stress is removed, while viscosity is the resistance of a material to flow. These two properties are crucial in determining the behaviours and applications of hydrogels (57). The viscoelastic behaviour of hydrogels is particularly interesting because it allows them to respond to stress with a time-dependent strain (Figure 1.12). This means that they can behave like viscous liquids under certain conditions and like elastic solids under others. The balance between these behaviours depends on factors such as the chemical composition of the polymer chains, the type and degree of crosslinking, and the interactions between the polymer and water molecules.

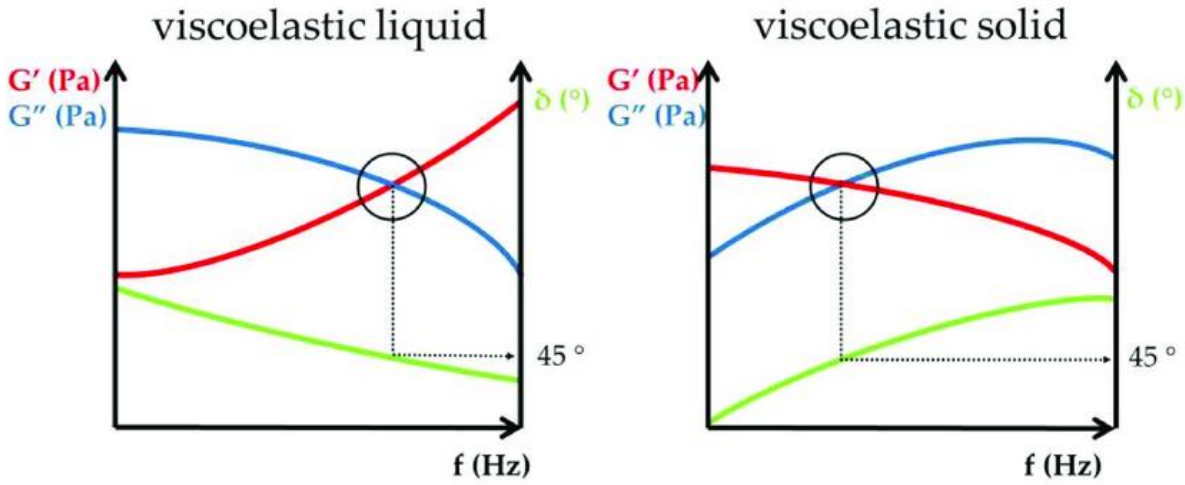

Figure 1.12. A scientific illustration depicting the viscoelastic behaviour of hydrogels (58), where f = Frequency (Hz), G' = storage (elastic) modulus, G" = loss (viscous) modulus and δ = the phase angle.

1.3 Introduction to hydrogels in sustainable agriculture

In recent years, increasing attention has been directed toward the development of biodegradable and environmentally friendly polymeric materials, particularly hydrogels, due to their wide

range of applications in agriculture (18, 59). Hydrogels have demonstrated significant potential in improving soil water retention, enhancing nutrient-use efficiency, and mitigating the negative impacts of water scarcity on crop productivity. Among natural polymer-based hydrogels, systems derived from gellan gum and cellulose, or its derivatives have attracted considerable research interest because of their biocompatibility, renewability, low toxicity, and favourable physicochemical properties (60, 61).

Gellan gum is an anionic extracellular polysaccharide produced by Sphingomonas elodea and is widely recognized for its ability to form strong hydrogels at low polymer concentrations (62). The gelation mechanism involves a temperature-dependent transition from random coils to ordered double helices, followed by aggregation and ionic crosslinking in the presence of mono- or divalent cations such as sodium or calcium ions (62). These properties have enabled the use of gellan gum in diverse applications, including food, biomedical, and agricultural systems. They are superabsorbent polymers that can retain large amounts of water relative to their mass. Their ability to gradually release water and nutrients from the three-dimensional network they form means they have been widely researched for use in sustainable agriculture (16, 63). Gellan gum is an anionic polysaccharide produced by Sphingomonas elodea and can form strong hydrogels at low polymer concentrations through a temperature-dependent gelation process involving double-helix formation and ionic crosslinking with mono- or divalent cations(62). These properties have enabled its use in food, biomedical, and agricultural applications. However, gellan gum hydrogels often exhibit drawbacks such as brittleness, limited mechanical strength, and inadequate control over swelling and water release.(18) Consequently, blending gellan gum with other natural polymers has been widely investigated to enhance its mechanical and functional properties. Cellulose is one of the most well-known materials and reinforcing biopolymer. Cellulose is the most abundant natural polymer and consists of linear β(1→4)-linked D-glucose units. Its high mechanical strength, and elasticity,(64) chemical stability, biodegradability, and abundance make it an attractive reinforcing and material for hydrogel systems (60, 65). In agricultural and environmental applications, different forms of cellulose, including microcrystalline cellulose, nanocellulose, and chemically modified cellulose derivatives such as carboxymethyl cellulose, have been incorporated into hydrogels to enhance their performance (66). When combined with gellan gum, cellulose contributes to the formation of physically crosslinked networks through hydrogen bonding interactions, resulting in improved mechanical properties, enhanced structural stability, and tenable swelling behaviour (67). These improvements are particularly important for hydrogels intended for soil applications, where repeated hydration and

dehydration cycles are common. Previous studies have shown that blending gellan gum with cellulose produces composite hydrogels with improved properties compared to gellan gum alone. These hydrogels are typically prepared by dissolving gellan gum in water at elevated temperature (67), followed by the addition of cellulose or its derivatives and subsequent gelation through cooling or ionic crosslinking.(62) The incorporation of nanocellulose enhances intermolecular interactions, leading to improved mechanical strength and structural stability, particularly under repeated wetting and drying conditions (68). In contrast, water-soluble cellulose derivatives are often used to improve hydrogel homogeneity and processability for agricultural applications.(69) Hydrogels based on gellan gum–cellulose systems have been extensively investigated for use as soil conditioners and controlled-release carriers for water and nutrients (59). These materials exhibit a high capacity for water absorption and can gradually release stored water, thereby improve soil moisture retention and reducing irrigation frequency (18, 59). In addition, the encapsulation of fertilizers within gellan gum–cellulose hydrogels have been shown to reduce nutrient leaching and enhance fertilizer-use efficiency. The incorporation of cellulose plays a key role in regulating hydrogel degradation rates and nutrient diffusion, allowing for more sustained and predictable release profiles (59). Various characterization techniques are used to evaluate gellan gum–cellulose hydrogels, including FTIR to identify intermolecular interactions, XRD to assess crystallinity, and SEM to examine morphology and pore structure. In addition, swelling behaviour, water-retention capacity, rheological properties, conductivity and biodegradation are commonly analysed to determine their suitability for agricultural applications.(70-73)

1.3.1 Role of Hydrogels in Sustainable Agriculture

Hydrogels primary purpose in agriculture is to provide a system for better water management, by enhancing soil water retention, reducing irrigation frequency and saving water. This is particularly beneficial in arid regions or during drought conditions(74, 75). Hydrogels help maintain consistent moisture levels around plant roots, preventing the stress that comes from fluctuations in water availability. This leads to healthier plants and potentially higher crop yields. Hydrogels can also act as nutrient carriers, which trap and slowly release fertilisers over time. This reduces nutrient leaching, pollution and fertiliser wastage, resulting in more efficient fertiliser use, reducing their environmental impact (63). Hydrogels, when used to coat seeds, create a moist environment that improves germination and seedling survival rates (75). Finally, hydrogels can help maintain soil health and fertility by improving soil structure and aeration

(76, 77). They can help prevent compaction, enhance pore connectivity, regulate moisture, and improve oxygen availability in the soil. By maintaining a balance between moisture retention and aeration, they create an optimal environment for root growth, microbial activity, and sustainable agriculture (figure 1.13) (21, 75).

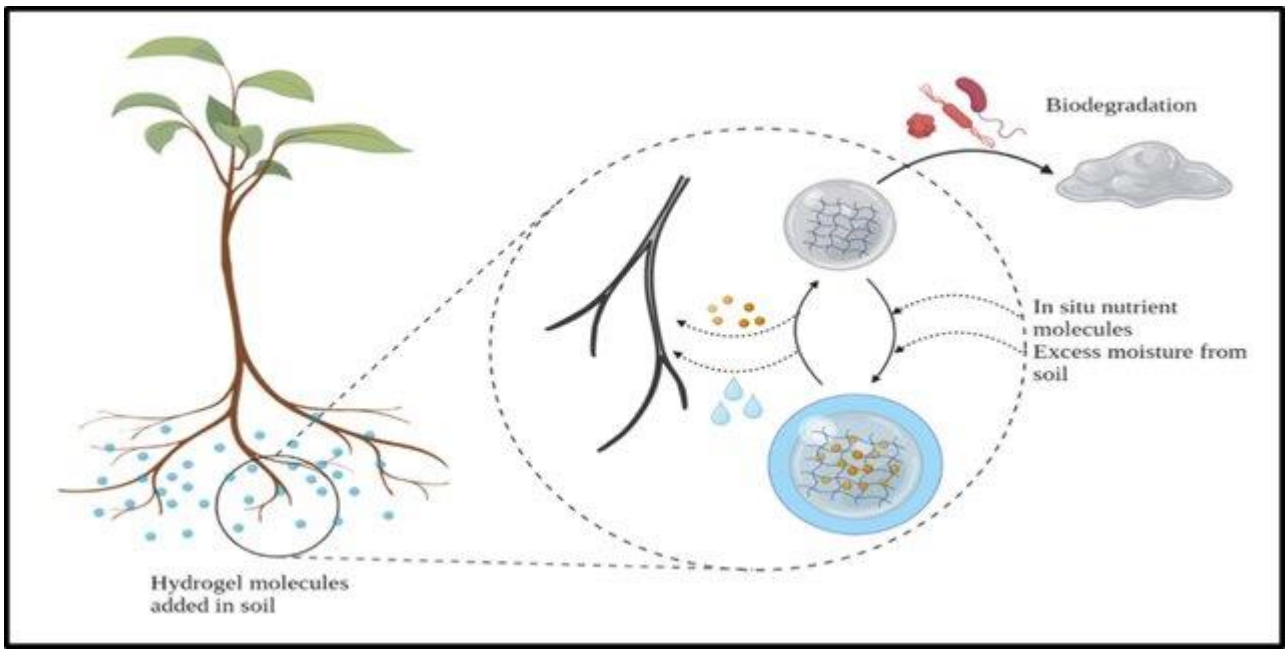

Figure 1.13. An educational diagram illustrating how hydrogels improve soil aeration (75).

When incorporated into soil, they absorb water during irrigation or rainfall and hold onto it. Over time, they release this water to plants as needed, reducing the frequency of watering (Figures 1.14 a and b) (16, 78).

a)

b)

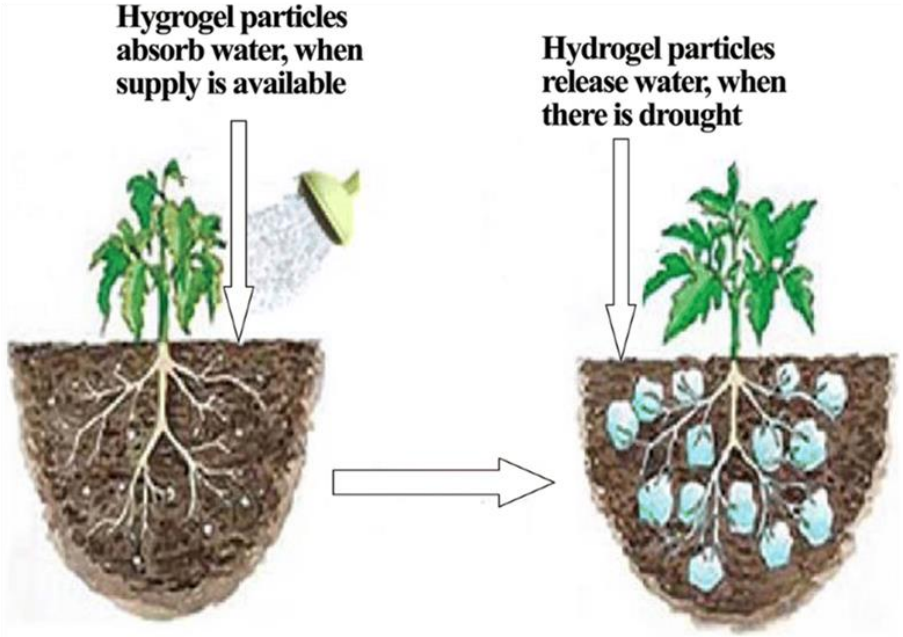

Figure 1.14: a) Hydrogels absorb water in proximity to the plant's roots. b) Change in soil porosity occurs with the swelling of hydrogels (21, 79).

This slow release of moisture helps maintain an optimal balance of water and nutrients in the soil, promoting better plant growth. Studies have indicated that hydrogels can have a significant effect on conserving nutrients and minimizing environmental pollution by reducing the loss of fertilizers, such as urea, into the ground water (80). Sustainable agriculture depends on this slow-release characteristic, which mitigates the risk of nutrient leaching and promotes efficient fertiliser use (77). Moreover, the biodegradable characteristics of numerous hydrogels, particularly those sourced from cellulose, ensure that they do not induce soil toxicity, making them environmentally sustainable alternatives for traditional chemical soil conditioners (81).

1.3.2 Types of Hydrogels Used in Agriculture

Hydrogels can be broadly grouped into three categories: synthetic, semi-synthetic and natural. Their classification is determined by the types of polymers used to make them, and these can have profound effects on their properties and applications. Each different type of hydrogel comes with its own advantages and disadvantages, as summarised in Table 1.2.

Table 1.2: A summary of advantages and disadvantages polymers in agricultural applications.

Kind of hydrogels	**Advantages**	**Disadvantages**
Synthetic Polymers	High durability, efficiency, water retention, slow-release properties.	Non-biodegradable variants cause plastic pollution, making them less sustainable.
Semi-Synthetic	Improved biodegradability, water absorption, and slow release	Higher production costs, potential chemical residues.
Natural Polymers	Sustainable, non-toxic, biodegradable, environmentally friendly.	Lower mechanical strength, limited stability under extreme conditions.

1.3.2.1 Synthetic Hydrogels

Synthetic hydrogels commonly have good mechanical resistance, high water absorption capacity, and long service life. This has made them attractive targets for a variety of applications. Despite this, they are often non-biodegradable and less sustainable (82). Even though synthetic hydrogels are not biodegradable, they are used because they offer strength, stability, customisability, and long-term performance that many natural alternatives cannot yet match. Synthetic hydrogels consist of synthetic polymers, which can be selected or modified to have characteristics such as mechanical strength, swelling behaviour, and degradation rates (83). Many synthetic hydrogels are made up of polymers derived from petrochemical sources. Polyacrylamide (PAM), poly (ethylene glycol) (PEG), and poly (vinyl alcohol) (PVA) have become common chemical compounds employed in the synthesis of hydrogels (Figure 1.16) (77, 84).

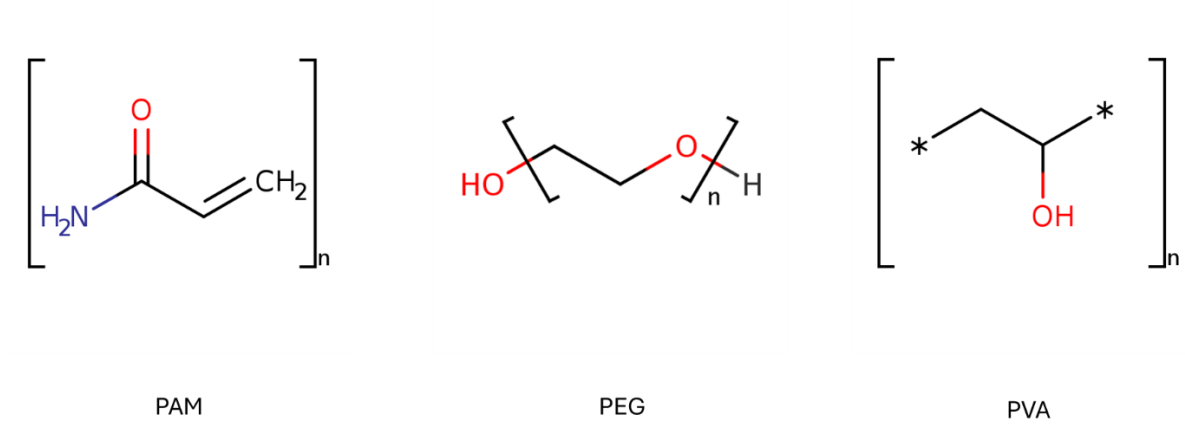

Figure 1.15: An illustration of the molecular structures of these materials PAM, PEG and PVA.

Synthetic hydrogels have significant absorbency and have been extensively utilised in agricultural applications due to their durability and water retention capabilities. These materials are preferred for their tuneable properties, which can be easily modified by altering their polymer composition, which can affect their chemical properties, crosslinking density, and molecular weight (85). The capacity to customise the physical and chemical properties of synthetic hydrogels is one of their greatest benefits. The mechanical properties of these hydrogels can be precisely adjusted to suit certain applications, including tissue scaffolding in biomedical engineering and soil components in agriculture (86). This tunability supports the creation of hydrogels that can respond to external stimuli, like pH or temperature, improving their functionality (87)**.**

1.3.2.2 semi-synthetic polymers

Semi-synthetic polymers are materials derived from natural polymers such as cellulose or proteins that have been chemically modified to improve their properties. They combine the advantages of natural materials (like biodegradability and biocompatibility) with those of synthetic materials (such as strength and stability). They are used in various fields including textiles, packaging, and medicine, and are environmentally important because they reduce reliance on petroleum-based materials and help decrease pollution.(88)

1.3.2.3 Natural hydrogels

Natural hydrogels are generated from substances from renewable biological sources. Protein-based materials, polysaccharide-based materials, and those derived from decellularized tissue are the three groups of naturally derived hydrogels (89).
Although often less absorbent than synthetic alternatives, natural hydrogels are biodegradable and environmentally friendly, making them more appropriate for use in sustainable agriculture (90, 91).

The selection between synthetic and natural hydrogels usually depends on agricultural requirements and environmental variables. Synthetic hydrogels have adjustable characteristics and superior performance (77), whereas natural hydrogels serve as a more sustainable and environmentally friendly option. Recent studies have concentrated on integrating synthetic and natural materials to develop hybrid hydrogels that amalgamate the benefits of both categories. One of the most widely researched hybrid hydrogels is the Chitosan-Polyacrylamide (Chitosan-PAM) hydrogel, which combines natural chitosan (a biopolymer) with synthetic polyacrylamide (PAM) to enhance water retention, mechanical stability, and nutrient release (77, 92).

1.4 Polysaccharide Hydrogels

Polysaccharide hydrogels have attracted considerable interest in agricultural applications because to their unique features, such as enhanced water retention capacity, biocompatibility, and biodegradability (93). Polysaccharides are complicated carbohydrates composed of ten or more repeating units of monosaccharides or disaccharides (Figure 1.16), and can come from plants (94). Their repeating units in the polymer backbone are typically six-carbon monosaccharides, and the usual formula can be expressed as $(C_6H_{10}O_5)n$, where "n" varies between 20 to 3000 usually. These repeating units include sugars such as glucose and fructose.

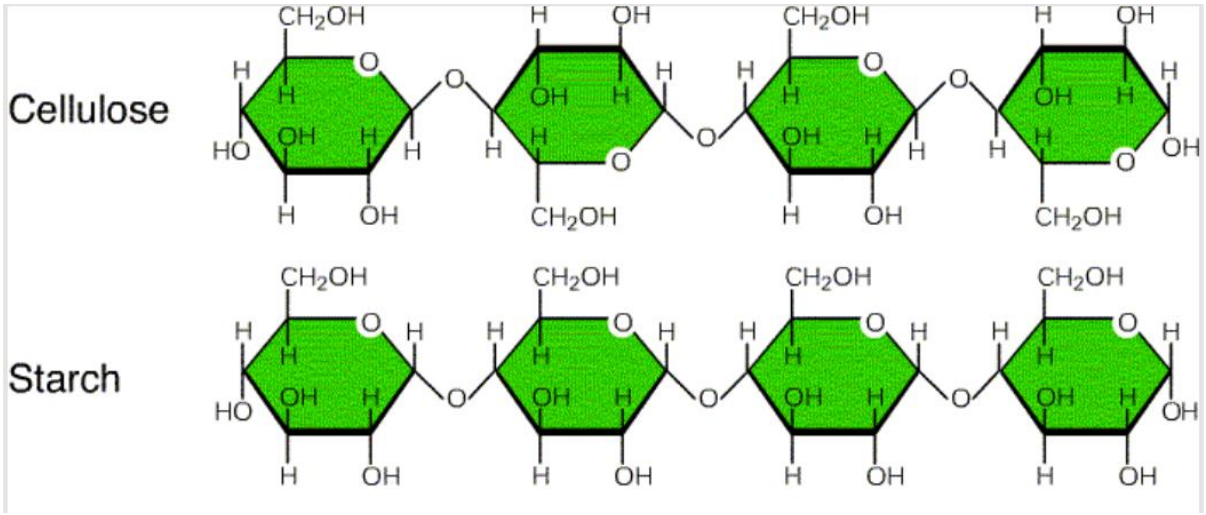

Figure 1.16: The polysaccharide molecular structures of cellulose and starch, showing the repeating units in the polymer backbone (95).

Polysaccharides are polymers that combine monosaccharides with glycosidic bonds. They are a crucial category of macromolecules that perform multiple functions in living organisms, including energy storage and structural support (96). These common molecules originate from multiple sources, including plant (cellulose, pectin, and guar gum) algal (alginate and carrageenan), microbial (dextran and xanthan gum), and animal (chondroitin sulphate, hyaluronan, chondroitin, and heparin) origins (96, 97).

Polysaccharides possess a molecular structure that can either be linear or highly branched. They can also be monofunctional or polyfunctional. These polysaccharides play crucial roles in various biological processes and have significant applications in food, medicine, and agriculture (98).

Polysaccharides are primarily made up of repeating monosaccharide units, which can include glucose, fructose, galactose, mannose, and others. The specific type of monosaccharide, as well as the ratio of different sugars, can greatly influence the properties of the polysaccharide (99). For example, cellulose is composed of β-D-glucose units (Figure 1.17), while starch consists of both α-D-glucose (amylose) and branched structures(amylopectin) (99).

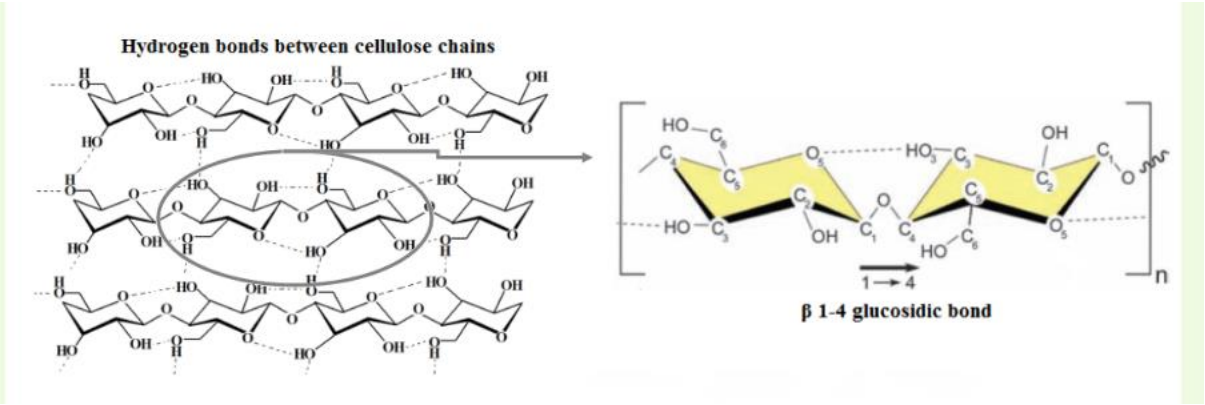

Figure 1.17: In cellulose, -D β -Glucose units are joined by β-(1,4) glycosidic linkage. There are no branching chains in cellulose.

Polysaccharides contain various functional groups, such as hydroxyl (-OH), carboxyl (-COOH), and amino (-NH_2) groups, which can be involved in chemical modifications. These modifications can enhance their properties for specific applications, such as improving solubility, stability, and bioactivity. For example, Carboxymethyl Cellulose (CMC) is made by the carboxymethylation of the hydroxyl (-OH) group of the polysaccharides. This happens by first oxidising them to a carboxylic acid and then methylating them to form the carboxymethyl (-CH_2COOH) functional group. This reaction improves water solubility, viscosity, gelation, and biodegradability.

Polysaccharides may possess substantial molecular weights, frequently attaining millions of Daltons, depending on the number of monosaccharide units. Furthermore, certain polysaccharides exhibit a linear structure, whilst others possess a branching configuration. Glycogen is a highly branched polysaccharide that facilitates the fast mobilisation of glucose (Figure 1.18) (100). The extent of branching influences solubility, viscosity, and gel formation, which are critical qualities in food and medical applications. For example, branching results in an increase in solubility, which means the presence of more branch points results in more free ends, which leads to more hydrophilic interactions.

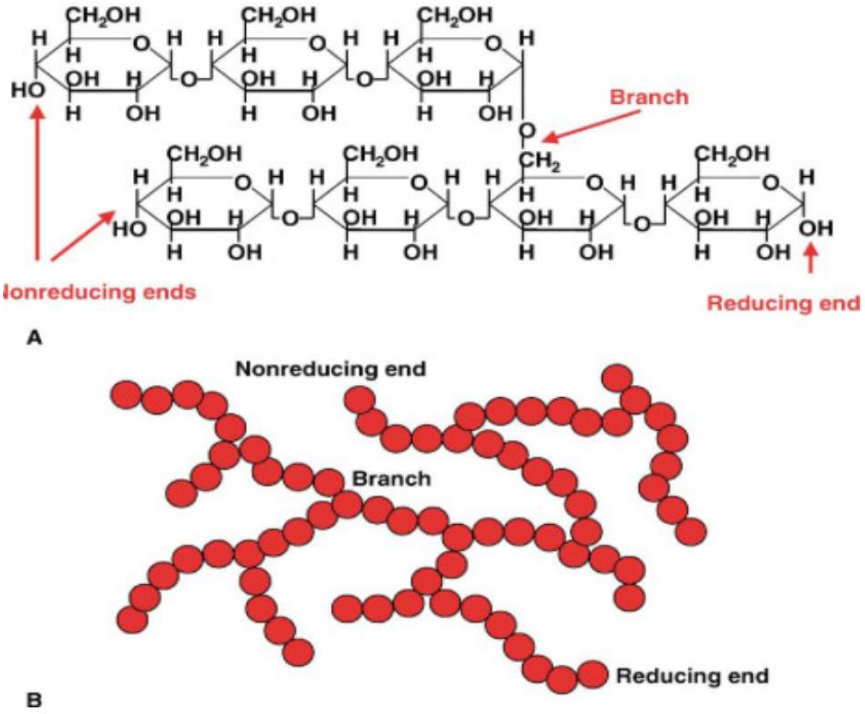

Figure 1.18: The structure of glycogen (100).

The way monosaccharides are linked together through glycosidic bonds determines the polysaccharide's structure and function. For instance, cellulose has β (1→4) glycosidic linkages (Figure 1.17), which provide rigidity and strength, making it a key structural component in plant cell walls. In contrast, starch has α (1→4) and α (1→6) linkages, allowing it to serve as an energy storage molecule in plants (Figure 1.19) *(99)*.

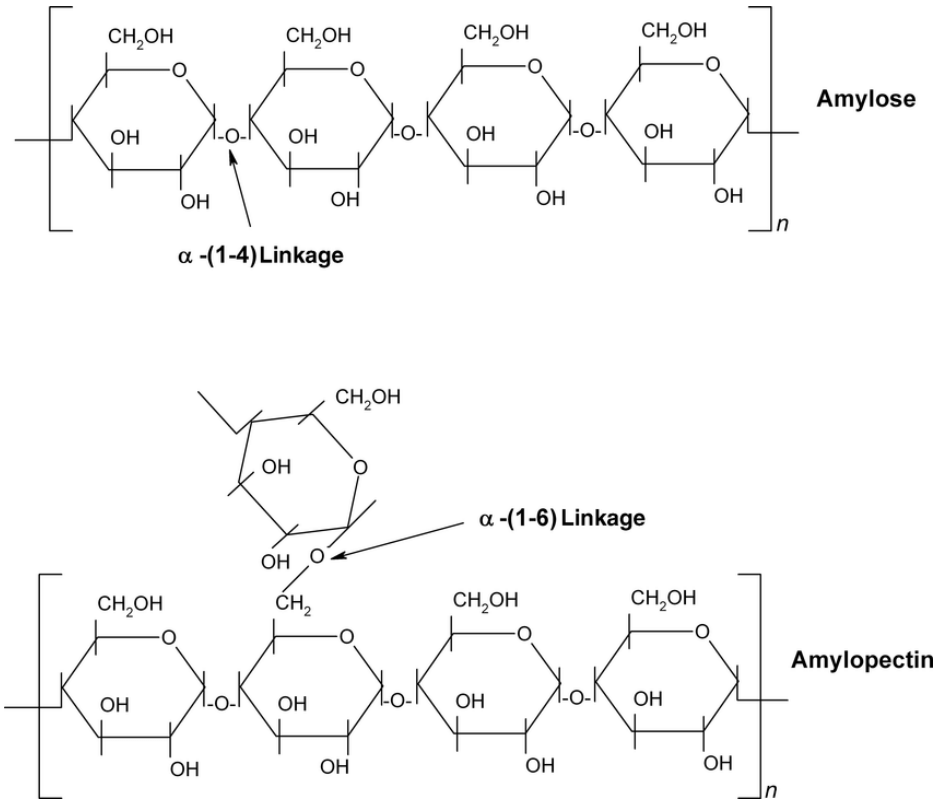

Figure 1.19 Amylose and amylopectin are the chemical structures of starch (101).

Linear polysaccharides are a class of carbohydrates characterized by their straight-chain structures, consisting of repeating monosaccharide units linked by glycosidic bonds. These polysaccharides play crucial roles in various biological processes and have significant applications in food, medicine, and agriculture.

1.4.1 Cellulose

Cellulose is a structural polymer that exists in the cell walls of plants and animals (102, 103). Cellulose is a linear polysaccharide consisting of β-D-glucose units connected by β (1→4) glycosidic bonds (Figure 1.20).

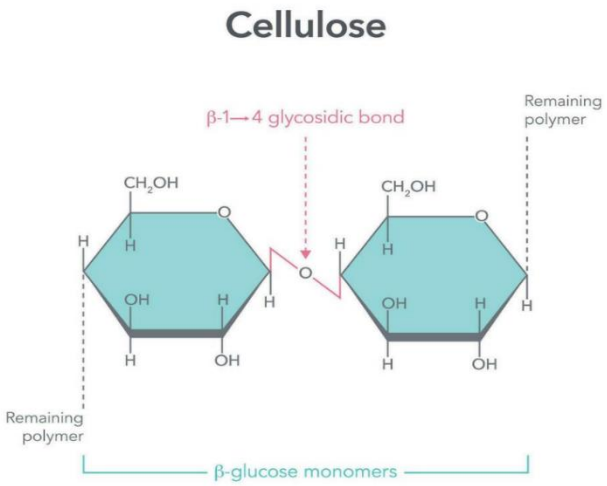

Figure 1.20: Fragment (repeating unit) of a cellulose chain (104).

This arrangement allows cellulose to build strong hydrogen bonds between chains, leading to a hard and insoluble fibre.

1.4.2 Gellan Gum

Gellan gum is a linear polysaccharide produced by the bacterium Sphingomonas elodea (105, 106). It is composed of repeating units of glucose, rhamnose, and glucuronic acid, linked together in a specific arrangement that gives it unique gelling properties. Gellan gum is known for its ability to form gels in the presence of cations, particularly calcium ions (107).

Gellan gum is widely used as a gelling agent in the food industry, particularly in the production of jellies, desserts, and sauces Gellan gum is produced in bulk by fermenting Sphingomonas elodea in large tanks, then separating, purifying, drying, and milling the polymer into a fine powder.(108, 109). It is produced commercially via microbial fermentation, typically using Sphingomonas species, followed by purification and drying. Its ability to form firm gels at low concentrations allows for the creation of products with desirable textures (74). In addition to its gelling properties, gellan gum acts as a stabilizer in emulsions and suspensions, helping to maintain the consistency and quality of food products (74). Gellan gum's gel-forming ability is also exploited in pharmaceutical applications for controlled drug release systems, where it can encapsulate active ingredients and release them gradually for example, gellan gum combined with Laponite, a synthetic clay, was investigated to create beads for the controlled release of drugs by Adrover *et al* (110). Laponite was incorporated to enhance the mechanical stability of

the beads and modify the release profile of the encapsulated drugs, making them suitable for oral drug delivery applications.

There are two structures of gellan gum 1- high acyl (H) and 2-low acyl (L) (Figure 1.21). The high acyl analogue carries acetate groups, which prevent ionic interactions across cross-linking (111). Most commercial products of gellan gum use a high pH medium to remove any acetyl groups. These substituents are removed by alkali treatment to yield low acyl gellan gum (LAGG) (112).

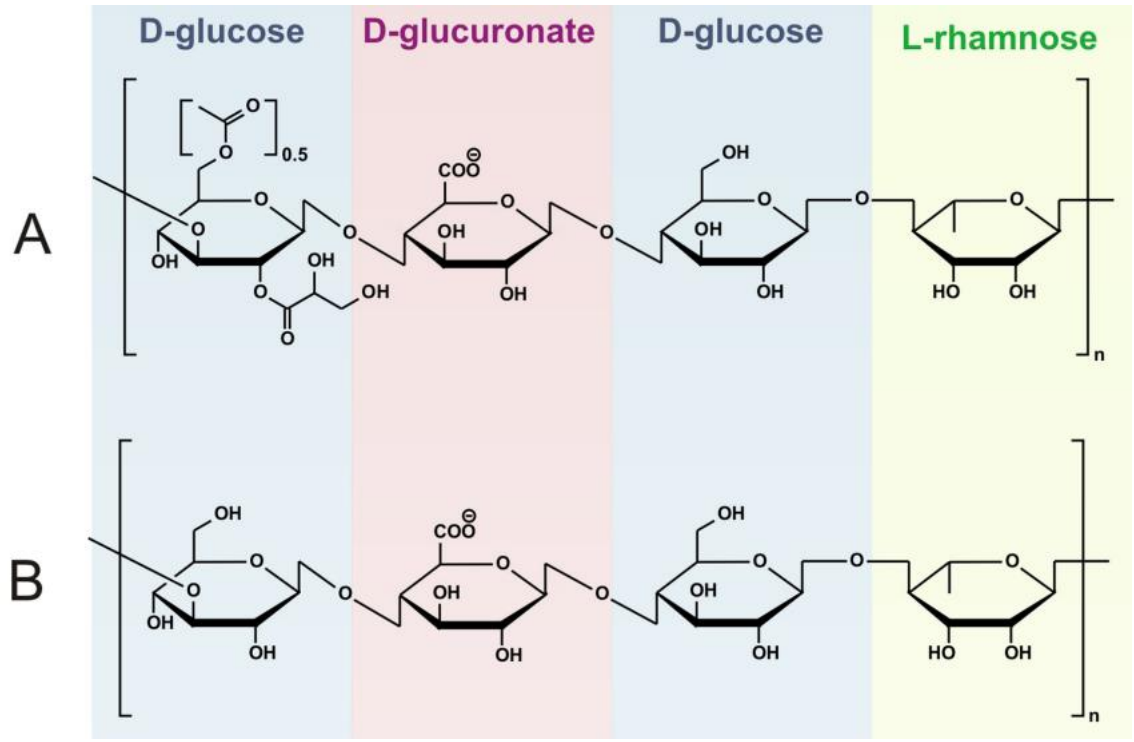

Figure 1.21: Gellan gum's structure differs between its native (A) and low-acyl (B) forms (113).

1.4.3 Guar Gum

Guar gum is another linear polysaccharide derived from the seeds of the guar plant. It is primarily composed of a mannose backbone with galactose side groups, forming a galactomannan structure (Figure 1.22) (114).

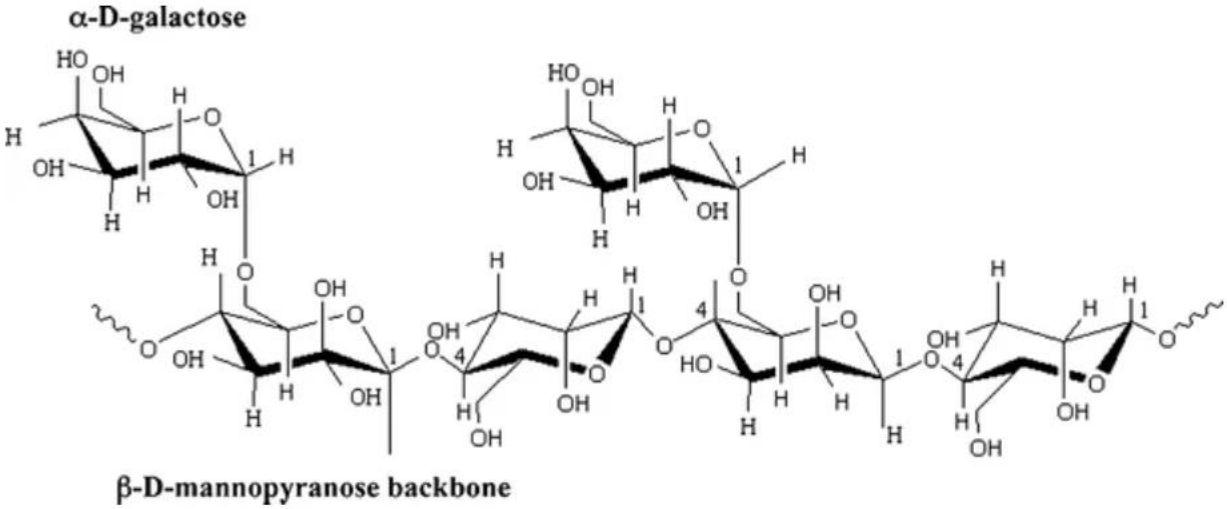

Figure 1.22: Molecular structure image for Guar Gum (114).

Guar gum is known for its high-water solubility and thickening properties, and it is widely used in the food industry as a thickening agent and stabilizer. It is particularly effective in controlling the viscosity of sauces, soups, and dairy products. Its ability to form viscous solutions at low concentrations makes it a valuable ingredient in many processed foods.(115) Guar gum is classified as a hydrocolloid, which means it can absorb water and swell to form a gel-like consistency. This property is beneficial in applications such as gluten-free baking, where it helps improve the texture and moisture retention of baked goods.(116) In agriculture, guar gum is used as a soil conditioner and water-retaining agent. Its ability to absorb and retain moisture helps improve soil structure and supports plant growth, particularly in arid regions.(117) Additionally, guar gum can be utilized in controlled-release fertilizer formulations, enhancing nutrient availability to crops (117).

1.5 Hydrogel Composites

Hydrogel composites are hybrid materials composed of a hydrogel matrix integrated with reinforcing or functional fillers, such as nanoparticles, fibers, clays, or carbon-based materials. The incorporation of these additives enhances the mechanical strength, stability, and functional performance of the hydrogel, enabling their use in a wide range of biomedical, tissue engineering, and environmental applications

They are a relatively new development in material research. Their specific properties result in them having varied applications in medicine, tissue engineering, and environmental science (118). These materials are generally produced by mixing hydrogels with diverse reinforcing agents or functional additives, which improve their mechanical properties, swelling characteristics, and response to external stimuli (119). The mechanical characteristics of hydrogel composites can be substantially enhanced with the incorporation of nanoparticles (120). The incorporation of nanoclays, such as Laponite, have shown to enhance the mechanical strength of hydrogel composites through the interaction between the polymeric matrix and nanosilicates, resulting a higher Young's modulus than that of pure hydrogels (121).Similarly, the use of reduced graphene oxide as a flexible crosslinking agent enhances the mechanical and electrical properties of polyacrylamide hydrogels, making them ideal for strain sensors and self-healing applications (Figure 1.23) (122, 123).

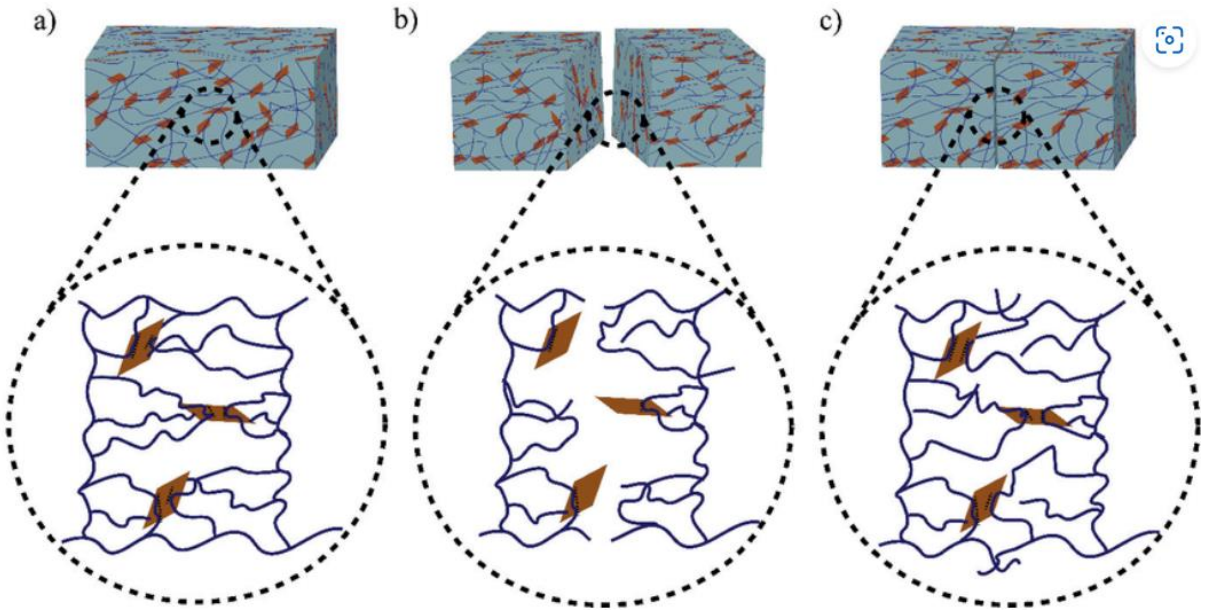

Figure 1.23: An illustration of how functionalized graphene oxide crosslinked polyacrylamide hydrogel heals. The bonding mechanism for (a) fresh hydrogel sample, (b) cut sample, and (c) healed sample.(124)

New methods of formulation and synthesis has also allowed further fine-tuning of the properties of hydrogel composites. Methods like 3D printing has enabled the production of complex structures with exact control over mechanical characteristics and porosity. This is especially crucial in tissue engineering, where the mechanical integrity and bioactivity of scaffolds are essential for facilitating cell proliferation and tissue regeneration, as shown by Jin *et al.* (121, 125)]. Moreover, the stimuli-responsive properties of composite hydrogels can be

improved by choosing constituent materials, such as conductive polymers. These materials facilitate the creation of electro responsive hydrogels that can alter their properties in reaction to electrical signals an attribute especially advantageous in regenerative medicine, where precise responses to physiological conditions are essential for directing tissue growth and repair. (126). One such example is Polypyrrole (PPy) which, when combined with natural hydrogels like alginate or gelatin, forms conductive scaffolds that aid nerve regeneration through electrical stimulation. These hydrogels are applied in treating spinal cord injuries (SCI) and peripheral nerve damage by promoting neural cell growth and axonal regeneration. The ability to create hydrogels that respond to pH changes or other stimuli opens new avenues for their application in drug delivery and biosensing (127). pH-responsive hydrogels, such as those made from chitosan or poly (acrylic acid), swell or degrade based on pH changes. They are used in targeted drug delivery in the gastrointestinal tract and in biosensing, particularly in glucose sensors, where pH variations trigger hydrogel swelling to signal glucose levels.

In this research we are focusing on hydrogels as they apply to the general areas of sustainable agriculture, with specific focus on hydrogel properness and characterisation in the context of to their unique ability to absorb and retain substantial amounts of water, regulate soil moisture, and supply nutrients in a controlled way.

Hydrogel composites are revolutionizing agriculture by improving soil moisture retention, plant growth, and sustainable farming practices by absorbing and retaining water, addressing water scarcity and soil degradation (128). Hydrogel composites utilised in agriculture often consist of a foundational hydrogel material (such as synthetic polymers or natural polysaccharides) amalgamated with other components that enhance their characteristics.

1.5.1 Types of Hydrogel Composites Used in Agriculture

Hydrogel composites can be made using synthetic, semi-synthetic, or natural hydrogels in combination with various additives or reinforcing agents. These composites largely retain the structural, stability, and biodegradability characteristics of the base hydrogel materials, while the added components are used to enhance specific properties such as mechanical strength, moisture retention, nutrient release, or resistance to environmental degradation in agricultural applications. A wide range of materials can be incorporated into hydrogel matrices to tailor their properties for specific agricultural needs. Among the most promising strategies is the use of bio-based and nano-scale additives,

1.5.1.1 Biochar-Composite Hydrogels

Biochar is a carbon-rich product obtained from the pyrolysis of organic materials (like wood, crop residues, or manure). When combined with hydrogels, biochar enhances the hydrogel's ability to retain water and nutrients. Biochar is also porous, which helps retain both water and nutrients within the hydrogel soil system. This retained moisture and nutrient availability creates a more stable and resource-rich environment that supports the growth and activity of beneficial soil microorganisms.

1.5.1.2 Nanoparticle-Enhanced Hydrogels

Nanoparticles such as clay, silica, or even graphene oxide can be embedded within hydrogel matrices to enhance their properties. These nanoparticles improve the mechanical strength and stability of the hydrogel, making them last longer in the soil. Additionally, they can act as carriers for slow-releasing nutrients or pesticides, providing sustained benefits to crops.
This report will outline aspects of work on composite hydrogels made from the polysaccharide gellan gum containing difunctionalised cellulose as additives. Whilst much has already been published on the application of similar composite gel materials for other applications, relatively less has been plublished on applications in sustainable agriculture. This is largely due to the historical focus of hydrogel research on biomedical and industrial applications, while agricultural applications have only recently gained attention and present greater environmental and experimental complexity. This thesis has focused more on studying the underlying behaviours of such composite materials and potential roles that they may play in sustainable agriculture rather than looking at any specific applications in that field.

1.6 Introduction to sustainable agriculture

Sustainable agriculture is essential for addressing the problems of environmental degradation, food security, and economic sustainability in farming systems (129).

1.6.1 Hydrogels in sustainable agriculture

Hydrogels are essential in agriculture, especially in improving seed germination and encouraging plant development (90). These three-dimensional polymer networks can absorb and store substantial quantities of water, making them beneficial for enhancing soil moisture

availability, which is crucial for seed germination. The utilisation of hydrogels in seed germination has shown beneficial results, especially under adverse soil conditions.

1.6.2 Role of Hydrogels in Seed Germination

1.6.2.1 Enhanced Water Availability and Reducing Watering Frequency

Hydrogels, when combined with soil or placed near seeds, hydrogels establish a stable moisture environment by absorbing water during irrigation and gradually releasing it to the surrounding soil as moisture levels decrease. This sustained water availability provides a continuous supply for seed germination, reduces plant water stress, and minimizes delayed or uneven germination, thereby improving overall germination efficiency and reducing the frequency of irrigation. (76, 130). Hydrogels improve soil water availability, aiding plants in surviving the physiological problems related to drought (130, 131). Hydrogels offer economic benefits in agriculture by reducing irrigation frequency, saving water costs and labour, and improving water efficiency, especially in regions with limited water resources (132). Hydrogels, when biodegradable, can enhance soil ecosystem health by absorbing and retaining water, reducing irrigation needs, and promoting microbial activity, which is crucial for nutrient cycling and plant health (133).

1.6.2.2 Improving Soil Structure

The physical structure of soil can also be enhanced using hydrogels (134). Hydrogels improve soil structure by increasing porosity and decreasing compaction, hence encouraging root health, transfer of gases, and germination, which aids in root penetration and seedling establishment. Despite initial delay due to mechanical compression, hydrogels' water retention properties enhance overall success, making them ideal for arid or drought-prone regions (135). Moreover, hydrogels have proven efficiency for increasing seed germination under poor soil conditions. For example, Peyrusson's research showed hydrogels significantly increased seed germination rates in sandy soils, demonstrating their potential in challenging environments like poor soil quality or limited water availability (136). The research utilized a commercial hydrogel known as STOCKOSORB® 660 Medium from Evonik Industries. This hydrogel is essentially a crosslinked potassium polyacrylic acid designed to absorb and retain water, thereby enhancing the moisture content of the soil (136). Experiments took place in Mars-regolith analog soils (sand, clay, alkaline pH ~9) collected near the Mars Desert Research Station in Utah (136). They tested both radish seeds (Raphanus sativus 'Scarlet Globe') and spearmint seedlings

(Mentha spicata) (Figure 1.24). They found that radish seed germination was entirely unsuccessful in both pure sand and clay soils without hydrogel. When 0.1% hydrogel was added to sand, germination improved significantly to 27% on average. However, the hydrogel had no effect in clay soil, where radish seeds still failed to emerge.

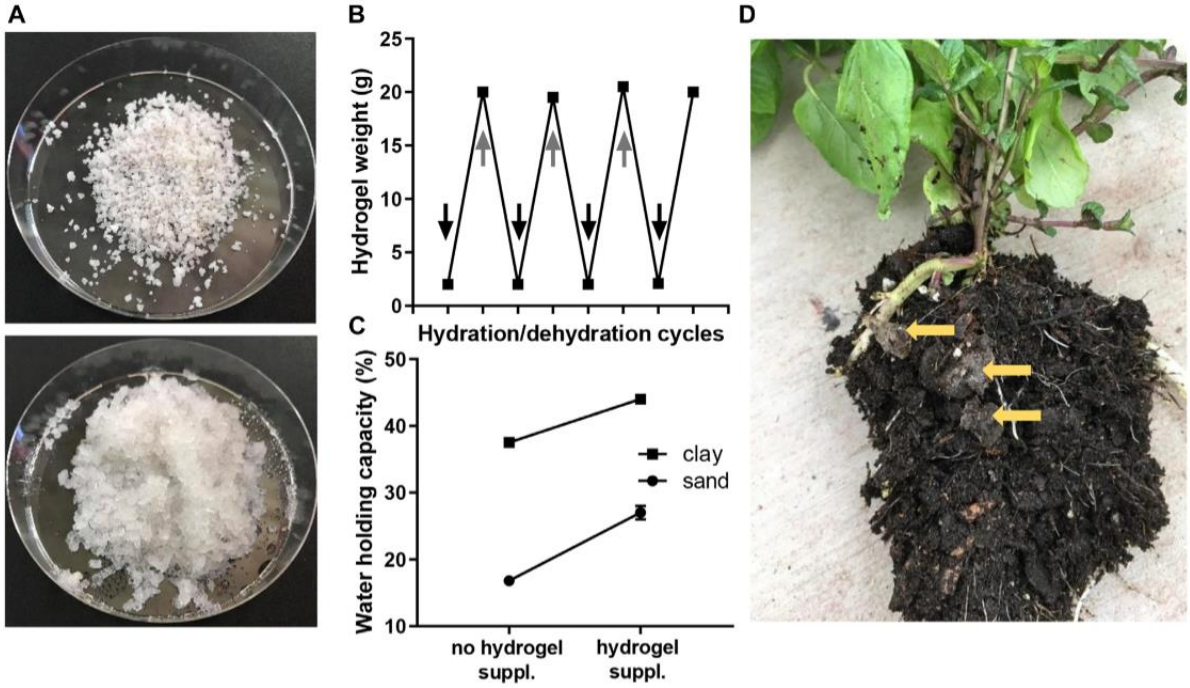

Figure 1.24: Hydrogels have been found to improve plant growth in Mars analog conditions. They have improved water holding and release properties and can be used to improve plant growth in sand and clay soils. The study was conducted on spearmint roots.(136)

1.6.2.3 Protecting Seeds from Drought Stress

Hydrogels support seeds in surviving drought by keeping consistent moisture levels, reducing the effects of temporary stress, and enhancing the chance of successful germination when incorporated into the soil or used as seed coatings, hydrogels absorb excess water during irrigation and release it gradually as the soil dries out, maintaining a more stable moisture profile over longer periods of time and promoting seed germination in low-water soil. Research indicates that the employment of hydrogels can dramatically enhance the germination rates of diverse crops, such as maize and barley, in drought circumstances (137-139).

1.6.2.4 Enhanced Nutrient Availability

Hydrogels have the potential to assist in the retention of nutrients in the soil. By holding water in the soil longer, they prevent nutrients from being washed away through leaching. This means

that the essential nutrients remain closer to the root zone, making them more available for uptake by the germinating seeds and young seedlings. Hydrogels not only enhance germination rates but also work as carriers for micronutrients, ensuring that seeds receive vital nutrients during germination. Nandkishore Thombare *et al.* investigated the application of guar gum-based hydrogels as a controlled delivery mechanism for micronutrients, illustrating that these hydrogels can facilitate an extended release of nutrients, leading to seedling growth (132). The authors work demonstrated how a guar-gum-based hydrogel effectively provided slow and controlled boron release in soil, extending nutrient availability and promoting seedling growth through improved germination conditions (132). Researchers tested a specially designed guar gum-based hydrogel—enhanced with boric acid and synthetic materials for its ability to retain water and slowly release nutrients. When applied to soil with chickpea seedlings, it improved early plant growth, showing promise for practical use in agriculture.

In conclusion, hydrogels present themselves as a promising soil addative for agricultural applications, particularly seed germination. Their ability to retain water, provide a controlled release of nutrients, and improve soil structure makes them valuable tools for enhancing plant growth and sustainability. As research continues to explore the potential of hydrogels in agriculture, their integration into farming practices is likely to play a pivotal role in addressing the challenges posed by water scarcity and soil degradation.

1.6.2.5 Hydrogels as additives to improve soil performance

To improve the performance of hydrogels in soil and increase their agricultural advantages, several additives may be included into the hydrogel matrix. These additions can enhance water retention, nutrient accessibility, soil structure, and offer advantages for plant growth.

1.6.3 Soil Nutrient Additives (Fertilizers)

1.6.3.1 Macronutrients (Primary Nutrients)

One of the most common additives to hydrogels is fertilizers, particularly those containing essential nutrients such as potassium (K), nitrogen (N), and phosphorus (P) (Table 1.3). Their incorporation into hydrogels allows for a controlled release of essential elements as the hydrogel slowly releases water. When exposed to water, such as from rain or irrigation, hydrogels absorb moisture and swell, forming a gel-like matrix as water permeates their three-dimensional polymer network. This swelling allows dissolved nutrients embedded within the

hydrogel to gradually diffuse from the interior to the surrounding soil. The rate of nutrient release is controlled by factors including the hydrogel's crosslink density (with tighter networks slowing release), as well as environmental conditions like temperature, pH, and soil moisture. Because the nutrients are retained within the swollen matrix, they are protected from rapid leaching, allowing for a sustained and buffered nutrient supply that supports steady plant uptake over time (140).

Table 1.3: The table shows how important elements can be beneficial for plants.

Elements	**Efficacy**	**Examples**
Nitrogen (N)	Supports leaf and stem growth	urea, ammonium nitrate
Potassium (K)	Enhances plant resilience and water regulation	potassium chloride, potassium sulphate.
Phosphorus (P)	Essential for root development and flowering	Superphosphate, rock phosphate

The slow release ensures that plants obtain a consistent supply of nutrients over time, enhancing nutrient usage efficiency and reducing the necessity for frequent fertilisation (128, 141). Researchers have demonstrated that hydrogels enriched with potassium and phosphorus improve their properties as fertilisers and significantly impact soil performance, especially in carbonate and saline rich soils (142). The addition of these nutrients directly enhances plant growth and development, making the hydrogel more effective in supporting crop yields. These hydrogels function by absorbing and retaining substantial amounts of water and dissolved nutrients, forming a gel-like matrix that serves as a reservoir. This matrix ensures a consistent supply of moisture and nutrients to plant roots, even during periods of limited rainfall or irrigation. In addition, slow-release fertilizers, such as urea formaldehyde, can be effectively encapsulated within hydrogels to provide a controlled and continuous supply of nitrogen to plants. Formaldehyde is a widely used slow-release nitrogen fertilizer, which aligns with plant uptake rates and minimizes leaching losses.

1.6.3.2 Secondary Nutrients

Secondary nutrients play crucial roles in various plant physiological processes and are vital for optimal growth and development (Table 1.4).

Table 1.4: Essential Secondary Nutrients for Plant Growth (143).

Nutrient Symbol	Primary Function	Common Sources
Calcium (Ca)	Strengthens cell walls and prevents diseases.	Calcium nitrate, lime, gypsum
Magnesium (Mg)	Essential for chlorophyll production and photosynthesis	Magnesium sulphate (Epsom salt), dolomite, kieserite
Sulphur (S)	Improves protein synthesis and enzyme activity	Gypsum, elemental sulphur, ammonium sulphate

1.6.3.3 Micronutrients (Trace Elements)

Incorporating small amounts of minerals including iron (Fe), zinc (Zn), manganese (Mn), copper (Cu) and boron (B) into hydrogels solves micronutrient shortages in soil, hence improving plant development and overall soil fertility (Table 1.5).

Table 1.5: Table: Micronutrients and Their Roles in Plant Physiology

Elements	Efficacy
Iron (Fe)	Helps in chlorophyll formation.
Zinc (Zn)	Aids enzyme function and seed production.
Manganese (Mn)	Involved in energy production.
Copper (Cu)	Supports photosynthesis and enzyme function.
Boron (B)	Crucial for cell wall structure and reproductive growth.

The interaction between soil organic matter (SOM) and chelated micronutrients is another important factor influencing nutrient availability (144). For example, chelation with humic substances: humic and fulvic acids, components of SOM, have functional groups that can bind iron ions, forming soluble chelated complexes. This chelation increases iron solubility, making it more accessible for plant uptake. The presence of these natural chelating agents in SOM is particularly beneficial in preventing iron deficiencies in crops.

1.6.3.4 Organic Matter Additives and Soil Organic Matter (SOM)

Organic matter additives are organic materials that are added to the soil to increase organic matter content. While SOM is the stable organic material in soil, resulting from the decomposition of organic matter additives over time (Table 1.6). (145)

Table 1.6: The definitions and clear differences between organic matter additives and soil organic matter.

Feature	Organic Matter Additives	Soil Organic Matter (SOM)
Definition	Raw organic inputs added to soil	Decomposed, stable organic material in soil
State	Fresh or partially decomposed	Fully decomposed and long-lasting
Examples	Compost, manure, crop residues, biochar	Humus, microbial biomass, decomposed plant & animal material
Function	Provides nutrients, feeds microbes, improves soil	Stores nutrients, retains moisture, improves structure
Longevity	Short-term impact (breaks down over weeks/months)	Long-term stability (can persist for decades)

The two most common Organic matter additives are compost and biochar. Compost is an organic material made from decomposed plant and animal waste and contains components such as carbon, nitrogen, microbial life and essential nutrients (N, P, K, Ca, Mg, S). Microbial breakdown and chemical transformations are necessary for compost to become SOM.

Compost, an organic matter, can be included into hydrogels to improve soil fertility, enhance soil structure, and increase microbial activity. This also enhances the soil's capacity to hold water and nutrients, hence increasing the efficacy of the hydrogel. In addition, Biochar is a carbon-rich material that is made through pyrolysis, which involves heating organic matter like wood, crop residues, or manure in a low-oxygen environment. It is a carbon-rich material derived from biomass, can be combined with hydrogels to enhance soil moisture retention and increase soil carbon content. It also promotes beneficial microbial growth, improves soil structure, and reduces nutrient leaching (146).

1.6.3.5 pH Adjusters and Buffers

Some additives can be added to hydrogels to act as pH adjusters and buffers. Adding lime (calcium carbonate) to hydrogels can help increase soil pH in acidic soils, improving plant growth. Similarly, gypsum (calcium sulphate) can be used to improve soil structure, particularly in saline soils, by replacing sodium ions with calcium.

In alkaline soils, sulphur can be incorporated into hydrogels to lower the pH, making the soil more suitable for crops that prefer slightly acidic conditions. Janani and Rajeswari found that gypsum and hydrogels effectively improve soil moisture retention and infiltration rates by facilitating soil particle flocculation and water movement (147).

1.6.3.6 Biodegradable additives

Additionally, the use of biopolymers, such as hydroxypropyl methylcellulose and polyvinyl alcohol, can improve the performance of hydrogels as slow-release fertilizers. Kareem *et al.* synthesized a slow-release fertilizer gel that demonstrated enhanced water retention and nutrient release characteristics (148). The use of nanomaterials in hydrogels can enhance their performance by improving their mechanical properties and water retention capabilities. This is especially beneficial in sandy soils. Combining hydrogels with other soil conditioners can improve soil structure and aeration, leading to better water infiltration and reduced runoff. This integration of hydrogels and their additives can contribute to soil health and sustainability, making them a crucial tool in modern farming (149, 150).

1.7 Analytical methods applied in this research

1.7.1 Dialysis

In chemistry, dialysis, refers to the use of different rates of diffusion through a semipermeable membrane for the purpose of separating a chemical mixture of suspended colloidal particles from dissolved ions. Dialysis separates small molecules from larger ones using a semipermeable membrane: small ions and solutes diffuse through the membrane into the surrounding solution, while large molecules remain trapped inside. A mixture containing suspended colloidal particles and dissolved ions is separated from the buffer solution (the dialysate) by a dialysis membrane. The dissolved ions and small molecules pass through the membrane, leaving the colloidal particles behind. This is driven diffusion, which is random motion of particles leading to a net motion from areas of high concentration to low concentration (Figure 1.25) (151).

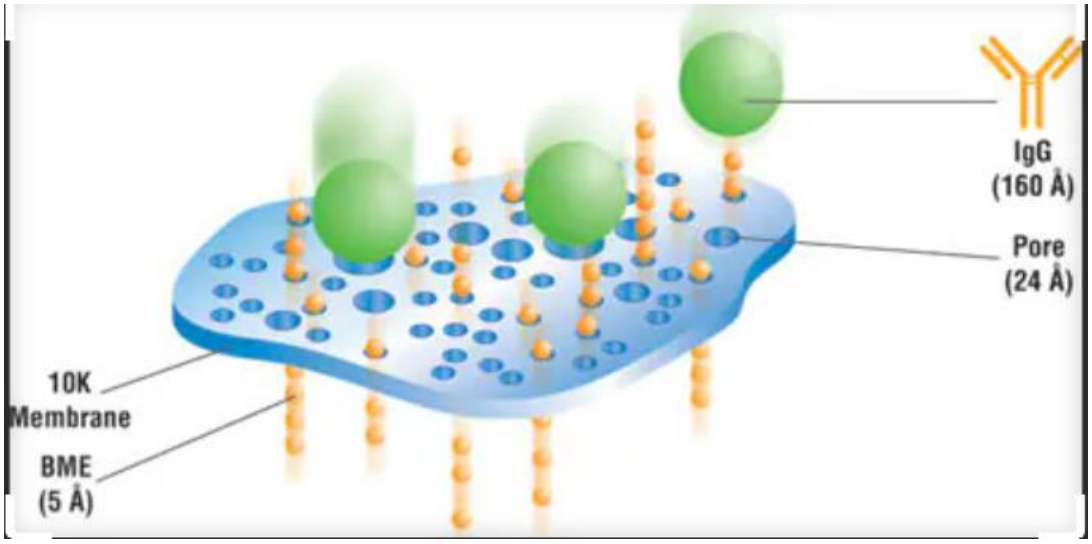

Figure 1.25: Dialysis process method showing the diffusion of small molecules/ions into the dialysate. The protein is too large to diffuse through the pores of the membrane (152).

The pores of the membrane can control the size of the molecules which are able to pass through to the dialysate. The membrane acts as an entity that moderates the permeation of chemical substances in contact with it (153). One of the membranes' properties of great significance is the ability to control the permeation rate of different species, by the membrane pore sizes or the chemical properties such as the charge. Among others, solution-diffusion is one of best processes where the permeants are “dissolved” in the membrane and diffuse through it according to the concentration gradient. Diffusion dialysis (DD) is a process where the solutes pass through the ion exchange membrane (IEM), from the high concentration side to the low concentration side (154). These membranes can be either anion exchange membranes or cation exchange membranes. Herein, we focus on the use of anion exchange membranes for hydrogels (155).

1.7.2 Freeze-drying (lyophilisation)

Freeze-drying, also known as lyophilisation, is a technique employed to remove water from a sample, while retaining its structure. The process proceeds in distinct stages: (i) the sample is initially cooled, often using liquid nitrogen, to freeze the solvent; (ii) the system’s pressure is then reduced; and (iii) the frozen water undergoes sublimation, transitioning directly from the solid to the gaseous phase, leaving behind the non-volatile constituents. This method is favoured over conventional drying approaches that rely on heat-induced evaporation, which can lead to structural deformation of the residual matrix due to surface tension effects (156). Sublimation, the direct phase transition from solid to gas without an intermediate liquid phase,

is central to this process (157). Freeze-drying is particularly advantageous for preserving sample integrity, as it operates at low temperatures and minimizes thermal and mechanical stress (158). It is widely applied in the stabilization of colloidal and biological systems, including bacterial cultures, biomedical products (e.g., blood), and food substances (159, 160). Additionally, it offers significant benefits for sample storage and transport by maintaining physicochemical stability, solubility, and reducing the risk of degradative reactions such as hydrolysis, oxidation, and ion exchange (159-161). The core principle underpinning freeze-drying is sublimation, which can be represented in phase diagrams as transitions from point C to D or C to E, as shown in Figure 1.26 (162).

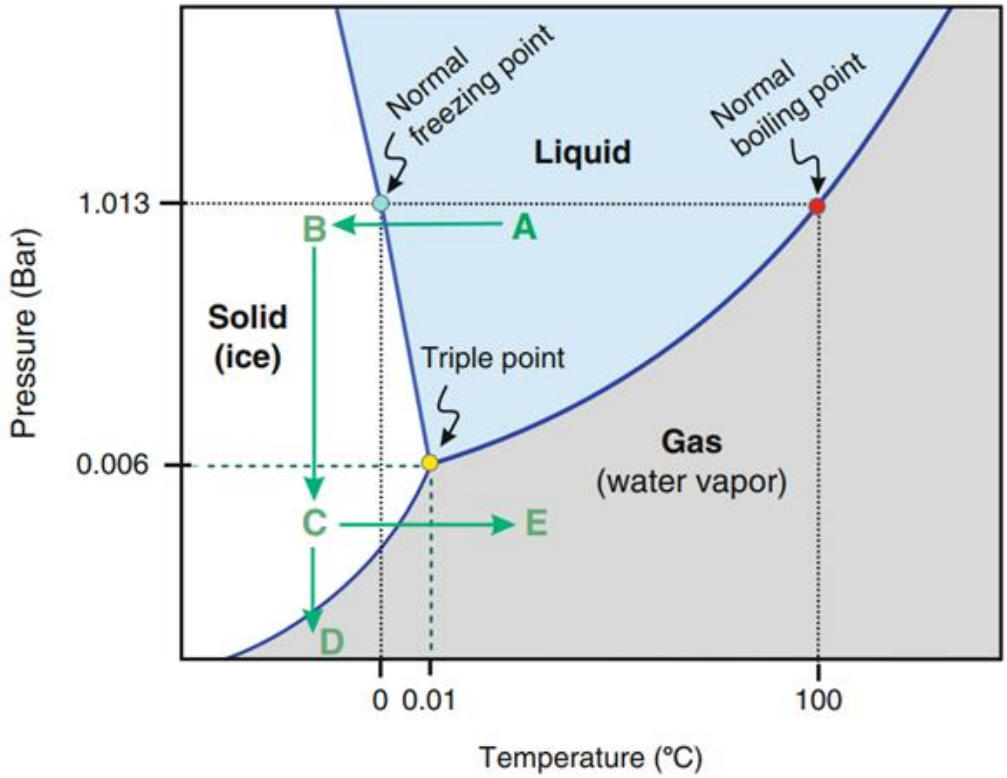

Figure 1.26: An example phase diagram with the different phase, From A to B the liquid is cooled at constant pressure until it freezes. From B to C the pressure is lowered while the substance remains solid. From C to D the solid is gently warmed at low pressure, causing it to sublime into a gas.(162).

1.7.3 Scanning Electron Microscopy (SEM) and Energy Dispersive Xray Spectroscopy (EDX)

An electron microscopy uses electrons to observe objects under extreme magnification. It is an important instrument that utilises a concentrated beam of electrons to generate images of a sample. The electrons have interactions with atoms within the sample, generating various signals that include valuable information regarding the surface structure and composition of

the sample. The scanning electron microscope (SEM) is a device which produces images from the surface being investigated. A conventional optical microscope uses photons and therefore is not suitable to see samples smaller than the photon wavelength (380-700 nm). However, In SEM, electron energies range from 0.1 keV to 30 keV, with lower energies providing surface detail and higher energies increasing penetration. The electron beam is focused using electromagnetic lenses, apertures, and stigmators, ensuring a sharp, high-resolution image for material analysis. SEM uses a beam of electrons instead of photons, which means it can achieve resolution better than 1 nm, as such it is very good for studying crystal morphology on a micro-scale (163, 164).

A typical SEM works by emitting an electron beam focused on one or two lenses at a spot that is about 0.4-5 nm in diameter. Electrons are generated using a process called thermionic emission from a heated filament inside the electron gun. (Figure 1.27a-1). The inner part of the SEM is under vacuum to allow the electrons to pass through to the sample effectively (Figure 1.27a-2). The electron beam is accelerated using an electric field created by a high-voltage power supply. towards the anode and focused through an electromagnetic coil (Figure 1.27a-3 and 4). Another coil then controls the movement of the beam in a raster scan pattern over a rectangular region of the surface of the sample (Figure 1.27a-5 and 6). Then, the electrons interact with the surface of the material under investigation. More precisely, this interaction is between the electron beam and regions of electron density in the sample. (Figure 1.27a-7). Several kinds of detectors can be installed in the device to collect information from different signals to image the region examined and turn it into a picture (Figure 1.27a-8 and 9).

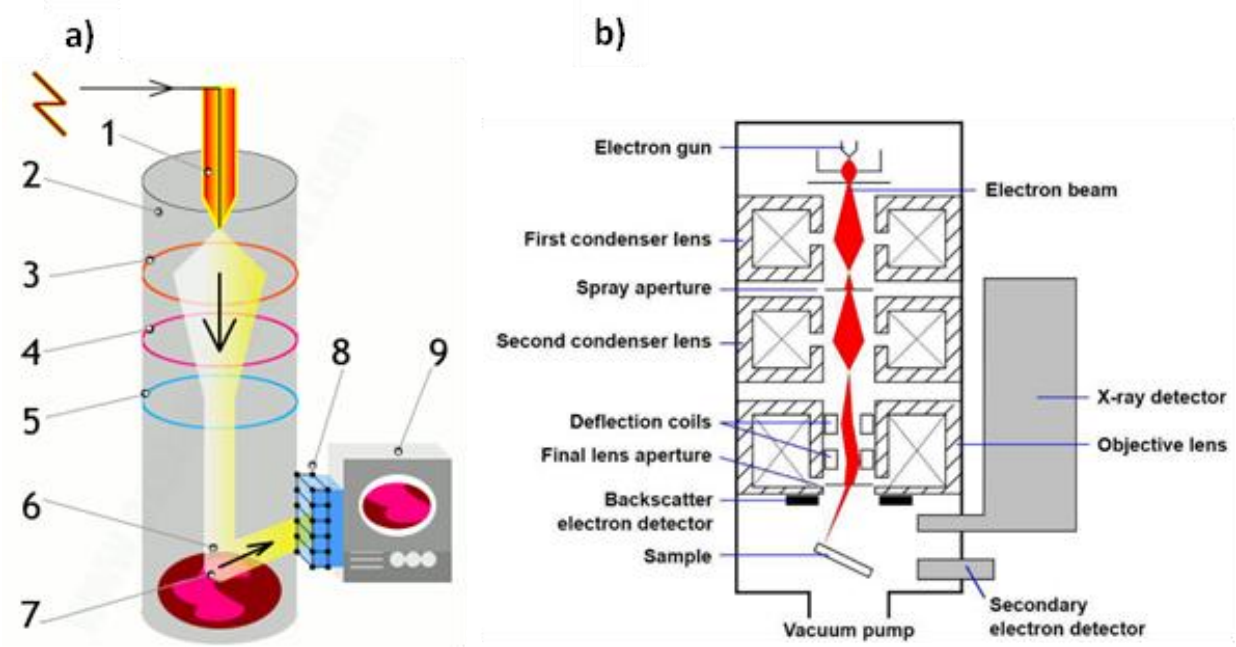

Figure 1.27: Schematic diagram of an SEM. a) The simplified parts 1-9. Figure from (89), b) The detailed schematic.

The SEM measures the different signals due to interactions of the electron beams with atoms located at various depths in the sample. In SEM, the depth of interaction depends on the electron beam energy (keV), the sample composition, and the type of signals generated. Different signals arise from different depths, affecting the type of information obtained from the sample. These signals are secondary electrons (SE), back-scattered electrons (BSE), and characteristic X-rays emitted (Figure 1.28) (165).

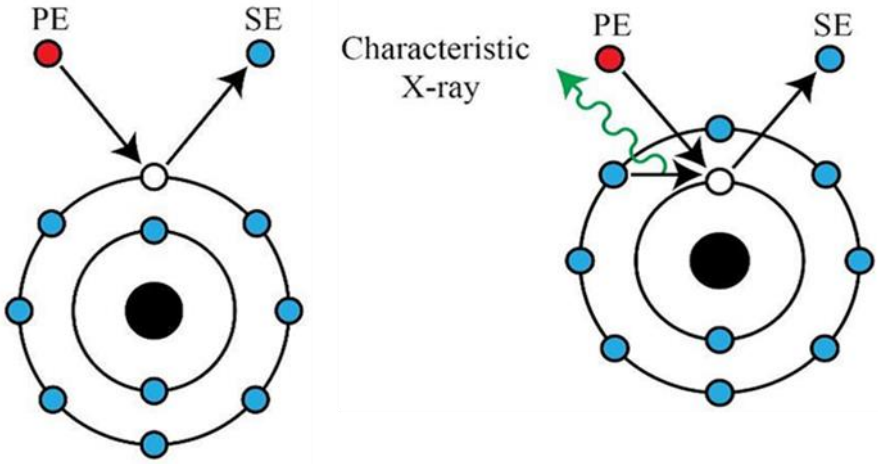

Figure 1.28: Mechanisms of emission of (a) secondary electrons (SE); and (b) characteristic X-rays from atoms of the sample. PE represents a primary electron.(166)

The secondary electron detectors are present in all SEMs, but the machine may have other detectors to measure other possible signals. Imaging using secondary electron procedure ensures the emission of secondary electron from atoms which are close to the surface of the

sample. Primary electrons (PE) emit an electron from the sample surface that escapes to the detector. The escaping electron is the secondary electron captured by the detector producing a signal forming the image. When electron beam causes emission of an inner shell electron from the sample, a characteristic X-ray is emitted (165). This can be detected to measure the distribution of elements in the sample. The back-scattered electrons are reflected by the sample by elastic scattering and can give information about atomic number (167).

Primary Electrons (PEs) are high-energy electrons from the electron gun, responsible for interacting with the sample. While Secondary Electrons (SEs) are low-energy electrons emitted from the sample surface, mainly used for detailed surface imaging in SEM (Table 1.7).

Table 1.7: Shows the most important differences between electrons.

Feature	**Primary Electrons (PEs)**	**Secondary Electrons (SEs)**
Source	Emitted from SEM's electron gun	Emitted from sample surface
Energy Level	1–30 keV (high-energy)	<50 eV (low energy)
Function	Generate various signals, penetrate deep	Surface imaging, high contrast
Penetration Depth	Deep (interaction volume)	Shallow (surface-sensitive)
Detection	Not directly detected	Collected by ETD (Everhart-Thornley Detector)

Scanning Electron Microscopy (SEM) is a powerful tool for material characterization, offering high-resolution visualization of surface topography, large surface areas for defects detection, and the ability to analyze surface atom composition with EDS, making it versatile for various sample types. SEM equipment is expensive, requires specialized training, and requires complex preparation processes. Samples must be vacuum-stable, and it's limited in studying non-conductive samples unless coated. Additionally, it doesn't provide colour information due to grayscale images based on electron interactions. (168).

1.7.4 BET surface area measurements

In materials science and other research areas, the surface area measurements are very important. Smaller particle sizes increased the surface area-to-volume ratio which can affect the properties of a material. Also, the internal pore volume and the pore size distribution are important to study for materials that are porous or have that potential internal void spaces(169). BET is the most common method for measuring the surface area and pore size distribution. Stephen Brunauer, Paul Hugh Emmett, and Edward Teller (BET) first published the BET theory in 1938. It involved the physical adsorption of gas particles onto a solid surface and acts as a

basis for an important analytical technique to measure the surface area of specific materials. It can also measure the total pore volume, micropore (<2 nm) and mesopore (>50 nm) distribution, surface energy, and modelling of pore size. The BET theory extends the Langmuir theory by considering multilayer adsorption.

$$X = \frac{P}{p_0} \qquad \textit{Equation 1.1}$$

Where:

- P = is the measured pressure of the adsorbate gas
- p_o = is its saturation pressure at the temperature of the experiment.

The surface area can then be calculated by equation 1.2.

$$S = \frac{p_0 . v_m N_A A}{m\ R\ T} \qquad \textit{Equation 1.2}$$

Where:

- **S** = surface area (m^2/g)
- $\mathbf{N_A}$ = Avogadro's number
- **A** = cross-sectional area of one gas molecule (m^2)
- **m** = mass of the sample (g)
- R = Universal gas constant.
- T = Temperature
- P_0 = Gas pressure
- v_m = monolayer adsorbed gas volume (m^3/mol or $cm^3(STP)/g$ depending on convention)

Equation 1.2 calculates the specific surface area of a material by relating the amount of gas required to form a monolayer on the surface to the molecular area and the mass of the sample. It normally uses nitrogen at its boiling point (-196 °C) and calculates the volume of nitrogen adsorbed to the sample surface.

While the BET theory provides a valuable framework for estimating surface area from nitrogen adsorption measurements, it relies on several idealized assumptions. These include a homogeneous surface, negligible interactions between nitrogen molecules, and the possibility of infinite multilayer adsorption at saturation. In practice, real surfaces are often surfaces aren't homogenous, nitrogen molecules at their condensing point will have some interactions, adsorption at saturation in a porous material can't be infinite and it will be limited by the pore size. (170, 171)

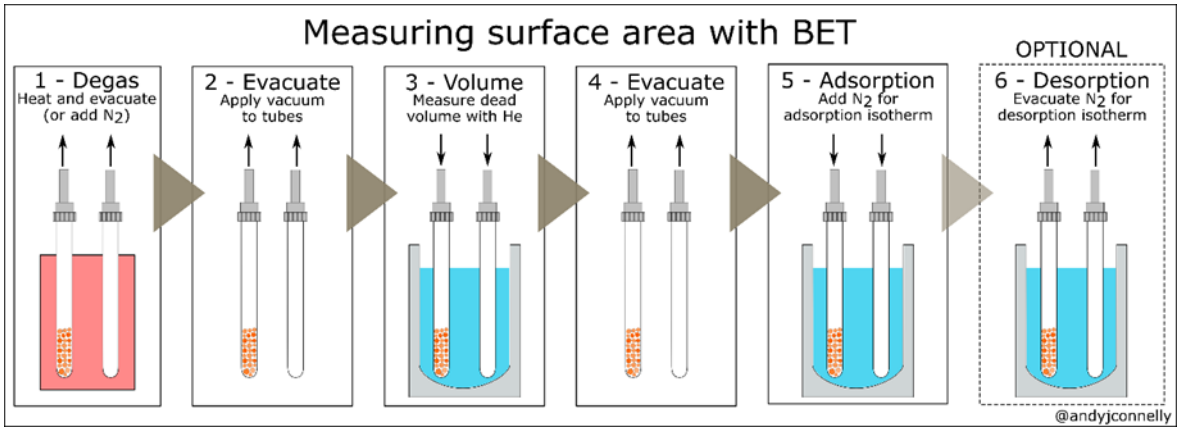

Figure 1.29: Measuring of surface area with BET. Figure from (93).

The BET surface area is calculated from measuring the nitrogen isotherm. The steps are shown in Figure 1.29. The first step is getting rid of gas the sample and then evacuate it and the sample tubes, to remove any adsorbed gasses that are present before the measurement. Then, the volume is measured for the "free space", usually with an inert gas. Then the inert gas is removed under vacuum, and the adsorption isotherm measurement is carried out. Nitrogen is dosed into sample at different pressures, and the volume of nitrogen adsorbed is corrected with the free space volume (Free space volume = Total chamber volume – volume occupied by the solid sample). It's a correction factor to isolate the true volume of gas adsorbed onto the material's surface. . The last step is the opposite of adsorption isotherm the desorption isotherm is measured using a vacuum in stepwise pressure reduction.

1.7.5 Ionic conductivity measurement using a conductivity meter

Conductivity measurements are a fundamental technique for monitoring ionic release from hydrogels, as high conductivity readings indicate an increased concentration of free, mobile ions in the surrounding solution. Ionic conductivity therefore reflects the extent of ion dissociation and transport rather than the total ionic content. Although ionic crosslinking introduces charged species into the hydrogel network, a high degree of ionic crosslinking can restrict ion mobility by binding ions within the polymer matrix, resulting in lower measured conductivity. In contrast, weaker or partially dissociated ionic crosslinks facilitate greater ion release and lead to higher conductivity readings. When applied effectively, it provides a non-destructive, real-time method for studying release kinetics, making it an essential analytical tool in materials science, agriculture, and biomedical research. High conductivity readings occur when the hydrogel releases many free ions into the surrounding solution, whereas

strongly ionically crosslinked hydrogels typically show lower conductivity because the ions remain tightly bound within the network.

1.7.5.1 Introduction to ionic conductivity

The device that measures ionic conductivity is commonly known as electrical conductivity meter or ionic conductivity meter. This device is used to measure the ability of a solution to conduct electricity, ionic Conductivity (κ) is the measurement of the electrical current of a solution, most measured in micro-Siemens per centimetre (μS/cm), where conductivity is the reciprocal of the resistivity ($\kappa = 1/\rho$). The key factor in studying ion transport in hydrogels is ionic conductivity. It measures how well ions move through a medium, providing insights into the release kinetics of elements from hydrogels (172). In hydrogel research, conductivity measurements help quantify the release of elements by monitoring changes in the solution's conductivity over time.

Ionic conductivity values depend on the ionic strength of the solution, the ions present, and the ion concentration(173-175). As the temperature can affect a solution's conductivity, calibration is required before use. A conductivity meter emits an electrical charge via a conductivity probe, which is dipped into the solution being tested. If there is an increase or decrease in the number of dissolved ions, it will result in an increase or decrease in the electrical charge. A conductivity metre can measure this charge and provide you with the solution's conductance (G, in Siemens, S) (176), which is the reciprocal of the resistance (R, in ohms, Ω): G = 1/ R).

1.7.5.2 Working principle of the conductivity meter

Ionic conductivity is indicative of the ability of the ions in the solution to transmit electric current. The greater the number of ions, the greater the ability of the solution to conduct electricity. A conductivity meter sends a small electric current through the solution and measures the resistance or electrical conductivity of the solution. This measurement is then converted to conductivity values. The conductivity readings are influenced by several factors, including the concentration of ions, temperature, and the nature of the solvent (177, 178).

The Jenway 4510 is a general-purpose meter that measures conductivity, total dissolved solids (TDS), and temperature. The Jenway 4510 conductivity metre is a widely utilised instrument in various scientific fields, particularly in chemistry and environmental science, for measuring the electrical conductivity of solutions. This device is noted for its accuracy and reliability, making it suitable for a range of applications, from basic laboratory experiments to complex

research studies. the Jenway 4510 conductivity meter is a critical tool in scientific research, providing accurate and reliable measurements of electrical conductivity across diverse applications, including surfactant studies (179, 180), environmental assessments (181), and biological investigations (182, 183).

Calibration of the Jenway 4510 is crucial for accurate measurements. Standard solutions, such as potassium chloride (KCl), or by directly entering the cell constant, are often used for this purpose. The calibration process ensures that the meter provides reliable readings, which is essential for applications in environmental science where precise conductivity measurements can indicate the presence of pollutants or the quality of water sources (184).

Furthermore, the device's ability to measure total dissolved solids (TDS) is also significant, as TDS levels can provide insights into the overall quality of water, which is critical in both ecological studies and industrial applications (184).

1.7.5.3 Components and Measurement Circuit

A conductivity metre typically consists of several key components: electrodes, a measurement circuit, and a display unit (Figure 1.30). The electrodes are fundamental to the operation of a conductivity metre. They are responsible for establishing an electrical connection with the sample being tested.

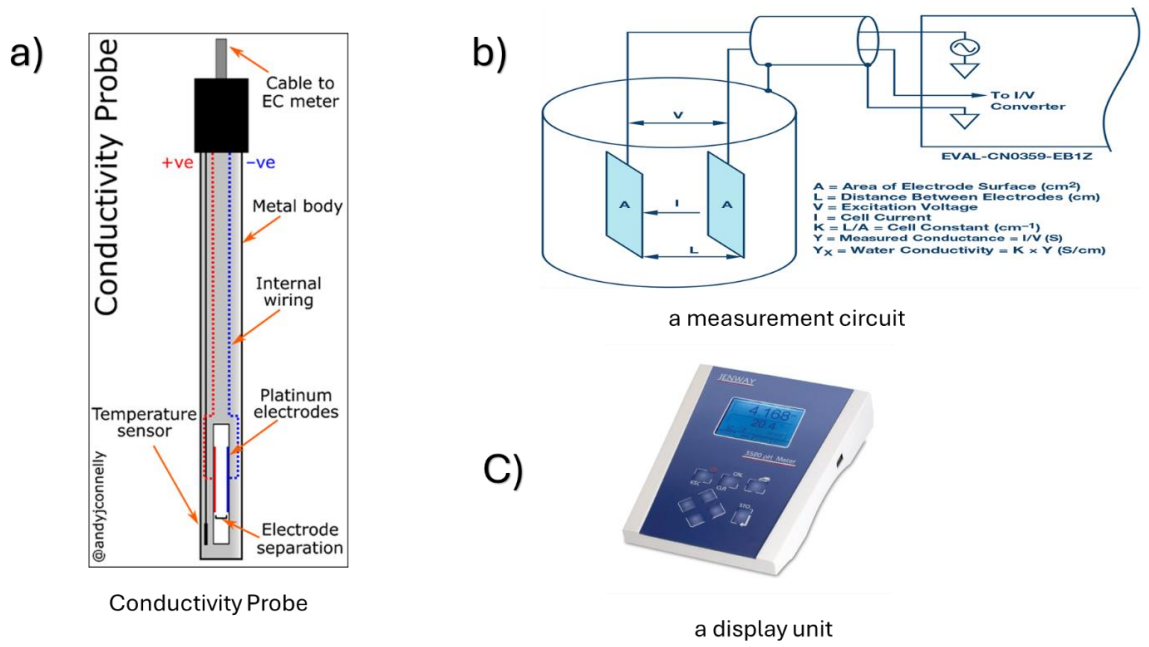

Figure 1.30: Components and working principle of an ionic conductivity measurement system, including a conductivity probe (a), electrode configuration and measurement principle (b), and a Jenway 4510 conductivity meter (c).

The measurement circuit is another critical component of the conductivity metre. It typically includes an oscillator that generates an alternating current, which is passed through the electrodes and the sample. The resulting current is measured to determine the conductivity of the sample. The circuit must be designed to minimise interference from external factors, such as temperature variations and electromagnetic noise, which can affect the accuracy of the readings. Research has indicated that the integration of advanced technologies, such as multi-sensor data fusion, can improve the reliability of conductivity measurements by compensating for these external influences (185). The display unit of a conductivity metre provides the user with the measurement results. This component must be designed for clarity and ease of use, allowing for quick interpretation of data. Modern conductivity metres often feature digital displays that can provide real-time data and may include additional functionalities, such as data logging and connectivity to external devices for further analysis.

1.7.5.4 Theoretical background and mathematical basis

The mathematical law governing electrical conductivity is primarily Ohm's Law, which relates voltage, current, and resistance in an electrical circuit. Conductivity, denoted by κ (kappa), is a property that determines how easily a material allows electric current to pass through it. Here's a breakdown of the key relationships and formulas: Ohm's Law, developed by Georg Simon Ohm during the 19th century, is a fundamental proposition in the fields of electrical engineering and physics. It establishes a straightforward correlation between voltage (V), current (I), and resistance (R) inside an electrical circuit, which can be mathematically represented as V = IR (186). Thus, conductivity is a critical factor in determining how much current a material can carry under a given voltage, and it's fundamentally tied to how much resistance or resistivity the material has.

Summary of the Mathematical Law of Conductivity:

Ohm's Law *relates voltage, current, and resistance:*	$V = IR$	*Equation 1.3*
Conductivity *is the inverse of resistivity:*	$\kappa = 1/\rho$	*Equation 1.4*
Resistance *depends on material properties and dimensions:*	$R = \rho \cdot L/A$	*Equation 1.5*
Current density *and electric field are linked via conductivity:*	$J = \sigma \cdot E$	*Equation 1.6*

Table 1.8: Shows the symbols and their related definitions for equations 2-5.

Symbol	Meaning	Symbol	Meaning
V	Voltage (volts)	L	Length of the material (meters)
I	Current (amperes)	A	Cross-sectional area (meters squared)
R	Resistance (ohms)	E	Electric field (volts per meter)
k or σ (kappa) or (sigma)	Electrical conductivity (siemens per meter) S/m	J	Current density (amps per meter squared)
ρ(rho)	Resistivity (ohmmeters,	G	Electrical Conductance Units: S (siemens)

1.7.6 Inductively Coupled Plasma

1.7.6.1 Inductively Coupled Plasma Mass Spectrometry (ICP-MS)

ICP-MS is a highly sensitive analytical method employed for the detection and quantification of the elements present in different materials, including liquids, solids, and gases (187). It combines the ionisation proficiency of inductively coupled plasma (ICP) with the accuracy and specificity of mass spectrometry (MS). This technology is characterised by its great sensitivity, fast analysing periods of time, and capacity to simultaneously test several elements, making it an attractive choice in environmental monitoring, food safety, and biological research (188-190).

The sample is usually placed into the ICP-MS system in a liquid state (though solid or gas samples can be analysed too), via a nebuliser that transforms the liquid into a fine spray. The mixture then flows into a spray chamber, where larger droplets are removed, ensuring that only fine droplets reach to the plasma. The aerosolised sample is introduced to an inductively coupled plasma, produced by transmitting argon gas through a high-frequency electromagnetic field. This procedure ionises the argon gas, generating a high-temperature plasma (about 10,000 K) that efficiently atomises and ions the sample components. The high temperature of the plasma ensures that almost all elements are transformed into ions. As the sample passes the plasma, atoms within the sample are ionised by the high-energy argon plasma. The ions are then directed towards the mass spectrometer, and pass into a mass analyser, where they are separated based on their mass-to-charge (m/z) ratio. Common mass analysers used in ICP-MS include quadrupole and time-of-flight (TOF) systems. The mass analyser allows for the identification and quantification of the ions present in the sample (176, 178). The ions are detected by an electron multiplier or other ion detector, and the signal is quantified, providing information on the concentration of specific elements in the sample (178). ICP-MS has many benefits, including high sensitivity, the ability to measure multiple elements, the ability to find isotope ratios, and a wide dynamic range. These features make it useful for a variety of tasks

in geochemistry, environmental science, and nuclear research, as well as for measuring elements at very low concentrations, often down to parts per trillion (ppt) levels (Figure 1.31).

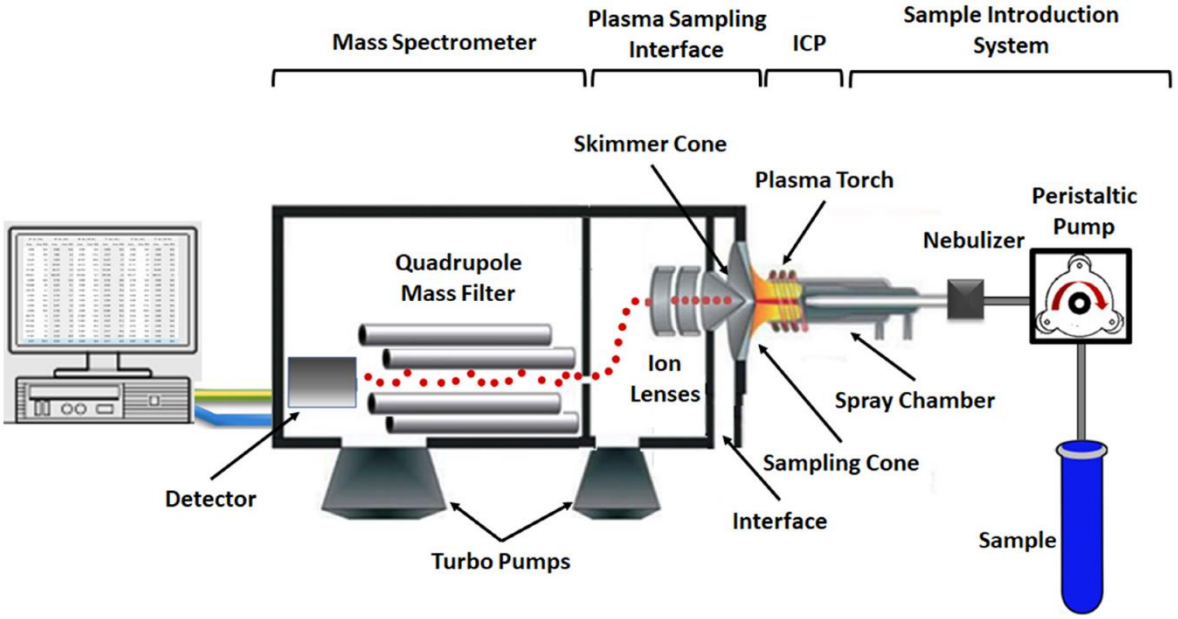

Figure 1.31: This image shows the stages of measurements ICP-MS (191).

1.7.6.2 Inductively Coupled Plasma Optical Emission Spectrometry (ICP-OES)

ICP-OES is a highly effective, multifunctional, and sophisticated analytical method with superior detection capabilities. Its exceptional qualities have made it a popular choice for the investigation of a large range of chemical elements in recent years. In addition to insignificant chemical interferences, it offers low detection limits (ppm–ppb range) although it is Less sensitive than ICP-MS (192).

The ICP-OES system involves introducing a sample, typically in liquid form, into the system using a pump (Figure 1.32-1). The sample is passed into a nebulizer (Figure 1.32-2) which converts it into an aerosol. This aerosol is then transported into a spray chamber (Figure 1.32-3), which filters out large droplets, allowing only fine droplets (~1-10 µm) to proceed into the plasma (Figure 1.32-2). plasma. In inductively coupled plasma (ICP) analysis, the liquid sample is first converted into an aerosol using a nebulizer and then transported into the plasma torch.(Figure 1.32-5). A radiofrequency (RF) coil generates a rapidly oscillating electromagnetic field, which ionizes the argon gas and produces a high-temperature plasma (~6000–10,000 K). As the aerosolized sample enters the plasma, it undergoes desolation, vaporization, atomization, and ionization, converting the sample constituents into free atoms and ions for subsequent detection. The high-energy plasma excites atoms and ions, raising their

electrons to higher energy states. When these excited atoms and ions return to a lower energy state, they emit light at element-specific wavelengths. The emitted light is collected by an optical system (mirrors and lenses) (Figure 1.32-6). The light passes through the spectrometer (Figure 1.32-7), containing a monochromator or polychromator, which disperses it into its component wavelengths. The detector (Figure 1.32-8) (CCD or PMT) captures the intensity of each wavelength for elemental analysis. Calibration is crucial for accurate quantification, involving analysing standard solutions with known concentrations of target elements (193-195). The collected data can then be processed and interpreted on a computer.

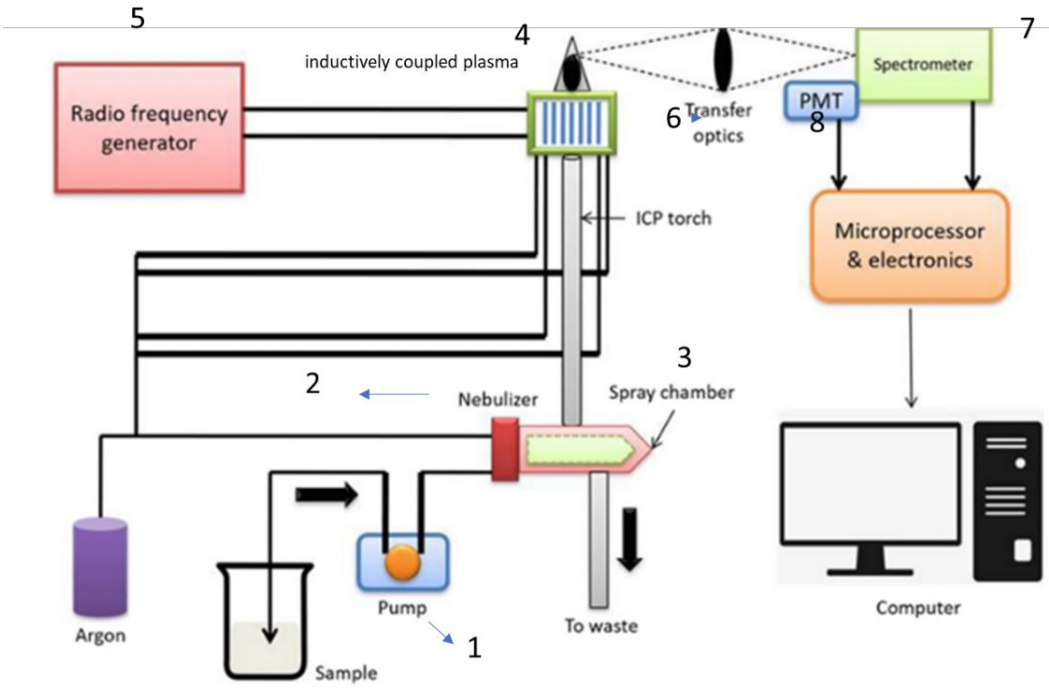

Figure 1.32. Instrumentation of ICP-OES (192).

1.7.7 Thermal Methods

Thermal methods of study, commonly known as thermo-, thermal analysis or thermo-analytical techniques, have been extensively used in the analysis of hydrogel systems (196). These approaches can be described as experimental techniques used to analyse a system (such as an element, compound, or mixture) by detecting changes in physico-chemical properties with changes in temperature (197). Thermal analysis (TA) is a collection of procedures, as defined by the International Confederation for Thermal Analysis and Calorimetry (ICTAC), that observe the alterations in the physical or chemical characteristics of a sample over time as it undergoes a temperature programme (198, 199). TA can be combined with other methods, including differential scanning calorimetry (DSC), differential thermal analysis (DTA), thermogravimetry (TG), thermomechanical analysis (TMA), and dynamic mechanical analysis

(DMA) (200). There are two main procedures used: (a) differential thermal analysis, which measures changes in heat content as a function of increasing temperature, and (b) thermogravimetric analysis, which measures changes in weight as a function of increasing temperature (201). A very common combination is the use of study TGA and DSC together in the same measurement. This combination is used in multiple industries, including food, pharmaceuticals, materials research, and environmental studies.

1.7.7.1 Thermogravimetric Analysis (TGA)

TGA is a commonly used method for thermal characterisation that offers significant insight into the behaviour of different materials' breakdown and thermal stability. TGA measures the mass change of a sample as a function of temperature or time under controlled atmospheres, allowing researchers to evaluate thermal degradation processes, kinetics, and material stability (202). This method is pivotal for understanding the thermal stability, composition, and decomposition behaviour of various materials, including polymers, metals, and composites (203).

The TGA equipment has several essential components that collaborate to provide accurate and reliable measurements of thermal characteristics, including a sample pan—typically made of aluminium or platinum designed to withstand high temperatures and ensure chemical inertness during analysis. (198). Temperature or time can be shown on the ordinate (X-axis) and weight (mg) or weight percent (%) can be shown on the abscissa (Y-axis). The following are the essential components of a TGA device: The sample holder, made of high-temperature resistant materials like aluminium or platinum, securely holds the analysed material, ensuring efficient heat transfer and minimal thermal gradients (204). The balance is a vital part of the TGA device, measuring sample mass during heating, ensuring accurate thermogravimetric measurements and being highly sensitive (205). The furnace, fitted with a programmable temperature controller, manages sample temperature to guarantee uniform heating for reliable results (206). TGA devices use a gas flow system to introduce inert or reactive gases into the sample chamber, controlling the atmosphere and affecting the sample's thermal behaviour (207).

The data acquisition system records mass changes and temperature data, generating thermogravimetric curves for real-time monitoring and analysis of mass loss based on temperature or time (208). The TGA device is controlled *via* a computer interface, allowing researchers to set experimental parameters and analyse data, often featuring visualization features for effective interpretation (Figure 1.33) (209).

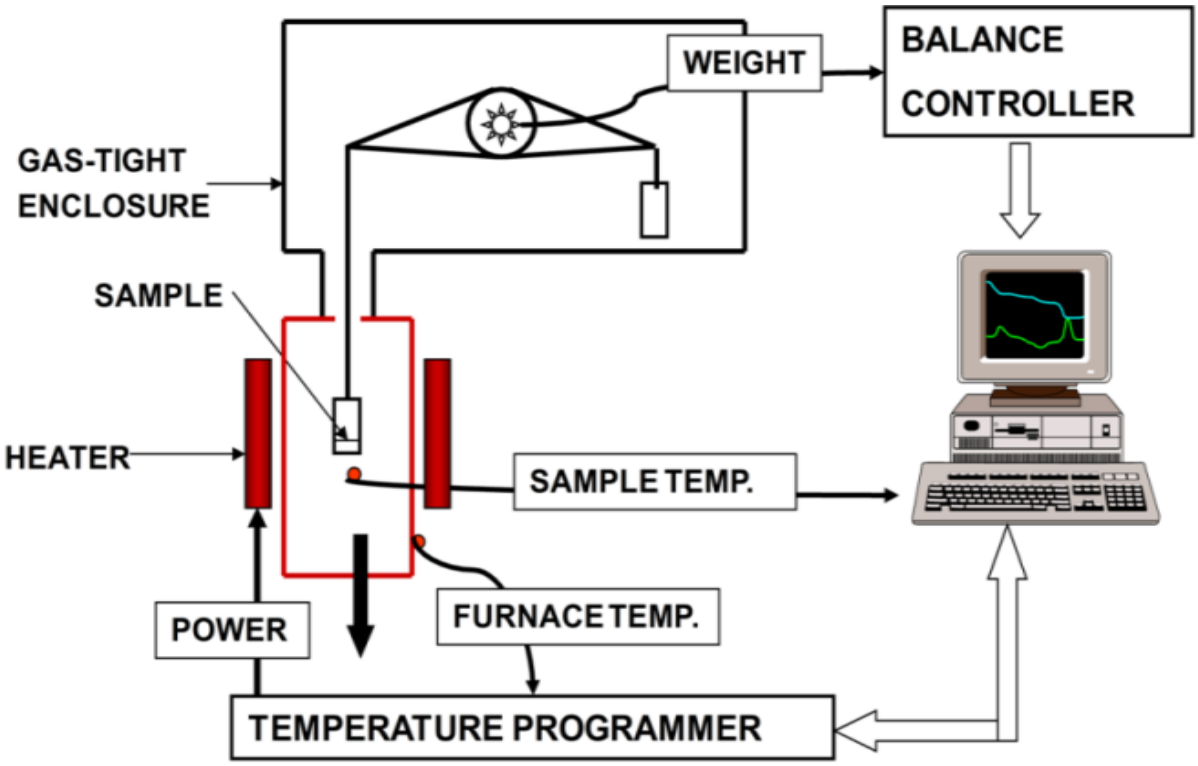

Figure 1.33: illustrates the components of the TGA instrument and the utilised weighing technique (210).

1.7.7.2 Differential Scanning Calorimetry (DSC)

DSC is a metanalytical method extensively employed for the characterisation of materials' thermal properties. It is particularly good for identifying transition temperatures (Tj), changes in enthalpy (ΔH), and fluctuations in heat capacity across various materials, including polymers, medicines, and food products (211). In addition, it facilitates the analysis of transitions such as melting, crystallization, glass transitions, and thermal stability. The technique functions by estimating the heat flow linked to phase transitions in a material as a function of temperature or time, helping the detection of thermal phenomena such as melting point, crystallisation, glass transition temperature (Tg), decomposition, and thermal stability of materials (212). The operation of DSC can be broken down into several key steps, each critical for obtaining accurate thermal data.

Heat flux measures the differences in heat flow between a reference material and a sample when they are exposed to a controlled temperature program. A sample (Figure 1.34-1) and reference pan (Figure 1.34-2) are placed on a single heating block, with the reference pan holding an inert substance for comparison. A heater (Figure 1.34-3) provides controlled heat

input, while a heat resistor (Figure 1.34-4) ensures uniform distribution. The thermocouples (Figure 1.34-5) located below both pans measure the temperature difference (ΔT) and detect phase transitions like melting, crystallization, or glass transitions. Heating conditions are regulated by a heat driver (Figure 1.34-6) and temperature control system (Figure 1.34-7), to ensure accurate measurements of the temperature are obtained. The amplified thermocouple signals (Figure 1.34-8) are processed by the CPU to record temperature (Figure 1.34-9) changes and calculate heat flow. The final output, a DSC thermogram, plots (Y-Axis) Heat Flow (mW) vs. temperature (X-Axis) (°C), with peaks indicating key thermal events like melting or crystallization (212-215). The difference in heat flow is recorded as a DSC curve, with exothermic processes releasing heat and endothermic processes absorbing it.

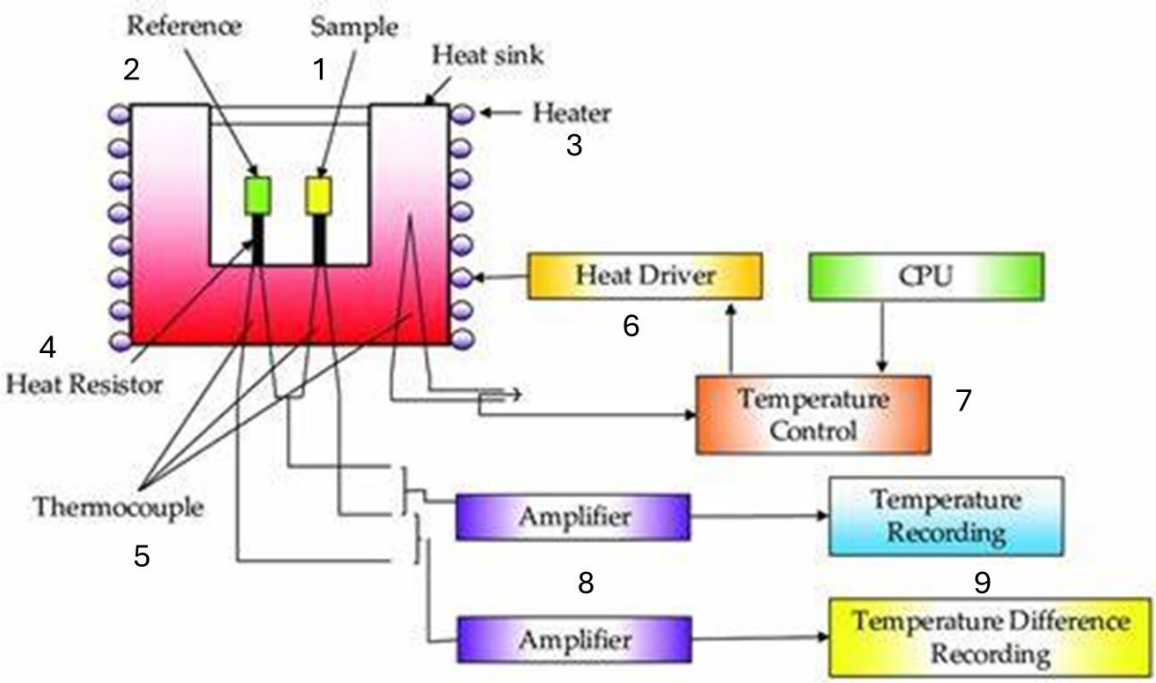

Figure 1.34: Diagram of a Differential Scanning Calorimetry (DSC) system and signal processing workflow(216)

1.7.8 Rheology and rheometer with a parallel-plate setup

1.7.8.1 Introduction to rheology

The objective of rheology today is to characterise the complex behaviour of many real substances when examined during a wide variety of stresses and deformations (217). Rheology is an interdisciplinary field of physics which combines fluid mechanics and materials science to clarify the behaviour of soft materials under deformation and flow. It is particularly important for complex fluids and soft materials such as polymers, hydrogels, suspensions,

pastes, emulsions, and biological fluids (218). Rheology is the study of how materials flow (viscous behaviour) and deform (elastic behaviour) when subjected to an external force. Rheology helps characterize how materials behave under steady-state conditions (not oscillatory). For example, Singular Viscosity measures a material's resistance to flow. In purely viscous materials, such as honey, water, oils and deformation occurs continuously under applied force, dissipating energy as heat. The relationship between shear stress (τ) and shear rate (γ̇) follows Newton's Law of Viscosity
(219), where eta (η) is a constant:

$$\tau = \eta \dot{\gamma} \qquad \textit{Equation 1.6}$$

In Newtonian fluids, viscosity remains constant (e.g., water, oils), while in non-Newtonian fluids, viscosity changes under shear stress (e.g., ketchup, blood). while Elasticity describes a material's ability to store and recover energy after deformation. A purely elastic solid, like rubber, gels or metal springs, deforms under force but returns to its original shape once the force is removed. Elastic materials follow Hooke's Law, which relates stress (σ), strain (γ) and the elastic modulus (G):

$$\sigma = G\gamma \qquad \textit{Equation 1.7}$$

Most real-world materials exhibit a combination of both viscous and elastic properties, leading to viscoelastic behaviour. When studying viscoelastic materials, we need to distinguish between singular viscosity as explained above and complex viscosity.

Complex viscosity (η*), which describes the combined viscous and elastic behaviour of materials in dynamic (oscillatory) rheology, is primarily governed by the principles of linear viscoelasticity rather than a single classical law. However, it is closely related to Newton's Law of Viscosity and Hooke's Law, depending on the material's behaviour. Newton's Law of Viscosity applies to the viscous component, where shear stress (τ) is proportional to shear rate (γ̇), describing fluid-like behaviour. Hooke's Law applies to the elastic component, where stress (σ) is proportional to strain (γ), describing solid-like behaviour. In oscillatory shear tests, complex viscosity is related to the **complex modulus (G)***, where η* is the complex viscosity and ω is the angular frequency of oscillation:

$$\eta^* = G^*/\omega \qquad \textit{Equation 1.8}$$

The complex modulus (G*) represents the overall mechanical response of the material, including both the storage modulus (G'), which represents elasticity, and the loss modulus (G''), which represents viscosity.

Complex viscosity follows the principles of viscoelasticity, integrating both Newtonian (viscous) and Hookean (elastic) responses, depending on the frequency of oscillation. At low frequencies, complex viscosity behaves similarly to zero-shear viscosity, reflecting Newtonian fluid behaviour. As frequency increases, η* shifts toward the elastic response, indicating the material's ability to store energy. This property is crucial in understanding viscoelastic materials such as polymers, gels, and biological tissues, which exhibit both fluid-like and solid-like characteristics depending on applied stress conditions.

1.7.8.2 A rheometer with a parallel-plate setup

A rheometer with a parallel-plate setup is a piece of advanced laboratory equipment utilised to measure the rheological properties of materials, particularly their viscosity and viscoelastic behaviour. It is especially useful for studying materials that cannot be defined by a singular viscosity measurement (220-222). These properties include viscosity, elasticity, and plasticity, making rheometers essential in characterizing materials that do not behave as ideal fluids or solids, such as polymers, gels, pastes, suspensions, biological materials and other non-Newtonian fluids. The parallel-plate geometry allows for precise control over the sample thickness and shear conditions, making it ideal for a wide range of applications in food science, materials engineering, and biomedical research. In a parallel-plate rheometer, two flat plates are positioned parallel to each other, with a small gap between them filled with the sample material. One plate is fixed, while the other is rotated or oscillated to apply shear stress to the sample. The resulting deformation of the material is measured, allowing for the calculation of various rheological parameters, such as viscosity, storage modulus (G′), and loss modulus (223, 224).

The base unit of the rheometer houses the motor and control electronics. It provides the necessary torque and rotational speed to the measuring system. The base unit is responsible for maintaining the desired temperature during measurements, which is crucial for accurate rheological characterization (225). The parallel plates can vary in diameter, typically ranging from a few millimetres to several centimetres, depending on the sample size and the specific application (Figure 1.35) (226). The gap between the parallel plates can be adjusted to accommodate different sample viscosities and to ensure that the sample is not subjected to excessive shear stress. This control mechanism is essential for maintaining consistent measurement conditions and for studying materials with varying rheological properties (227). Many rheometers are equipped with a temperature control system that allows for precise

regulation of the sample temperature during measurements. This is particularly important for materials that exhibit temperature-dependent rheological behaviour, such as thermoplastic polymers and hydrogels (228). The rheometer is equipped with sensors that measure the torque and angular displacement of the rotating plate. This data is processed by the rheometer's software to calculate rheological parameters such as viscosity, storage modulus (G′), and loss modulus (G″). The data acquisition system also allows for real-time monitoring of the material's response to applied stress (229). The control software is an integral part of the rheometer, enabling users to set experimental parameters, control the measurement process, and analyse the data. The software typically provides various rheological models and analysis tools to interpret the results effectively (230).

The sample holder is designed to securely position the sample between the parallel plates. It ensures that the sample remains in place during measurements and minimizes any potential slippage that could affect the accuracy of the results (231).

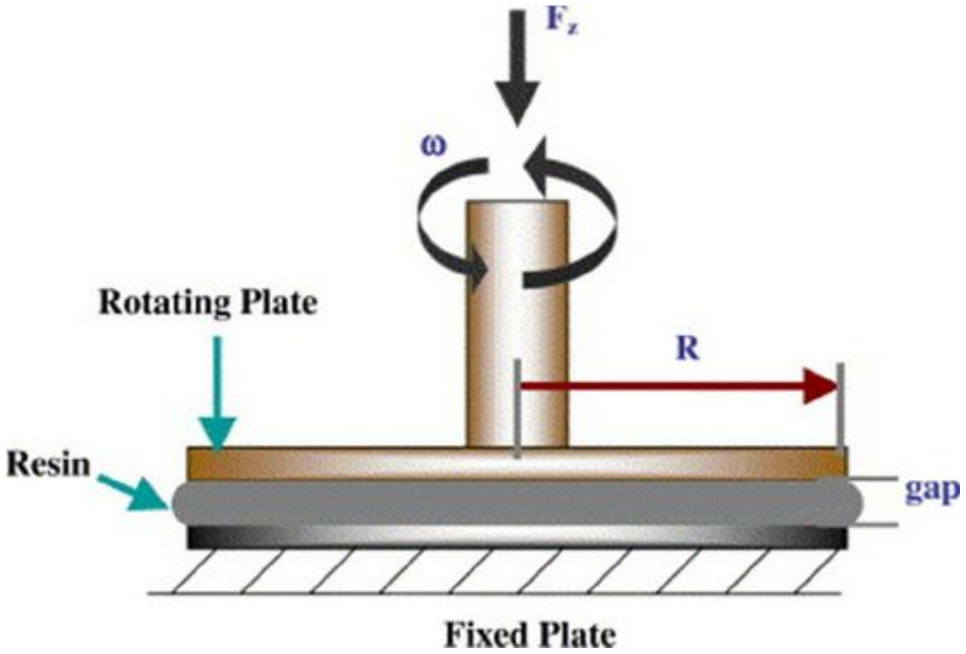

Figure 1.35: Schematic illustration of the parallel plate configuration (232).

1.8 Conclusion

Chapter 1 outlines the complex and interconnected challenges facing global agriculture, including climate change, resource scarcity, soil degradation, and the increasing food demand driven by population growth. Addressing these challenges requires sustainable and innovative solutions, particularly in water-stressed regions such as India and parts of Africa, where agriculture consumes over 70% of global freshwater resources. Among the promising solutions

introduced in this chapter are polymer hydrogels—superabsorbent materials that play a crucial role in enhancing water management and agricultural sustainability.

Hydrogels are hydrophilic, three-dimensional polymer networks capable of absorbing and retaining significant amounts of water—often more than ten times their weight. Their ability to swell, retain, and gradually release water and nutrients makes them highly effective in improving soil moisture retention, reducing irrigation frequency, minimizing fertilizer leaching, and enhancing soil structure and root development. These characteristics help alleviate plant stress, improve crop yields, and support resilient agricultural systems, especially in arid and drought-prone environments.

Hydrogels have evolved significantly since their first appearance as colloidal gels in the 19th century. The development of the first synthetic hydrogel in 1954 marked a turning point, leading to modern innovations such as temperature-responsive, self-healing, and biodegradable hydrogels. These materials are now used widely in agriculture, medicine, drug delivery, biosensing, and tissue engineering, thanks to their biocompatibility, viscoelastic behaviour, and capacity to mimic biological tissues.

Hydrogels used in agriculture are broadly categorized into synthetic, semi-synthetic, and natural types: Synthetic hydrogels, such as those based on polyacrylamide, are durable and highly absorbent but often non-biodegradable. Semi-synthetic hydrogels are chemically modified natural polymers that offer improved performance but may be costly. Natural hydrogels, derived from renewable sources like plants, algae, and microbes, are biodegradable and environmentally friendly, though typically lower in mechanical strength.

A particularly promising class of natural hydrogels is polysaccharide-based hydrogels, known for their excellent water retention, soil enhancement, and eco-friendly characteristics. Examples include Cellulose, which offers structural support and can be modified (e.g., into carboxymethyl cellulose) for improved solubility and moisture control; Gellan gum, a microbial polysaccharide that forms stable gels in the presence of cations and is useful in controlled-release systems; Guar gum, a plant-derived galactomannan used for soil conditioning and slow nutrient delivery.

These polysaccharide hydrogels serve as sustainable alternatives to synthetic polymers by improving soil moisture, reducing water demand, and enhancing crop productivity. Further innovation in this field includes the development of hydrogel composites, which involve combining base hydrogels with functional additives such as nanoparticles, biochar, or chemically modified cellulose. These composites enhance water retention, nutrient delivery, and mechanical stability, making them highly effective in sustainable agriculture. This study

focuses specifically on gellan gum–cellulose composite hydrogels, investigating their potential role in improving soil and water management, rather than focusing on a single agricultural application. Hydrogels also act as carriers for nutrients and soil amendments, enabling slow and targeted release of essential inputs: Macronutrients (Nitrogen, Phosphorus, Potassium) to support plant growth and development; Secondary nutrients (Calcium, Magnesium, Sulphur) for plant structure and metabolic processes; Micronutrients (Iron, Zinc, Manganese, Copper, Boron), often delivered in chelated form to improve bioavailability; Organic matter additives, such as compost and biochar, to enhance microbial activity and soil fertility; pH adjusters, including lime, gypsum, or sulphur, to regulate soil acidity or alkalinity; Biodegradable polymers and nanomaterials to improve hydrogel strength, nutrient retention, and environmental performance.

In summary, hydrogels—and especially hydrogel composites—offer a versatile, eco-friendly solution to many of the pressing challenges in modern agriculture. Their integration into farming practices supports more sustainable water and nutrient management, enhances soil health, and contributes to long-term agricultural resilience in the face of climate change and resource limitations.

1.9 Aims and Objectives of the Current Work

The overall aim of this project is to: develop hydrogel systems based on organic gelators such as Gellan Gum, (Gellan Gum -CMC) and (Gellan Gum HEC), with the capability of promoting controlled release of nutrient sources (such as nitrates, phosphates and key metal ions such as potassium, calcium, zinc and iron) These elements (K, P, N) are fundamental for plant growth, metabolism, and structural integrity and called primary macronutrients.(220) In addition to macronutrients, several additional elements are important micronutrients including like Iron (Fe), Manganese (Mn) and Zinc (Zn). These elements are crucial for enzyme function, metabolic processes, and stress resistance (221).

To achieve this overall aim, the project is divided into a suite of work-packages (WP) each of which has key deliverables. These together will address the overall aim of the project as outlined in the section on Methodology below.

Work packages (WP) of this Project.

Work-Package 1. Selection of Gelator Systems to Explore with and without Nutrient.

This first element of the project focuses on preparing a range of composite hydrogel systems based on polysaccharide organic polymers. The principal hydrogel component used is gellan gum which has been extensively studied for multiple applications in, for example, the food-

industry (see references in Chapter 1). In this work, gellan gum has been composited with additional organic, polysaccharides such as hydroxyethyl cellulose and carbomethoxy cellulose. (See figure 1.36 a, b, c.) Composite hydrogels have been prepared in two main categories, those with plant nutrients and those without.

a) Gellan gum (GG)

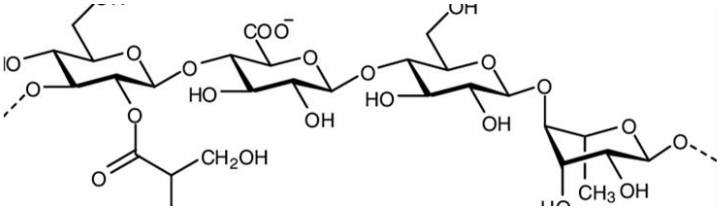

b) HEC:

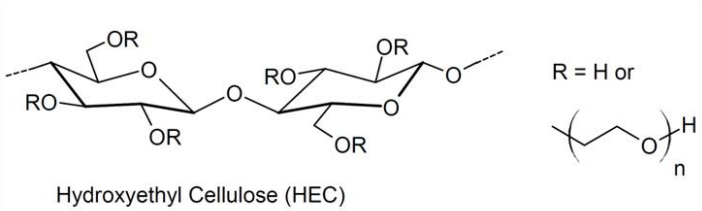

c) CMC

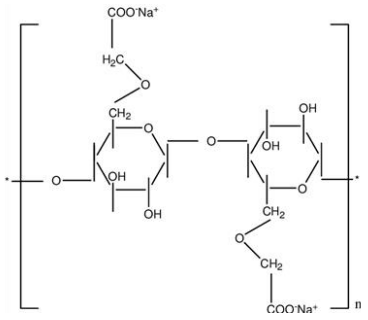

Figure 1.36: Some structure polysaccharide a) GG B) HEC c) CMC.

The key deliverables of Work Package 1 include the selection and preparation of gelator systems by identifying and selecting appropriate polysaccharide hydrogels, with gellan gum serving as the principal component. Composite hydrogels are developed by incorporating additional polysaccharides such as hydroxyethyl cellulose (HEC) and carboxymethyl cellulose (CMC) into the gellan gum matrix. Formulation efforts focus on preparing both pure gellan gum hydrogels and composite systems combining gellan gum with HEC and CMC. Additionally, two categories of hydrogels are prepared: one without added plant nutrients and another loaded with essential nutrients including potassium (K), phosphorus (P), manganese (Mn), iron (Fe), copper (Cu), zinc (Zn), and molybdenum (Mo).

In Work Package 2, the matrix microstructure of gellan gum hydrogels (GGH) and GGH composites have been analysed using both scanning electron microscopy (SEM), surface area measurements (BET), and energy dispersive X-ray (EDX) analysis where relevant. Samples were dried using lyophilization prior to surface analysis.

The key deliverables of Work Package 2 include the preparation of GGH and GGH composite samples through lyophilization to preserve their structural integrity for microstructural analysis. We examine the surface morphology, pore structure, and network architecture of both pure and composite hydrogels using scanning electron microscopy (SEM).

Work-Package 3. Conducting thermal studies on Gellan Gum and Composite Hydrogels.

The composite polysaccharide hydrogels prepared in Work-Package 1 were subsequently examined by thermogravimetric analysis (TGA) and differential scanning calorimetry (DSC), with the aim being to see how thermal degradation of each system is influenced by the presence of metal-ion macro and micro-nutrients.

The key deliverables of Work Package 3 focus on the thermal characterisation of Gellan Gum (GGH) and composite hydrogels through thermogravimetric analysis (TGA), which is used to assess their thermal stability and decomposition patterns. In addition, differential scanning calorimetry (DSC) is performed to determine key thermal transitions, including the glass transition temperature (Tg), melting points, and crystallisation behaviour. Furthermore, the influence of incorporating macro- and micro-nutrients (such as K, P, Mn, Fe, Cu, Zn, and Mo) on the thermal degradation and stability of the hydrogel matrices is systematically analysed. Comparisons are then made between pure GGH hydrogels and composite systems (GGH-HEC and GGH-CMC), both with and without nutrient loading, to highlight differences in thermal performance. Through the analysis of TGA data, important stages of degradation are identified, linking specific weight loss events to processes such as water evaporation, polymer backbone decomposition, and nutrient-related transformations.

Those macro and micronutrient-containing composite hydrogels have been analysed for nutrient release during dialysis experiments using both: (i) ionic conductivity to follow bulk charge -carrier release and (ii) inductively coupled plasma studies to probe detailed elemental speciation during dialysis.

The key deliverables of Work Package 4 include the selection and preparation of composite hydrogels loaded with macro- and micro-nutrients for nutrient release studies. Dialysis experiments are conducted to monitor nutrient release over time into an external medium. Throughout the dialysis process, changes in ionic conductivity are measured to track the overall release of charged species from the hydrogels. Additionally, elemental concentrations are determined using inductively coupled plasma (ICP-OES or ICP-MS) techniques to provide detailed profiles of nutrient release, including elements such as K, P, Mn, Fe, Cu, Zn, and Mo. Release profiles and elemental speciation are analysed to understand the kinetics, efficiency, and behaviour of nutrient release under dialysis conditions. Comparisons are made across

different hydrogel formulations, such as pure GGH, GGH-HEC, and GGH-CMC, both with and without nutrient incorporation. Finally, conductivity and ICP data are systematically collected, organised, and interpreted, with release profiles graphically presented to summarise key findings and enhance the understanding of nutrient release mechanisms from the composite hydrogels.

Work-Package 5. Conducting Rheological Studies of Gellan Gum Hydrogels and Composite Hydrogels.

In work-package 5, we have investigated the rheological behaviours of our composite hydrogel systems, focusing specifically on the viscoelastic properties through oscillatory tests, frequency sweep tests and rheological rotational strength tests.

The key deliverables of Work Package 5 involve the preparation of Gellan Gum (GGH) and composite hydrogels (GGH-HEC, GGH-CMC), both with and without nutrient loading, for rheological testing. Oscillatory shear tests are performed to investigate the viscoelastic properties of the hydrogels, focusing on measurements of storage modulus (G') and loss modulus (G"). In addition, frequency sweep tests are conducted to assess how the viscoelastic behaviour changes across different oscillation frequencies, providing insights into the structural stability of the gels. Rotational strength tests are also carried out to evaluate flow characteristics, viscosity profiles, and yield stress under steady shear conditions. Comparisons are made between pure GGH and composite systems, with and without nutrients, to understand the influence of composition and nutrient incorporation on mechanical behaviour. Finally, rheological data are systematically collected, organised, and interpreted, with clear graphical outputs and summaries prepared to support conclusions regarding the mechanical performance and application potential of the hydrogel systems.

Chapter 2: Structural and Surface Studies on Gellan Gum Hydrogels and Gellan Gum Composites

2.1 Introduction

The primary objective of this section is to prepare and characterise a series of gellan gum (GG) and modified gellan gum hydrogels both with and without nutrient incorporation—formulated at three concentrations: 10, 12, and 14 mg/cm^3. These mixtures have set amounts of hydroxyethyl cellulose (HEC), carboxymethyl cellulose (CMC), and nutrient additives, allowing us to carefully study how they affect the structure and physical properties of the hydrogels.

The full compositional details of the samples are provided in Tables 2.1, 2.2 and 2.3. The samples listed in Tables 2.1, 2.2, and 2.3 were initially synthesised, lyophilised (freeze-dried), and subsequently analysed using scanning electron microscopy (SEM). Energy-dispersive X-ray spectroscopy (EDX) was employed to determine the elemental composition and distribution within the matrix, with EDX mapping being used to visualise spatial element dispersion. Surface area and porosity were further assessed via Brunauer–Emmett–Teller (BET) nitrogen adsorption analysis. In this study, we chose the low-acyl version of gellan gum (233) because it is known to create strong and heat-resistant gels in body-like conditions, where the strength of the gel is greatly affected by the number of ions present. To make the hydrogel, we mixed GG with deionised water at high temperatures (80–90°C) while stirring constantly to make sure it fully dissolved. We examined concentrations ranging from 0.5% to 3% (w/v) (234). This thermal preparation protocol was applied consistently across all GG and composite hydrogel formulations. Gelation can be induced by cooling or adding divalent cations, affecting the hydrogel's mechanical properties and stability (235, 236). Nutrients, such as vitamins, minerals, or growth factors, may be included into gellan gum hydrogels during the preparation phase. Nutrients are often dissolved in the gellan gum solution before gelation (237-239). For biological applications, nutrients, growth factors, or pharmaceuticals may be included in the gellan gum solution prior to gelation. This allows controlled release and release of bioactive compounds (240). The interaction between gellan gum and HEC can lead to combined effects, where the properties of the resulting hydrogel are superior to those of the individual components. For instance, the presence of HEC can improve the viscosity and mechanical strength of the hydrogel (241), while gellan gum can enhance the thermal stability and gelation properties (242). Gellan gum, an anionic polysaccharide, forms hydrogels with divalent cations. Sodium carboxymethyl cellulose, a water-soluble derivative, has biocompatibility and

thickening properties, making it used in drug delivery systems and stabilizers. Combining these two polymers improves hydrogels' mechanical strength, swelling capacity, and nutrient release profiles (243).

2.2 Hydrogel formation (GGH, GGH composites)

2.2.1 Formation of Gellan gum hydrogels with Nutrient and without Nutrient

Three solutions of gellan gum were prepared at the following concentrations: 10, 12 and 14 mg/cm³. We measured different amounts of gellan gum (0.5 g, 0.6 g, and 0.7 g) in a volume of 50 mL of deionised water. We measured this volume and transferred it into a 50 mL round-bottom flask using a magnetic stirrer, gradually adding the gellan gum. When the sample contained nutrients, 49 mL of distilled water was used with 1 mL of concentrated Miracle-Gro (Table 2.1). We heated the flask to 80 °C using a small beaker and a temperature-controlled hot plate. The hot plate has two critical components: a thermocouple sensor to regulate the solution's temperature in this experiment (in these experiments the temperature does not exceed 80) and a magnetic stirring mechanism to maintain constant stirring (in these experiments left to stirring at 7500 rpm). After stirring and heating for four hours at 80 °C, the heating and stirring were stopped, and the mixtures were moved to 50 mL Falcon tubes to cool at room temperature, which helps finish the gelation process. The gelation occurs as the polymer chains aggregate and entrap water molecules within the network structure.

Table 2.1: Concentrations and components used in the production of gellan gum hydrogel.

Sample ID	GG (g)	GG (mg/cm³)	Nutrient Added (mL)	Added Distilled Water (mL)
10GGH	0.5	10	0	50
12GGH	0.6	12	0	50
14GGH	0.7	14	0	50
10GGH-MG	0.5	10	1	49
12GGH-MG	0.6	12	1	49
14GGH-MG	0.7	14	1	49

2.2.2 Formation of Gellan gum - hydroxyethyl cellulose hydrogel composites with Nutrient and without Nutrient

In this study, six hydrogel formulations were prepared by combining Gellan Gum (GG) and Hydroxyethyl Cellulose (HEC) in a fixed total volume of 50 mL. The GG content was varied across three concentrations: 0.5 g, 0.6 g, and 0.7 g, corresponding to 10.00 mg/cm³, 12.00 mg/cm³, and 14.00 mg/cm³, respectively. HEC was held constant at 0.25 g (5.00 mg/cm³) in all

formulations. Three of these formulations contained no nutrient additives, while the other three included 1 mL of nutrient solution, with the volume of distilled water adjusted to 49 mL to maintain the total volume. See the below table. The inclusion of HEC aimed to improve hydrogel viscosity and structural integrity, while nutrient incorporation was intended for element release evaluation. The preparation procedure began by dissolving Gellan Gum (GG) in 25 mL of distilled water in a 50 mL beaker, gradually heating the solution to 80°C with continuous stirring for four hours. Simultaneously, Hydroxyethyl Cellulose (HEC) was added to a separate 50 mL beaker containing 25 mL of distilled water, also heated to 80°C and stirred under the same conditions for four hours to ensure complete dispersion. In the presence of nutrients, 24 mL of distilled water was used along with 1 mL of nutrient solution, as outlined in the corresponding formulation table. After the initial mixing steps, the GG and HEC solutions (with or without nutrients) were combined and stirred together at 80°C for an additional four hours to achieve a homogeneous mixture. Following this, heating and stirring were stopped, and the resulting hydrogel mixtures were transferred into 50 mL conical-bottom centrifuge tubes (Falcon tubes). The samples were then left to cool and rest at room temperature for 48 hours, allowing complete gelation. During this period, gellan gum polymer chains aggregated, forming a three-dimensional network that effectively entrapped water molecules, resulting in a stable hydrogel structure (Table 2.2).

Table 2.2: Concentrations and components used in the production of gellan gum hydrogels with HEC.

Sample ID	GG (g)	GG (mg/cm³)	HEC (g)	HEC (mg/cm³)	Nutrient Added	Added Distilled Water (mL)
10GGH-HEC	0.5	10	0.25	5	No	50
12GGH-HEC	0.6	12	0.25	5	No	50
14GGH-HEC	0.7	14	0.25	5	No	50
10GGH-HEC-MG	0.5	10	0.25	5	Yes (1mL)	49
12GGH-HEC-MG	0.6	12	0.25	5	Yes (1mL)	49
14GGH-HEC-MG	0.7	14	0.25	5	Yes (1mL)	49

2.2.3 Formation of Gellan gum - carboxymethyl cellulose hydrogel composites with Nutrient and without Nutrient

The preparation of Gellan Gum–CMC hydrogels involved accurately weighing 0.5 g, 0.6 g, or 0.7 g of Gellan Gum along with 0.25 g of Carboxymethyl Cellulose (CMC) for each

formulation. For nutrient-loaded samples, 1 mL of nutrient solution was prepared in advance. Gellan Gum was dissolved in 25 mL of distilled water, heated to 80°C in a 50 mL beaker under constant magnetic stirring for 4 hours until fully dissolved. Simultaneously, CMC was dissolved in a separate 50 mL beaker containing another 25 mL of distilled water, also heated to 80°C and stirred continuously for 4 hours until a uniform solution formed. Once both polymers were completely dissolved, the GG and CMC solutions were combined into a single beaker. For nutrient-containing samples, 1 mL of nutrient solution was added at this stage, reducing the distilled water to 49 mL to maintain a consistent volume. The combined mixture was stirred at 80°C for an additional 4 hours to ensure complete homogenisation. Finally, the prepared hydrogels were transferred to 50 mL Falcon tubes, cooled to room temperature, and left to stand for 48 hours to allow for complete gelation.

Table 2.3: Concentrations and components used in the production of gellan gum hydrogel with CMC.

Sample ID	GG (g)	GG (mg/cm³)	CMC (g)	CMC (mg/cm³)	Nutrient Added	Added Distilled Water (mL)
10GGH-CMC	0.5	10	0.25	5	No	50
12GGH-CMC	0.6	12	0.25	5	No	50
14GGH-CMC	0.7	14	0.25	5	No	50
10GGH-CMC-MG	0.5	10	0.25	5	Yes (1mL)	49
12GGH-CMC-MG	0.6	12	0.25	5	Yes (1mL)	49
14GGH-CMC-MG	0.7	14	0.25	5	Yes (1mL)	49

2.3 Characterisation of Gellan Gum and Modified Gellan Gum

2.3.1 SEM Analysis of Gellan Gum and Modified Gellan Gum

In Figures 2.1-2.18 are collected scanning electron micrographs of gellan gum (GG) and modified gellan gum hydrogels both with and without nutrient incorporation formulated at three concentrations: 10, 12, and 14 mg/cm3. These mixtures have set amounts of hydroxyethyl cellulose (HEC), carboxymethyl cellulose (CMC), and nutrient additives. In each case, the hydrogels were prepared as described above and dried using lyophilisation to afford a dried gel matrix. Each sample was imaged at four different levels of magnification (500, 200, 100 and 50 microns), and some samples contained additional components (cellulosic gel additives or nutrients).

2.3.1.1 SEM Analysis of Gellan Gum and Gellan Gum with and without nutrients

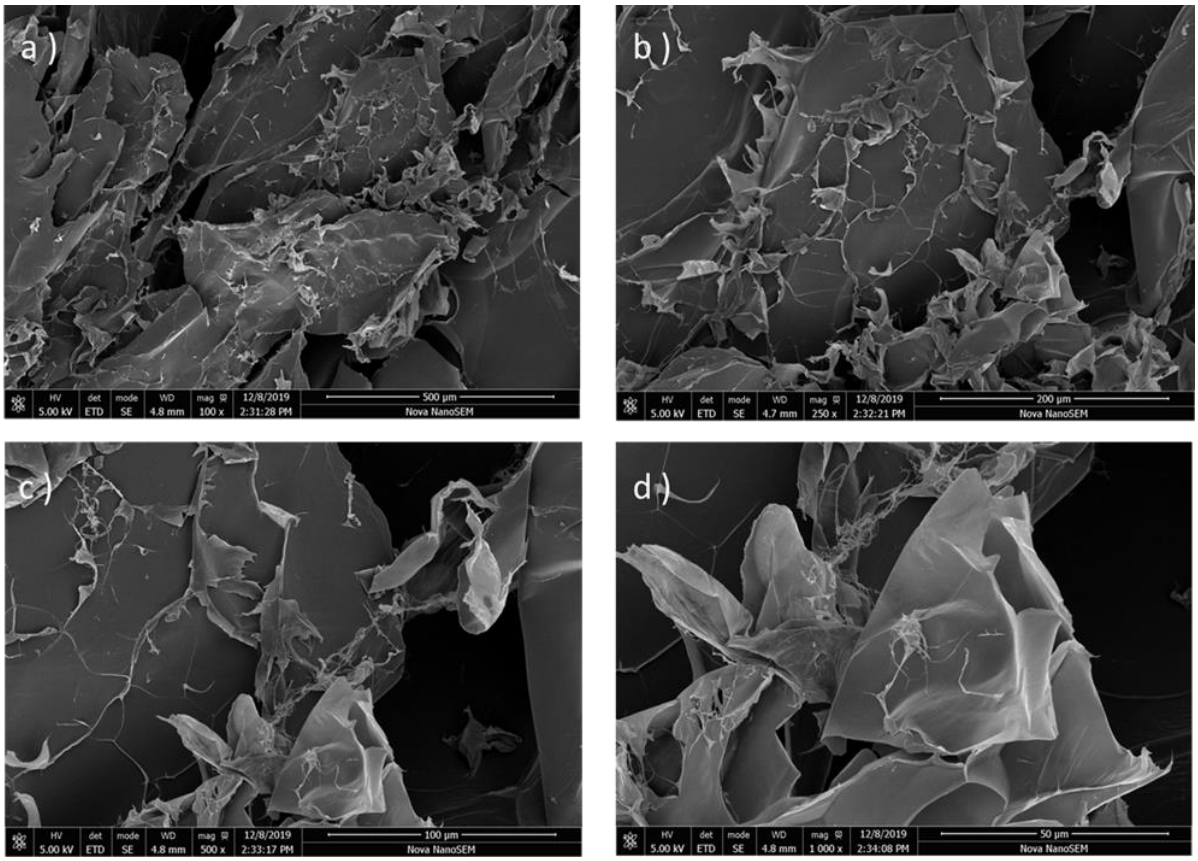

Figure 2.1: SEM micrographs of 10 GGH and various magnifications. scale bar: a) 500 µm b) 200 µm c) 100 µm d) 50 µm.

The Figure 2.1 presents SEM micrographs of Gellan Gum at a concentration of 10 mg/cm³, captured at progressively higher magnifications. Image (a), with a scale bar of 500 µm, provides an overview of the material's structure, showing large, irregularly shaped flakes or sheets with wrinkled surfaces. In image (b), at 200 µm scale, the flake-like morphology becomes more pronounced, and finer surface features start to emerge. Image (c), with a 100 µm scale, reveals sharper edges and more intricate surface details of the material, while image(d), at the highest magnification (scale bar: 50 µm), highlights thin, layered regions with well-defined folds and textured surfaces. These micrographs illustrate the morphological characteristics of Gellan Gum at different observational scales, emphasizing its layered, sheet like appearance.

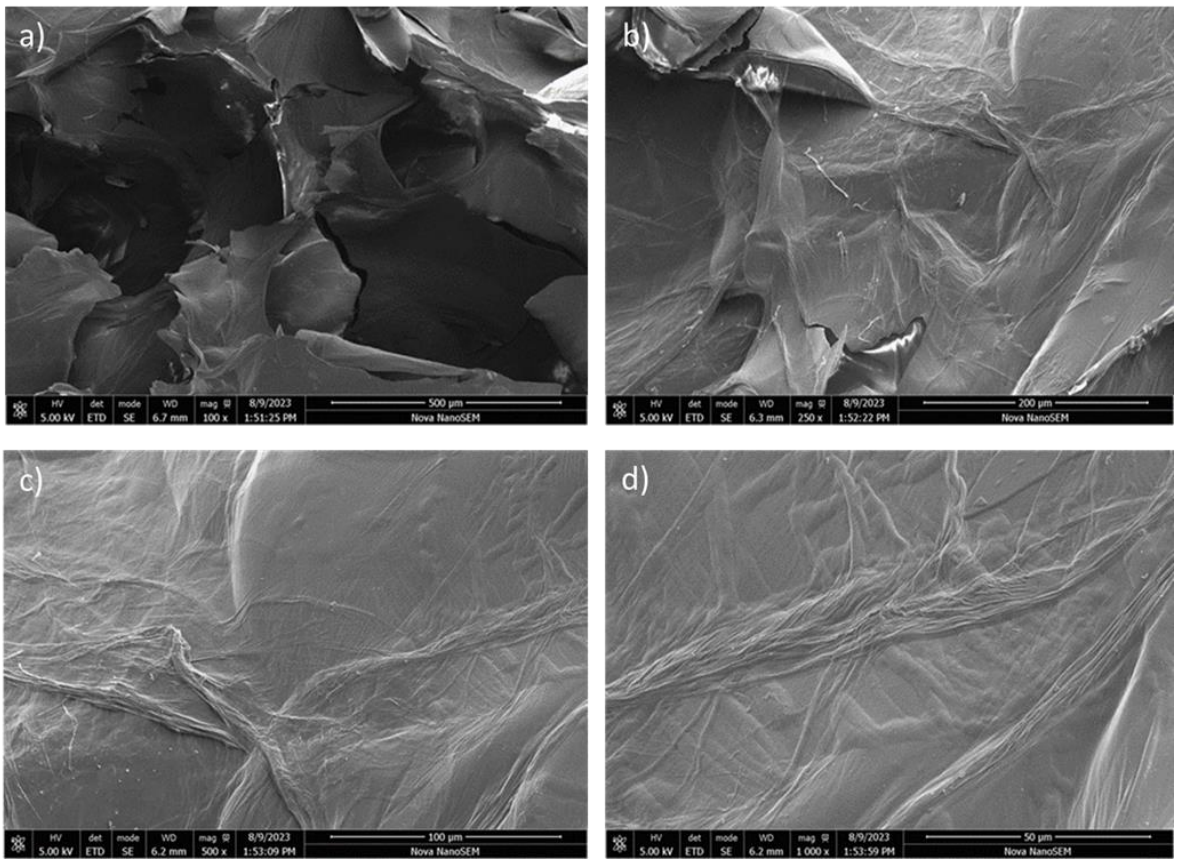

Figure 2.2: SEM micrographs of 10 GGH-MG and various magnifications. scale bar: a) 500 µm b) 200 µm c) 100 µm d) 50 µm.

The Figure 2.2 presents SEM micrographs of Gellan Gum containing Miracle-gro at a concentration of 10 mg/cm³, captured at progressively higher magnifications. The images obtained are very similar in nature to those obtained for samples which did not contain Miracle-Gro, suggesting there is no effect on the surface structure of the samples.

The SEM analysis compared two samples: Sample 1 (10 mg/cm³ Gellan Gum) and Sample 2 (10 mg/cm³ Gellan Gum with 1 mL of Miracle-Gro added). Sample 1 displayed fractured, angular sheet-like structures with irregular surfaces and sparse, disorganized web-like strands visible across all magnifications (100× to 1,000×). In contrast, Sample 2 exhibited more continuous and uniform surfaces, with well-defined, increasingly organized fibrillar features at higher magnifications. Morphologically, Sample 1 appeared more fragmented with less connectivity between structural elements, while Sample 2 demonstrated enhanced cohesion, smoother surfaces, and denser, more aligned filamentary networks. The clearer directional patterns and continuous structural arrangements observed in Sample 2, especially at high magnification, suggest that the addition of the 1 mL component influences surface integrity and the organization of microstructural features.

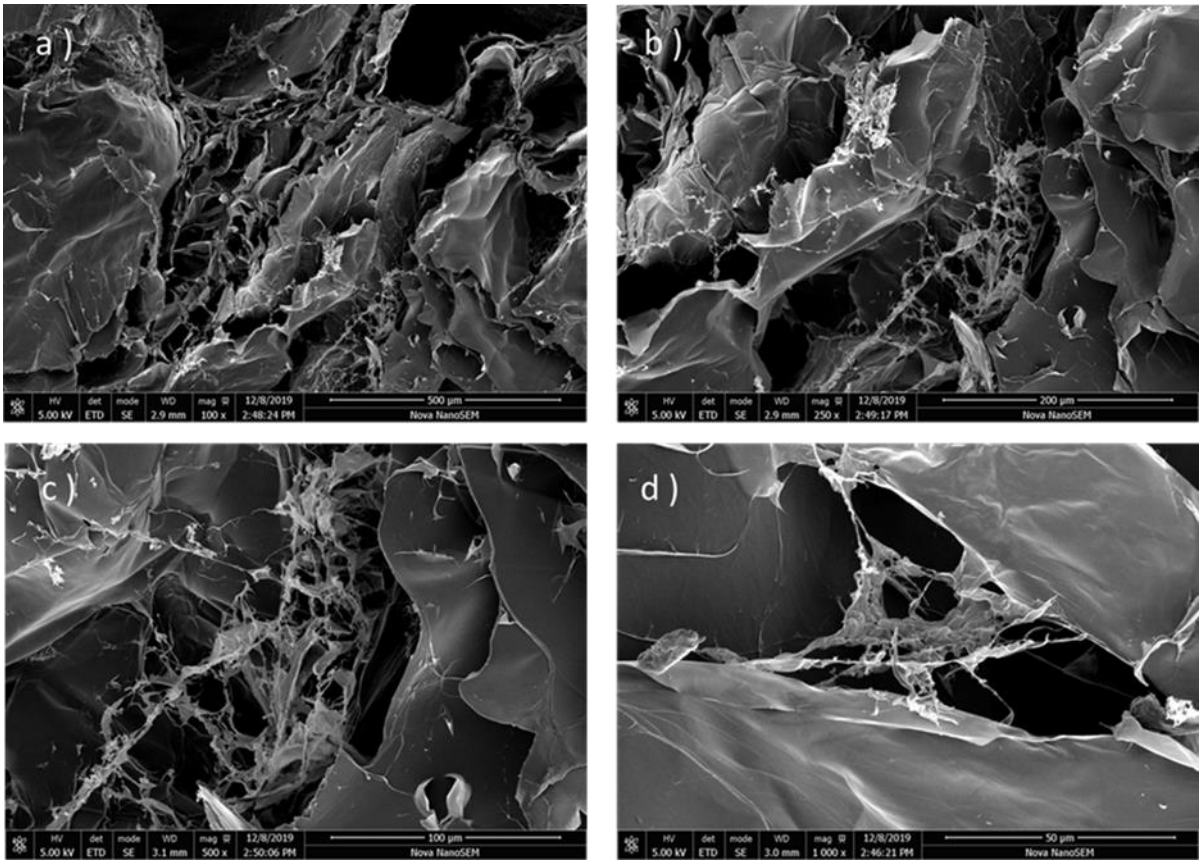

Figure 2.3: SEM micrographs of 12 GGH and various magnifications. scale bar: a) 500 µm b) 200 µm c) 100 µm d) 50 µm.

Figure 2.3 presents SEM micrographs of Gellan Gum hydrogel at a concentration of 12 mg/cm³ across increasing magnifications, highlighting its structural and surface morphology. At low magnification (a, 500 µm), the hydrogel displays a rugged, layered architecture with fractured, sheet-like regions, suggesting mechanical deformation during freeze-drying. At higher magnifications (b and c), fibrous connections and bridging structures become apparent, indicating partial network integrity and polymer chain entanglement across the matrix. The highest magnification (d, 50 µm) reveals fine, stretched fibrils spanning smooth lamellar surfaces, suggesting directional alignment and cohesive internal interactions. Collectively, these images demonstrate a heterogeneous but interconnected microstructure, combining lamellar domains with filamentous networks features that are critical for understanding the material's stability, mechanical behaviour, and potential for controlled nutrient release in agricultural applications.

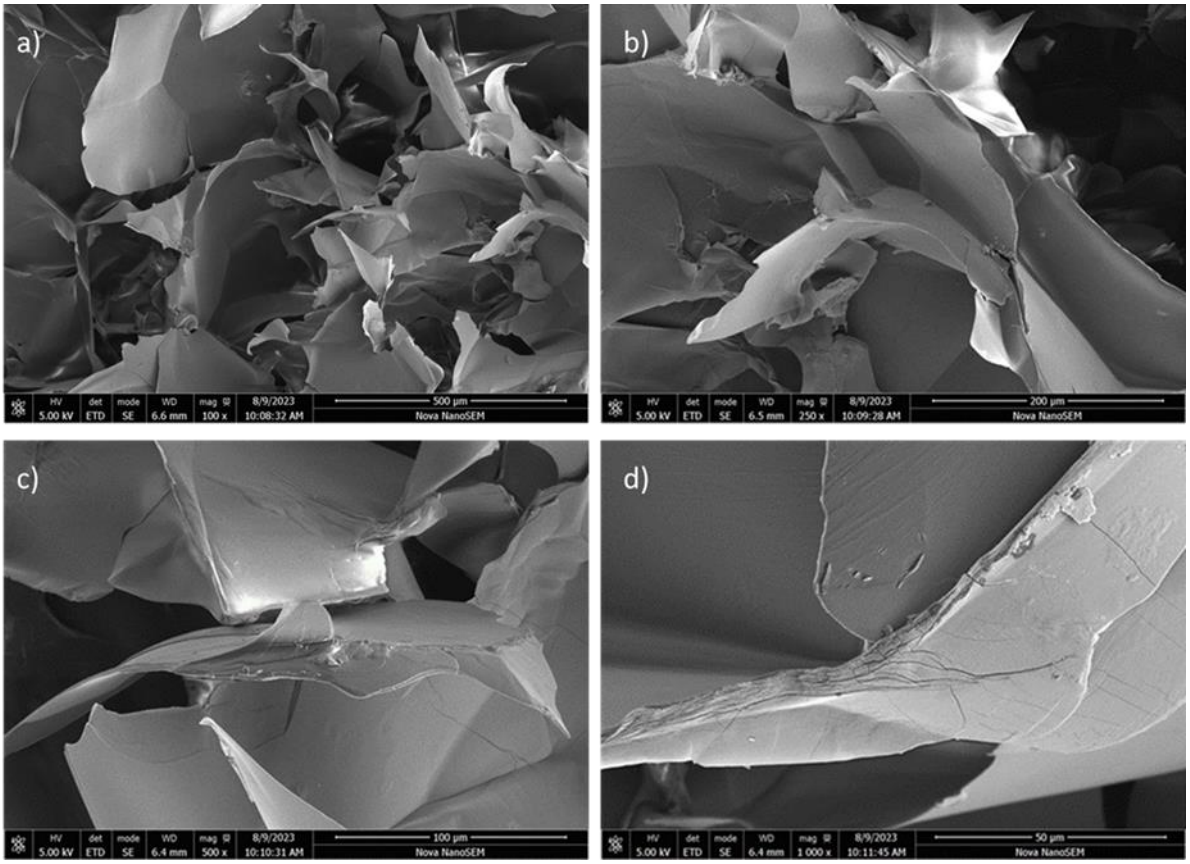

Figure 2.4: SEM micrographs of 12 GGH-MG and various magnifications. scale bar: a) 500 µm b) 200 µm c) 100 µm d) 50 µm.

The SEM images of the 12 mg/mL GGH hydrogel with Miracle-Gro reveal a dense, layered morphology with pronounced fracturing and limited porosity. The rough, fractured surfaces and sharp edges suggest brittle behavior, likely influenced by drying or environmental stresses. Features such as layer delamination and micro-cracking observed at higher magnifications indicate stress-induced degradation and possible element diffusion or swelling. Overall, the structure appears more compact and plate-like, with fewer interconnected or filamentous features compared to previous samples.

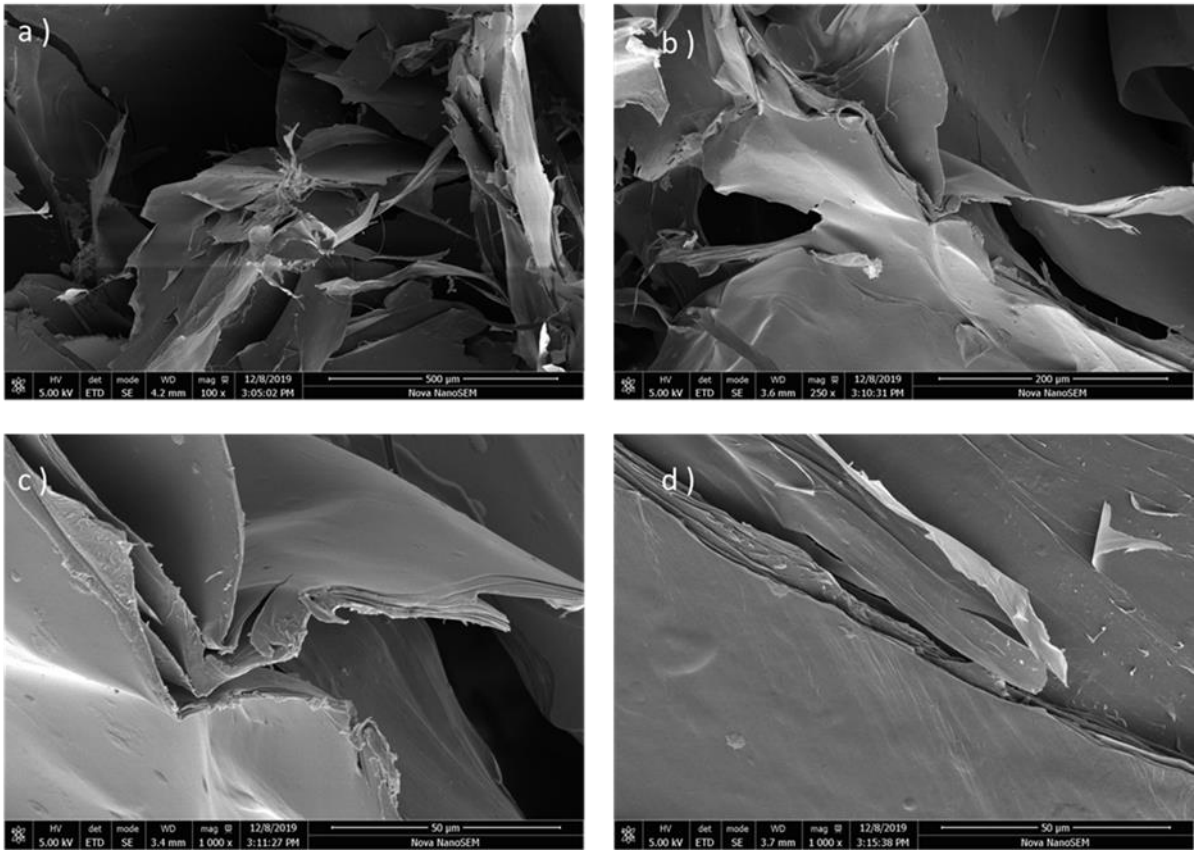

Figure 2.5: SEM micrographs of 14 GGH and various magnifications. scale bar: a) 500 µm b) 200 µm c) 100 µm d) 50 µm.

Figure 2.5 shows SEM micrographs of Gellan Gum hydrogel at a concentration of 14 mg/cm³, captured at progressively increasing magnifications to examine its microstructural features. At 500 µm magnification (a), the hydrogel displays compact, multilayered sheet-like structures with dense stacking and folding, suggesting a more rigid and consolidated matrix. At 200 µm (b), the surfaces appear smoother with sharply defined edges and minimal fibrillar bridging, indicating limited network interconnectivity. The 100 µm image (c) further emphasizes the lamellar morphology, revealing tightly packed layers with clear fracture lines and smooth, continuous planes. At the highest magnification of 50 µm (d), the micrograph shows fine linear features and closely aligned surfaces with occasional delamination, suggesting internal stress and compression during drying. Overall, the 14 mg/cm³ sample exhibits a dense, highly ordered, and plate-like microstructure, which reflects strong gelation and reduced flexibility features that could impact nutrient diffusion and release behaviour in functional agricultural applications.

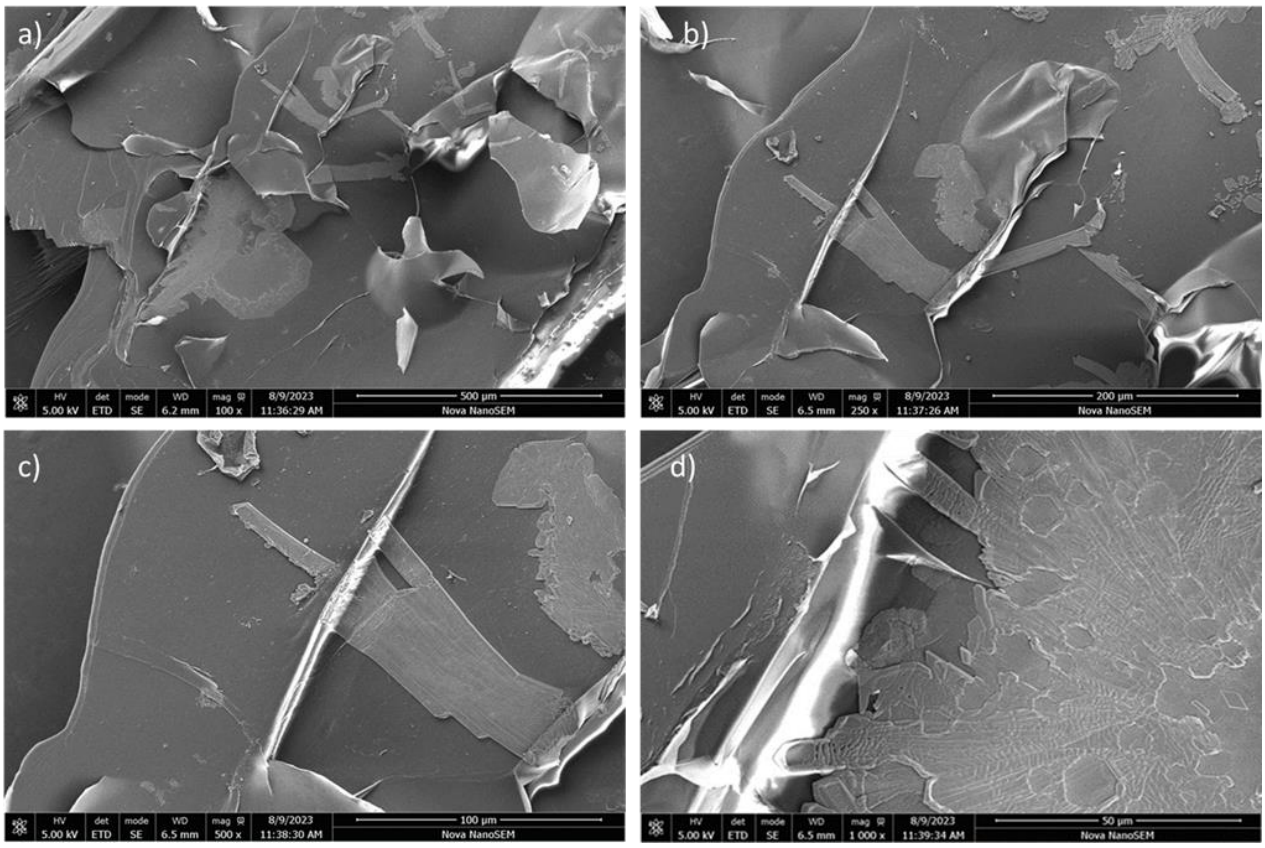

Figure 2.6: SEM micrographs of 14 GGH-MG and various magnifications. scale bar: a) 500 µm b) 200 µm c) 100 µm d) 50 µm.

Figure 2.6 displays SEM micrographs of Gellan Gum hydrogel at a concentration of 14 mg/cm³ with the addition of 1 mL concentrated nutrient, captured at magnifications ranging from 100× to 1,000×. At 100× magnification (a), the structure shows broad, angular sheet-like domains with relatively smooth surfaces and sharp edges, indicating a consolidated and rigid morphology. As magnification increases to 250× (b), thin, fractured layers become more evident, some of which appear delaminated or misaligned, possibly due to mechanical stress during freeze-drying. In image (c, 500×), distinct plate-like formations are visible, intersected by straight-edged segments that may reflect crystallization or reorganization influenced by the nutrient additive. The highest magnification at 1,000× (d) reveals a strikingly organized pattern with radial and polygonal features suggesting localized crystallinity or phase separation, likely induced by the interaction between Gellan Gum and the nutrient solution during gel formation. Overall, the images suggest that nutrient incorporation significantly alters the hydrogel's microstructure, promoting greater ordering and potentially affecting properties such as nutrient encapsulation, release rate, and mechanical response.

Table 2.4: SEM analysis summary of GG s at different gellan gum concentrations, with constant nutrient content across all samples.

Gellan Gum Concentration	General Morphology	Fiber Distribution	Surface Texture	Interpretation
10 GGH Matrix.	Layered sheets with visible web-like fibres	Fairly uniform, increasing visibility with magnification	Moderate roughness	Demonstrates effective fibre distribution and suggests the possibility of acceptable mechanical performance.
10 GGH-MG Matrix.	Sheet-like structure with embedded aligned fibres	Fine, directional, well-spread	Smooth with linear features	Shows that the fibres are well aligned and embedded; this may indicate improved tensile strength or directional qualities.
12 GGH Matrix.	Highly irregular, rough matrix with dense fibre networks.	Dense, entangled, well-distributed	Very rough, fibrous.	Suggests excellent fibre-matrix interlocking, likely enhancing strength and toughness
12 GGH-MG Matrix	Fragmented, flaky layers with brittle fracture signs	Very sparse or absent	Sharp, angular, brittle	Appears poorly reinforced; likely a control or sample with low filler content; reduced mechanical integrity
14 GGH Matrix.	Smooth, fractured, layered structure	Minimal or absent	Flat and clean	Suggests poor or no fibre reinforcement; likely a control or weakly reinforced sample.
14 GGH-MG Matrix.	Smooth, flat fractured layers	No clear fibre presence	Very smooth and brittle	Again suggests low or no reinforcement; ideal as a baseline for comparison

The SEM analysis of gellan gum (GG) matrices at varying concentrations, both with and without concentrated nutrients, reveals distinct morphological and structural trends. At 10 mg/cm³, the plain GG matrix exhibits layered sheets with visible fibres, suggesting effective distribution and moderate mechanical integrity, while the addition of nutrients results in well-aligned, embedded fibres and smoother surfaces, potentially enhancing directional strength. Increasing the concentration to 12 mg/cm³ without nutrients leads to a highly fibrous, rough matrix indicative of strong fibre-matrix interlocking and improved toughness; however, with nutrients, the matrix becomes fragmented and brittle, showing minimal fibre reinforcement and

reduced structural integrity. At the highest concentration, 14 mg/cm³, both samples with and without nutrients—display smooth, fractured layers with little to no fibre presence, suggesting poor reinforcement and functioning as control-like baselines. Overall, nutrient addition seems to promote fibre alignment at lower GG concentrations but may compromise reinforcement at higher concentrations.

2.3.1.2 SEM Analysis of Gellan Gum and Gellan Gum with HEC with and without Nutrients

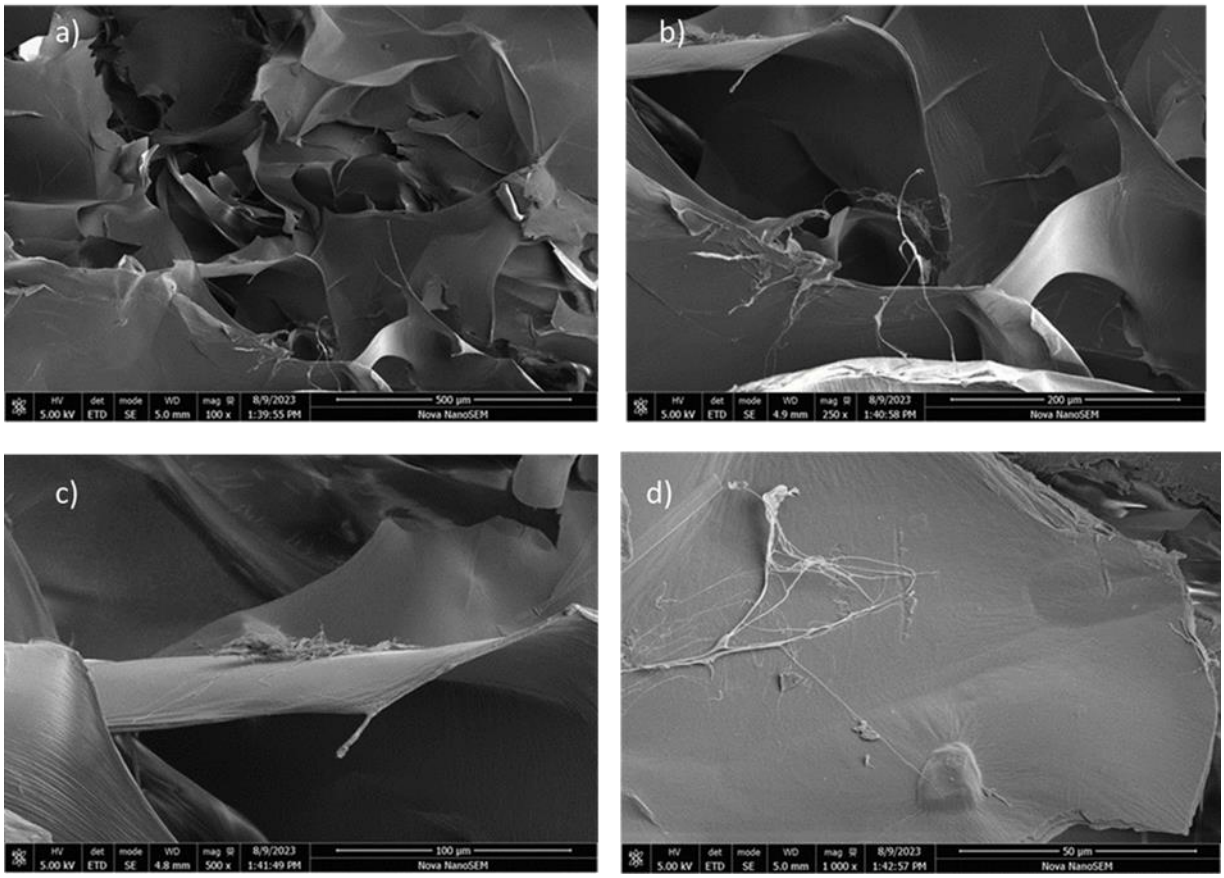

Figure 2.7: SEM micrographs of 10 GGH- HEC and various magnifications. scale bar: a) 500 µm b) 200 µm c) 100 µm d) 50 µm.

Figure 2.7 presents SEM micrographs of a composite hydrogel composed of 10 mg/cm³ Gellan Gum and 5 mg/cm³ Hydroxyethyl Cellulose (HEC), examined at magnifications of 500, 200, 100, and 50 µm to evaluate structural morphology. At 500 µm (image a), the structure shows a fragmented, layered morphology with extensive folding and overlapping sheets, indicating heterogeneous distribution and potential phase interaction between the two polymers. In image (b, 200 µm), distinct curved lamellae and smooth surfaces are observed, interwoven with thin, fibrous structures bridging gaps between layers likely representing HEC entanglements

integrated into the Gellan matrix. The 100 µm view (c) reveals more prominent fibrillar connections stretching across open regions, suggesting enhanced cohesion and interfacial bonding. At 50 µm magnification (d), fine polymeric filaments are clearly visible over broad, smooth Gellan-rich domains, confirming HEC's contribution to fibre formation and increased network complexity. Collectively, these images indicate that incorporating HEC into Gellan Gum significantly influences the microstructure, enhancing interconnectivity and potentially improving mechanical flexibility and nutrient delivery properties in hydrogel formulations.

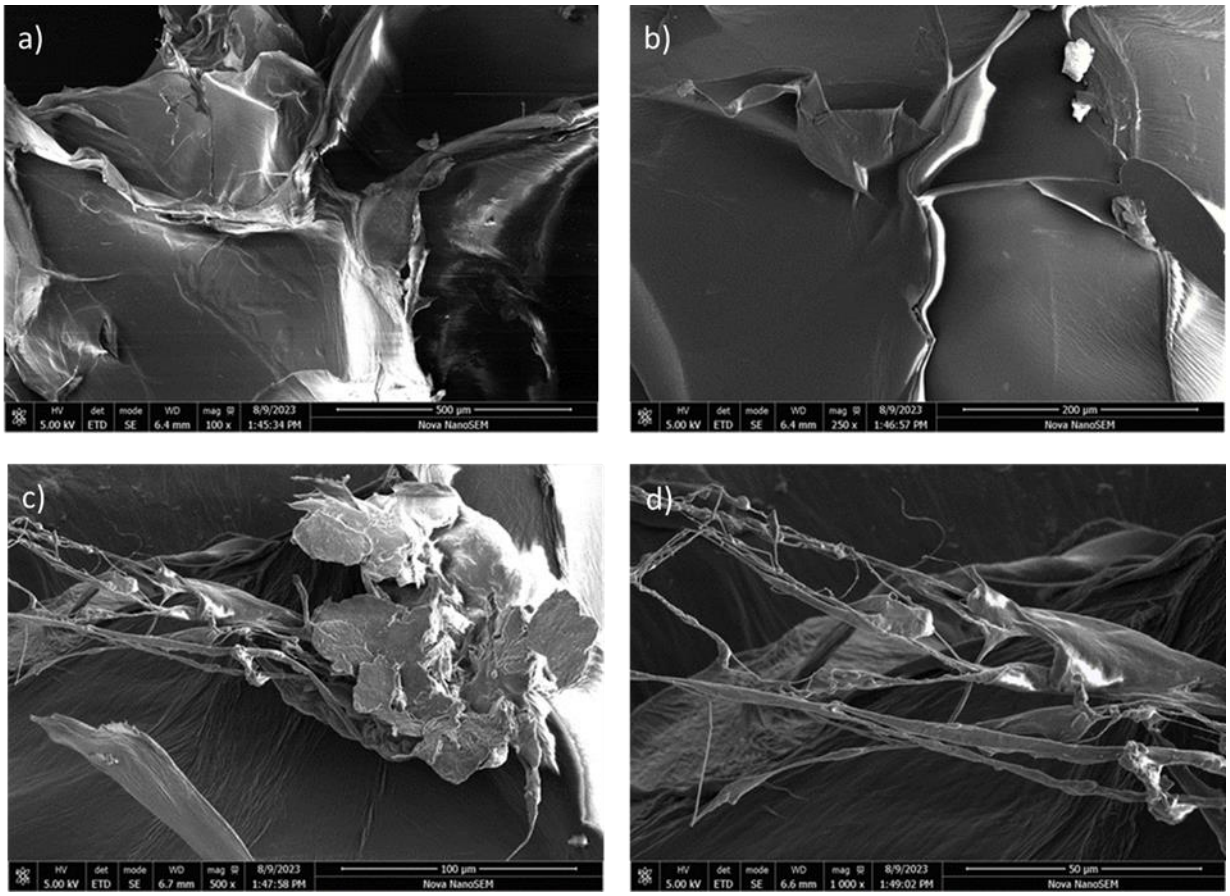

Figure 2.8: SEM micrographs of 10 GGH-HEC-MG and various magnifications. scale bar: a) 500 µm b) 200 µm c) 100 µm d) 50 µm.

Figure 2.8 presents SEM micrographs of a composite hydrogel containing 10 mg/cm³ Gellan Gum, 5 mg/cm³ Hydroxyethyl Cellulose (HEC), and 1 mL concentrated nutrient, imaged at progressively higher resolutions with scale bars of 500 µm, 200 µm, 100 µm, and 50 µm, respectively. At the 500 µm scale (a), the structure is dominated by large, smooth, fractured sheets with minimal folding, indicating a consolidated morphology influenced by polymer blending and nutrient incorporation. At 200 µm (b), the sheet-like features appear more sharply defined with clean edges, suggesting increased rigidity and film formation. The 100 µm image

(c) reveals the presence of embedded particulate clusters within the matrix likely nutrient residues or mineral aggregates highlighting localized heterogeneity introduced by the concentrated additive. At the finest scale of 50 µm (d), extensive filamentous structures are observed spanning across lamellar surfaces, forming a branched and entangled network that likely results from interactions between HEC chains and the nutrient phase. Together, these images demonstrate a highly integrated microstructure with dense lamellar zones, embedded particulates, and extended fibrous bridges, which may enhance the hydrogel's mechanical integrity, nutrient encapsulation capacity, and controlled release behaviour in agricultural systems.

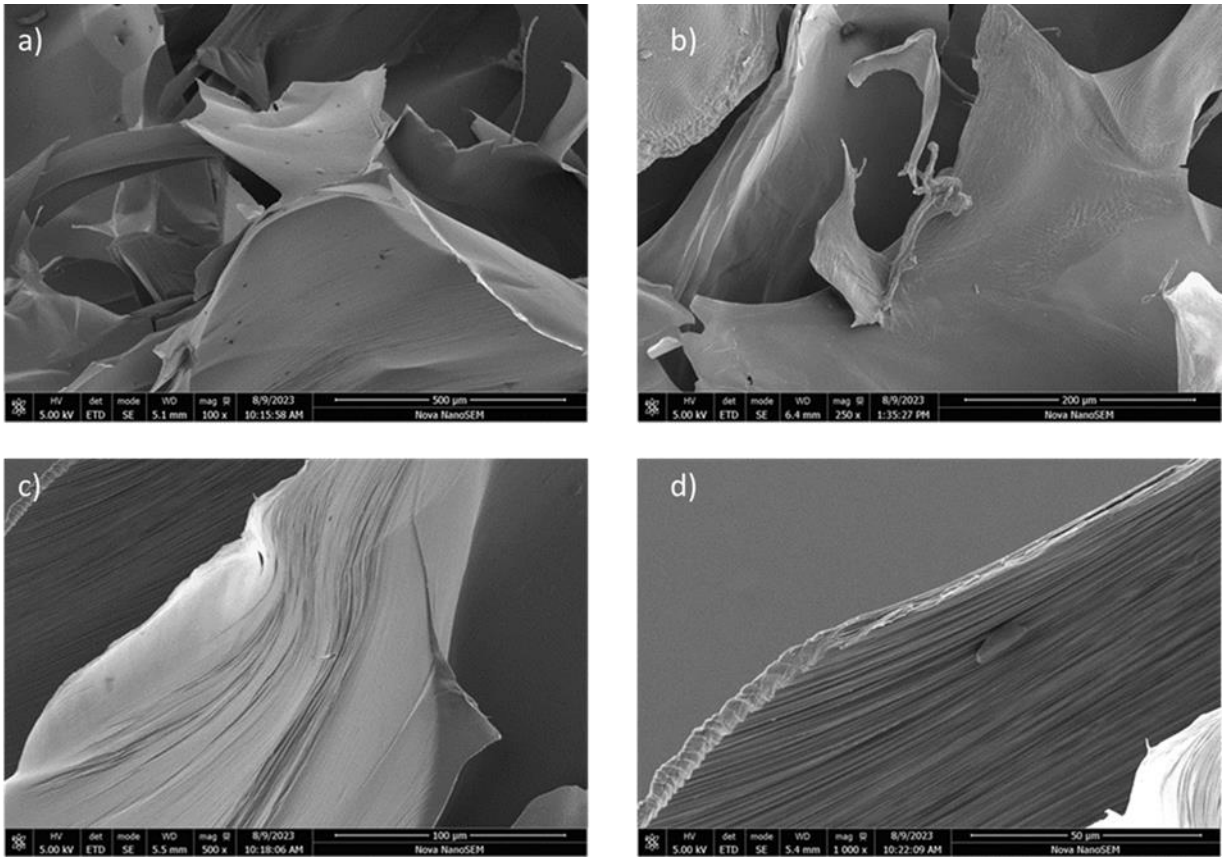

Figure 2.9: SEM micrographs of 12 GGH-HEC and various magnifications. scale bar: a) 500 µm b) 200 µm c) 100 µm d) 50 µm.

Figure 2.9 presents SEM micrographs of a hydrogel composed of 12 mg/cm³ Gellan Gum and 5 mg/cm³ Hydroxyethyl Cellulose (HEC), examined at four magnification levels corresponding to scale bars of 500 µm, 200 µm, 100 µm, and 50 µm. At the 500 µm scale (a), the hydrogel exhibits large, broad lamellar sheets with smooth surfaces and minimal fragmentation, suggesting a relatively uniform and well-formed gel matrix. Image (b, 200 µm) reveals more pronounced structural folds and undulations, with occasional curling and tearing at the edges, possibly caused by differential shrinkage or localized mechanical stress during

freeze-drying. At the 100 µm scale (c), the structure shows tight layering with flowing, wave-like features, indicating alignment or polymer orientation likely enhanced by HEC's film-forming characteristics. Finally, image (d, 50 µm) reveals a highly compact and stratified surface with fine linear grooves and a laminated appearance, indicative of strong intermolecular cohesion and potential for anisotropic mechanical behaviour.

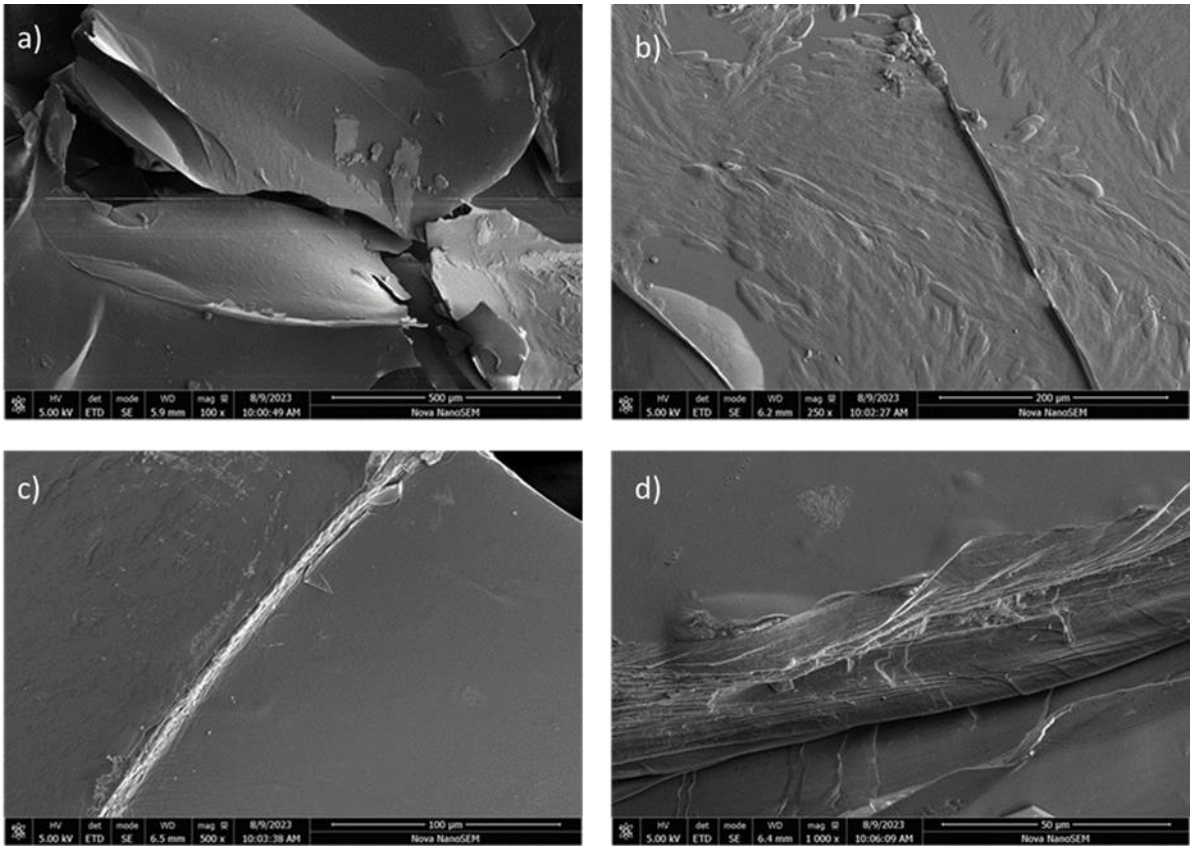

Figure 2.10: SEM micrographs of 12 GGH-HEC-MG nutrient and various magnifications. scale bar: a) 500 µm b) 200 µm c) 100 µm d) 50 µm.

Figure 2.10 shows SEM micrographs of a composite hydrogel composed of 12 mg/cm³ Gellan Gum, 5 mg/cm³ Hydroxyethyl Cellulose (HEC), and 1 mL of concentrated nutrient, visualized at scale bars of 500 µm, 200 µm, 100 µm, and 50 µm, respectively. In image (a, 500 µm), the hydrogel exhibits broad, compact lamellar structures with clear fracture planes, suggesting a brittle but well-formed gel matrix. The surface appears dense and layered, typical of strong internal packing and minimal porosity. At 200 µm (b), finer surface features emerge, including subtle texturing and embedded channels, possibly formed by nutrient phase diffusion or minor surface deformation during drying. In image (c, 100 µm), an elongated fibrillar feature is visible running across the lamellar plane, indicating localized polymer stretching or nutrient-induced fibre formation. The structure here appears smoother, but with embedded directional textures, hinting at polymer alignment during gelation. At the highest resolution in image (d,

50 µm), the surface reveals a tightly bundled fibre structure with intricate, thread-like extensions and branching, possibly formed by HEC interactions under nutrient-rich conditions. These features suggest enhanced structural complexity, reinforcing the hydrogel's matrix and indicating a more interconnected polymer network. Overall, the incorporation of both HEC and nutrient solution into the 12 mg/cm³ Gellan Gum hydrogel leads to a highly ordered and reinforced microstructure, with smooth lamellae, embedded fibrils, and surface detail that may enhance mechanical strength, swelling control, and nutrient retention—critical traits for functional agricultural hydrogels.

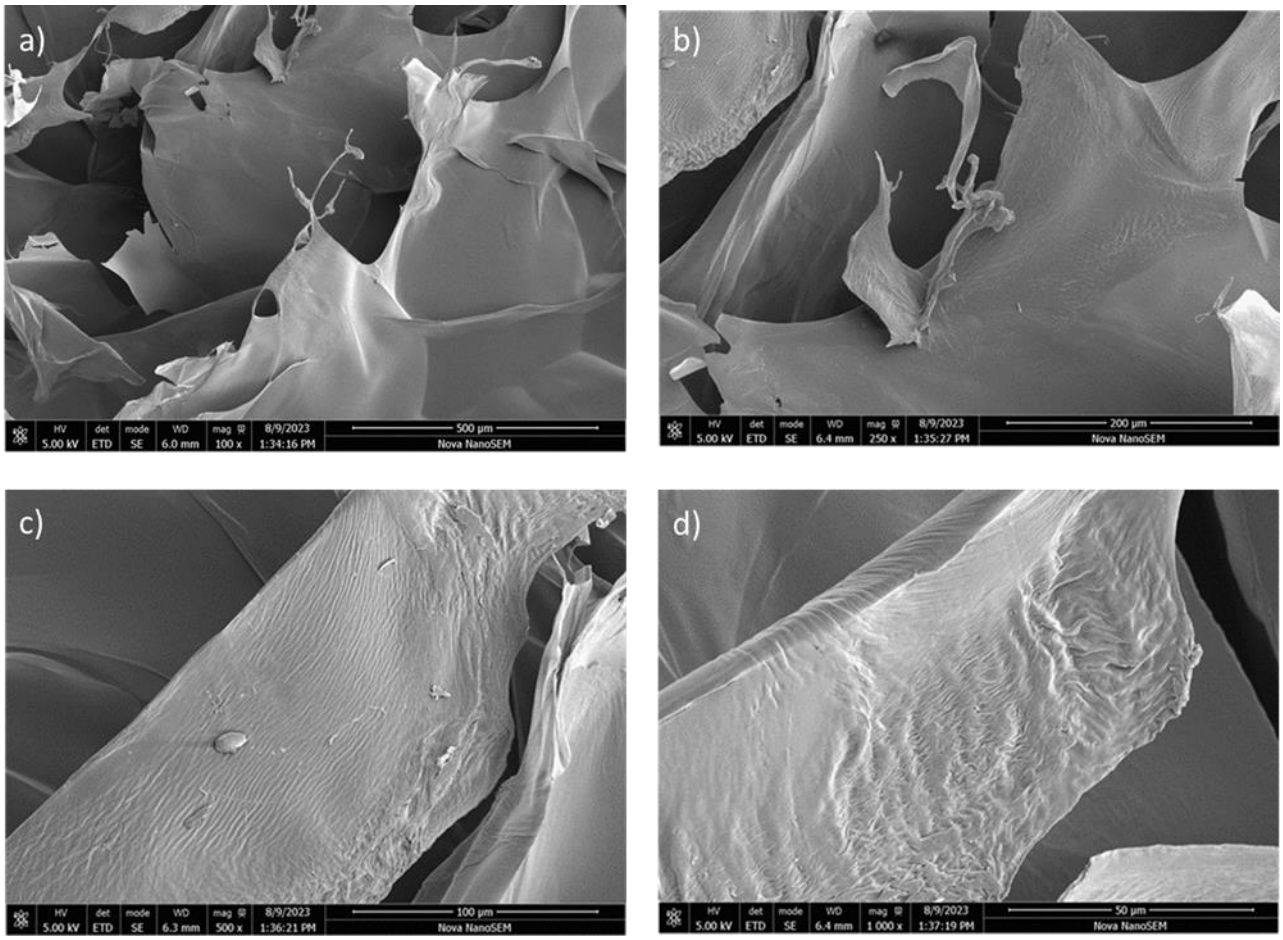

Figure 2.11: SEM micrographs of 14 mg/cm³ of Gellan Gum+ 5 mg/cm³ of HEC and various magnifications. scale bar: a) 500 µm b) 200 µm c) 100 µm d) 50 µm.

Figure 2.11 presents SEM micrographs of a hydrogel composed of 14 mg/cm³ Gellan Gum and 5 mg/cm³ Hydroxyethyl Cellulose (HEC) at increasing resolutions corresponding to scale bars of 500 µm, 200 µm, 100 µm, and 50 µm. In image (a, 500 µm), the microstructure appears as an interconnected matrix of fractured, thin sheets with curled edges, indicating a brittle or highly crosslinked morphology likely due to the high concentration of Gellan Gum. The surfaces are largely smooth but irregularly oriented, reflecting a compact network. At 200 µm

(b), more detailed features emerge, including torn and fibrous protrusions that suggest partial stretching or shearing during drying, which may be influenced by HEC's entanglement within the matrix. Image (c, 100 µm) reveals a smoother lamellar surface with fine linear textures and minor bulges, indicating regions of aligned polymer chains and possibly local swelling or nutrient interaction during gelation. In image (d, 50 µm), the surface shows a prominent transition from smooth to roughened textures, with rippling and wrinkling at the edges. This suggests mechanical deformation or phase separation during freeze-drying, and possibly the influence of HEC on surface topology.

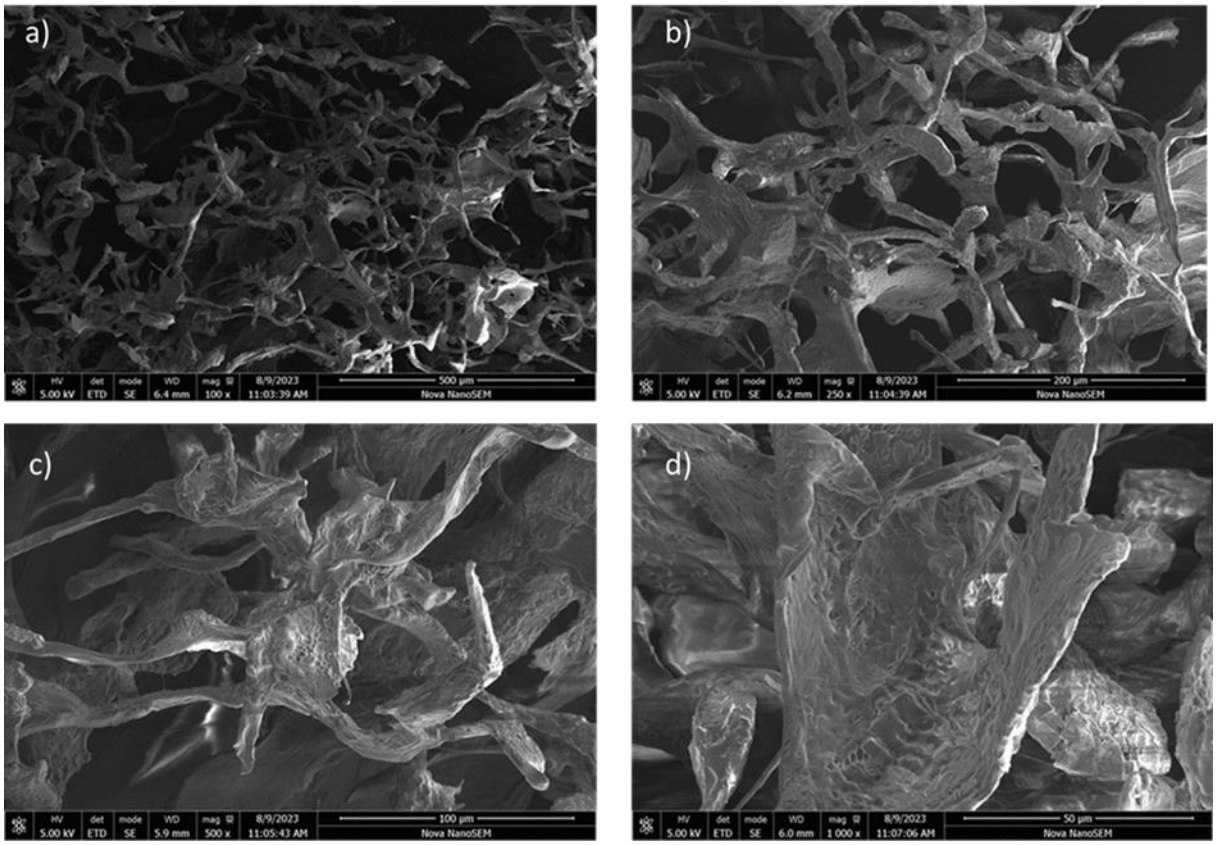

Figure 2.12: SEM micrographs of 14 GGH-HEC-MG and various magnifications. scale bar: a) 500 µm b) 200 µm c) 100 µm d) 50 µm.

Figure 2.12 presents SEM micrographs of a highly functionalized hydrogel composed of 14 mg/cm³ Gellan Gum, 5 mg/cm³ Hydroxyethyl Cellulose (HEC), and 1 mL of concentrated nutrient solution, shown at four magnification levels corresponding to scale bars of 500 µm, 200 µm, 100 µm, and 50 µm. At the 500 µm scale (a), the structure appears as a highly branched, sponge-like network with significant open spaces between polymeric strands, suggesting extensive gel swelling and structural expansion. Moving to 200 µm (b), the network becomes more detailed and reveals interconnected, web-like structures that display a high degree of uniformity and continuity, indicative of strong gelation and crosslinking between

Gellan Gum and HEC. At 100 µm magnification (c), individual fibrillar branches are clearly discernible, with twisted and rough surface textures likely formed by polymer entanglement and nutrient interaction. These features indicate good structural integrity and potential for nutrient entrapment. Finally, at 50 µm (d), the image reveals intricate, bark-like surface textures and dense micro-scale ridges on the hydrogel struts, reflecting fine-scale phase interactions and possibly nutrient crystallization within the polymeric matrix.

Table 2.5: SEM analysis summary of GG-HEC composites at different gellan gum concentrations, with constant HEC and nutrient content across all samples.

Gellan Gum Concentration	**General Morphology**	**Fiber Distribution**	**Surface Texture**	**Interpretation**
10 GGH-HEC Matrix.	Folded and interconnected matrix with fibre bridges	Sparse, some localized clusters	Mixed smooth and rough regions	Moderate reinforcement visible; suggests partial embedding and weak fibre-matrix bonding
10 GGH-HEC - MG Matrix.	Layered and cracked matrix with fibrous surface features	Sparse but extended fibre traces, some aggregation	Mixed smooth and slightly fibrous	Some fibre exposure and entanglement present; modest reinforcement; rougher texture at higher magnification
12 GGH-HEC Matrix.	Fragmented, brittle sheet layers	Very minimal or absent	Clean, striated surfaces	Appears brittle with weak cohesion; likely a control or low-reinforcement sample
12 GGH-HEC - MG nutrient Matrix	Brittle and delaminated sheets with striations	Thin linear features, but sparse fibre presence	Smooth with occasional surface lines	Limited fibre integration: cracks suggest brittle failure; poor interfacial bonding
14 GGH-HEC Matrix.	Fractured matrix with striated patterns	No clear fibrous structure	Rough ridges and tear line	Clear signs of fracture mechanics; no evident fibre presence, low interfacial bonding likely
14 GGH-HEC-MG Matrix.	Highly porous, sponge-like 3D network	Dense, entangled fibre web throughout	Irregular, textured surface	Very strong fibre network visible at all magnifications; likely excellent porosity and interfacial interaction; potentially ideal for high surface area applications (e.g., scaffolds or filtration)

The SEM analysis of GG-HEC matrices at varying concentrations, both with and without the addition of concentrated nutrients, reveals significant structural and morphological differences.

At 10 mg/cm³, the plain GG-HEC matrix shows a folded structure with sparse, localized fibre bridges, suggesting only moderate reinforcement, while nutrient addition leads to a cracked matrix with more visible fibre entanglement and slightly rougher texture, indicating modest improvement in fibre integration. At 12 mg/cm³, both matrices—without and with nutrients—exhibit brittle, fragmented or delaminated sheets with minimal fibre presence, striated surfaces, and poor interfacial bonding, suggesting low mechanical integrity. In contrast, at 14 mg/cm³, the plain matrix remains fractured and fibrously deficient, but the nutrient-enriched version transforms into a highly porous, sponge-like 3D network with a dense, entangled fibre web and irregular surface, pointing to significantly enhanced porosity and fibre interaction, potentially advantageous for filtration or scaffold-based applications.

2.3.1.3 SEM Analysis of Gellan Gum and Gellan Gum with CMC with and without Nutrients

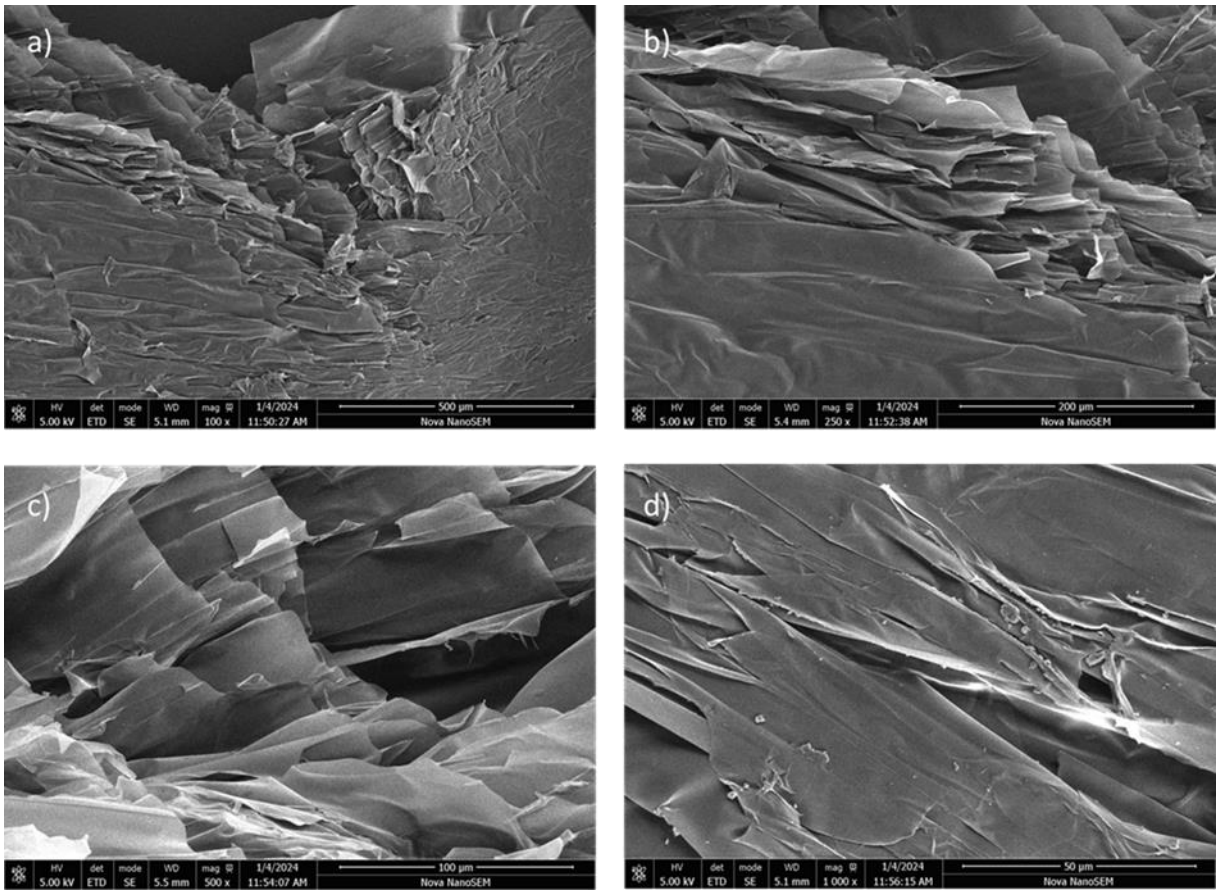

Figure 2.13: SEM micrographs of 10 GGH-CMC and various magnifications. scale bar: a) 500 µm b) 200 µm c) 100 µm d) 50 µm.

Figure 2.13, which presents SEM micrographs of a composite made from 10 mg/cm³ of Gellan Gum (GG) + 5 mg/cm³ of Carboxymethyl Cellulose (CMC) at four different magnifications: At low magnification (500 µm, a), the structure reveals layered, sheet-like morphology,

indicating a well-stacked composite. This might reflect how the GG and CMC interact to form a lamellar or stratified matrix. With increased magnification (200 µm, b), the layered architecture becomes more prominent, showing the organized stacking of flat sheets. These formations suggest limited interpenetration between polymer phases, favouring parallel alignment. At 100 µm, c), fractures and separations between sheets begin to emerge, indicating potential brittleness or points of mechanical weakness, likely due to insufficient crosslinking or weak interfacial bonding. The highest magnification (50 µm, c) reveals fine surface cracks and delamination, with no visible fibrous reinforcement. This surface morphology suggests poor energy dissipation and may correlate with a brittle fracture mode under mechanical stress.

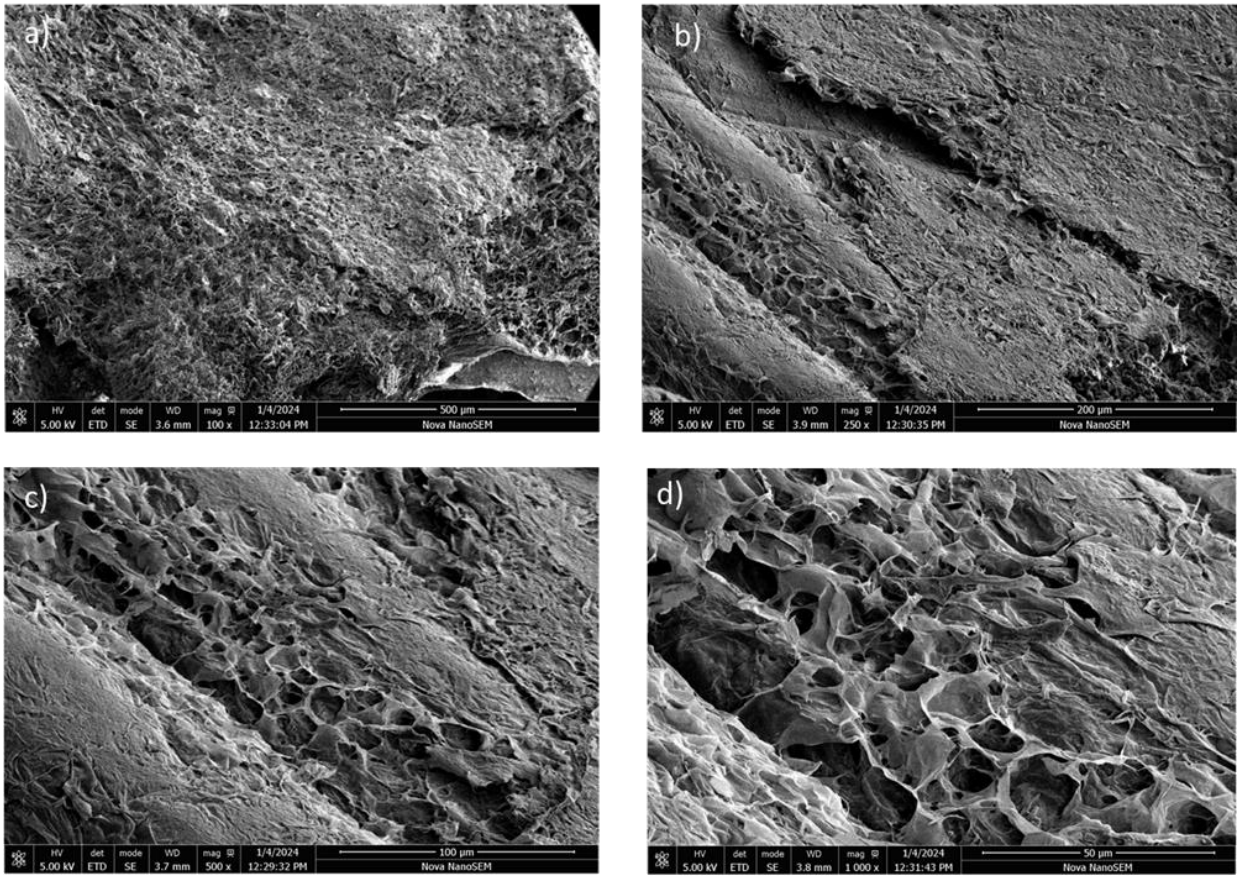

Figure 2.14: SEM micrographs of 10 GGH-CMC-MG and various magnifications. scale bar: a) 500 µm b) 200 µm c) 100 µm d) 50 µm.

Figure 2.14 displays SEM micrographs of a composite composed of 10 mg/cm³ gellan gum (GG), 5 mg/cm³ carboxymethyl cellulose (CMC), and 1 mL of concentrated nutrient, observed at four magnifications (a–d). At low magnification (a, 500 µm), the surface appears densely packed with a rough, sponge-like texture, indicating a highly porous macrostructure. At

medium magnifications (b, 200 µm and c, 100 µm), interconnected pores and channel-like features become increasingly visible, suggesting good internal connectivity. At the highest magnification (d, 50 µm), the material reveals a well-defined, open porous network with rounded cavities and thin walls, indicating a highly porous microarchitecture. These structural features suggest that the nutrient addition promotes pore formation and phase separation, resulting in a scaffold-like material suitable for applications requiring high surface area, such as biomedical scaffolds, controlled release systems, or filtration media.

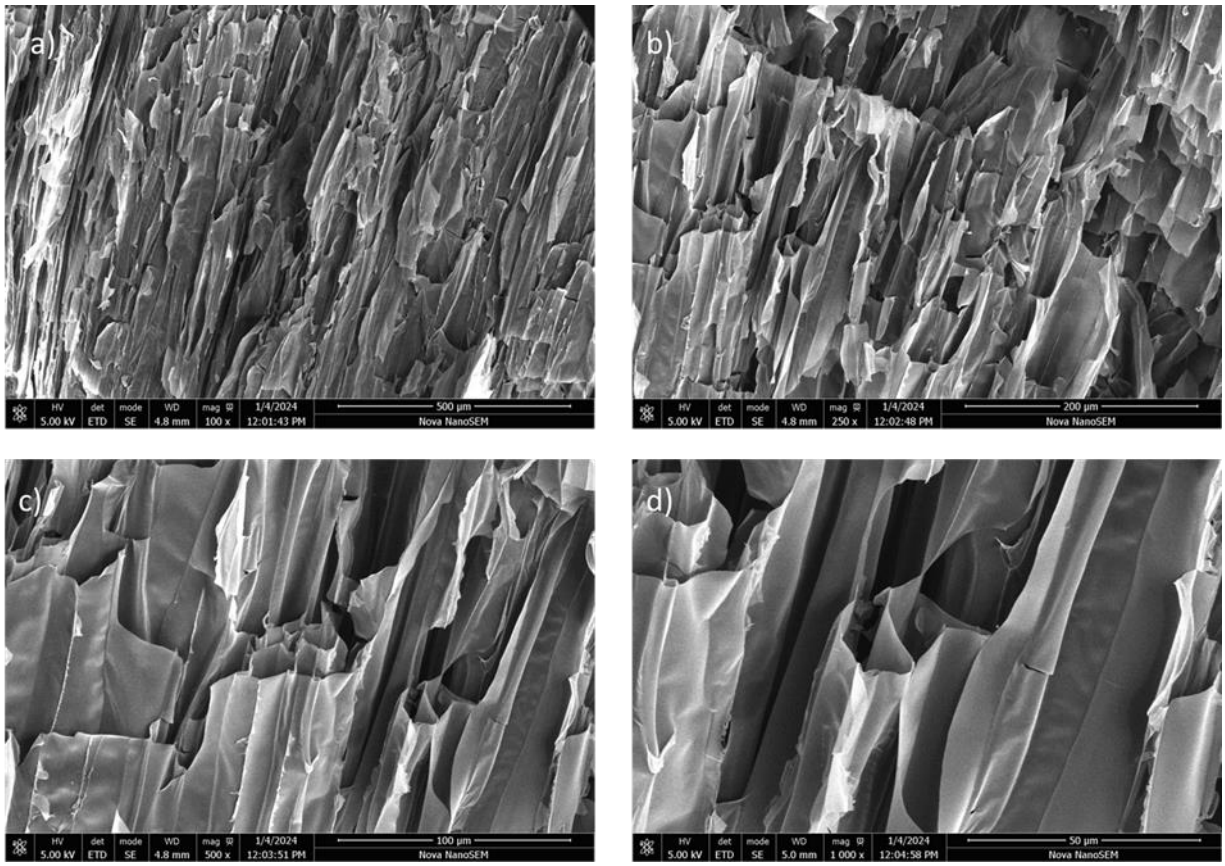

Figure 2.15: SEM micrographs of 12 GGH-CMC and various magnifications. scale bar: a) 500 µm b) 200 µm c) 100 µm d) 50 µm.

Figure 2.15 presents SEM micrographs of a composite made from 12 mg/cm³ gellan gum (GG) and 5 mg/cm³ carboxymethyl cellulose (CMC) at increasing magnifications: At (a (500 µm scale): The image reveals a distinct vertically aligned lamellar architecture, resembling a columnar or blade-like structure. The organization suggests directional solidification or phase alignment during processing. At (b) (200 µm scale): The lamellae become more defined and clearer at this magnification, with noticeable parallel alignment and spacing. This pattern indicates structural regularity and potentially directional mechanical strength. At (c) (100 µm scale): A closer view shows tightly packed, elongated lamellae with smooth, layered surfaces

and consistent vertical orientation. The clear separation between layers reflects a high degree of internal order, enhancing anisotropic properties such as stiffness or diffusion along the vertical axis. At (d) (50 µm scale): At the highest magnification, individual lamellar walls appear sharp-edged, thin, and continuous, with minimal surface defects. This refined structure may contribute to enhanced mechanical integrity and controlled transport pathways, making it suitable for filtration, barrier materials, or scaffold applications.

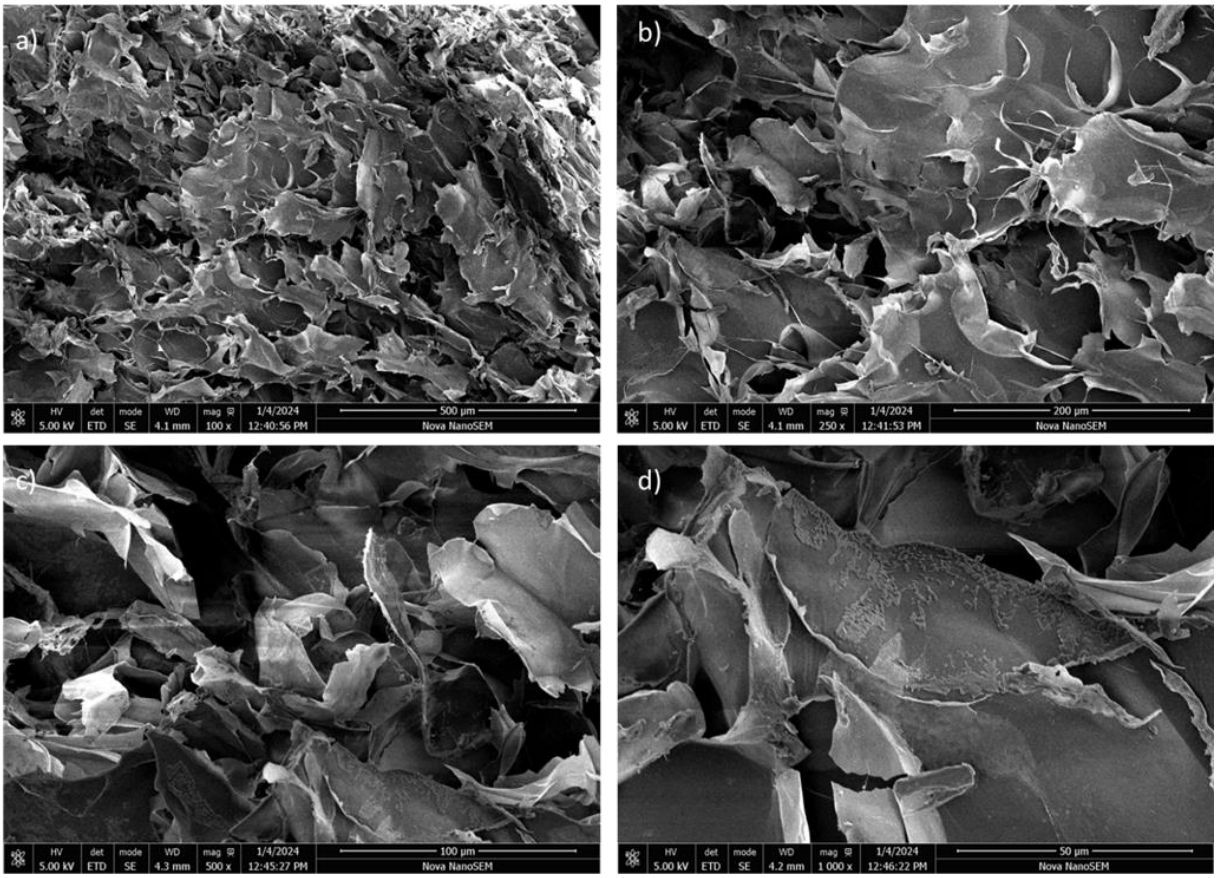

Figure 2.16: SEM micrographs of 12 GGH-CMC-MG and various magnifications. scale bar: a) 500 µm b) 200 µm c) 100 µm d) 50 µm.

Figure 2.16 presents SEM micrographs of a composite composed of 12 mg/cm³ gellan gum (GG), 5 mg/cm³ carboxymethyl cellulose (CMC), and 1 mL of concentrated nutrient, captured at increasing magnifications. At low magnification (a, 500 µm), the structure appears as a disordered and crumpled sheet-like matrix with significant surface roughness, indicating a loosely packed, layered formation. As the magnification increases (b, 200 µm), fibrous bridges and torn sheet edges become more apparent, suggesting partial fibre exposure and uneven integration within the matrix. At 100 µm (c), the fractured morphology becomes clearer, revealing irregular gaps and thin overlapping flakes, indicative of a fragile and heterogeneous internal structure. Finally, at the highest magnification (d, 50µm), the surface shows signs of

possible nutrient-induced aggregation or phase separation, with some areas appearing denser or roughened. Overall, this composite displays a heterogeneous, brittle morphology with incomplete fibre-matrix bonding, likely leading to weak mechanical cohesion but increased surface area, which could be useful in applications like absorption or low-load scaffolding.

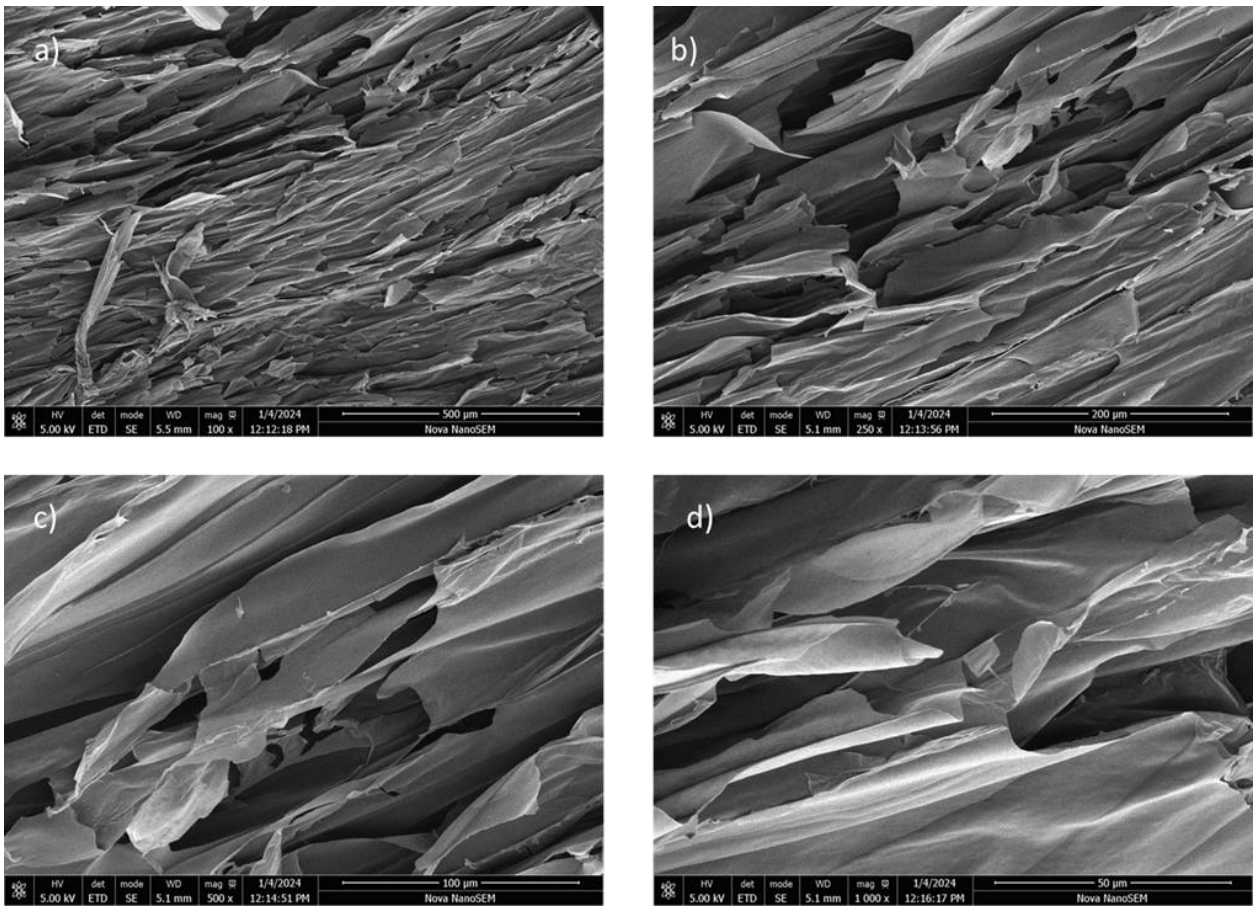

Figure 2.17: SEM micrographs of 14 mg/cm³ of Gellan Gum+ 5 mg/cm³ of CMC and various magnifications. scale bar: a) 500 µm b) 200 µm c) 100 µm d) 50 µm.

Figure 2.17 presents SEM micrographs of a composite composed of 14 mg/cm³ gellan gum (GG) and 5 mg/cm³ carboxymethyl cellulose (CMC) at four magnifications. At the lowest magnification (a, 500 µm), the structure reveals a densely packed, highly aligned lamellar formation, with layers appearing tightly stacked in a uniform direction. As magnification increases (b, 200 µm and c, 100 µm), this layered, sheet-like morphology becomes more pronounced, showcasing thin, elongated sheets with sharp interfaces and minimal disruption indicative of a well-ordered internal structure. At the highest magnification (d, 50 µm), the surface features remain smooth and consistent, with tightly adhered layers and no visible porosity or fibre exposure.

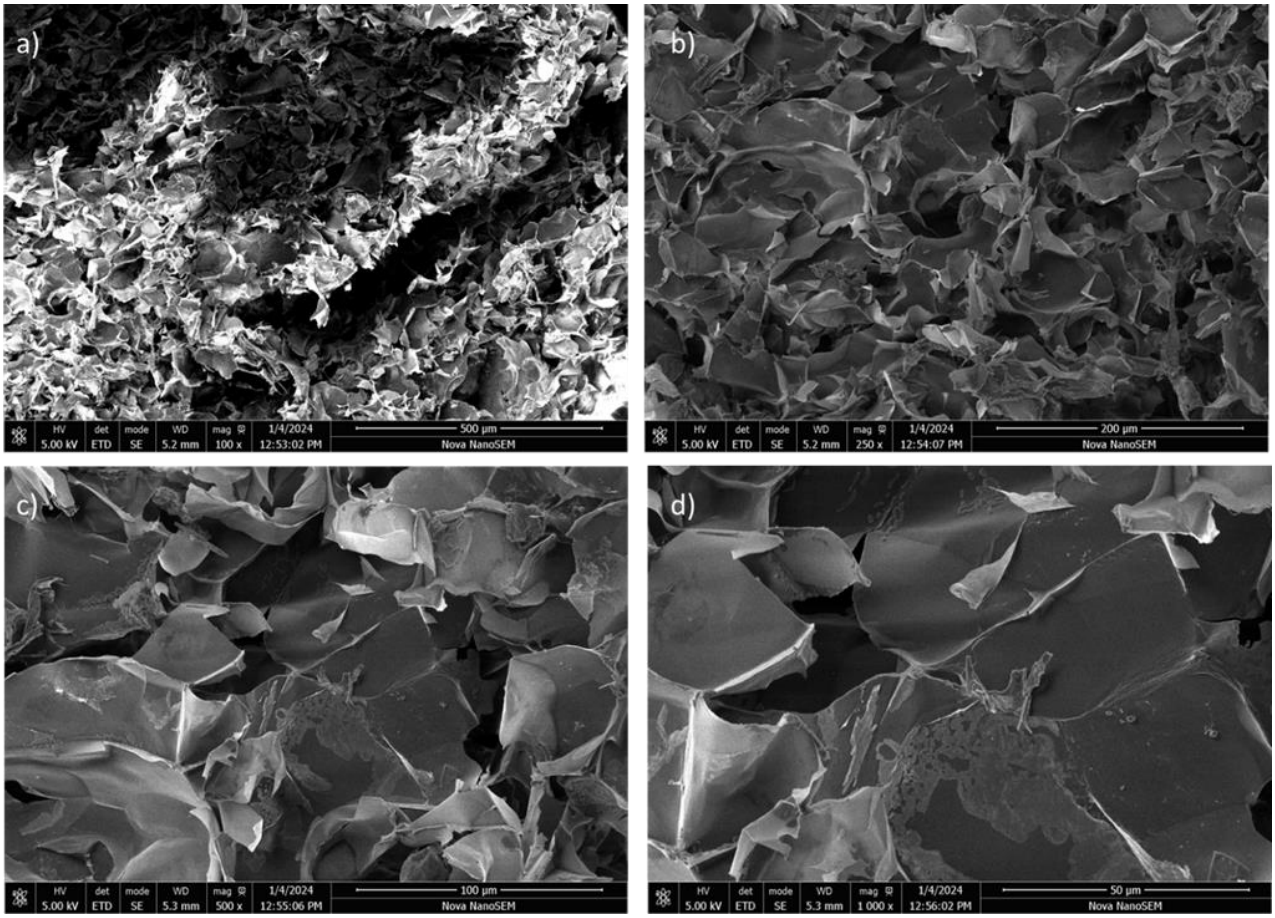

Figure 2.18: SEM micrographs of 14 GGH-CMC-MG nutrient and various magnifications. scale bar: a) 500 µm b) 200 µm c) 100 µm d) 50 µm.

Figure 2.18 shows SEM micrographs of a composite made from 14 mg/cm³ gellan gum (GG), 5 mg/cm³ carboxymethyl cellulose (CMC), and 1 mL concentrated nutrient, captured at four magnifications. At low magnification (a, 100×), the surface appears highly disordered and fragmented, with a rough, uneven morphology and loosely packed flakes. As the magnification increases (b and c), the structure reveals a chaotic network of overlapping sheets and irregular voids, suggesting weak matrix cohesion and poor structural uniformity. At the highest magnification (d, 1000×), the image shows some surface roughening and partial fibre entanglement, but the sheets remain largely delaminated, with limited bonding between layers. Overall, this composite displays a heterogeneous, brittle morphology influenced by nutrient addition, which seems to disrupt the lamellar alignment seen in the non-nutrient sample (Figure 2.17). The resulting structure may offer increased surface area but likely suffers from reduced mechanical strength and interfacial stability, making it more suited to low-load or functional applications such as adsorption or diffusion-based systems.

Table 2.6: SEM analysis summary of GG-CMC composites at different Gellan gum concentrations, with constant CMC and nutrient content across all samples.

Gellan Gum Concentration	General Morphology	Fiber Distribution	Surface Texture	Interpretation
10 GGH-CMC Matrix.	Layered and fractured structure with partial compaction	Horizontal lamellar stacking with step-like edges	Smooth and dense with limited porosity	Indicates a brittle, anisotropic structure; suggests potential for mechanical strength in one direction but limited flexibility or diffusion.
10 GGH-CMC - MG Matrix.	Irregular and interconnected network	Clearly visible, forming an internal web	Rounded and continuous surface cavities	Indicates a well-integrated structure with fibre interaction; likely offers good internal complexity and interaction potential
12 GGH-CMC Matrix.	Vertically aligned lamellar network	Highly ordered, upright layers in parallel	Very smooth, with crisp edges and minimal voids	Excellent structural alignment; likely improves directional stiffness and controlled flow. Suitable for scaffolds or directional barriers.
12 GGH-CMC - MG Matrix	Crumpled, layered flakes	Sparse, partially embedded	Rough, uneven, with flake overlap	Suggests weak interfacial bonding and moderate fibre reinforcement; may exhibit limited strength and cohesion
14 GGH-CMC Matrix.	Overlapping, tightly packed sheets	Horizontally stacked lamellae, moderately disordered	Smooth and continuous with faint delamination lines	Suggests good compaction and mechanical cohesion. Suitable for dense film-like applications or structural matrices
14 GGH-CMC - MG Matrix.	Fragmented and disordered layers	Minimal, poorly defined	Smooth in some regions, with signs of cracking	Reflects a brittle, weakly bonded matrix; reduced mechanical integrity and limited fibre effectiveness

2.3.2 EDX and EDX map of Gellan Gum and Modified Gellan Gum

An Energy Dispersive X-ray Spectroscopy EDX analysis was conducted on every sample. (EDX) analysis was conducted to compare the samples GGH with and without nutrients and notice any obvious variations at three different concentrations. As well as Examine and contrast the disparities between gellan gum hydrogels and composites of gellan hydroxyethyl cellulose hydrogels and carboxymethyl cellulose (GGH-HEC and GGH-CMC) with and without nutrients.

2.3.2.1 EDX and EDX map of GGH and GGH-MG at three concentrations

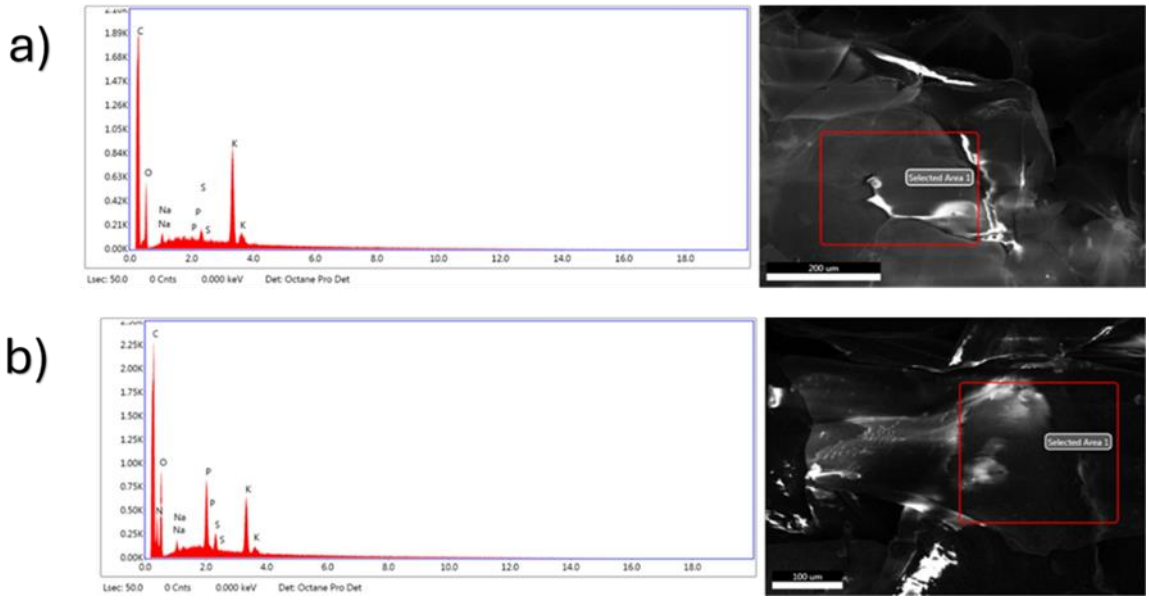

Figure 2.19: EDX mineral analysis of a)10 GGH, b) 10 GGH-MG.. Showing the elemental composition (%) within the selected area (red square).

Figure 2.19 presents EDX (Energy-Dispersive X-ray Spectroscopy) mineral analysis of two hydrogel samples: (a) 10 mg/cm³ gellan gum hydrogel, and (b) 10 mg/cm³ gellan gum hydrogel supplemented with 1 mL of nutrient solution. The red squares in the SEM images indicate the regions selected for elemental analysis. In image (a), the EDX spectrum shows main peaks for carbon (C) and oxygen (O), which are normal parts of the organic gellan gum structure. Small amounts of sodium (Na), sulphur (S), phosphorus (P), and potassium (K) are also found, likely coming from the gellan gum or the buffers used in preparation. In image (b), the EDX spectrum shows a similar mix of elements but with much stronger signals for P, S, K, and Na, indicating that adding nutrients boosted the levels of these elements in the hydrogel. The higher amounts of these minerals match the added nutrients and show that the solution successfully added minerals to the hydrogel. Overall, the EDX comparison shows that adding nutrients changes the elemental makeup of the hydrogel, especially by raising the levels of important mineral elements that play a role in biological or chemical functions.

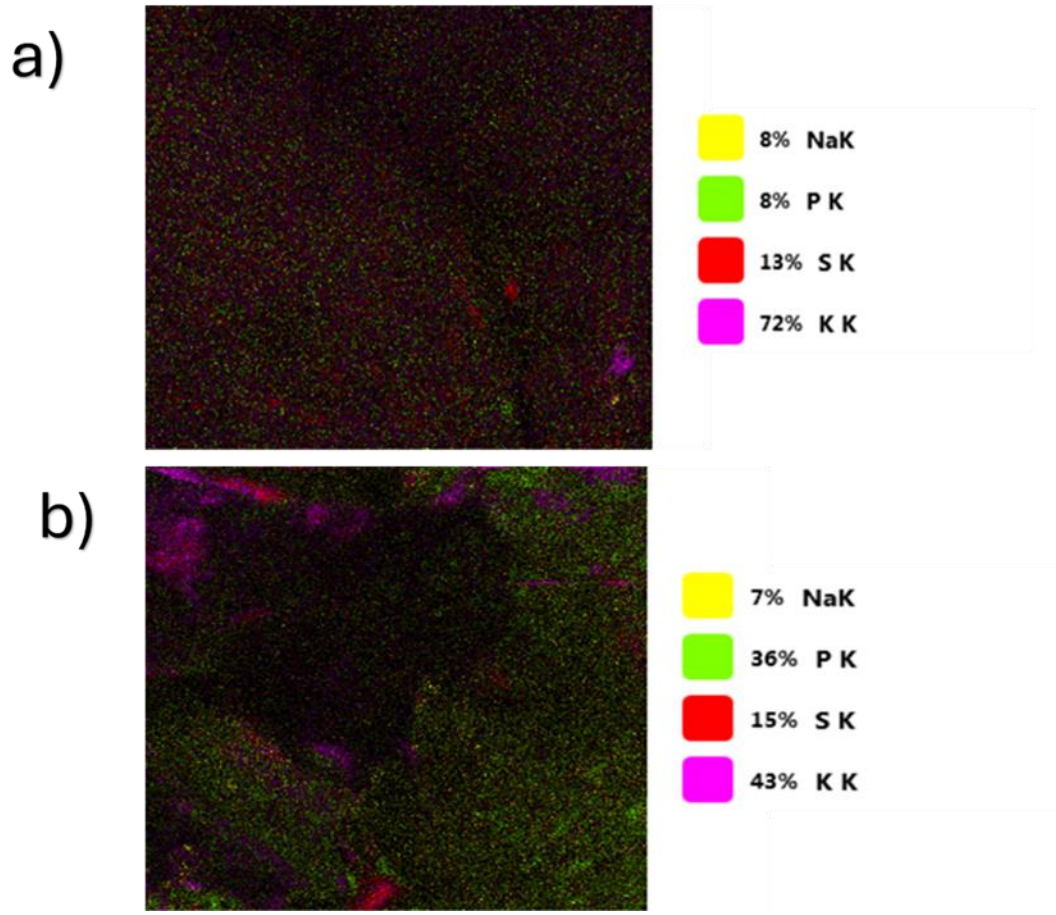

Figure 2.20: EDX mineral mapping of gellan gum hydrogel with a) 10 GGH and b) 10 GGH-MG. The elemental map illustrates the distributions and relative percentages of each element.

Figure 2.20 presents EDX mineral mapping of gellan gum hydrogels under two conditions: (a) with 10 mg/cm³ of gellan gum alone, and(b) with 10 mg/cm³ of gellan gum supplemented by 1 mL of concentrated nutrients. Each map shows the spatial distribution and relative abundance of four key elements: sodium (Na), phosphorus (P), sulphur (S), and potassium (K), color-coded as yellow, green, red, and magenta respectively. In image (a), potassium (K) dominates the elemental composition at 72%, while sulphur (S), sodium (Na), and phosphorus (P) each appear at much lower levels (13%, 8%, and 8% respectively). This suggests a more uniform, potassium-rich baseline composition in the untreated gellan gum hydrogel. In contrast, image (b) shows a distinct shift in elemental distribution following nutrient addition. Phosphorus increases dramatically to 36%, while potassium drops to 43%, and sulphur rises slightly to 15%. Sodium remains relatively constant at 7%. The enhanced phosphorus signal indicates successful incorporation of phosphate-rich nutrient components, while the more balanced presence of elements reflects a broader mineral profile and more complex chemical

environment compared to the untreated sample. Overall, the EDX maps confirm that the nutrient-enriched hydrogel exhibits increased elemental diversity and mineral uptake, particularly phosphorus, which is a strong indicator of nutrient retention within the matrix.

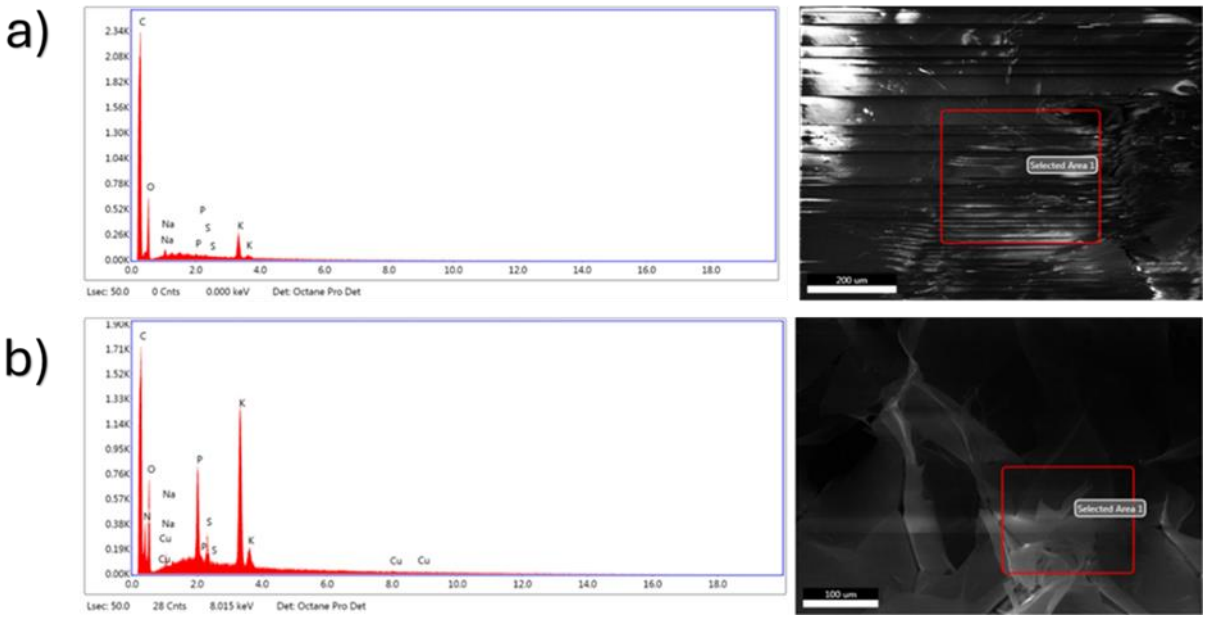

Figure 2.21: EDX mineral analysis of a)12 GGH, b) 12 GGH-MG. Showing the elemental composition (%) within the selected area (red square).

Figure 2.21 displays EDX (Energy-Dispersive X-ray) mineral analysis for two gellan gum hydrogel samples, both with a gellan gum concentration of 12 mg/cm³. (a) shows the sample without nutrient supplementation(b) shows the sample with 1 mL of concentrated nutrient added. Each analysis focuses on a specific region marked by a red square in the accompanying SEM images. In image (a), the EDX spectrum reveals dominant peaks for carbon (C) and oxygen (O), consistent with the organic composition of the hydrogel. Smaller peaks for sodium (Na), phosphorus (P), sulphur (S), and potassium (K) suggest the presence of residual salts or naturally occurring ions within the gellan gum matrix. In image (b), after nutrient addition, the elemental profile becomes more pronounced: the potassium (K) peak is significantly stronger, and both phosphorus (P) and sulphur (S) also show increased intensity. This confirms the successful incorporation of nutrient-derived elements. Interestingly, copper (Cu) peaks also appear in this spectrum, likely from sample preparation or trace contamination. The comparison clearly demonstrates that the addition of nutrients alters the mineral content of the hydrogel, particularly enhancing levels of K, P, and S, which are critical for biochemical or biological performance. This suggests improved mineral uptake capacity of the matrix, likely

affecting its functional properties depending on the intended application (e.g., agriculture, biomedical scaffolds, or nutrient delivery systems).

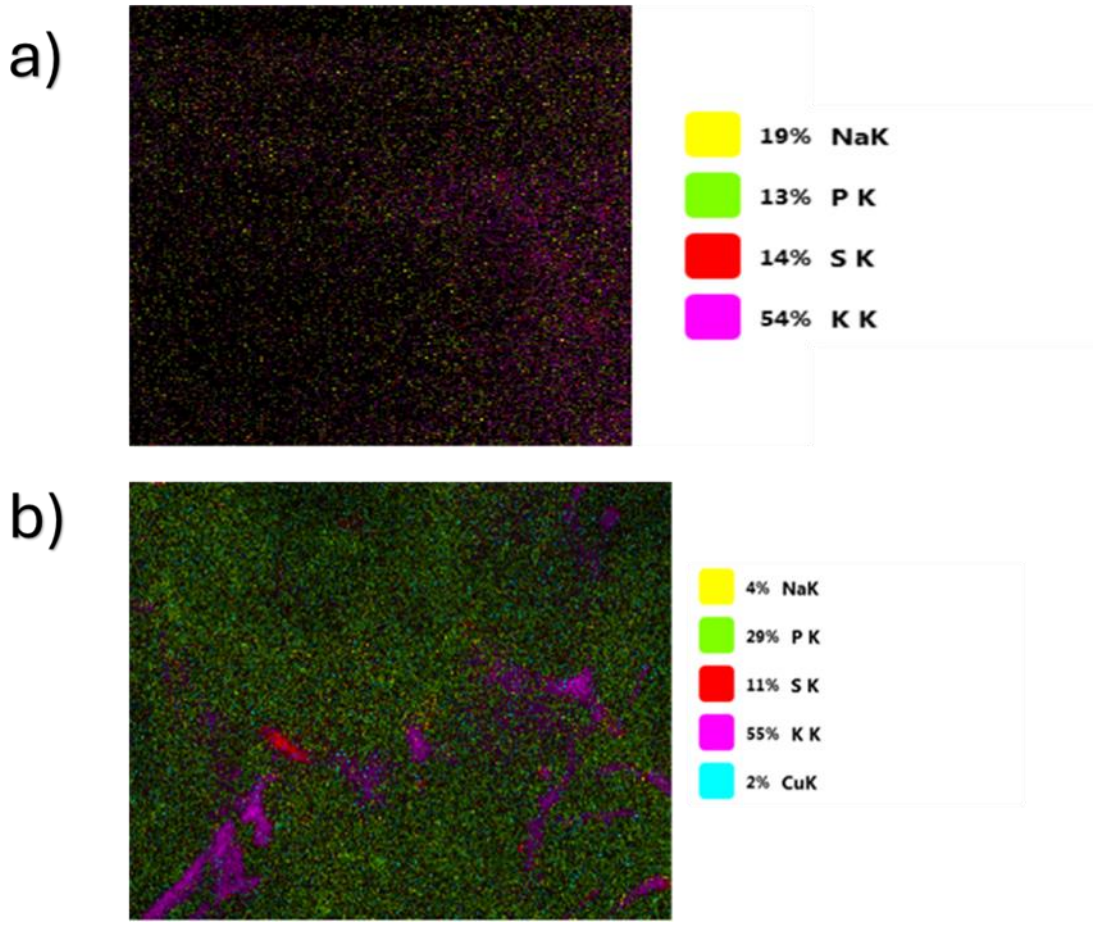

Figure 2.22: EDX mineral mapping of gellan gum hydrogel with a) 12 GGH and b) 12 GGH-MG. The elemental map illustrates the distributions and relative percentages of each element.

Figure 2.22 presents EDX (Energy-Dispersive X-ray) mineral mapping of gellan gum hydrogels at a fixed concentration of 12 mg/cm³, comparing two conditions: (a) gellan gum alone, and (b) gellan gum with 1 mL of concentrated nutrient solution. Each map visualizes the distribution of detected elements using colour codes and their corresponding percentages. In image (a), the hydrogel without nutrient supplementation is primarily composed of potassium (K, 54%), followed by sodium (Na, 19%), sulphur (S, 14%), and phosphorus (P, 13%). The map shows a relatively uniform but faint distribution of these elements, indicating a naturally occurring ionic profile typical of the base gellan gum matrix. In image (b), the addition of nutrients results in a marked shift: phosphorus increases significantly to 29%, while sodium decreases sharply to 4%, sulphur drops to 11%, and potassium remains similar at 55%. A trace amount of copper (Cu, 2%) is also detected, likely due to nutrient formulation or contamination

during processing. The colour density in this map is more vibrant and localized, especially for phosphorus and potassium, indicating increased mineral incorporation accompanied by non-uniform spatial distribution within the hydrogel matrix. Together, these maps highlight the impact of nutrient addition on the elemental composition and spatial distribution within the hydrogel. The elevated phosphorus levels in the treated sample suggest enhanced mineral loading, while the decrease in sodium could imply ionic displacement or exchange within the matrix. The result supports the conclusion that nutrient supplementation alters not just composition, but also the distribution behaviour of key elements.

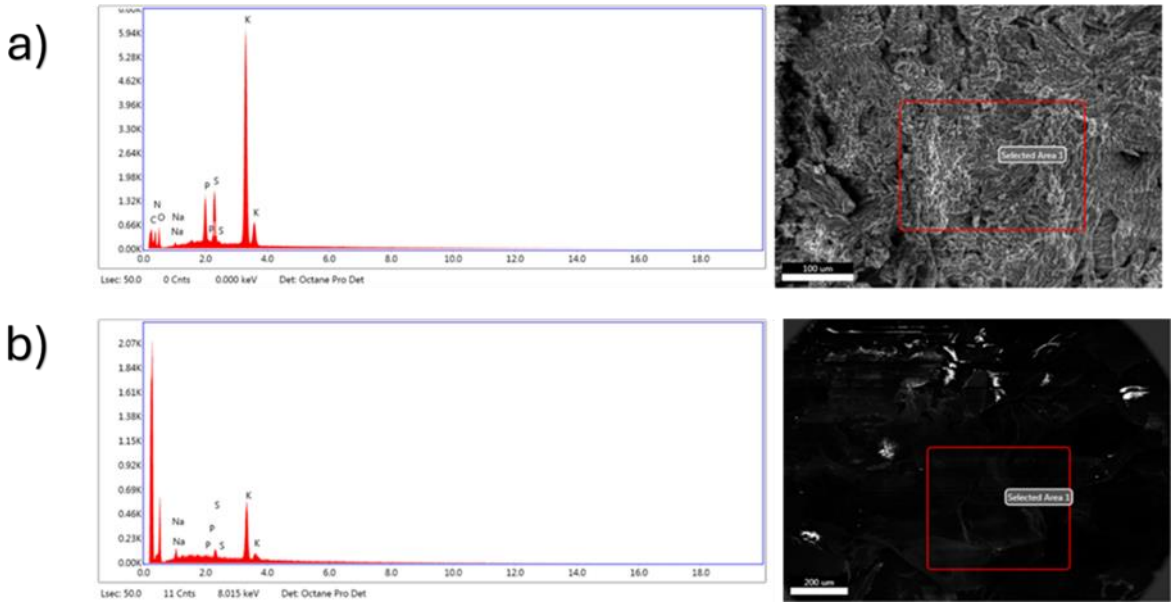

Figure 2.23: EDX Mineral Analysis of a)14 GGH, b) 14 GGH-MG. Showing the Elemental Composition (%) Within the Selected Area (Red Square).

Figure 2.23 illustrates EDX (Energy-Dispersive X-ray) mineral analysis of gellan gum hydrogels at a concentration of 14 mg/cm³, comparing: (a) the hydrogel without nutrient addition and (b) the hydrogel with 1 mL of concentrated nutrient solution. The selected areas for analysis are marked with red squares on the accompanying SEM images. In image (a), the EDX spectrum reveals dominant peaks for potassium (K), along with noticeable signals for sodium (Na), phosphorus (P), sulphur (S), and trace elements like nitrogen (N) and cobalt (Co). The strong K peak suggests a high baseline potassium content within the gellan gum matrix, while the presence of P and S may come from natural impurities or residuals from preparation. In image (b), representing the nutrient-enriched sample, the elemental composition is more balanced: the intensity of potassium is lower than in (a), and phosphorus, sulphur, and sodium

peaks appear more defined and consistent. This indicates a redistribution or dilution of potassium and a relative enrichment of nutrient-derived elements such as phosphorus and sulphur. Overall, the comparison highlights how nutrient incorporation alters the mineral profile of the hydrogel. The shift from a potassium-dominant matrix in (a) to a more balanced elemental spectrum in (b) supports the conclusion that nutrient addition enhances elemental diversity and integration within the hydrogel structure, potentially influencing its chemical behaviour and performance.

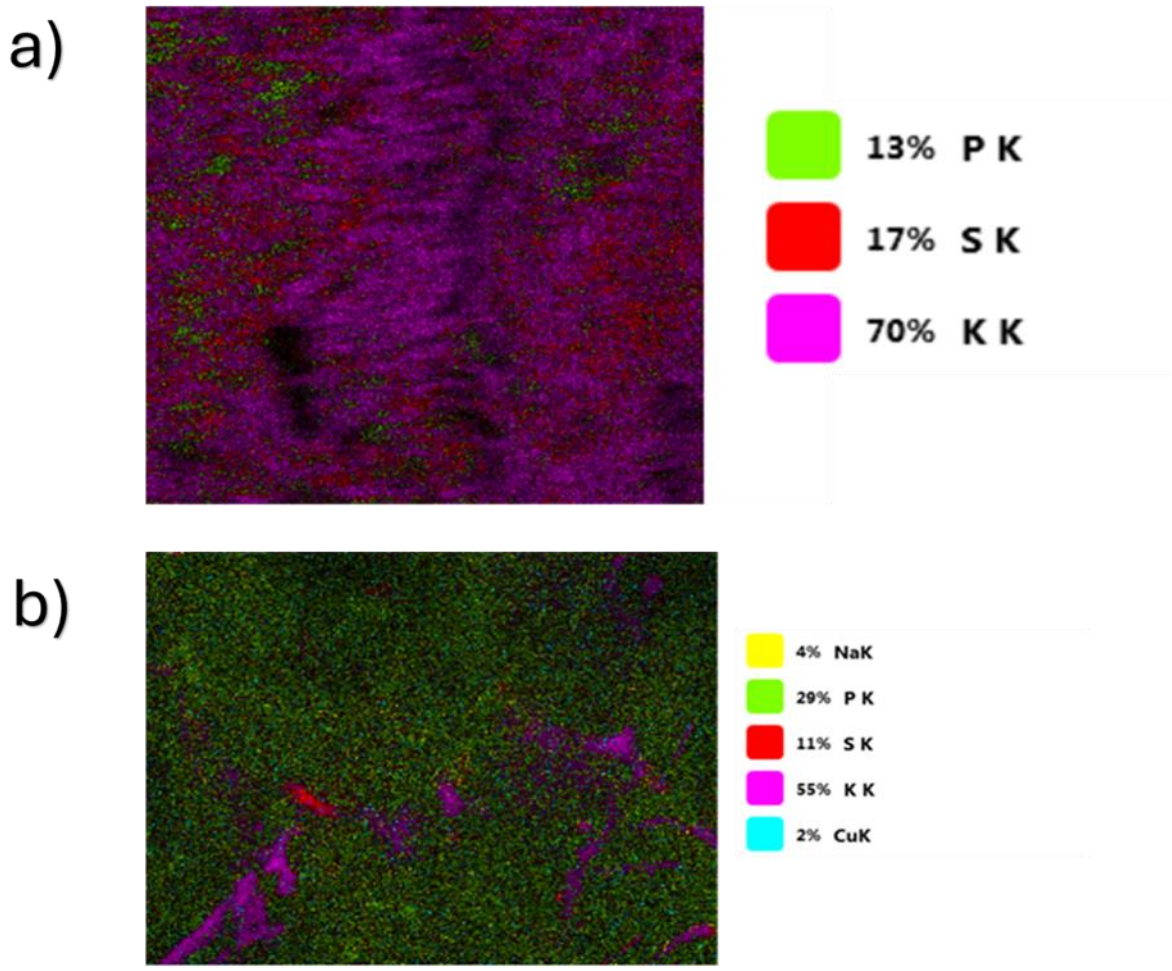

Figure 2.24 EDX mineral mapping of gellan gum hydrogel with a) 14 GGH and b) 14 GGH-MG. The elemental map illustrates the distributions and relative percentages of each element.

Figure 2.24 displays EDX mineral mapping of gellan gum hydrogels at a fixed concentration of 14 mg/cm³, comparing two conditions: (a) without added nutrients and (b) with 1 mL of concentrated nutrient solution. The maps show the spatial distribution and relative abundance of key elements within the selected analysis regions. In image (a), the elemental profile is dominated by potassium (K, 70%), with lower contributions from sulphur (S, 17%) and phosphorus (P, 13%). The high concentration of potassium indicates that the base gellan gum

hydrogel is inherently rich in this element, with a relatively uniform distribution and minimal external supplementation. In contrast, image (b) exhibits a significantly altered mineral composition following nutrient addition. Phosphorus increases markedly to 29%, while potassium decreases to 55%, and sulphur drops to 11%. Additionally, trace amounts of sodium (Na, 4%) and copper (Cu, 2%) appear, likely introduced through the nutrient formulation. The elemental distribution in this sample is more diverse and localized, especially with enhanced phosphorus and copper presence. Together, these maps highlight the clear impact of nutrient supplementation on the elemental composition and distribution of the hydrogel. The reduction in potassium and corresponding rise in phosphorus, sodium, and copper suggest active incorporation and retention of externally provided nutrients, potentially enhancing the functional properties of the material.

2.3.2.2 EDX and EDX map of GGH-HEC and GGH-HEC-MG at three concentrations

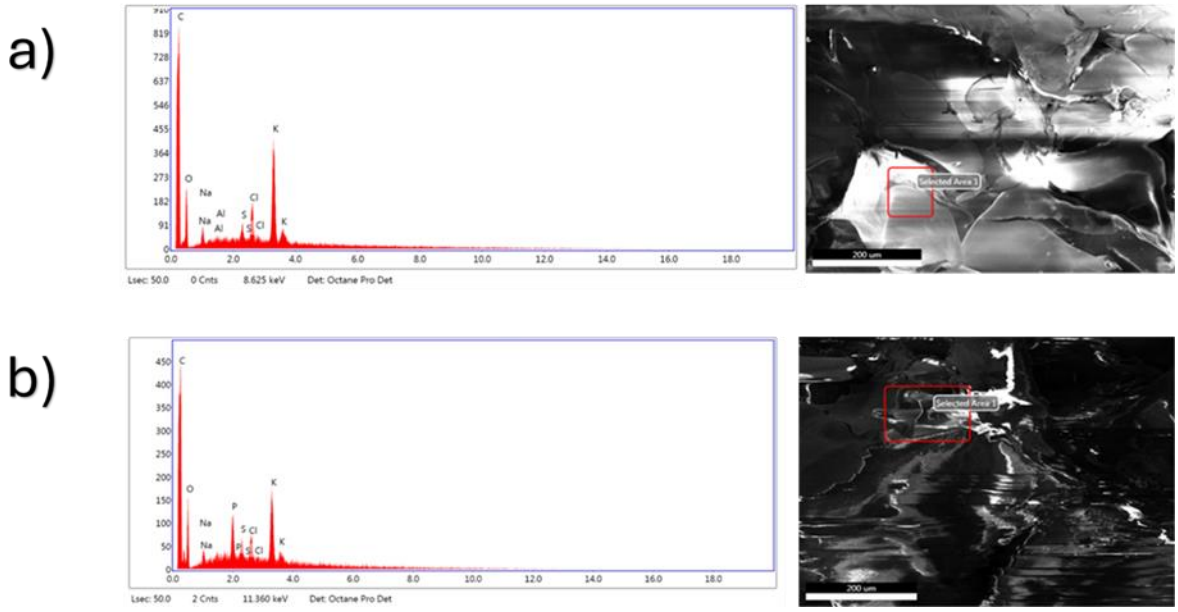

Figure 2.25: EDX Mineral Analysis of Gellan Gum Hydrogel containing a)10 GGH -HEC b) 10 GGH-HEC-MG. The red square highlights the selected area used to determine the elemental composition and corresponding mineral percentages.

Figure 2.25 illustrates the EDX mineral analysis of gellan gum hydrogels combined with hydroxyethyl cellulose (HEC), comparing a base formulation (10 mg/cm³ Gellan Gum + 0.25 g HEC) with a nutrient-enriched version containing an additional 1 mL of nutrient solution. SEM images show the analysed areas, while the EDX spectra confirm the presence of key elements such as carbon (C), oxygen (O), sodium (Na), potassium (K), sulphur (S), phosphorus (P), and

chlorine (Cl) in both samples. Notably, sample (a) also displays small peaks of aluminium (Al) and silicon (Si), likely due to trace contamination. In contrast, sample (b) shows enhanced peaks for phosphorus and potassium, suggesting successful mineral incorporation from the nutrient solution.

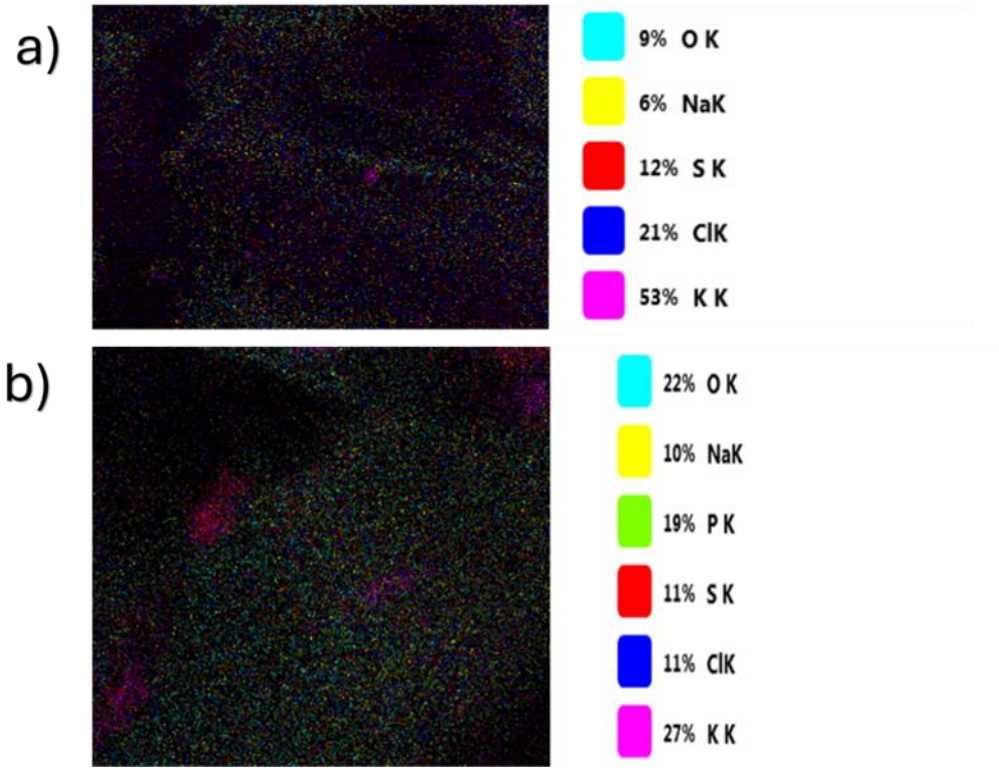

Figure 2.26: EDX mineral mapping of gellan gum hydrogel containing a)10 GGH-HEC. b) 10 GGH-HEC-MG. The map illustrates the distribution and relative percentages of each detected element within the analysed region.

Figure 2.26 presents EDX mineral mapping of gellan gum hydrogels containing hydroxyethyl cellulose (HEC), comparing two samples: (a) 10 mg/cm³ of gellan gum with 5 mg/cm³ of HEC, and (b) the same formulation with an added 1 mL of nutrient solution. The maps display the spatial distribution and relative percentages of various elements within the selected regions. In sample (a), potassium (K) is the dominant element (53%), followed by chlorine (Cl), sulphur (S), and minor amounts of oxygen (O) and sodium (Na). In sample (b), oxygen content significantly increases (22%), and phosphorus (P) appears at 19%, which was absent in (a), indicating successful nutrient incorporation. The notable changes in elemental composition—particularly the rise in oxygen and phosphorus and the redistribution of potassium and chlorine—suggest that the addition of nutrients alters the chemical makeup and possibly the functional properties of the hydrogel.

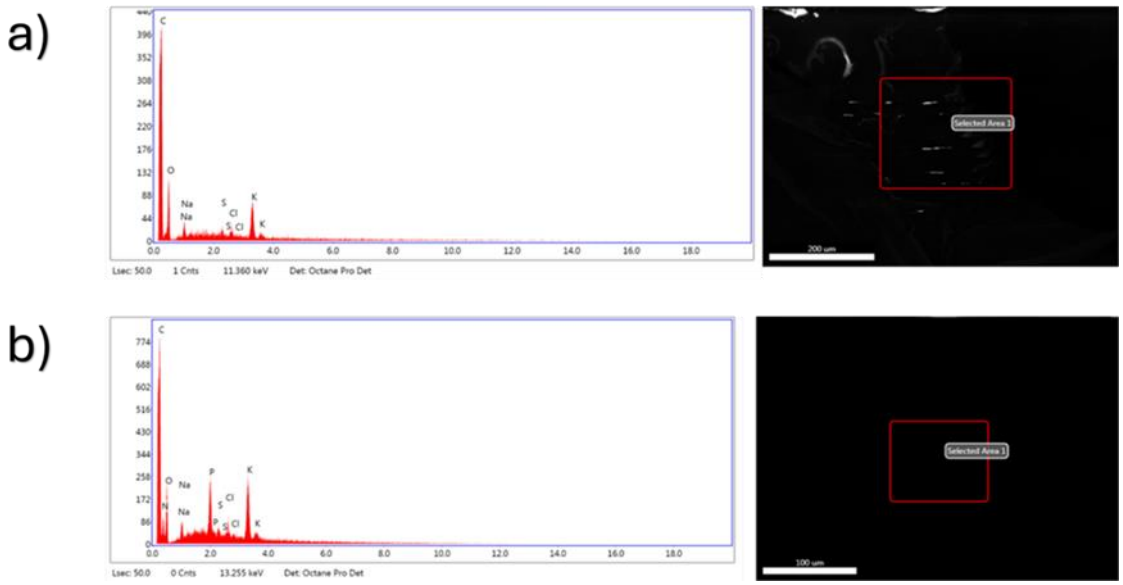

Figure 2.27: EDX Mineral Analysis of Gellan Gum Hydrogel containing a)12 GGH-HEC b) 12 GGH-HEC-MG. The red square highlights the selected area used to determine the elemental composition and corresponding mineral percentages.

Figure 2.27 presents EDX analysis of gellan gum hydrogels with HEC at 12 mg/cm³ GG and 5 mg/cm³ HEC. Sample (a) shows the base formulation, while (b) includes added nutrients. Both reveal core elements like C, O, Na, S, Cl, and K. However, the nutrient-enhanced sample (b) exhibits increased signals for K, Cl, and the presence of phosphorus, indicating successful mineral enrichment from the nutrient solution.

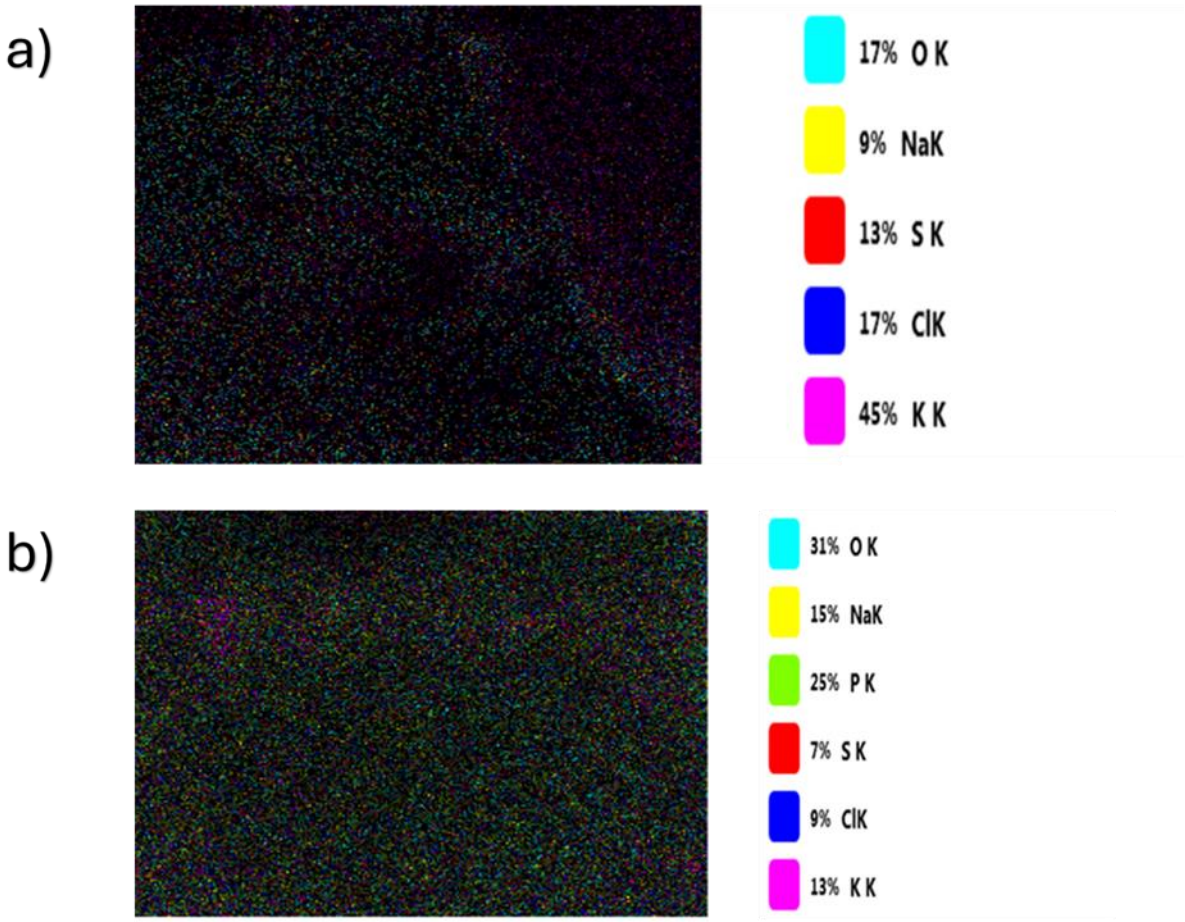

Figure 2.28: EDX mineral mapping of gellan gum hydrogel containing a)12 GGH- HEC. b) 12 GGH- HEC-MG. The map illustrates the distribution and relative percentages of each detected element.

Figure 2.28 shows EDX mineral mapping of gellan gum hydrogels with HEC, comparing (a) 12 mg/cm³ Gellan Gum + 5 mg/cm³ HEC and (b) the same formulation with added nutrient. In (a), potassium (K), chlorine (Cl), sulphur (S), oxygen (O), and sodium (Na) are present, with K being the dominant element. In (b), there is a notable increase in oxygen and phosphorus, along with reduced potassium and sulphur levels, indicating that the nutrient addition shifts the elemental balance particularly enhancing phosphorus presence likely due to nutrient composition.

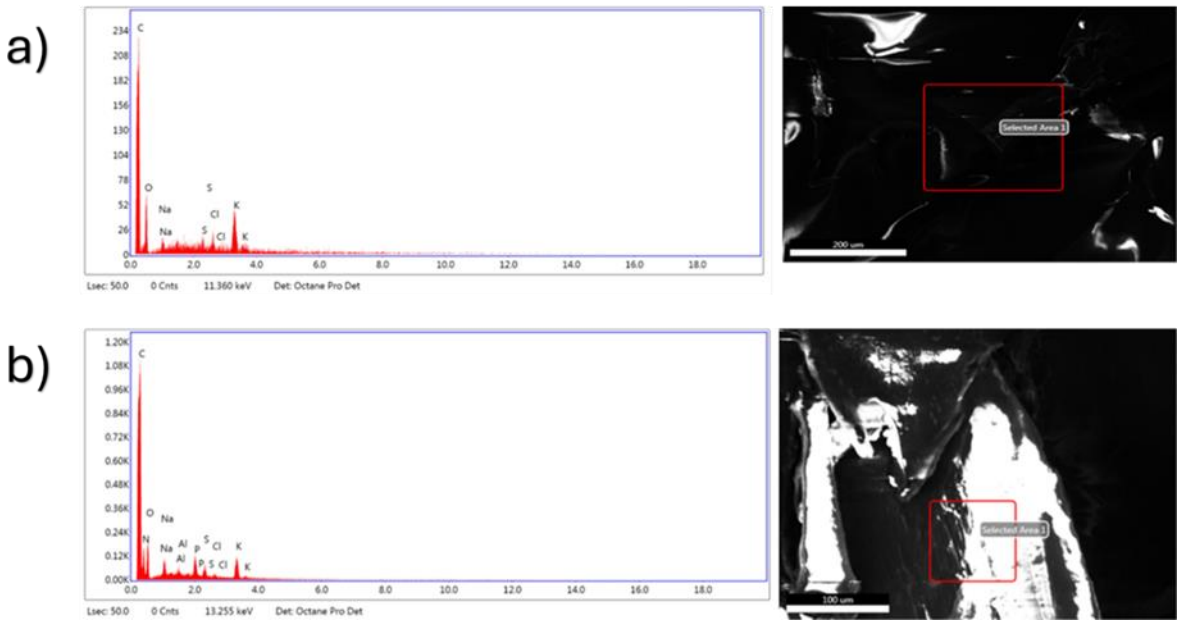

Figure 2.29: EDX Mineral Analysis of Gellan Gum Hydrogel containing a)14 GGH-HEC b) 14 GGH-HEC-MG. The red square highlights the selected area used to determine the elemental composition and corresponding mineral percentages.

Figure 2.29 presents EDX mineral analysis for gellan gum hydrogels with hydroxyethyl cellulose (HEC), comparing (a) 14 mg/cm³ Gellan Gum + 5 mg/cm³ HEC and (b) the same formulation with 1 mL of nutrient added. Both spectra show the presence of key elements like carbon (C), oxygen (O), sodium (Na), sulphur (S), chlorine (Cl), and potassium (K). Notably, the sample with nutrients (b) displays more prominent peaks for phosphorus (P) and potassium (K), indicating enhanced mineral presence from the nutrient addition. Minor traces of aluminium (Al) also appear, likely due to sample handling or equipment contact.

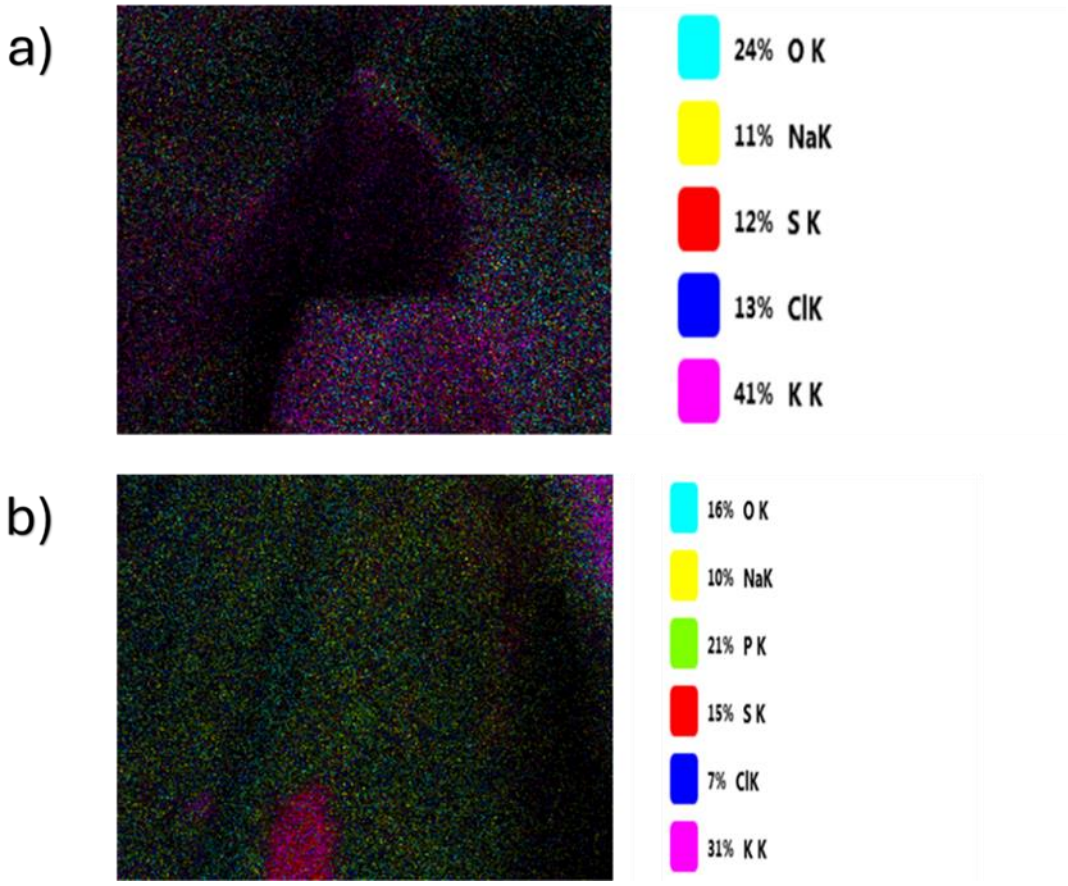

Figure 2.30: EDX mineral mapping of gellan gum hydrogel containing a)14 GGH-HEC. b) 14 GGH-HEC-MG. The map illustrates the distribution and relative percentages of each detected element.

Figure 2.30 presents EDX mineral mapping of gellan gum hydrogels containing hydroxyethyl cellulose (HEC), comparing two formulations: (a) 14 mg/cm³ Gellan Gum with 5 mg/cm³ HEC, and (b) the same composition with an additional 1 mL of nutrient. In both maps, common elements such as oxygen (O), sodium (Na), sulphur (S), chlorine (Cl), and potassium (K) are detected. However, in sample (b), the presence of phosphorus (P) increases noticeably (21%), reflecting the contribution of the nutrient solution. Additionally, potassium content drops slightly in (b), while oxygen and phosphorus levels rise, suggesting an altered elemental distribution and a more active mineral exchange or retention influenced by the nutrient supplementation.

2.3.2.3 EDX and EDX map of GGH-CMC and GGH-CMC-MG at three concentrations

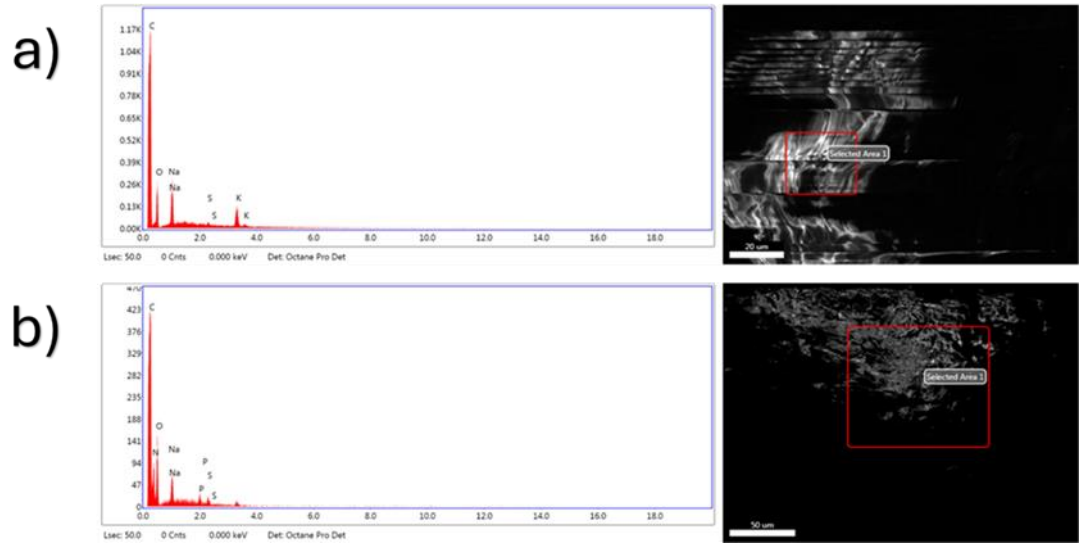

Figure 2.31: EDX Mineral Analysis of Gellan Gum Hydrogel containing a) GGH-CMC. b) 10 GGH-CMCMG. The red square highlights the selected area used to determine the elemental composition and corresponding mineral percentages.

Figure 2.31 displays EDX mineral analysis of gellan gum hydrogels formulated with carboxymethyl cellulose (CMC), comparing two samples: (a) 10 mg/cm³ Gellan Gum with 5 mg/cm³ CMC, and (b) the same formulation supplemented with 1 mL of nutrient solution. The SEM images on the right highlight the areas analysed (marked in red), while the EDX spectra on the left reveal elemental composition. Both samples exhibit typical elements like carbon (C), oxygen (O), sodium (Na), sulphur (S), and potassium (K). Notably, in sample (b), there is a visible increase in phosphorus (P) and sodium (Na) peaks, reflecting the mineral contribution from the nutrient addition. This suggests enhanced mineral incorporation in the matrix upon nutrient addition.

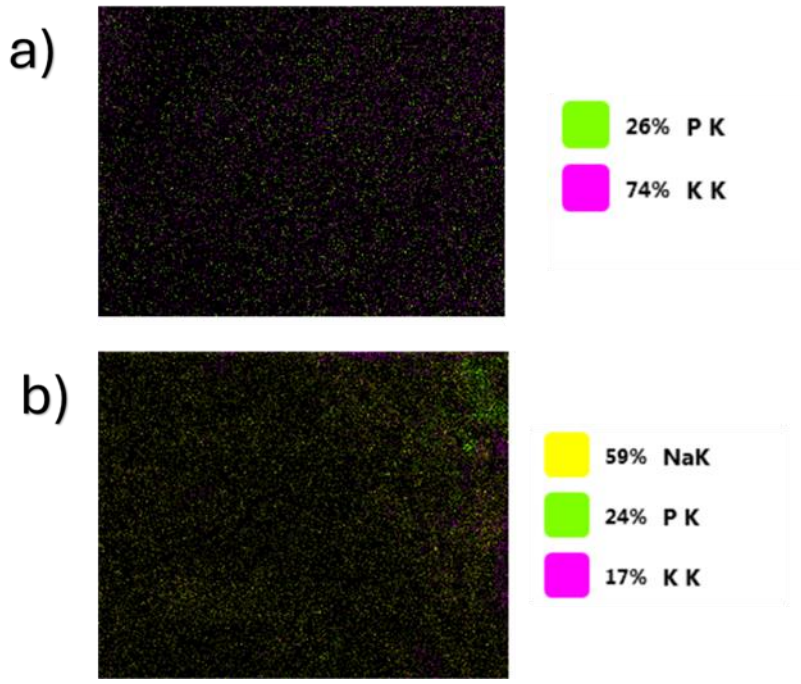

Figure 2.32: EDX mineral mapping of gellan gum hydrogel containing a)10 GGH-CMC. b) 10 GGH-CMC-MG. The map illustrates the distribution and relative percentages of each detected element.

Figure 2.32 presents EDX mineral mapping of gellan gum hydrogels with carboxymethyl cellulose (CMC), comparing (a) a sample with 10 mg/cm³ Gellan Gum + 5 mg/cm³ CMC, and (b) the same formulation supplemented with 1 mL of nutrient. In (a), the distribution is primarily composed of potassium (K, 74%) and phosphorus (P, 26%), indicating a relatively simple mineral profile. In contrast, sample (b) shows a more complex mineral presence with a dominant amount of sodium (Na, 59%), alongside phosphorus (24%) and potassium (17%). This shift in elemental composition demonstrates the impact of nutrient addition, enriching the sample with sodium and altering the overall mineral balance.

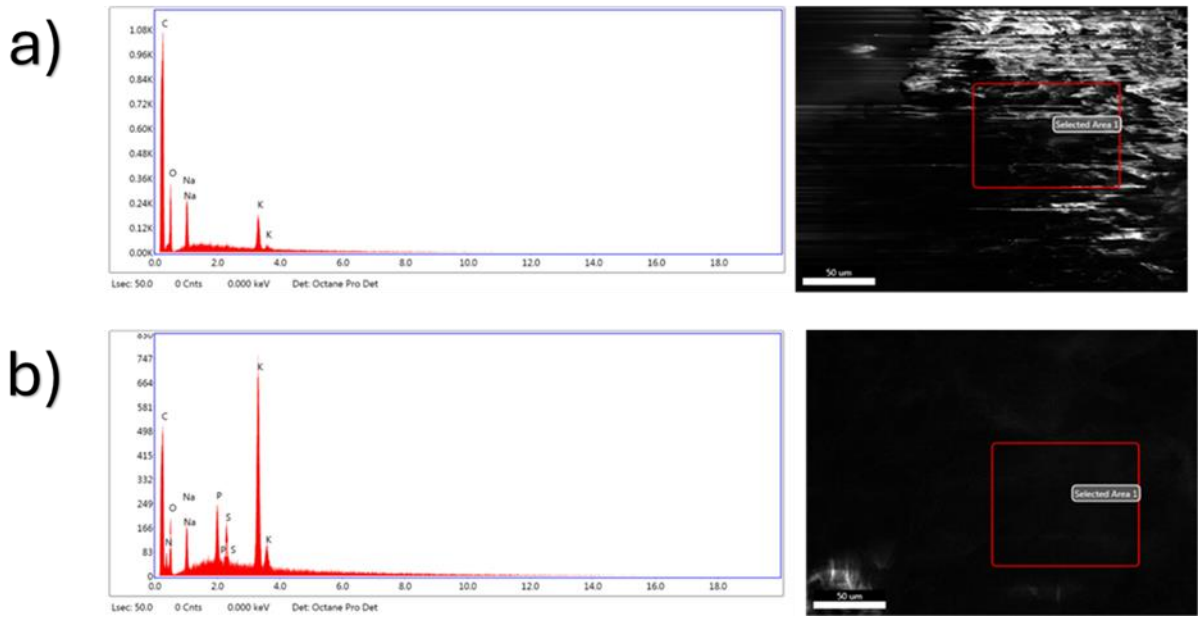

Figure 2.33: EDX Mineral Analysis of Gellan Gum Hydrogel containing a)12 GGH-CMC b) 12 GGH-CMC-MG. The red square highlights the selected area used to determine the elemental composition and corresponding mineral percentages.

Figure 2.33 presents EDX mineral analysis of gellan gum hydrogels combined with carboxymethyl cellulose (CMC), comparing two conditions: (a) 12 mg/cm³ Gellan Gum + 5 mg/cm³ CMC, and (b) 12 mg/cm³ Gellan Gum + 5 mg/cm³ CMC with 1 mL of nutrient. In both cases, SEM micrographs show the selected regions for elemental analysis (highlighted in red), while the corresponding spectra illustrate the detected elemental peaks. Sample (a) shows dominant peaks for carbon (C), oxygen (O), sodium (Na), and potassium (K), typical of a base hydrogel matrix. Sample (b), which includes added nutrients, reveals increased peaks for potassium (K), phosphorus (P), and sulphur (S), indicating enhanced mineral content from the nutrient solution. The addition of nutrients enriches the elemental profile and suggests improved ion availability, which may influence the hydrogel's functionality or bioactivity.

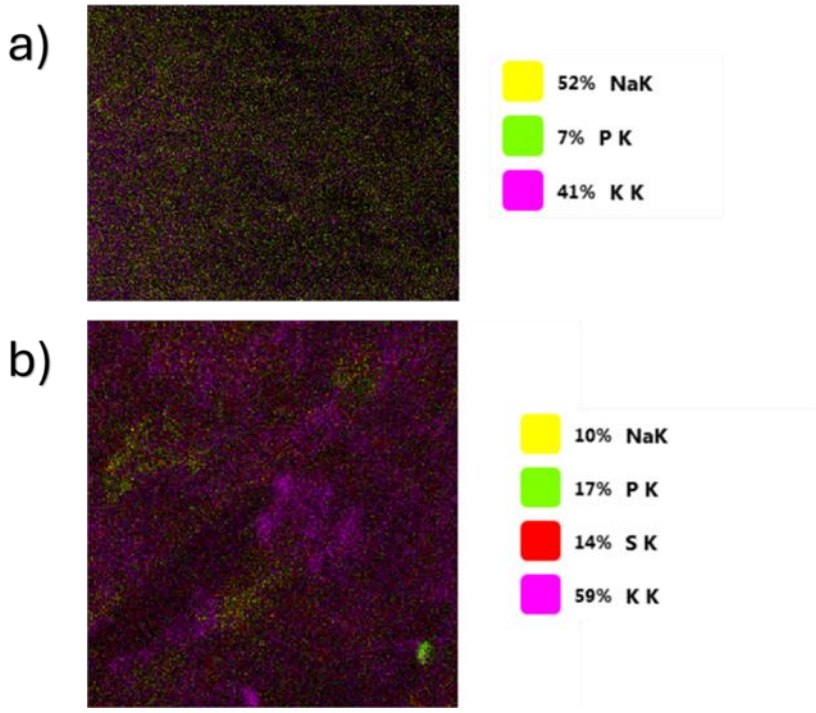

Figure 2.34: EDX mineral mapping of gellan gum hydrogel containing a)12 -GGH-CMC. b) 12 GGH-CMC-MG. The map illustrates the distribution and relative percentages of each detected element.

Figure 2.34 displays EDX mineral mapping of gellan gum hydrogels combined with carboxymethyl cellulose (CMC), comparing two conditions: (a) 12 mg/cm³ Gellan Gum + 5 mg/cm³ CMC, and (b) 12 mg/cm³ Gellan Gum + 5 mg/cm³ CMC + 1 mL nutrient solution. In sample (a), the elemental composition is dominated by sodium (Nak, 52%) and potassium (KK, 41%), with a small presence of phosphorus (PK, 7%). After the addition of the nutrient in sample (b), the composition shifts to higher potassium (59%) and a noticeable increase in phosphorus (17%) and sulphur (14%), while sodium decreases to 10%. These changes suggest enhanced nutrient uptake and mineral distribution in the hydrogel matrix due to the added nutrient solution.

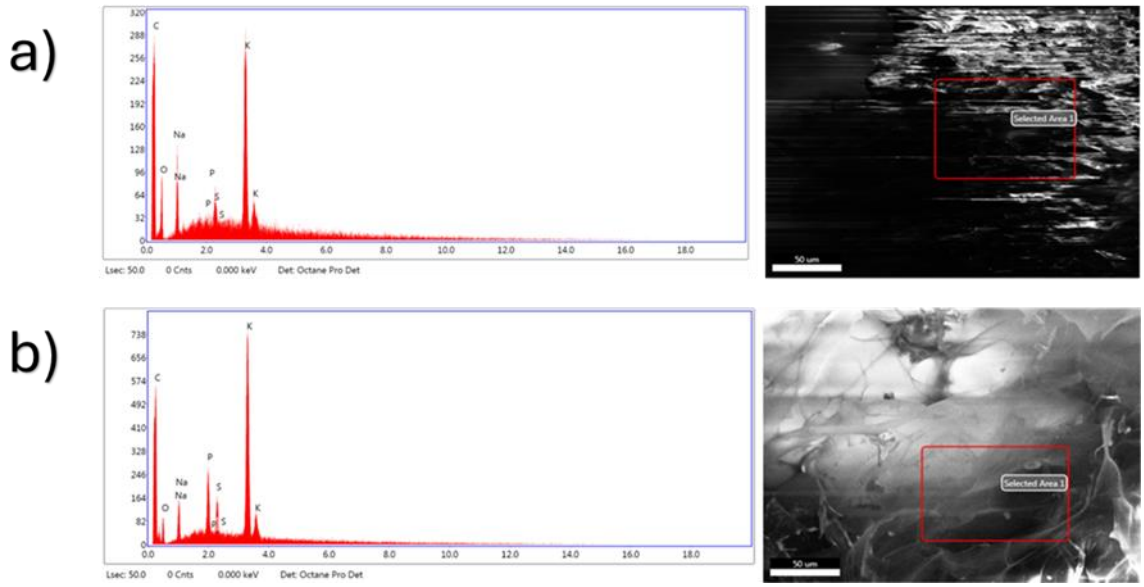

Figure 2.35: EDX Mineral Analysis of Gellan Gum Hydrogel containing a) 14 GGH-CMC. b) 14 GGH-CMC-MG. The red square highlights the selected area used to determine the elemental composition and corresponding mineral percentages.

Figure 2.35 presents EDX mineral analysis of gellan gum hydrogels with carboxymethyl cellulose (CMC), comparing: (a) 14 mg/cm³ Gellan Gum + 5 mg/cm³ CMC, and (b) 14 mg/cm³ Gellan Gum + 5 mg/cm³ CMC + 1 mL nutrient solution. Both spectra confirm the presence of key elements including carbon (C), oxygen (O), sodium (Na), phosphorus (P), sulphur (S), and potassium (K). In sample (a), potassium and carbon exhibit dominant peaks, with smaller signals for phosphorus and sodium. After nutrient addition in sample (b), the intensity of potassium and phosphorus peaks increases significantly, reflecting the enrichment from the nutrient solution. This indicates enhanced mineral incorporation into the hydrogel matrix due to nutrient supplementation, particularly of phosphate and potassium-based components.

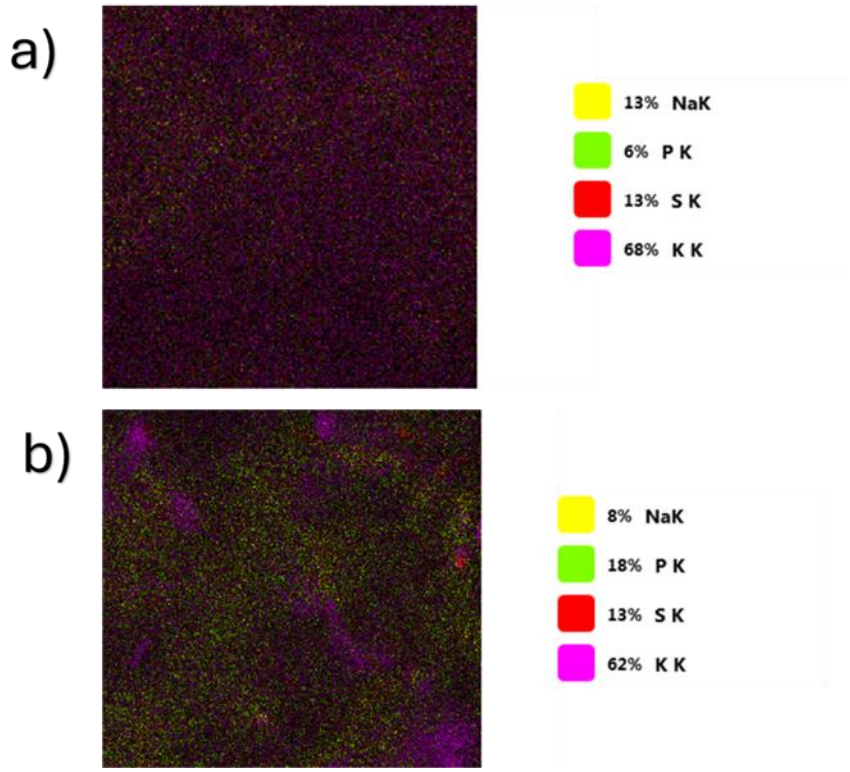

Figure 2.36: EDX mineral mapping of gellan gum hydrogel containing a)14 GGH-CMC. b) 14 GGH-CMC-MG. The map illustrates the distribution and relative percentages of each detected element.

Figure 2.36 shows EDX mineral mapping of gellan gum hydrogels with CMC at a concentration of 14 mg/cm³ gellan gum and 5 mg/cm³ CMC, comparing: (a) without nutrient addition and (b) with 1 mL of concentrated nutrient solution. In both images, the predominant elements are potassium (K), sulphur (S), and sodium (Na), with trace phosphorus (P). In sample (a), potassium dominates at 68%, with moderate levels of sodium and sulphur (13% each) and minimal phosphorus (6%). Upon addition of nutrient (b), potassium remains high but decreases slightly to 62%, while phosphorus increases significantly from 6% to 18%, indicating nutrient uptake. The consistent sulphur levels (13%) suggest stability in sulphur content, while sodium shows a mild reduction. These changes reflect enhanced mineral incorporation—especially phosphorus due to the nutrient addition.

2.3.3 BET of Gellan Gum and Modified Gellan Gum

2.3.3.1 BET of GGH and GGH-MG at three concentrations

The table 2.7 presents the BET surface area measurements of gellan gum hydrogels (GGH) combined , with and without the addition of a nutrient solution (denoted with “MG”).

BET surface area results show a decrease in surface area with increasing GGH content in the nutrient-free samples (from 7.99 ± 0.70 m^2/g at 10 GGH to 4.03 ± 0.41 m^2/g at 14 GGH). However, due to missing data for 10 GGH-MG and 14 GGH-MG, a direct comparison of nutrient effects across all compositions is not possible.

At 12 GGH, the only composition where both conditions are available, the nutrient-added sample (7.25 ± 0.77 m^2/g) shows a higher surface area than the nutrient-free sample (5.81 ± 0.92 m^2/g). Therefore, no general conclusion can be drawn that nutrient addition reduces surface area. Instead, the effect of nutrient addition appears to be composition-specific and cannot be generalized across all GGH concentrations based on the available dataset.

Table 2.7: BET surface area of Gellan hum hydrogels with and without nutrient addition.

Sample number	Sample components	BET Surface Area m^2/g
Sample 1	10 GGH	7.99 ± 0.70
Sample 2	12 GGH	5.81 ± 0.92
Sample 3	14 GGH	4.03 ± 0.41
Sample 4	10 GGH-MG	
Sample 5	12 GGH-MG	7.25 +/- 0.77
Sample 6	14 GGH-MG	

A more careful analysis of the BET surface area results indicates that the effect of nutrient addition is not consistent across all GGH concentrations. For the 12 GGH samples, the surface area values for the nutrient-free and nutrient-added systems are within experimental uncertainty, suggesting only a marginal difference. However, due to incomplete data for some compositions (e.g., 10 GGH-MG and 14 GGH-MG), a definitive trend across all GGH levels cannot be established. Overall, the results suggest that any influence of nutrient addition on surface area is composition-dependent rather than systematically increasing or decreasing with GGH content. BET surface area results indicate that there is no clear trend demonstrating that nutrient addition leads to an increase in surface area at lower GGH content only. Overall, the values for the 0.5g GGH with and without nutrient are within error, but for higher GGH the samples with nutrient have lower surface areas.

2.3.3.2 BET of GGH-HEC and GGH-HEC-MG at three concentrations

Table 2.8 shows the BET surface area measurements of gellan gum hydrogels (GGH) mixed with hydroxyethyl cellulose (HEC), both with and without a nutrient solution (marked as "MG"). The surface area values, measured in m^2/g, reflect the extent of the accessible surface area within the hydrogel structure, which is an important factor for applications like adsorption, catalysis, or nutrient delivery. Samples 1–3 (without nutrient): These samples show relatively higher surface area values compared to those with nutrient addition. Surface area decreases slightly as the GGH content increases from 0.5 g to 0.7 g, suggesting that a denser matrix reduces porosity and surface accessibility. Samples 4–6 (with nutrient): All samples with added nutrients exhibit lower surface area values than their corresponding counterparts without nutrients. This trend may result from pore filling or structural collapse during drying due to nutrient interaction, which reduces the measurable surface area. The surface area generally decreases with increasing GGH concentration and even more so when nutrients are added, indicating that both factors contribute to a denser and less porous hydrogel matrix. This pattern suggests that while HEC maintains moderate surface area in combination with GGH, nutrient addition significantly reduces this property, possibly by compacting the network or occupying internal pore spaces.

Table 2.8: BET Surface Area of Gellan Gum–HEC Hydrogels with and without nutrient addition.

Sample number	Sample components	BET Surface Area m^2/g
Sample 1	10 GGH-HEC	7.48 ± 0.82
Sample 2	12 GGH-HEC	7.26 ± 0.82
Sample 3	14 GGH-HEC	5.20 ± 0.67
Sample 4	10 GGH-HEC-MG	4.60 ± 0.40
Sample 5	12 GGH-HEC-MG	3.09 ± 0.28
Sample 6	14 GGH-HEC-MG	1.93 ± 0.24

2.3.3.3 BET of GGH-CMC and GGH-CMC-MG at three concentrations

The BET surface area results presented in Table 2.9 show a clear and systematic decrease in accessible surface area as the concentration of gellan gum hydrogel (GGH) increases, both in samples with and without added nutrient. For hydrogels without nutrients (Samples 1–3), the surface area decreases markedly from 12.60 m^2/g at 10 mg/cm^3 GGH to 4.80 m^2/g at 14 mg/cm^3 GGH, indicating that higher GGH content produces a denser, more compact polymer network

with reduced porosity. A similar pattern is observed in nutrient-containing hydrogels (Samples 4–6), where the BET surface area declines from 13.60 m²/g to 1.19 m²/g over the same concentration range. Although nutrient addition slightly increases the surface area at low GGH levels suggesting a more open structure facilitated by nutrient incorporation—this effect becomes negligible at higher GGH concentrations, where the network compaction dominates the structural behaviour. Importantly, the values are not considered "equal"; despite overlapping uncertainties, the decreasing trend is significant and reflects genuine structural differences across the samples.

Overall, these results indicate that lower GGH concentrations favour the formation of more porous hydrogel structures, whether nutrient is present or not, whereas higher GGH concentrations yield tightly packed matrices with limited internal surface area. This behaviour is highly relevant for applications where surface accessibility governs performance, such as nutrient release, sorption efficiency, diffusivity, or biological loading capacity.

Table 2.9: BET Surface Area of Gellan Gum–CMC Hydrogels with and without nutrient addition.

Sample number	Sample components	BET Surface Area m²/g
Sample 1	10GGH-CMC	12.60 ± 1.30
Sample 2	12GGH-CMC	10.46 ± 0.95
Sample 3	14GGH-CMC	4.80 ± 1.73
Sample 4	10GGH-CMC-MG	13.60 ± 2.13
Sample 5	12GGH-CMC-MG	7.24 ± 0.55
Sample 6	14GGH-CMC-MG	1.19 ± 0.40

2.4 Conclusions

The values for the 0.5g GGH with and without nutrient are within error, but for higher GGH the samples with nutrient have lower surface areas

Chapter 3: Thermogravimetric and differential scanning calorimetry analysis of hydrogels

3.1 The Effect of Adding Nutrients on Gellan Gum (GG) on Thermal Behaviour

Thermal analysis techniques are critical in studies of hydrogels, especially polysaccharide-based hydrogels like Gellan Gum, as they provide essential insights into thermal stability, phase transitions, and degradation behaviours (244, 245). This information is valuable for understanding the performance and application of hydrogels in various fields, including drug delivery, tissue engineering, agriculture and food technology (246). Thermal analysis techniques play a crucial role in material characterisation, with three key methods being Thermogravimetric Analysis (TGA), Derivative Thermogravimetry (DTG), and Differential Scanning Calorimetry (DSC). Each of these methods offers unique insights into the thermal characteristics and behaviours of materials.

3.1.1 Adding Miracle-Gro to Gellan Gum (GG)

The incorporation of nutrients such as metal ions of Fe, Cu, and Zn ions into gellan gum hydrogels enhances their thermal stability by promoting additional cross-linking within the polymer matrix. This modification not only improves the thermal resistance of the hydrogels but also contributes to their mechanical robustness, making them more suitable for applications requiring stability under elevated temperatures (247). The incorporation of additives such as zinc oxide nanoparticles in a gellan gum matrix significantly increased the thermal stability properties. The formation of strong intermolecular hydrogen bonds between gellan gum, polyacrylamide, and zinc oxide improved stability and increased resistance to thermal degradation (248). Like Zinc, Kanesaka *et al.* indicated that the addition of copper ions to gellan gum systems improved thermal stability. Copper ions interact with carboxyl groups in gellan gum, enhancing gel structure and stability. The presence of Cu^{2+} affects the thermal properties by modifying the physical interactions within the gel matrix (249). Liu *et al.*'s work showed how several metal ions, including iron (Fe), affected gellan gum's ionic cross-linking behaviour. Fe ions' contribution to the gels' increased heat stability confirms their function in improving polysaccharide matrix characteristics (250).

In this project we used Miracle-gro due to including organic/inorganic components present in the nutrient formulation. Miracle-Gro is a (nitrogen–phosphorus–potassium) NPK fertilizer

solution with micronutrients and a well-known brand specializing in garden products, particularly fertilizers and soil amendments (Table 3.1).

Table 3.1: "Chemical composition of the nutrient solution used in hydrogel formulations"

Components	Percentage (%)	Components	Percentage (%)
Urea nitrogen	3.5	Iron (Fe)	0.03
Nitric nitrogen	1.7	Copper (Cu)	0.002
Ammoniacal nitrogen	1.8	Zinc (Zn)	0.002
Phosphorus pentoxide (P2O2)	3 (1.3% P)	Manganese (Mn)	0.01
Potassium oxide (K_2O)	5 (4.2%K)	Molybdenum (Mo)	0.001

3.1.2 Modifying Gellan Gum by HEC and CMC

The incorporation of Hydroxyethyl Cellulose (HEC) and Carboxymethyl Cellulose (CMC) into Gellan Gum (GG) alters its thermal, mechanical, and gelation properties, making it more suitable for various biopolymer, pharmaceutical, agriculture and food applications it. The introduction of HEC and CMC can positively affect the thermal stability of gellan gum. Das et al. found that adding CMC to Gellan Gum formulations not only enhanced viscosity but also boosted thermal stability. These improvements were linked to the synergistic molecular interactions between CMC and GG, which strengthened the gel structure and increased its overall stability (248). A study by Tiwari and Bhattacharya revealed that incorporating HEC into Gellan Gum formulations improved thermal stability and gel strength. Their research emphasized HEC's interaction with GG, which contributed to a thermal expansion profile that helped the gel retain its structure when exposed to heat (251).

3.2 Thermogravimetric Analysis (TGA)

Thermogravimetric analysis (TGA) measures the change in mass of a material as it is subjected to a controlled temperature program. This technique is essential in determining the thermal stability and composition of materials by detecting mass loss due to moisture, decomposition, oxidation processes, which result from different physical and chemical processes (248). TGA has the benefit of being able to detect multiple decomposition events and the corresponding temperature ranges for each event (249). TGA provides valuable data on the temperatures at which these reactions occur and the percentage of material lost during heating (250).

3.2.1 TGA for GG12

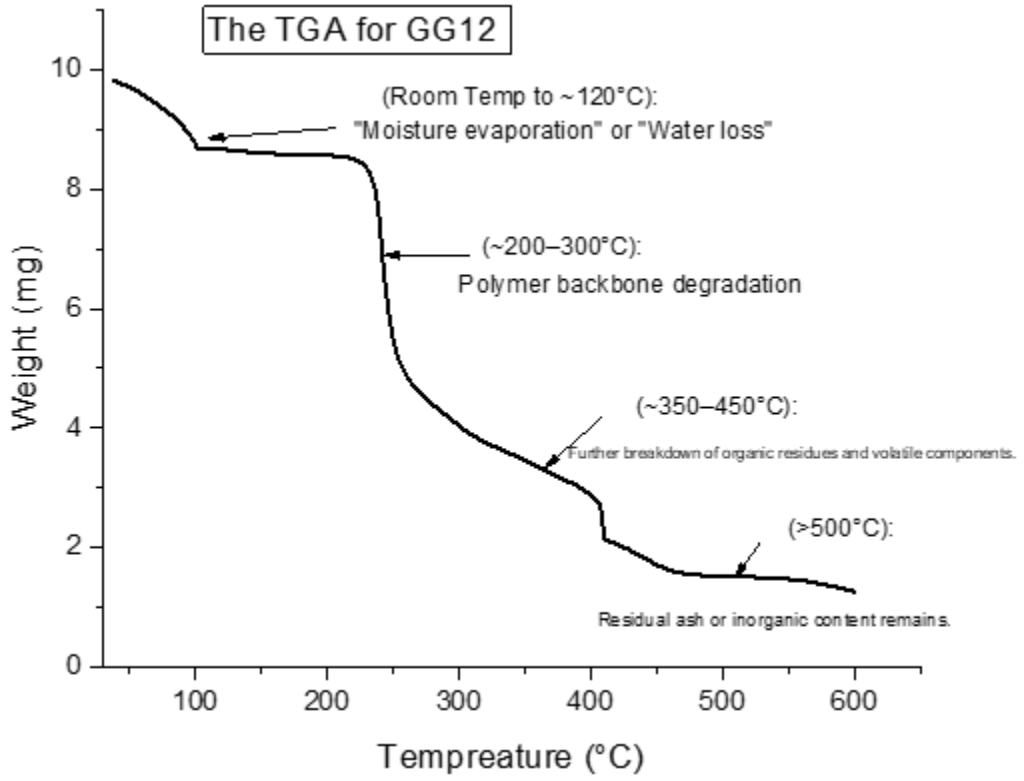

Figure 3.1: The TGA curve for GG12 during its decomposition temperature ranges from 30 °C to 600 °C with a heating rate of 10.0 K/min, air 50.0 ml/min, and a weight of the original sample = 10.24 mg.

Figure 3.1 presents the Thermogravimetric Analysis (TGA) curve for GG12, showing the percentage of weight loss as the temperature increases. This curve illustrates the thermal stability and decomposition behaviour of gellan gum under heating, revealing four distinct degradation stages: Stage 1 – Moisture Loss (≈ 30–120 °C): In this initial phase, the sample undergoes about 11% weight loss due to the evaporation of bound water (251). This low-temperature process reflects dehydration rather than chemical breakdown, typical for polysaccharide-based materials. Stage 2 – Primary Decomposition (≈ 200–300 °C): A significant weight reduction of around 44% is observed in this stage. Decomposition begins near 220 °C, attributed to the breakdown of glycosidic bonds in the gellan gum structure. This leads to the release of volatile fragments, including low molecular weight byproducts like acetic acid. The polymer loses approximately half of its original mass by the time the temperature reaches 300 °C (252). Stage 3 – Secondary Decomposition (≈ 350–450 °C): Gradual mass loss continues as residual carbonaceous materials undergo further degradation. This stage includes slow pyrolysis and oxidation, accounting for an additional 20–25% loss.

The weight reductions occur in small steps, reflecting complex char-forming reactions. Stage 4 – Final Residue (≈ 500 °C): By the end of the heating cycle, a stable residue (char or ash) remains. Approximately 20–30% of the original mass is retained, indicating that 70–80% of the total material has decomposed. Overall, Gellan gum exhibits thermal stability up to ~180-200 °C. Beyond this point, rapid degradation begins, with a prominent exothermic event near 237 °C, corresponding to the polymer's structural collapse.

3.2.2 TGA for GG12-MG

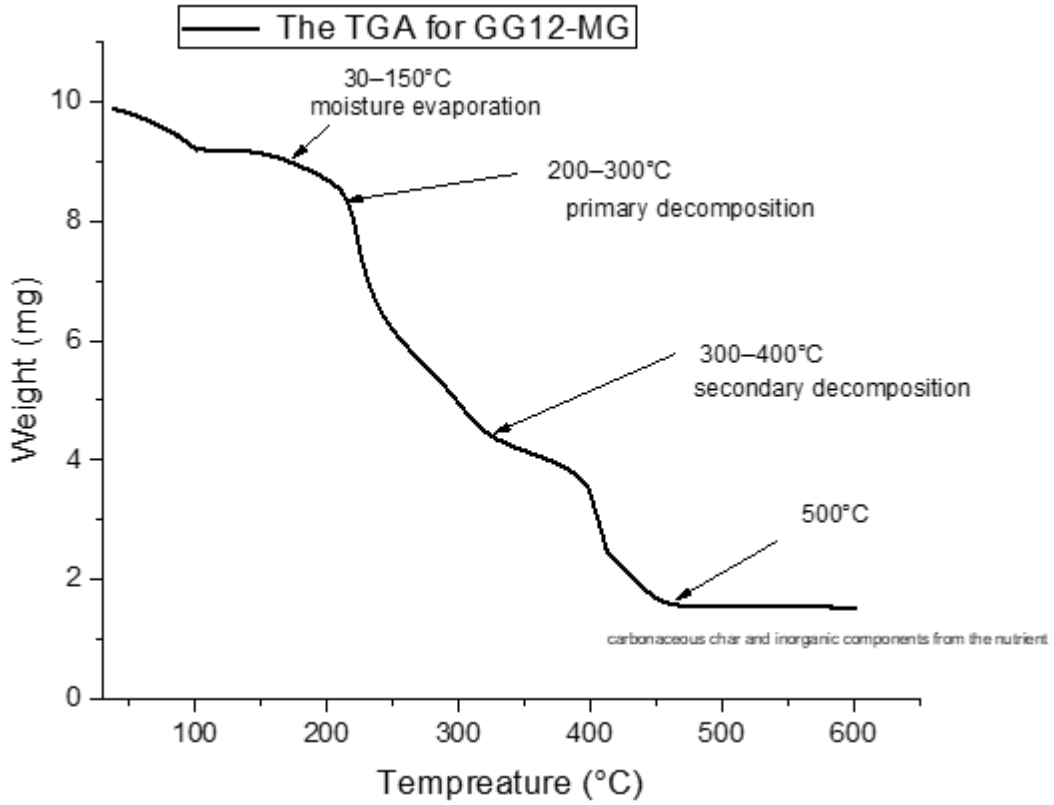

Figure 3.2: The TGA curve for GG12-MG during its decomposition temperature ranges from 30 °C to 600 °C with a heating rate of 10.00 K/min, air of 50.0 ml/min, and a weight of the original sample = 10.10 mg.

Figure 3.2 presents the Thermogravimetric Analysis (TGA) curve for GG12-MG, illustrating the thermal decomposition profile of gellan gum with added nutrient components. The sample begins at full weight (~10.10 mg) at room temperature (~30 °C), showing no initial degradation. The first stage of weight loss, approximately 6.8%, occurs between 30–150 °C and corresponds to moisture evaporation. A sharp primary decomposition follows between 200–300 °C, where about 35% of the sample mass is lost due to the breakdown of glycosidic bonds in the gellan gum structure. The secondary decomposition phase occurs between

300-400 °C, with a further 15% weight loss caused by the oxidation of remaining organic material and breakdown of carbon residues. Beyond 400 °C, weight loss continues more gradually, with around 17% lost between 400–500 °C and another 9% beyond 500 °C. By the end of the run, a stable residue of about 15% of the original mass remains, likely consisting of carbonaceous char and inorganic mineral content contributed by the nutrient addition. Overall, this TGA curve reveals that the sample remains stable up to ~200 °C, after which it undergoes progressive degradation. This data is essential for evaluating the material's performance under heat and helps determine its applicability in thermally sensitive environments.

When we compare between the two samples, Figures 3.1 and 3.2 we find that the presence of the nutrient does not significantly impact the thermal stability of Gellan Gum, as the decomposition process follows a similar pattern. However, the nutrient slightly alters the degradation kinetics and increases the final residue. This indicates that the nutrient contains non-volatile or inorganic components, which contribute to char formation and higher residual mass after thermal decomposition.

3.2.3 TGA for GG12-HEC

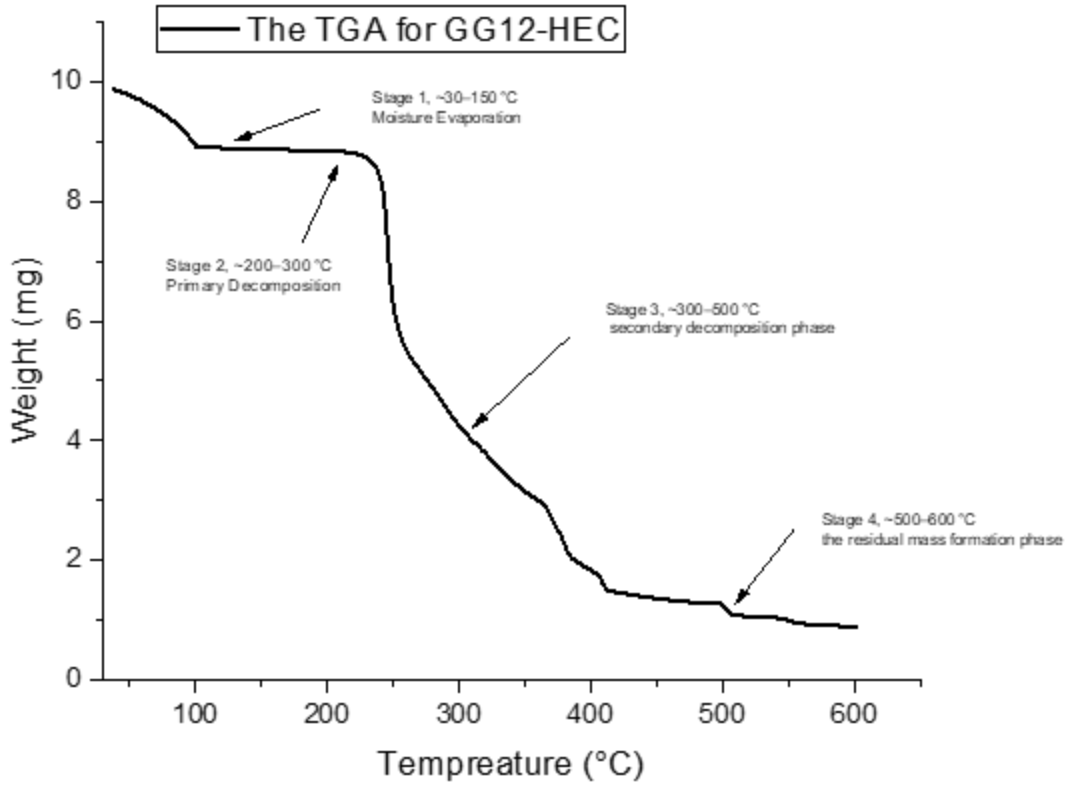

Figure 3.3: The TGA curve for GG12 -HEC during its decomposition temperature range from 30 °C to 600 °C with a heating rate of 10.00 K/min and air at 50.0 ml/min. Weight of the original sample = 9.95 mg.

Figure 3.3 presents the Thermogravimetric Analysis (TGA) curve for a gellan gum and hydroxyethyl cellulose composite hydrogel (GG12-HEC), showing how its weight changes as temperature increases from 30 °C to 600 °C. The analysis was conducted at a heating rate of 10 K/min under an airflow of 50 mL/min, with an initial sample weight of 9.95 mg. The curve is divided into four distinct decomposition stages:

During the initial stability phase (Stage 1, ~30–150 °C), a modest weight loss of approximately 9.8% (~0.98 mg) is observed, primarily due to the evaporation of free and bound water in the hydrogel matrix. The hydrophilic properties of hydroxyethyl cellulose (HEC) likely contribute to extended moisture retention, slightly delaying water release. In the primary decomposition phase (Stage 2, ~200–300 °C), a significant weight loss of around 37.9% (~3.77 mg) occurs, corresponding to the thermal breakdown of gellan gum and HEC. This involves cleavage of glycosidic bonds in GG and decomposition of HEC's cellulose backbone, indicating rapid degradation of both polymers. The secondary decomposition phase (Stage 3, ~300–500 °C) shows a series of gradual weight losses approximately 12.3%, 8.4%, 11.1%, 7.1%, and 2.4% as residual organic matter continues to oxidise and decompose. HEC may help moderate the degradation rate, resulting in more stable thermal behaviour. Finally, during the residual mass formation phase (Stage 4, ~500–600 °C), a small additional weight loss of about 1.5% (~0.15 mg) is recorded, leaving a final char residue of roughly 8.9% (~0.89 mg), suggesting that stable polymeric interactions—possibly enhanced by HEC—contribute to improved thermal resistance.

3.2.4 TGA for GG12-HEC-MG

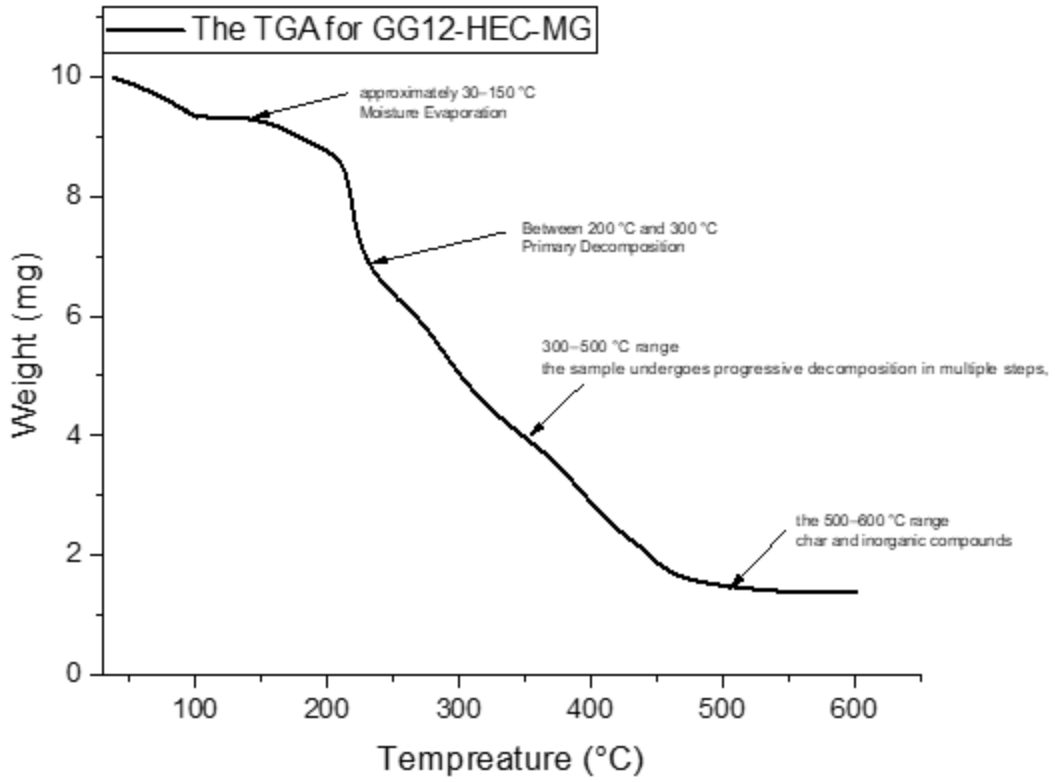

Figure 3.4: The TGA curve for GG12 HEC-MG during its decomposition temperature range from 30 °C to 600 °C with a heating rate of 10.00 K/min and air of 50.0 ml/min. Weight of the original sample = 10.03 mg.

Figure 3.4 displays the Thermogravimetric Analysis (TGA) curve for GG12-HEC-MG, showing how the sample's weight changes as a function of temperature from 30 °C to 600 °C. The original sample weighed 10.03 mg, and the test was conducted under an air atmosphere with a flow rate of 50.0 mL/min and a heating rate of 10.00 K/min. The TGA curve reveals four major thermal decomposition phases: During the initial heating phase (approximately 30-150 °C), the sample shows a weight loss of about 6.5% (roughly 0.65 mg), primarily due to the evaporation of free and bound water in the hydrogel. The hydrophilic nature of hydroxyethyl cellulose (HEC) enhances moisture retention, potentially extending this phase. The presence of nutrients may also influence the water retention and contribute to the thermal response. Between 200 °C and 300 °C, a significant weight loss of approximately 30.9% (around 3.1 mg) occurs. This is mainly due to the thermal degradation of gellan gum and HEC, involving the breakdown of glycosidic bonds in GG and the cellulose backbone in HEC. Some decomposition of nutrient additives may also contribute to this stage. In the 300–500 °C range, the sample undergoes progressive decomposition in multiple steps, with weight losses of around 16.8%, 22.6%, 8.3%, and 0.6%. These losses are linked to the continued breakdown of

organic matter, likely influenced by residual nutrient content. Finally, in the 500–600 °C range, about 13.9% of the original mass (roughly 1.4 mg) remains. This residual mass suggests the presence of thermally stable char and inorganic compounds, possibly from the nutrient additives, that resist further degradation.

3.2.5 TGA for GG12-CMC

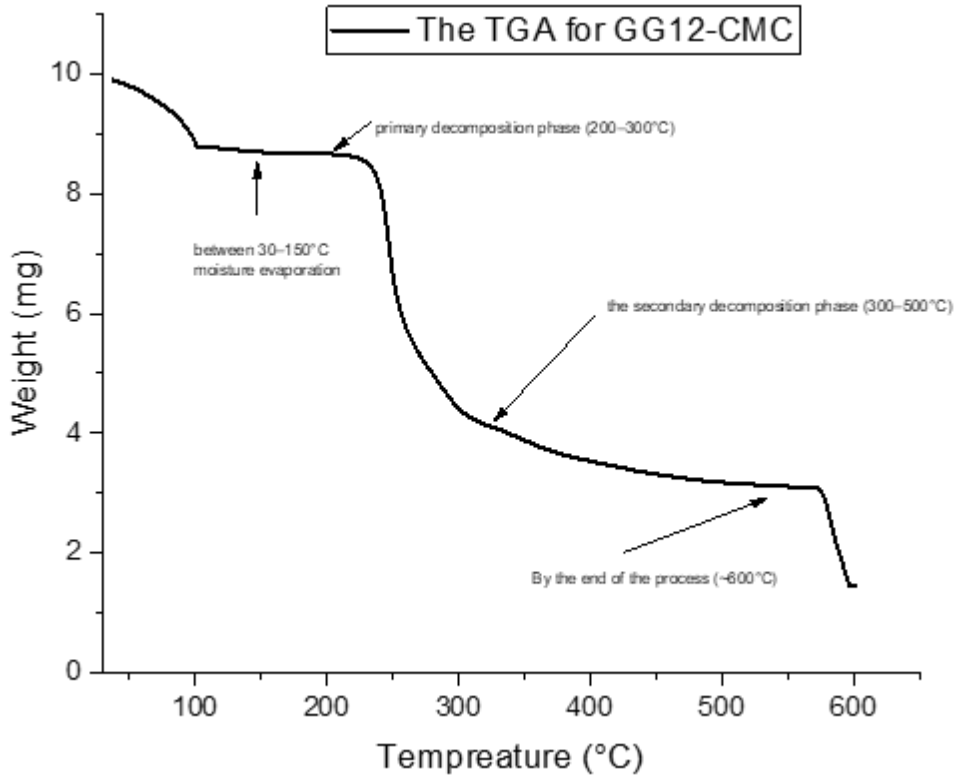

Figure 3.5: The TGA curve for GG12-CMC during its decomposition temperature ranges from 30 °C to 600 °C with a heating rate of 10.00 K/min and air at 50.0 ml/min. Weight of the original sample = 9.94 mg.

The TGA analysis of GG12-CMC reveals a multi-stage decomposition process. The sample begins at 9.94 mg and initially loses about 12.3% of its weight (~1.23 mg) between 30–150 °C, primarily due to moisture evaporation. During the primary decomposition phase (200–300 °C), significant degradation of gellan gum's glycosidic bonds and CMC's cellulose backbone occurs, resulting in a weight loss of approximately 37.2% (~3.70 mg). This is followed by the secondary decomposition phase (300–500 °C), characterized by oxidation of the remaining organic matter, where weight loss takes place in three distinct steps: 8.8%, 9.9%, and 16.9%, amounting to a combined loss of around 3.54 mg. By the end of the process (~600 °C), a residual mass of 14.5% (~1.45 mg) remains, which is slightly higher than that of pure gellan gum. This suggests improved structural stability due to the presence of CMC. The mass loss

above 500 °C is associated with oxidation and degradation of residual char, indicating the final stage of thermal decomposition.

3.2.6 TGA for GG12-CMC-MG.

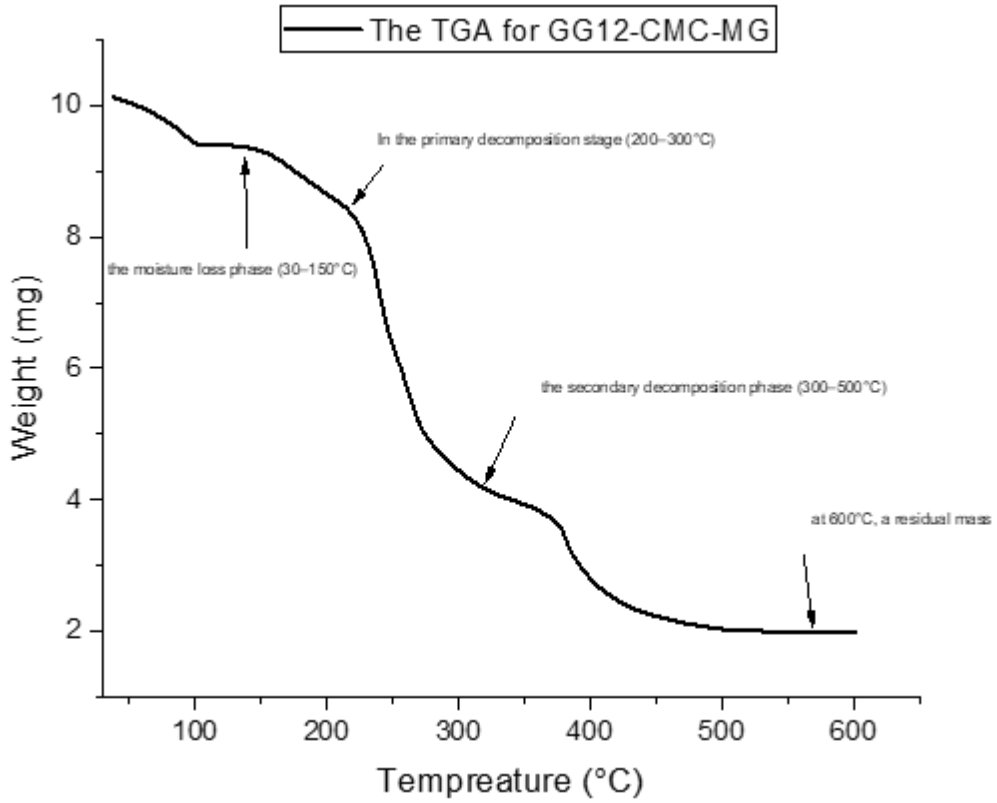

Figure 3.6: The TGA curve for GG12-CMC-MG + 1 ml nutrient during its decomposition temperature range from 30 °C to 600 °C with a heating rate 10.00 K/min and air at 50.0 ml/min. Weight of the original sample = 10.26 mg.

The TGA analysis of GG12-CMC-MG with nutrient reveals a multi-phase decomposition profile. The initial sample weight was 10.26 mg, and during the moisture loss phase (30-150 °C), a gradual weight reduction occurred in two steps, totalling approximately 14.7% (~1.51 mg), due to evaporation of both free and bound water. This process may be extended by interactions between CMC and the nutrient. In the primary decomposition stage (200–300 °C), a significant weight drops of 23.5% (~2.41 mg) is observed, attributed to the thermal breakdown of gellan gum's glycosidic bonds and CMC's cellulose backbone. The presence of organic compounds in the nutrient may also contribute to decomposition in this range. During the secondary decomposition phase (300–500 °C), further weight loss occurs in two steps: about 21.7% (~2.22 mg) and 19.6% (~2.04 mg). This stage involves the oxidation of residual organic matter, and the nutrient appears to extend the degradation process, resulting in a broader, more gradual weight reduction profile. By 600 °C, a residual mass of approximately

19.3% (~1.98 mg) remains. This suggests the presence of stable inorganic compounds from the nutrient that do not fully decompose, leading to higher residue levels compared to GG-CMC samples without nutrient.

3.3 Derivative Thermogravimetry (DTG)

The second important tool in thermal analysis is DTG. DTG is essentially a derivative of TGA, measuring the rate of mass loss as a function of temperature. By calculating the first derivative of the TGA curves (the mass loss per unit temperature change). The main aim of DTG is to enhance the interpretation of thermogravimetric (TGA) data by identifying precise points of thermal events, such as: Peak Decomposition Temperatures, Kinetic Studies and Component Identification (253-256).

3.3.1 DTG analysis on GG12

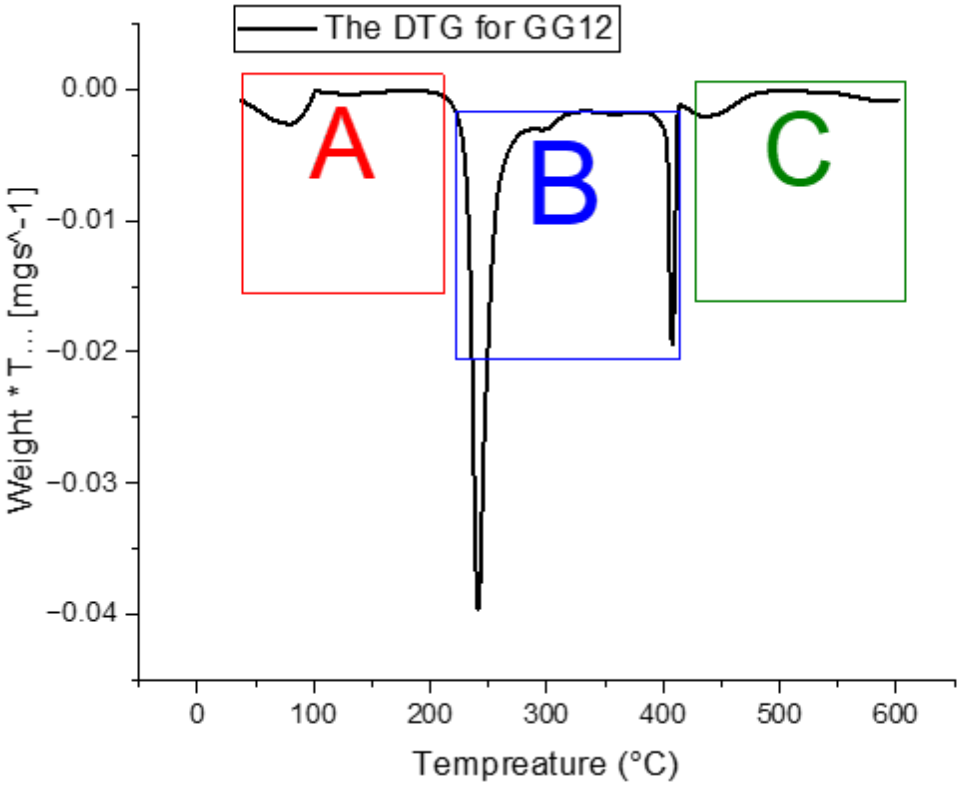

Figure 3.7: The DTG curve for GG12 during its decomposition temperature ranges from 30 °C to 600 °C with a heating rate of 10.00 K/min, air 50.0 ml/min, and a weight of the original sample = 10.24 mg.

In figure 3.7 derivative thermogravimetry (DTG) curve illustrates the rate of weight loss (mg/s) as a function of temperature (°C) for 12 GG. Zone A (Red box), occurring between approximately 30 °C and 150 °C with a peak around 79.98 °C, corresponds to the evaporation of free and bound moisture within the gellan gum sample. This initial stage involves a minor weight loss, which highlights the hydrophilic nature of gellan gum, as water is loosely retained

within its polymer network. Importantly, no chemical degradation takes place during this phase only the physical release of moisture. Zone B (Blue box), spanning approximately 180–400 °C with primary and secondary peaks around 241–295 °C, represents the main degradation phase of gellan gum. During this stage, substantial weight loss occurs due to the thermal breakdown of the polysaccharide backbone, involving cleavage of glycosidic linkages and the transformation of polymer chains into volatile by-products such as CO_2, acetic acid, and other small organic compounds. A secondary inflection or shoulder near 356 °C indicates the continued decomposition of residual semi-volatile fragments or carbon-rich structures, marking the transition toward more advanced stages of thermal degradation. Zone C (Green box), covering the temperature range of approximately 400–600 °C with a peak around 435 °C, represents the final stage of thermal degradation involving carbonization and residual oxidation. In this phase, the remaining stable char or carbonaceous materials gradually decompose, evidenced by a slower but consistent rate of weight loss. This steady degradation is associated with the oxidation of residual organic matter, ultimately leading to thermal stabilization of the sample. By the end of this process, the material leaves behind a small amount of inorganic ash, typically accounting for about 20–30% of the original sample weight (Table 3.2).

Table 3.2: DTG peak temperatures for GG12 Decomposition Stages.

Decomposition Stage	**Tmax (°C)**	**Decomposition Stage**	**Tmax(°C)**
Moisture Evaporation	80	Residual Oxidation	365
Primary Decomposition	241	Late-Stage Decomposition	408
Secondary Decomposition	296	Final Residual Mass	436

3.3.2 DTG analysis on GG12-MG

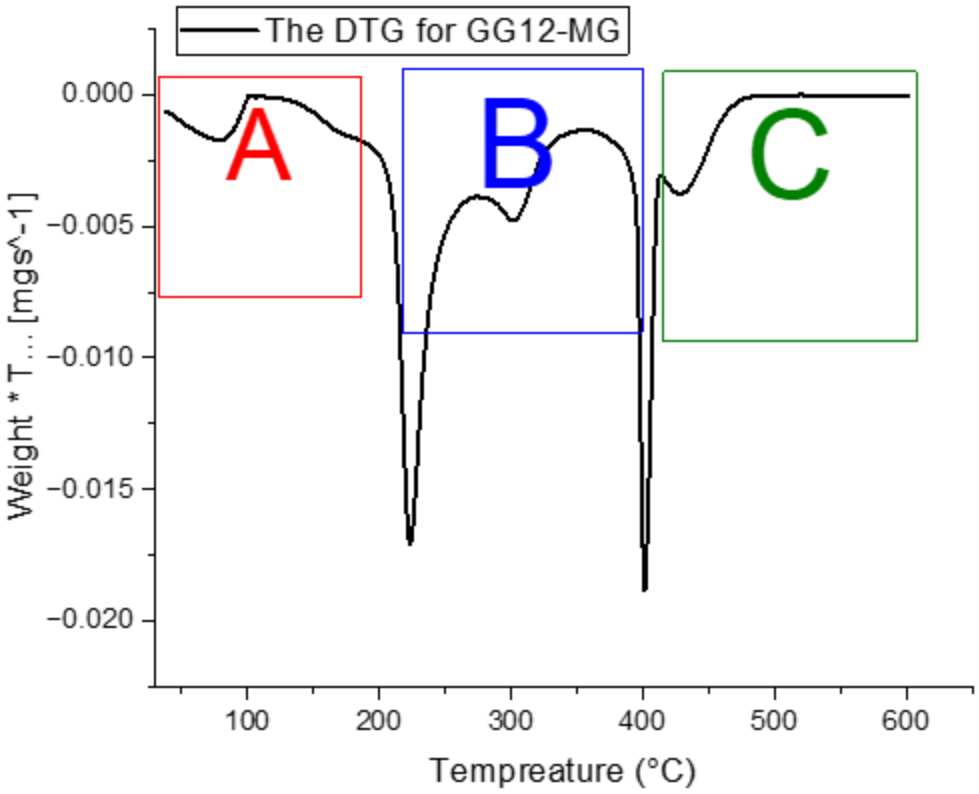

Figure 3.8: The DTG curve for GG12-MG during its decomposition temperature ranges from 30 °C to 600 °C with a heating rate of 10.00 K/min, air of 50.0 ml/min, and a weight of the original sample = 10.10 mg.

In figure 3.8, the derivative thermogravimetry (DTG) curve illustrates the rate of weight loss (mg/s) as a function of temperature (°C) for 12 mg/cm³ Gellan Gum (GG) with 1 mL nutrient. The DTG curve for the Gellan Gum + 1 mL nutrient composite reveals a three-stage thermal decomposition process. In Zone A (~30–150 °C), a minor weight loss peak reflects moisture evaporation, confirming the hydrophilic nature of Gellan Gum without any chemical degradation. Zone B (~180–400 °C) captures the main degradation phase, with a sharp peak around 241–295 °C indicating the breakdown of glycosidic bonds and the release of volatile by-products like CO_2 and small organic molecules; a secondary shoulder near 356 °C suggests continued decomposition of semi-volatile residues. Zone C (~400–600 °C) shows gradual carbonization and residual oxidation, with a steady weight-loss peak around 435 °C due to the degradation of remaining carbon-rich matter. After 500 °C, the curve stabilizes, indicating the formation of inorganic residues, typically constituting 20–30% of the original sample mass. Overall, the addition of nutrients appears to slightly shift decomposition events and increase thermal complexity in the Gellan Gum matrix.

Here is a Tmax Values Table 3.3 summarizing the peak decomposition temperatures for each thermal event in the DTG analysis.

Table 3.3: Thermal Decomposition Stages and Corresponding Peak Temperatures (Tmax) of Gellan Gum Based on TGA Analysis for GG12-MG.

Decomposition Stage	**T_{max} (°C)**	**Decomposition Stage**	**T_{max}(°C)**
Moisture Evaporation	80	Residual Oxidation	404
Primary Decomposition	223	Late-Stage Decomposition	430
Secondary Decomposition	302		

3.3.3 DTG analysis on GG12-HEC

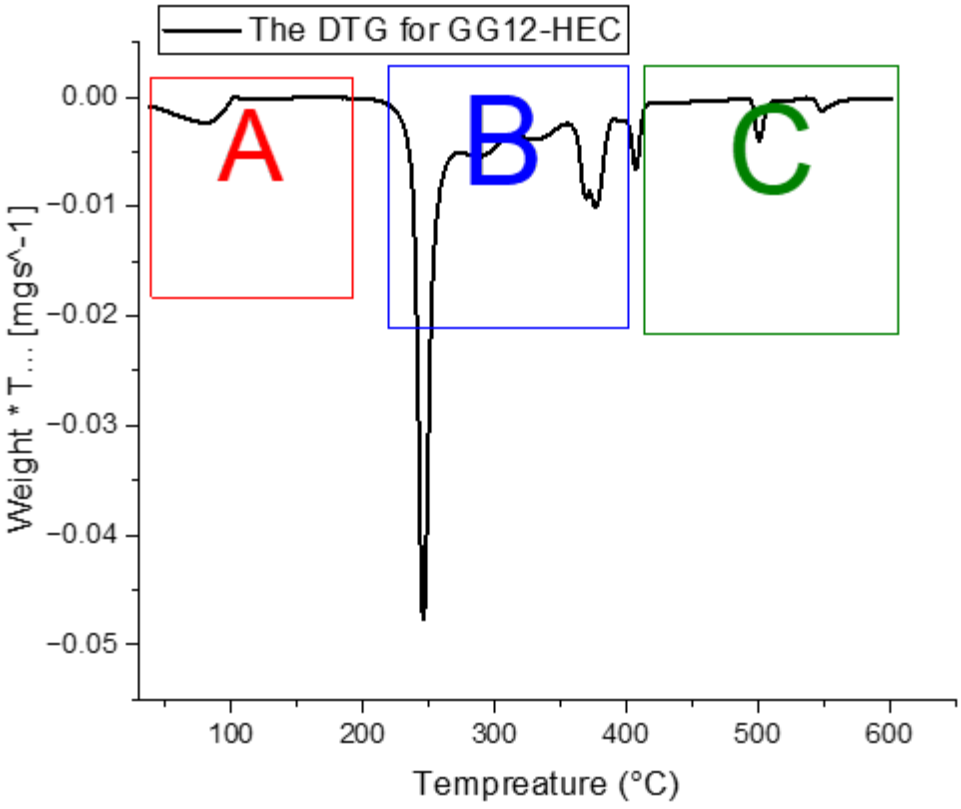

Figure 3.9: The DTG curve for GG12 -HEC during its decomposition temperature ranges from 30 °C to 600 °C with a heating rate of 10.00 K/min, air 50.0 ml/min, and a weight of the original sample = 9.95 mg.

In Figure 3.9 the DTG (Derivative Thermogravimetric) curve presented for the GG12–HEC composite illustrates the rate of weight loss across a temperature range of 30 °C to 600 °C, under an air flow of 50.0 mL/min and a heating rate of 10.00 K/min. The curve reveals three distinct thermal degradation zones: Zone A (Red, ~30–150 °C) represents the initial moisture evaporation phase, where a small peak indicates the release of both free and bound water. This confirms the hydrophilic properties of both Gellan Gum and HEC, and no chemical degradation occurs in this zone. Zone B (Blue, ~180–400 °C) corresponds to the main degradation phase.

The sharp peak around ~241–295 °C is attributed to the cleavage of glycosidic bonds in Gellan Gum and degradation of the HEC backbone. This phase is characterised by substantial mass loss due to the formation of volatile by-products such as CO_2 and small organics. The presence of additional shoulders or inflections in this region indicates overlapping degradation events typical in polymer blends. Zone C (Green, ~400–600 °C) marks the carbonization and residual oxidation stage. A less intense but consistent peak around ~435 °C suggests further breakdown and oxidation of the remaining carbonaceous residues. The curve levels off after 500 °C, indicating thermal stability of the residual inorganic matter, typically comprising 20–30% of the initial mass.

Table 3.4: Thermal Decomposition Stages and Corresponding Peak Temperatures (Tmax) of Gellan Gum Based on TGA Analysis for GG12-HEC.

Decomposition Stage	**Tmax(°C)**	**Rate of mass**
Moisture Evaporation	81	9.82% (- 0.98 mg)
Primary Decomposition	246	38.06% (-3.79 mg)
Secondary Decomposition	286	12.17% (-1.21)
Residual Oxidation	329	8.34% (-0.83)
Late-Stage Decomposition	379	11.09% (-1.10), 7.08% (-0.70)
Final Residual Mass Formation	503	3.78% (-0.34 mg +-0.13 mg)

3.3.4 DTG analysis on GG12-HEC-MG

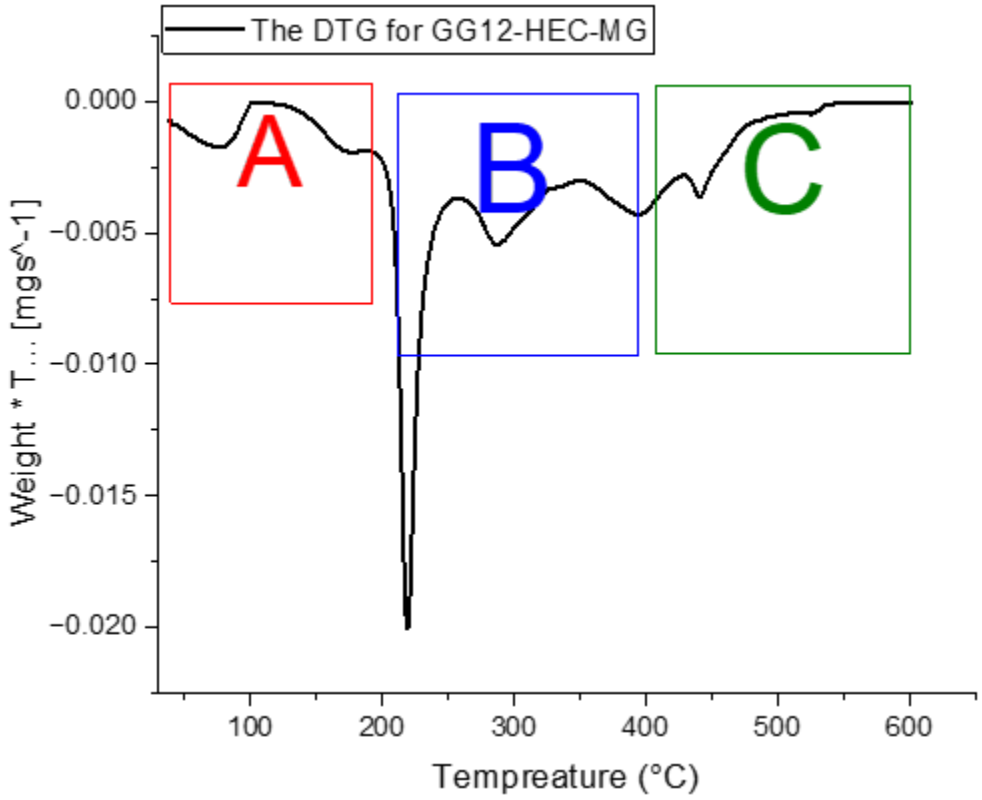

Figure 3.10: The DTG curve for GG12-HEC-MG during its decomposition temperature ranges from 30 °C to 600 °C with a heating rate of 10.00 K/min, air 50.0 ml/min, and a weight of the original sample = 10.08 mg.

In Figure 3.10 the DTG curve for the GG12–HEC-MG composite reveals a three-stage thermal degradation process between 30 °C and 600 °C, conducted at a heating rate of 10.00 K/min under an air flow of 50.0 mL/min, with an initial sample mass of 10.08 mg. Zone A (~30-150 °C) shows a minor weight loss corresponding to the evaporation of moisture (free and bound water), highlighting the hydrophilic nature of the biopolymer blend. Zone B (~180-400 °C) features the main decomposition events, with a prominent peak indicating breakdown of the glycosidic bonds in Gellan Gum and degradation of the HEC network, likely producing volatile degradation products such as CO_2 and acetic acid. Multiple inflections in this region suggest overlapping decomposition stages due to complex interactions between Gellan Gum, HEC, and nutrient additives. Zone C (~400–600 °C) marks the carbonization and oxidation of remaining organic residues, with a gradual weight-loss rate and a stabilizing curve above 500 °C, implying the formation of thermally stable inorganic residue. The presence of nutrients appears to influence decomposition temperatures and peak profiles, suggesting enhanced thermal complexity and possibly improved thermal resistance due to additive interactions.

Table 3.5: Thermal Decomposition Stages and Corresponding Peak Temperatures (Tmax) of Gellan Gum Based on TGA Analysis for GG12-HEC-MG.

Decomposition Stage	Tmax (°C)
Stage 1	345
Stage 2	108
Stage 3	237.

3.3.5 DTG analysis on GG12-CMC

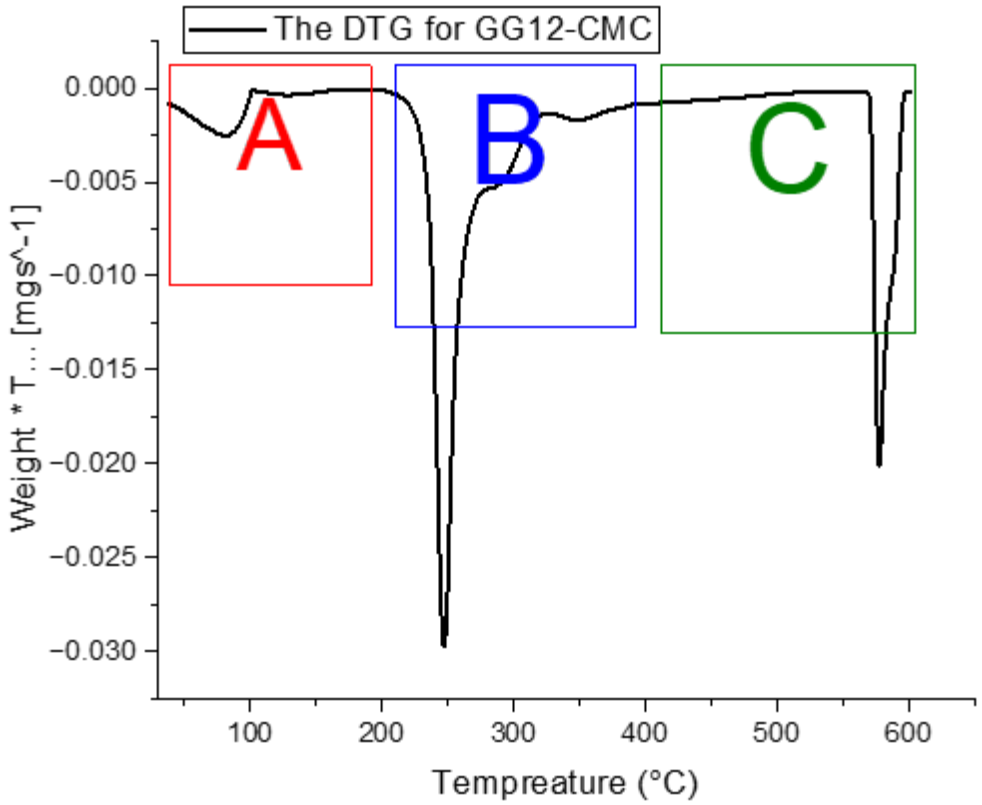

Figure 3.11: The DTG curve for GG12-CMC during its decomposition temperature ranges from 30 °C to 600 °C with a heating rate of 10.00 K/min, air 50.0 ml/min, and a weight of the original sample = 9.94 mg.

Figure 3.11 displays the DTG curve for GG12 –CMC composite, showing its thermal degradation profile across a temperature range of 30 °C to 600 °C, at a heating rate of 10.00 K/min under an air flow of 50.0 mL/min, with an initial mass of 9.94 mg. The decomposition process can be divided into three zones: Zone A (~30–150 °C) corresponds to moisture evaporation, where a small endothermic peak indicates the release of both free and bound water, confirming the hydrophilic nature of the material. Zone B (~180–400 °C) represents the primary and secondary thermal degradation of the polysaccharide matrix,

involving cleavage of glycosidic bonds in Gellan Gum and structural breakdown of the carboxymethyl cellulose (CMC). This zone includes the evolution of volatile products and carbonaceous residues, with multiple small peaks reflecting overlapping degradation events. Zone C (~400–600 °C) captures the final oxidation and carbonization stages, where residual organic matter is converted to char and stable inorganic residues. A sharp peak at higher temperatures suggests intensified degradation due to CMC's contribution. Overall, the DTG curve highlights the multistep decomposition of the Gellan Gum–CMC system and its complex thermal behaviour.

Table 3.6: Thermal Decomposition Stages and Corresponding Peak Temperatures (Tmax) of Gellan Gum Based on TGA Analysis for GG12-CMC.

Decomposition Stage	**Peak T_{max} (°C)**
Moisture Evaporation	81.2
Primary Polymer Decomposition	247.2
Second Decomposition	281.4
Late-Stage Decomposition	347.4
Final Residual Decomposition	582.4

3.3.6 DTG analysis on GG12-CMC-MG

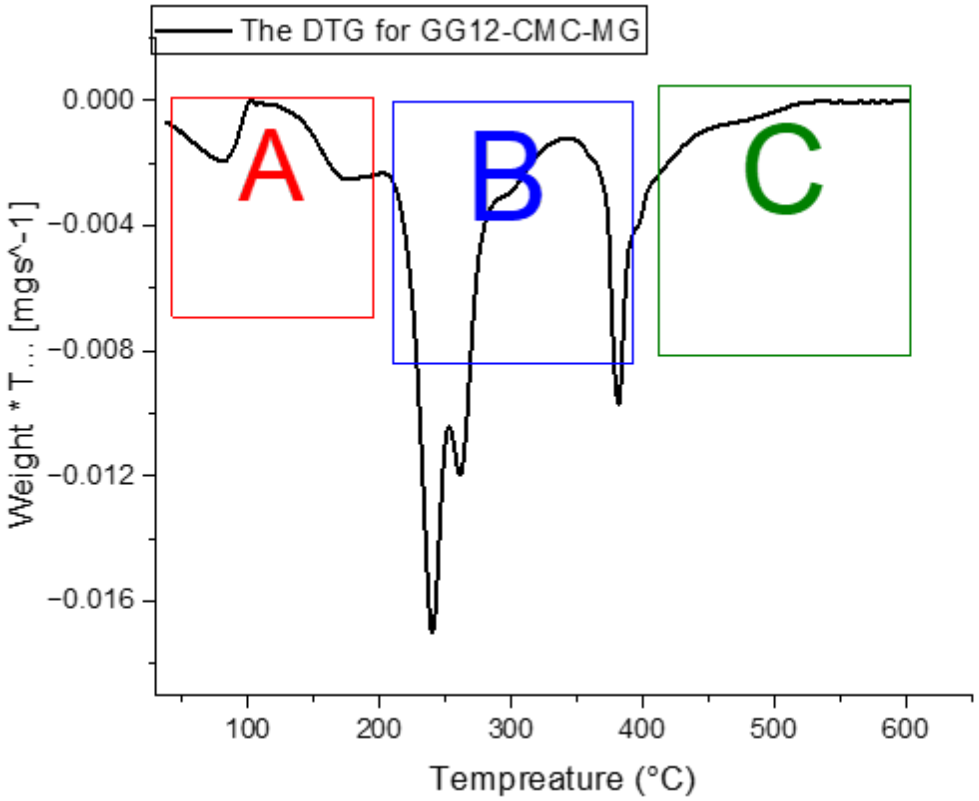

Figure 3.12: The DTG curve for GG12 -CMC-MG during its decomposition temperature ranges from 30 °C to 600 °C with a heating rate of 10.00 K/min, air 50.0 ml/min, and a weight of the original sample = 10.26 mg.

In Figure 3.12 the DTG (Derivative Thermogravimetric) curve shown illustrates the thermal decomposition profile of GG12-CMC-MG. Conducted under air flow (50.0 mL/min) with a heating rate of 10.0 K/min, the curve spans a temperature range of 30 °C to 600 °C and uses an initial sample mass of 10.26 mg. The DTG signal, which represents the rate of mass loss, reveals three main decomposition stages: Region A (30 °C–180 °C) corresponds to moisture loss and evaporation of volatile components, evidenced by a small peak. Region B (≈200 °C–380 °C) displays the most significant mass loss, indicating the primary decomposition of the gellan gum and CMC polymers, including depolymerization and degradation of the biopolymer backbone. Region C (≈400 °C–520 °C) shows a smaller peak, likely associated with the oxidation of residual carbonaceous material. This thermal behaviour highlights the multi-stage degradation typical of biopolymer systems, with major decomposition centered in the mid-temperature range. The table below provides a summary of the Tmax values and corresponding temperature ranges for each stage of decomposition.

Table 3.7: Thermal Decomposition Stages and Corresponding Peak Temperatures (Tmax) of Gellan Gum Based on TGA Analysis for GG12-CM-MG.

Process	**Peak T_{max} (°C)**
Moisture Evaporation	81.1
Primary Polymer Decomposition	176.5
Second Decomposition	240.2
Late-Stage Decomposition	261.2
Final Residual Decomposition	381.5

3.4 Differential Scanning Calorimetry (DSC)

The third tool in thermal measurements is DSC. DSC indicates the thermal flow related to phase transitions in materials as a function of temperature. This method is especially effective for analysing thermal events, including melting, crystallisation, glass transitions, and various endothermic or exothermic reactions (248, 249). DSC data can provide insight into the precise temperatures where certain transitions occur, leading to a better understanding of material stability under thermal stress.

3.4.1 DSC analysis on GG12

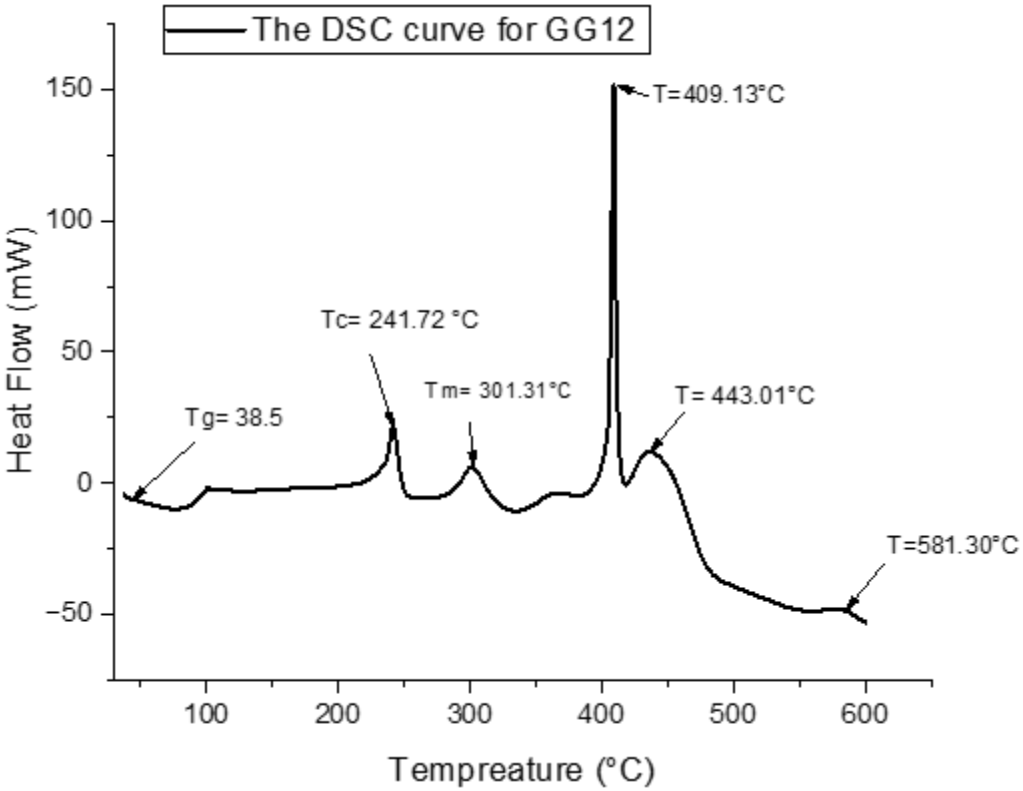

Figure 3.13 The DSC curve for GG12 during its decomposition temperature ranges from 30 °C to 600 °C with a heating rate of 10.00 K/min, air 50.0 ml/min, and a weight of the original sample = 10.24 mg.

This Figure 3.13 displays a Differential Scanning Calorimetry (DSC) curve for GG12, plotting heat flow (mW) vs. temperature (°C). The curve shows glass transition and crystallisation, melting, crosslinking and oxidation or decomposition. Firstly, Glass Transition (Tg) (~38-89 °C) a broad change in heat flow around 38.5 °C to 89.2 °C. This corresponds to the polymer transitioning from a glassy, brittle state to a rubbery, more flexible phase. Secondly, Crystallization (Tc) occurs within the temperature range of 233.3 °C, marked by an exothermic peak at 241.7 °C with an onset at 233.7 °C. This process involves the reorganization of polymer chains into a structured, crystalline form. The presence of Tc indicates partial crystallinity, which contributes to enhanced mechanical strength and improved thermal stability of the material. The melting transition (Tm) occurs between 284–320 °C, characterized by a distinct endothermic peak at 301.3 °C, with an onset at 284.1 °C and an endset at 320.7 °C. The apparent similarity in peak direction arises from the DSC display convention used in this study. The crystallization peak at ~242 °C corresponds to an exothermic process, while the melting peak at ~301 °C is endothermic, consistent with polymer thermal behavior.

This peak represents the melting of crystalline regions within the polymer matrix, where the ordered structure breaks down into a disordered state. The Tm value defines the material's upper thermal threshold before degradation initiates, providing insight into its thermal stability and processing limitations. The melting transition (Tm) occurs between 284-320 °C, characterized by a distinct endothermic peak at 301.3 °C, with an onset at 284.1 °C and an endset at 320.7 °C. This peak represents the melting of crystalline regions within the polymer matrix, where the ordered structure breaks down into a disordered state. The Tm value defines the material's upper thermal limit before degradation initiates, providing insight into its thermal stability and processing limitations. The crosslinking or secondary reactions occur within the temperature range of 345–381 °C, marked by a minor exothermic peak at 362.2 °C. During this phase, chemical crosslinking or structural rearrangement likely takes place, reinforcing the polymer network. These reactions contribute to improved thermal stability and mechanical durability, enhancing the material's resistance to further degradation at elevated temperatures. The thermal degradation process is characterized by three distinct exothermic peaks, indicating progressive polymer breakdown. The first major peak appears at 409.1 °C (onset at 404.4 °C, endset at 412.0 °C), followed by another significant peak at 443.0 °C (onset at 423.6 °C, endset at 476.6 °C). Finally, a high-temperature degradation event occurs at 581.3 °C (onset at 559.4 °C, endset at 600.1 °C). These peaks correspond to the stepwise breakdown of polymer chains, oxidative degradation, and final decomposition, marking the material's thermal resistance and stability limits.

3.4.2 DCS analysis on GG12-MG

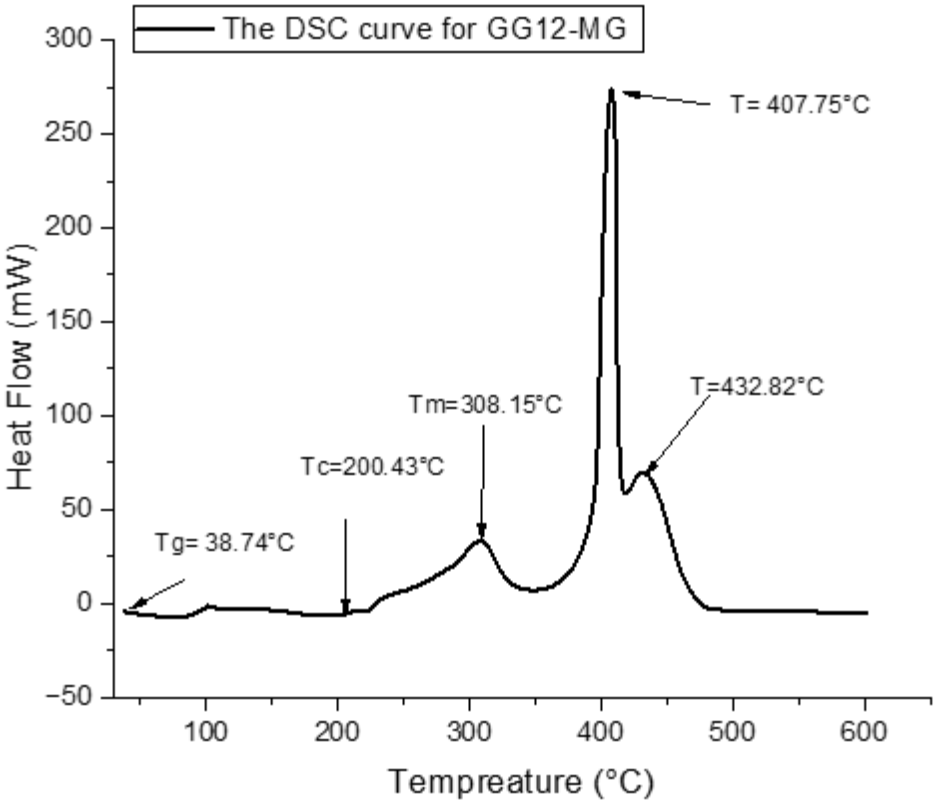

Figure 3.14: The DSC curve for GG12 -MG during its decomposition temperature ranges from 30 °C to 600 °C with a heating rate of 10.00 K/min, air of 50.0 ml/min, and a weight of the original sample = 10.10 mg.

In Figure 3.14, the behaviour is like that of Figure 3.13, with only slight variations between them. Firstly, the glass transition temperature remains nearly unchanged, indicating that the addition of nutrients does not significantly affect the amorphous phase mobility. Where the difference between the two cases in glass transition temperature is 0.24 °C. secondly, the crystallisation temperature is lower (-41.3 °C) for the nutrient-modified sample, suggesting that the presence of the nutrient alters the polymer crystallisation behaviour, possibly due to interactions disrupting molecular ordering. Thirdly, a slight increase in Tm (-6.84) for the nutrient sample suggests that the crystalline regions are more thermally stable, possibly due to interactions between gellan gum and the nutrient. The major decomposition peaks are marginally lower in the nutrient-modified sample, suggesting a slight reduction in thermal stability. The overall thermal profile remains similar, but the nutrient incorporation affects crystallisation behaviour and degradation kinetics.

3.4.3 DSC analysis on GG12-HEC

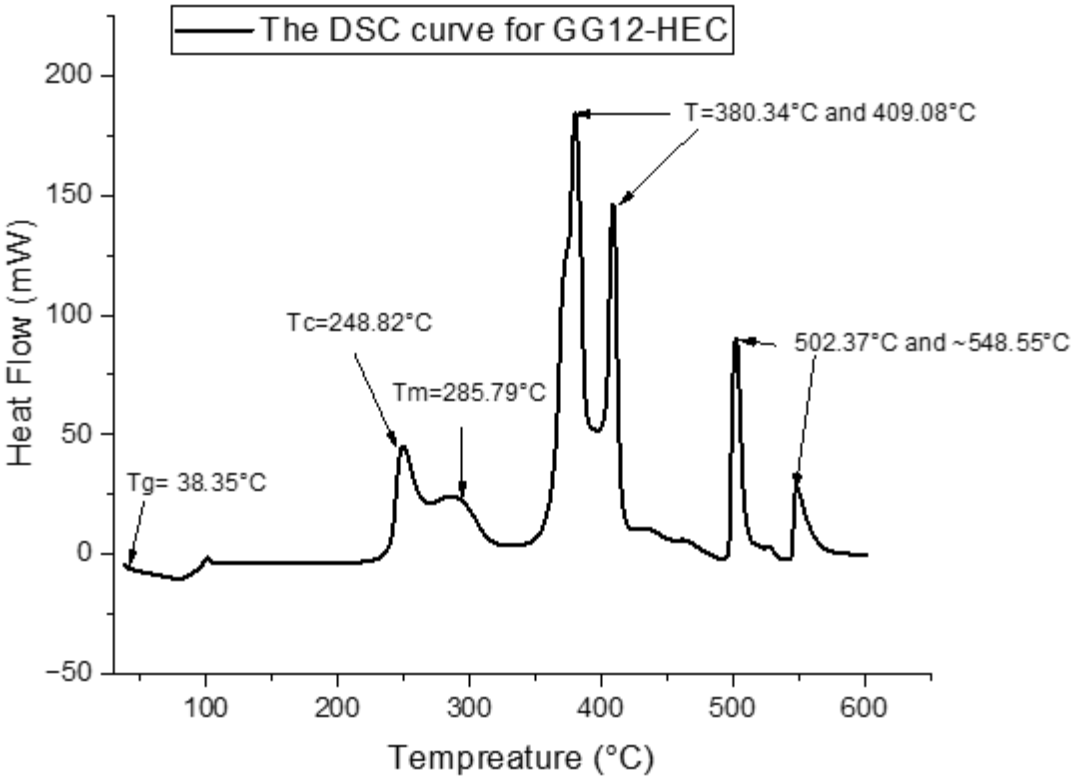

Figure 3.15: The DSC curve for GG12 - HEC during its decomposition temperature range from 30 °C to 600 °C with a heating rate of 10.00 K/min and air at 50.0 ml/min. Weight of the original sample = 9.95 mg.

In Figure 3.15 presents a Differential Scanning Calorimetry (DSC) curve for GG12-HEC (Hydroxyethyl Cellulose), displaying key thermal transitions across different temperature ranges. The glass transition (Tg) occurs at approximately 38.4 °C, marking the shift from a rigid, glassy state to a more flexible, rubbery state, which reflects the polymer's thermal stability at lower temperatures. Crystallization (Tc) is identified around 248.8 °C, where polymer chains reorganize into a more ordered structure, enhancing mechanical strength and stability. The melting transition (Tm) at 285.8 °C signifies the breakdown of crystalline regions, indicating the highest temperature before the material transitions into a molten phase. Further heating leads to crosslinking or secondary reactions, evident from peaks at 380.3 °C and 409.1 °C, suggesting the formation of stronger chemical bonds that improve thermal stability and durability. Finally, oxidation and decomposition take place at 502.4 °C and 548.6 °C, marking the breakdown of polymer chains and complete thermal degradation, which defines the material's upper thermal stability limit.

3.4.4 D*SC* analysis on GG12-HEC-MG

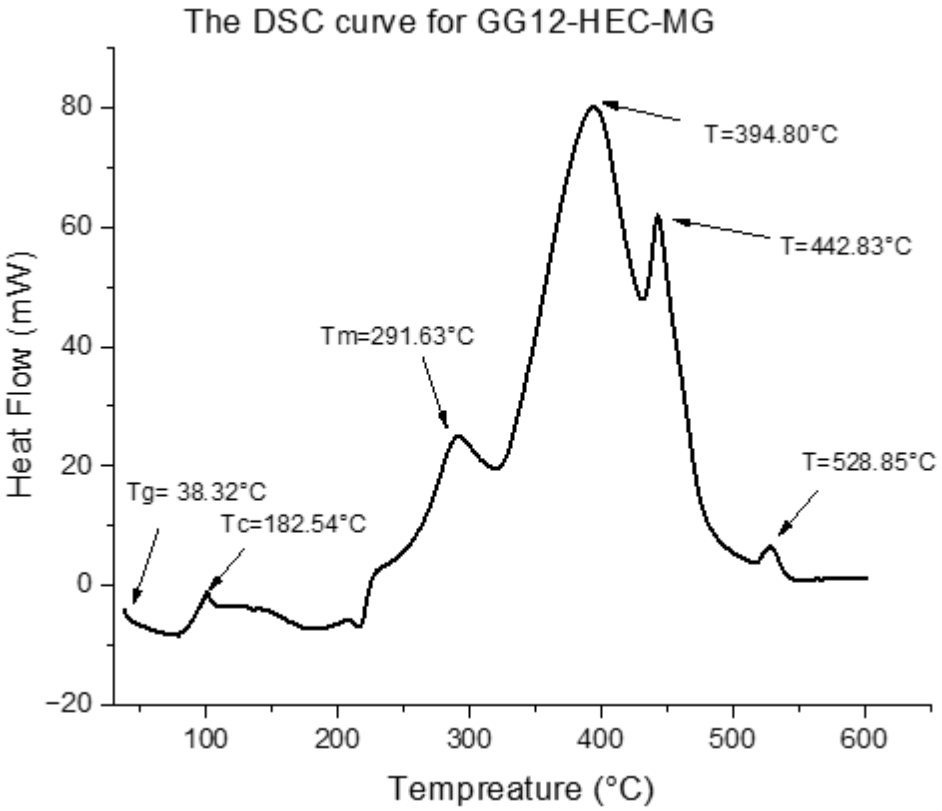

Figure 3.16: The DSC curve for -HEC During its decomposition temperature ranges from 30 °C to 600 °C with a heating rate of 10.00 K/min and air of 50.0 ml/min. Weight of the original sample = 10.03 mg.

In Figures 3.16 and 3.15 have similar Tg values (~38.3 °C for the nutrient sample and ~38.4 °C for the pure sample), indicating comparable polymer flexibility and initial thermal stability. The crystallization temperature (Tc) for GG12-HEC sample is 248.8 °C, whereas for the Gellan Gum12-HEC-MG, it is 182.5 °C. This notable decrease in Tc upon the addition of nutrients suggests that the presence of these components disrupts the polymer's ability to organize into a crystalline structure, likely due to interactions between the nutrient molecules and the polymer chains, which hinder the formation of an ordered phase. The Gellan Gum-HEC sample has a melting temperature (Tm) of 285.8 °C, while the Gellan Gum-HEC + Nutrient sample exhibits a slightly higher Tm of 291.6 °C. This increase suggests that the addition of nutrients enhances the thermal stability of the crystalline phase, possibly by reinforcing intermolecular interactions within the polymer matrix, making it more resistant to thermal breakdown. The Gellan Gum-HEC sample exhibits crosslinking and secondary reaction peaks at 380.3 °C and 409.1 °C, whereas the Gellan Gum-HEC + Nutrient sample demonstrates these reactions at 394.8 °C and 442.8 °C. The increase in reaction temperatures in the nutrient-enhanced sample suggests that the presence of nutrients promotes stronger crosslinking interactions within the

polymer network, thereby enhancing its thermal stability and resistance to degradation at elevated temperatures. The Gellan Gum-HEC sample exhibits major decomposition peaks at 502.4 °C and ~548.6 °C, whereas the Gellan Gum-HEC + Nutrient sample presents a single dominant decomposition peak at 528.9 °C. The shift in the final decomposition peak toward a higher temperature in the nutrient-enhanced sample indicates improved thermal degradation stability. This suggests that the presence of nutrients contributes to structural reinforcement, delaying the onset of complete thermal breakdown.

3.4.5 DSC analysis on GG12-CMC

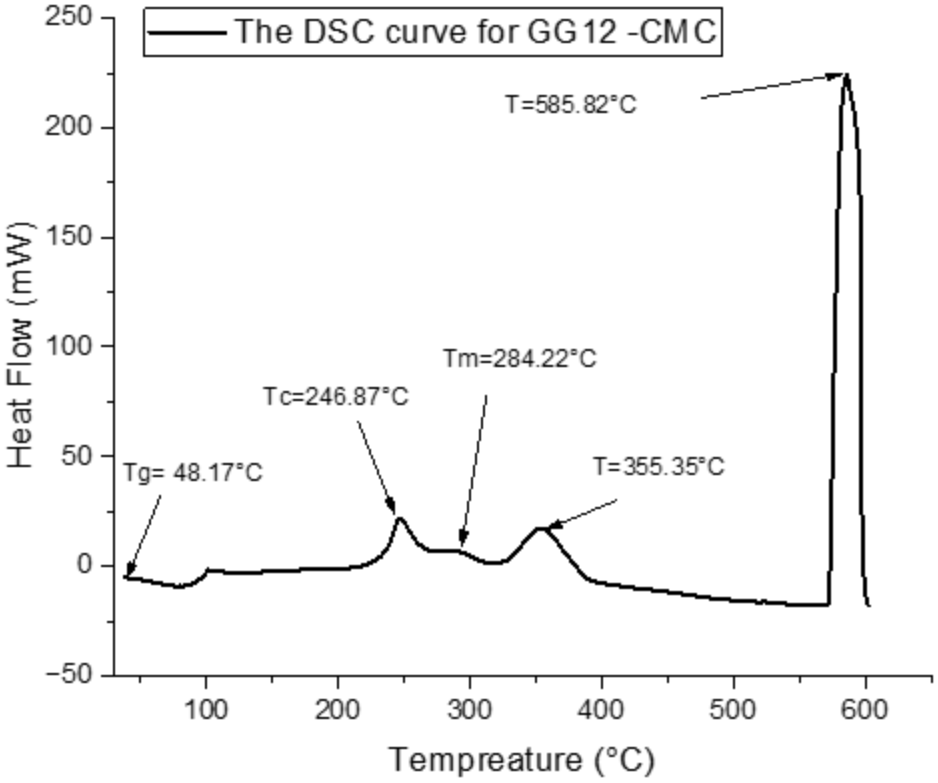

Figure 3.17: The DSC curve for GG12 -CMC during its decomposition temperature ranges from 30 °C to 600 °C with a heating rate of 10.00 K/min and air at 50.0 ml/min. Weight of the original sample = 9.94 mg.

The DSC analysis reveals distinct thermal transitions of the material, starting with the glass transition (Tg) between 48.2–103.4 °C, with a peak at 79.2 °C, indicating a shift from a rigid to a flexible state. Crystallization (Tc) occurs between 233.9–268.7 °C, marked by an exothermic peak at 246.9 °C, signifying the rearrangement of polymer chains into a more ordered structure, enhancing mechanical and thermal stability. The melting transition (Tm) is observed between 278.2–309.7 °C, with a peak at 284.2 °C, representing the breakdown of

crystalline regions and establishing the upper thermal limit before structural loss. Crosslinking or secondary reactions take place between 327.1–386.0 °C, with a peak at 355.4 °C, suggesting chemical bonding or molecular rearrangements that contribute to increased durability and thermal stability. Finally, oxidation and decomposition occur in the 572.8-597.6 °C range, with a prominent exothermic peak at 585.8 °C, signifying polymer degradation and complete material breakdown. Overall, the material demonstrates partial crystallinity, enhanced crosslinking stability, and excellent thermal endurance, as evidenced by a final decomposition peak above 500 °C.

3.4.6 DSC analysis on GG12-CMC-MG

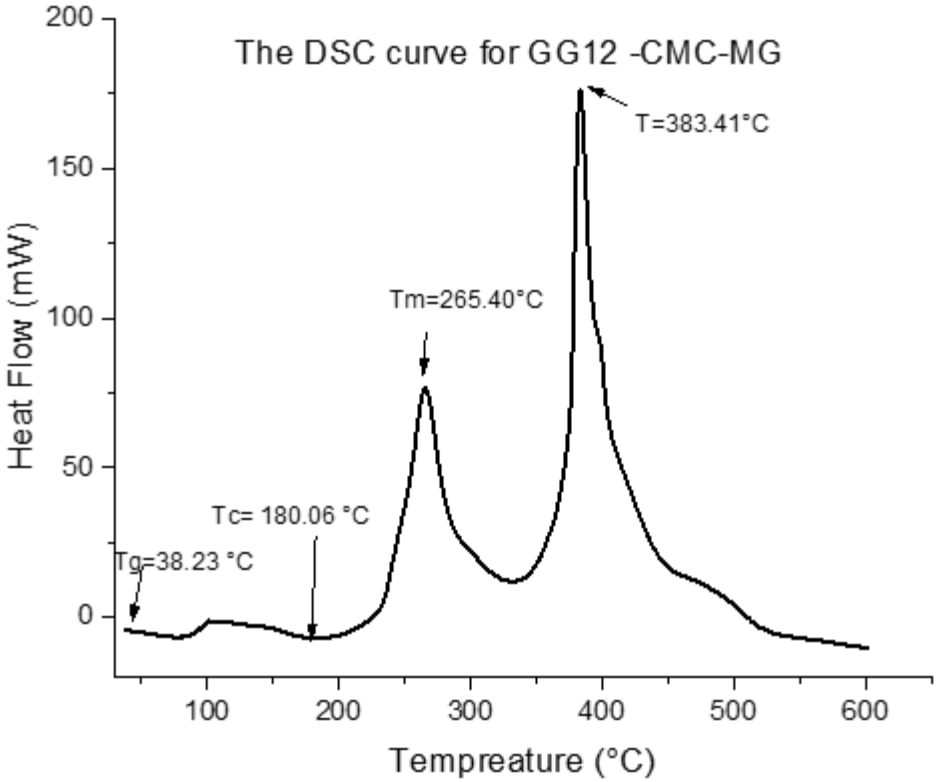

Figure 3.18: The DSC curve for GG12 -CMC -MG during its decomposition temperature range from 30 °C to 600 °C with a heating rate 10.00 K/min and air at 50.0 ml/min. Weight of the original sample = 10.26 mg.

The DSC analysis reveals notable thermal differences between GG12-CMC in Figure 3.17 and GG12-CMC-MG in Figure 3.18. The glass transition temperature (Tg) decreases from 48.2 °C to 38.2 °C with nutrient addition, indicating increased molecular mobility and a plasticizing effect. Similarly, the crystallization temperature (Tc) is significantly reduced from 246.9 °C to 180.1 °C, suggesting that the nutrients interfere with polymer chain packing and reduce crystallinity. The melting temperature (Tm) also decreases from 284.2 °C to 265.4 °C, implying weakened intermolecular forces within the crystalline regions. However, the crosslinking or

secondary reaction temperature shifts upward from 355.4 °C to 383.4 °C, suggesting enhanced structural stability due to the nutrient's influence. In contrast, thermal decomposition peaks shift from 585.8 °C in the pure sample to a lower 383.4 °C in the nutrient-containing sample, indicating reduced overall thermal stability. In conclusion, while nutrient incorporation enhances crosslinking, it reduces crystallinity, melting temperature, and thermal degradation resistance, ultimately making the material more structurally modified but thermally less stable.

3.5 Conclusions

The TGA curves obtained in this study illustrate the thermal degradation behaviour of gellan gum hydrogels; highlighting how they differ upon inclusion of a nutrient guest. All measured samples begin with an initial weight around 10 mg and exhibit four major stages of weight loss, as highlighted in the DTG plots. The first phase (up to ~150 °C) represents moisture evaporation. Primary decomposition occurs between 200–300 °C, indicating the breakdown of the polymer backbone. Subsequent degradation stages (up to ~500–600 °C) correspond to further oxidation of organic matter and residue formation.

Native material (12GG) exhibited a 16% reduction in mass below 120 °C, underwent bulk decomposition at around 230 °C before a final oxidative loss at 400+ °C. The composite materials generally exhibited similar thermal stability, but with reduced water retention. HEC composite material (12GG-HEC) exhibited an 11% reduction in mass below 120 °C, underwent bulk decomposition at around 230 °C before a final oxidative loss above 360 °C. CMC composite material (12GG-CMC) exhibited an 12% reduction in mass below 120 °C, underwent bulk decomposition at around 230 °C before a final oxidative loss above 560 °C. The denser composite frameworks have less available space for water. 12GG-HEC exhibits similar thermal stability but undergoes a more stepwise oxidative decomposition due to the presence of multiple components, while 12GG-CMC exhibits a final loss at much higher temperature. This could indicate greater stability of the residue material produced by bulk material decomposition in 12GG-CMC, but this requires further investigation. The DSC agrees that the native material has a higher thermal stability, with the melting and thermal degradation peaks appearing at similarly lower temperatures in both the composites (melting peaks: 12GG = 301.3 °C, 12GG-HEC = 285.8 °C, 12GG-CMC = 284.2 °C, thermal degradation: 12GG = 409.1 °C and 443.0 °C, 12GG-HEC = 380.3 °C and 409.1 °C, 12GG-CMC = 355.4.3 °C).

Expectedly, the addition of miracle gro shows similar effects across the board. All three materials show lower water retention and a reduction in thermal stability. All three materials start to decompose at 150 °C. This reduction is likely because miracle gro has a lower thermal

stability than the hydrogel, so the miracle gro incorporated in the structure of the material decomposes and causes structural degradation of the hydrogel in the process. The only major change observed in the DSC measurements is in the temperature of crystallisation, which exhibits a large reduction upon the addition of miracle gro for all samples. For GG12, the addition of miracle gro shifts Tc from 241.7 °C to 200.4 °C, for GG12-HEC the addition of miracle gro shifts Tc from 248.8 °C to 182.5 °C and for GG12-CMC the addition of miracle gro shifts Tc from 246.9 °C to 180.1 °C. In all cases, the final residue has a slightly higher mass than the material without miracle gro. This is likely due to some residue being formed from the decomposition of miracle gro.

Chapter 4: Release Studies on Nutrient-Embedded Composite Hydrogels

4.1 Ionic conductivity studies on GGH-composite hydrogels containing plant nutrients

Hydrogels are three-dimensional polymeric networks capable of retaining large amounts of water or biological fluids, making them highly suitable for applications in controlled nutrient release, drug delivery, and environmental remediation (257, 258). A critical aspect of understanding and optimizing the functionality of hydrogels lies in the precise characterization and monitoring of ion dynamics during both the synthesis and post-synthesis phases. This chapter outlines the analytical approaches employed to investigate the presence, release, and transport behaviour of ions in hydrogel matrices developed during this research.

To comprehensively monitor the ionic environment within and around the hydrogel systems, two complementary techniques were employed: (i) **ionic conductivity measurements** and (ii) **inductively coupled plasma-based spectroscopy**, including ICP-MS (Mass Spectrometry) and ICP-OES (Optical Emission Spectrometry). Ionic conductivity was used as a rapid, non-destructive, and real-time monitoring tool to evaluate the overall ionic strength of the hydrogel formulations over time. This method provided valuable insights into the monitor of ion diffusion and release behaviour under various experimental conditions.

To obtain detailed, element-specific, and quantitative data on individual ion species present in the hydrogel systems, ICP-MS and ICP-OES were used. These techniques enabled the detection of both major and trace elements with high sensitivity and accuracy. ICP-MS was particularly valuable for trace metal analysis due to its low detection limits, while ICP-OES allowed for the simultaneous measurement of multiple elements with robust throughput, making it suitable for routine monitoring of macro- and micronutrient profiles.

Together, these analytical methods provided a comprehensive framework for characterizing the behaviour of ions in hydrogel networks, offering both qualitative trends and quantitative precision. The integration of conductivity and ICP data was critical for correlating structural properties of the hydrogel with their functional performance in ion retention and release. This chapter presents key findings derived from the application of these techniques while the experimental methodologies and protocols employed are presented in Chapter 6.

4.1.1 Ionic conductivity studies on GGH

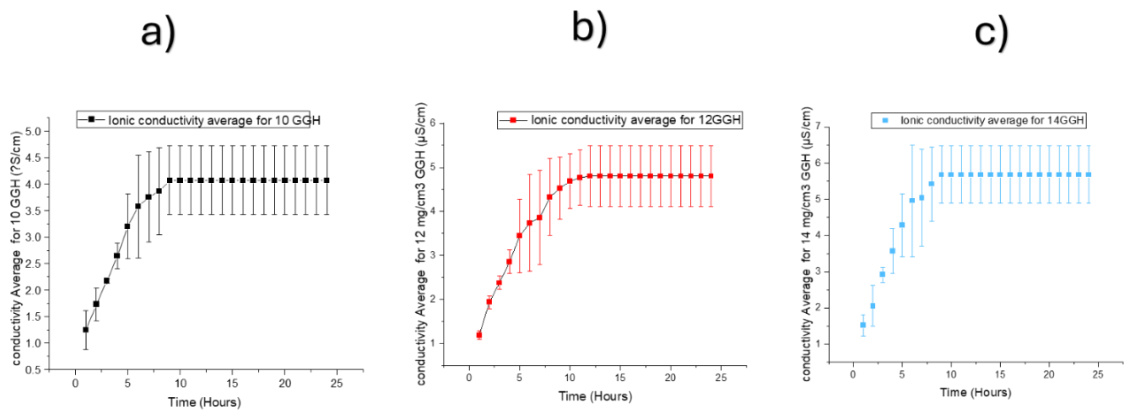

Figure 4.1: Ionic Conductivity Measurements of GGH Hydrogel Samples Over Time with Standard Deviation Error Bars at concentrations of a) 10 b) 12 and c) 14 mg/cm³.

Figure 4.1 illustrates the ionic conductivity profiles of Gellan Gum Hydrogel (GGH) samples at concentrations of a) 10, b) 12, and c) 14 mg/cm³, measured over time. Conductivity (in µS/cm) is plotted against time (in hours), with error bars representing the standard deviation from three replicates, indicating measurement reproducibility. The graph reveals that all hydrogel samples begin with relatively low conductivity values (~1.2–1.4 µS/cm) at the initial time point. Conductivity rises rapidly within the first 10 hours for all concentrations, with the 14 mg/cm³ gellan gum sample showing the highest conductivity (~5.7 µS/cm), followed by the 12 mg/cm³ (~4.8 µS/cm), and the 10 mg/cm³ sample reaching the lowest plateau (~4.0 µS/cm). After 10–12 hours, the conductivity levels off, indicating that the system has reached a state of equilibrium. Overall, the results suggest that higher gellan gum concentrations facilitate greater ion mobility or release, as reflected in the increased conductivity values, with the plateau phase representing a steady-state condition. The increase in conductivity in nutrient-free gels is attributed to the release of intrinsic counter-ions from the gellan gum network and enhanced ion mobility due to hydrogel swelling over time.

4.1.2 Ionic conductivity studies on GGH-dilute MG

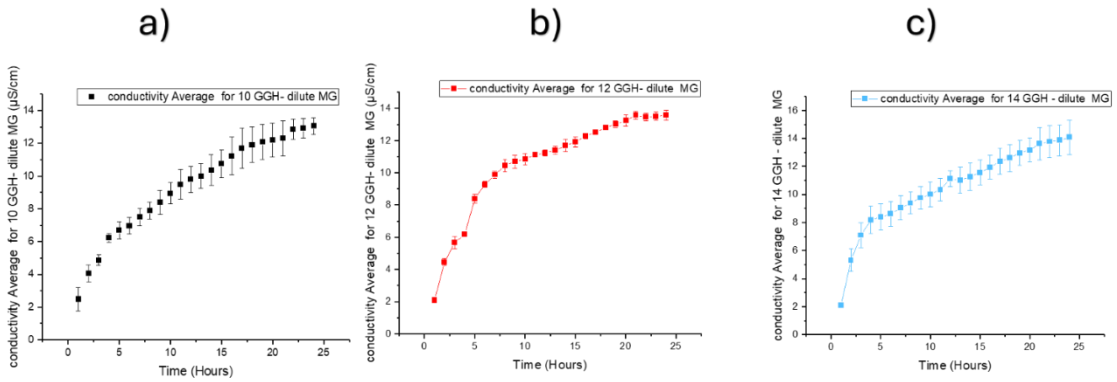

Figure 4.2: Ionic conductivity measurements of GGH-dilute MG hydrogel samples over time with standard deviation error bars at concentrations of a) 10 b) 12 and c) 14 mg/cm³.

Figure 4.2 displays the ionic conductivity profiles of Gellan Gum Hydrogels modified with diluted Miracle-Gro (30 mL of Miracle-Gro diluted in 1000 mL of distilled water) (GGH-MG) over time, assessed at three concentrations: (a) 10 mg/cm³ (black), (b) 12 mg/cm³ (red), and (c) 14 mg/cm³ (blue). The y-axis represents ionic conductivity in µS/cm, while the x-axis denotes time in hours. Error bars indicate standard deviations from three replicate measurements per time point, reflecting the precision and variability of the data.

The graph shows that higher concentrations of GGH lead to increased conductivity over time, with the 14 mg/cm³ sample exhibiting the fastest initial rise, followed by the 12 mg/cm³ and 10 mg/cm³ samples. Between 10 and 20 hours, conductivity continues to increase for all concentrations but at a slower rate, with the 14 mg/cm³ sample maintaining the highest values. After approximately 20 hours, all samples begin to plateau, suggesting the system is approaching equilibrium. While higher GGH concentrations generally result in greater conductivity, the gain becomes less significant at higher levels, indicating a possible saturation point or conductivity limit.

4.1.3 Ionic conductivity studies on GGH-concentrated MG

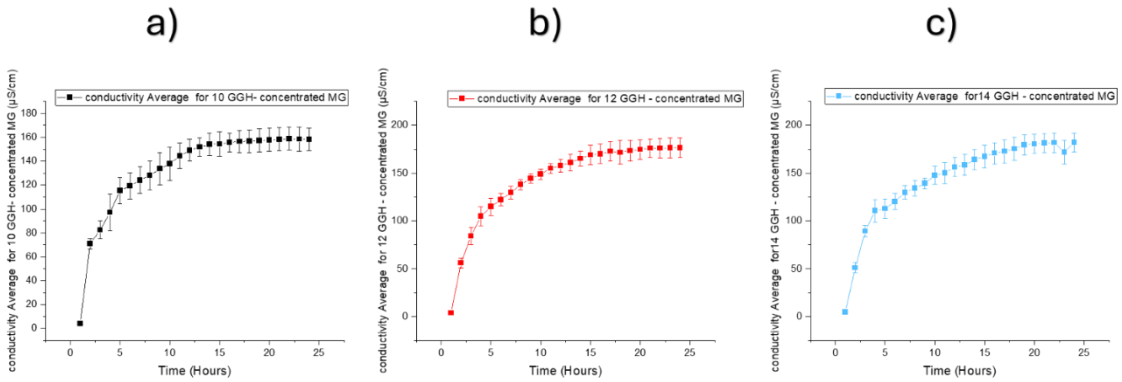

Figure 4.3: Ionic conductivity measurements of GGH-concentrated MG hydrogel samples over time with standard deviation error bars at concentrations of a) 10 b) 12 and c) 14 mg/cm³.

Figure 4.3 illustrates the ionic conductivity profiles of Gellan Gum Hydrogels supplemented with concentrated 1 mL of Miracle-Gro (MG) across three different concentrations (a) 10 mg/cm³ (black), (b) 12 mg/cm³ (red), and (c) 14 mg/cm³ (blue) measured over a 24-hour period. Conductivity (in µS/cm) is plotted on the y-axis against time (in hours) on the x-axis. Error bars represent standard deviations calculated from three replicate measurements, indicating the variability and reliability of the data. The ionic conductivity profiles reveal that all GGH-concentrated MG hydrogel samples exhibit a rapid initial rise in conductivity, indicating a burst release of ions from the hydrogel matrix into the surrounding solution. After approximately 6–8 hours, conductivity levels begin to plateau, suggesting that ion diffusion is approaching equilibrium and that most mobile ions have been released. Among the concentrations tested, the 12 mg/cm³ sample (red) consistently demonstrated the highest conductivity values, implying enhanced ion release likely due to an optimally structured matrix that facilitates ionic mobility. In contrast, the 10 mg/cm³ sample (black) showed a lower maximum conductivity, indicating more moderate release, while the 14 mg/cm³ sample (blue) exhibited a slower conductivity increase and lower final values, likely due to a denser network structure impeding ion diffusion. Overall, the results indicate that the 12 mg/cm³ concentration offers the most efficient ionic conductivity, whereas too low or too high concentrations reduce ion release performance.

4.1.4 Ionic conductivity studies on GGH-HEC and GGH-HEC-MG

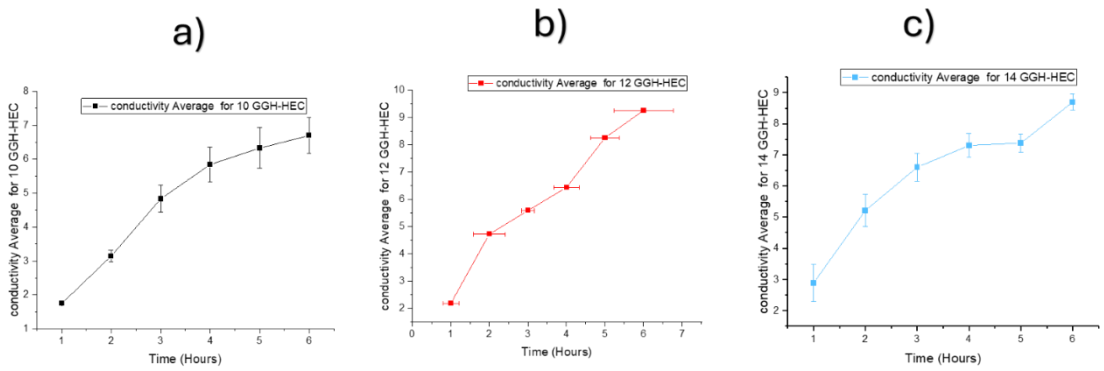

Figure 4.4: Ionic conductivity measurements of GGH-HEC hydrogel samples over time with standard deviation error bars at concentrations of a) 10 b) 12 and c) 14 mg/cm³ from 1 to 6 hours.

Figure 4.4 illustrates the ionic conductivity of GGH-HEC hydrogel samples over a 6-hour period, measured at three different concentrations: 10 mg/cm³ (black), 12 mg/cm³ (red), and 14 mg/cm³ (blue). The conductivity (µS/cm) is plotted against time (hours), with each data point representing the average of three measurements and accompanied by standard deviation error bars to reflect variability. Figure 4.4 illustrates that the ionic conductivity of GGH-HEC hydrogels increases progressively during the initial hours, indicating a gradual ion release from the hydrogel matrix into the surrounding medium. Among the concentrations tested, the 12 mg/cm³ sample (red) exhibits the highest conductivity throughout the experiment, suggesting it provides an optimal network structure that enhances ion mobility without excessive matrix compaction. In contrast, the 10 mg/cm³ sample (black) shows the lowest conductivity, likely due to limited ion content or weaker matrix interactions, while the 14 mg/cm³ sample (blue) demonstrates moderate conductivity, potentially affected by higher matrix density that restricts ion diffusion. Overall, the results suggest that an intermediate concentration (12 mg/cm³) offers the most efficient ion release profile and favourable conductivity performance within the 6-hour test period.

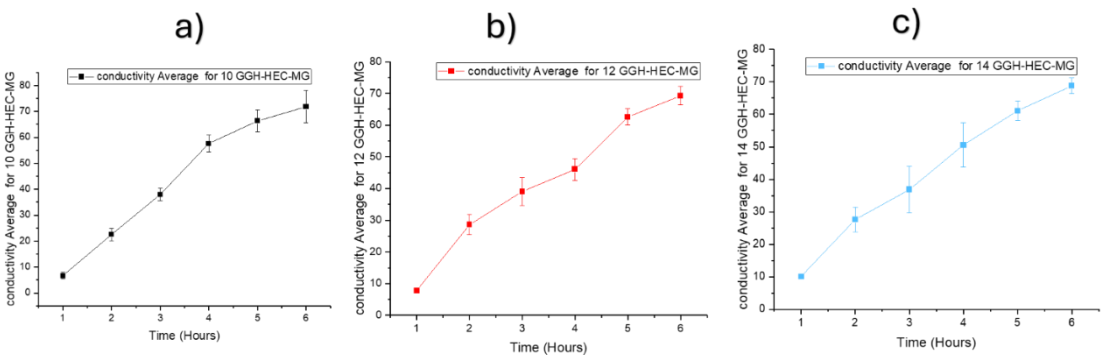

Figure 4.5: Ionic conductivity measurements of GGH-HEC-MG hydrogel samples over time with standard deviation error bars at concentrations of a) 10 b) 12 and c) 14 mg/cm³ from 1 to 6 hours.

Figure 4.5 shows the ionic conductivity profiles of GGH-HEC-MG hydrogel samples over a 6-hour period, measured at three different concentrations: 10, 12, and 14 mg/cm³. Each graph displays conductivity (µS/cm) on the y-axis versus time (hours) on the x-axis, with error bars indicating standard deviation from triplicate measurements, ensuring data reliability. All concentrations show a clear upward trend in conductivity, reflecting continuous ion release over time. While the 12 mg/cm³ sample exhibits higher ionic conductivity during the intermediate stages of the experiment, the 10 mg/cm³ sample shows comparable or slightly higher conductivity at later time points (after ~6 hours). This suggests that different concentrations may favour ion release at different stages, reflecting a balance between porosity, network density, and ion mobility. while the 14 mg/cm³ sample (blue) exhibits a slightly lower conductivity, likely due to increased matrix density restricting ion diffusion. These results indicate that the addition of Miracle-Gro to the GGH-HEC system enhances ionic release, with 12 mg/cm³ offering the most favourable ion transport characteristics within the monitored timeframe.

4.1.5 Ionic conductivity studies on GGH-CMC and GGH-CMC-MG

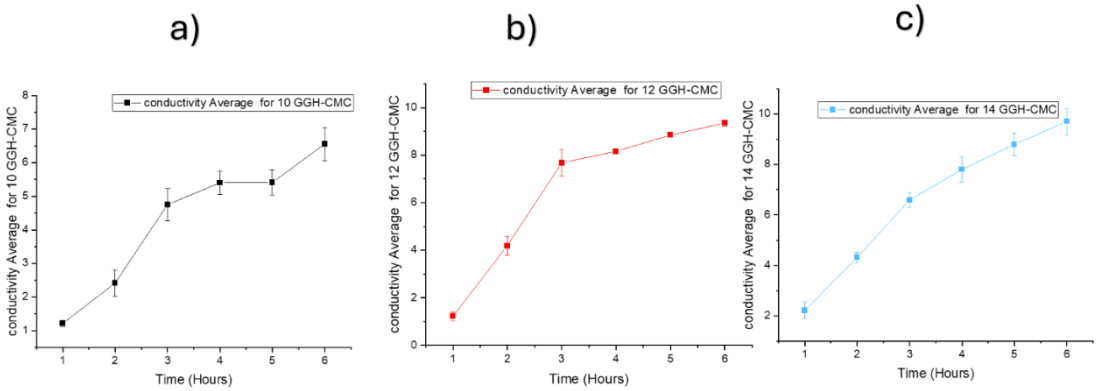

Figure 4.6: Ionic conductivity measurements of GGH-CMC hydrogel samples over time with standard deviation error bars at concentrations of a) 10 b) 12 and c) 14 mg/cm³ from 1 to 6 hours.

Figure 4.6 displays the ionic conductivity profiles of GGH-CMC hydrogel samples over a 6-hour period for three concentrations: 10, 12, and 14 mg/cm³. Conductivity (µS/cm) is plotted against time (hours), and each data point includes standard deviation error bars derived from triplicate measurements, ensuring statistical reliability. The data show that all samples experience a steady rise in conductivity over time, indicating continuous ion release from the GGH-CMC matrix. Within the GGH–CMC–MG system, the 12 mg/cm³ sample (red) exhibits the highest ionic conductivity throughout the measured timeframe, indicating enhanced ion mobility. The 14 mg/cm³ sample (blue) shows intermediate conductivity values, while the 10 mg/cm³ sample (black) consistently displays the lowest conductivity. The reduced conductivity at lower concentration may be associated with less developed conductive pathways, whereas increased matrix compaction at higher concentrations may limit ion diffusion.

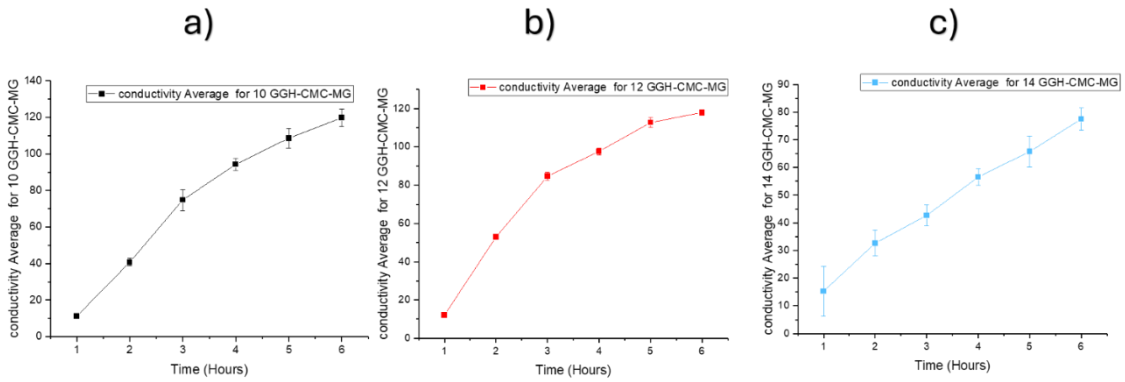

Figure 4.7: Ionic conductivity measurements of GGH-CMC-MG hydrogel samples over time with standard deviation error bars at concentrations of a) 10 b) 12 and c) 14 mg/cm³ from 1 to 6 hours.

Figure 4.7 illustrates the ionic conductivity behaviour of GGH-CMC-MG hydrogel samples over a 6-hour period at three different concentrations: 10 mg/cm³ (black), 12 mg/cm³ (red), and 14 mg/cm³ (blue). The y-axis represents ionic conductivity in µS/cm, while the x-axis shows time in hours. Each data point includes error bars that represent standard deviations based on three replicates per time point, providing a measure of consistency and variability. Obviously, all the samples which contain nutrients will have higher conductivity readings because we have been adding salts which ionize and hence during dialysis are released. Across all concentrations, the data show a general upward trend in conductivity, indicating ongoing ion diffusion from the hydrogel into the surrounding medium. Both the 10 mg/cm³ sample (black) and the 12 mg/cm³ sample (red) exhibit very similar ionic conductivity throughout the time course, suggesting that this concentration achieves an optimal balance, in this range, between nutrient loading and matrix porosity, which facilitates efficient ion release. The 14 mg/cm³ sample (blue) presents the lowest conductivity profile, likely due to excessive compaction of the matrix that limits ion movement. These results indicate that incorporating Miracle-Gro into GGH-CMC hydrogels enhances ion release most effectively at an intermediate concentration (12 mg/cm³).

4.2 Inductively coupled plasma studies on GGH-composite hydrogels containing plant nutrients; 0.5, 0.6. 0.7 GGH systems

The error bars in Fig. 4.8 and all of them were calculated from replicate measurements. The plotted values represent the mean, and the error bars show the standard deviation (SD), indicating variability between repeats. Both the mean and SD were calculated using Microsoft Excel (AVERAGE and STDEV.S functions), and the SD values were used directly to generate the error bars.

4.2.1 Inductively coupled plasma studies on 10 mg/cm^3 GGH in all conditions

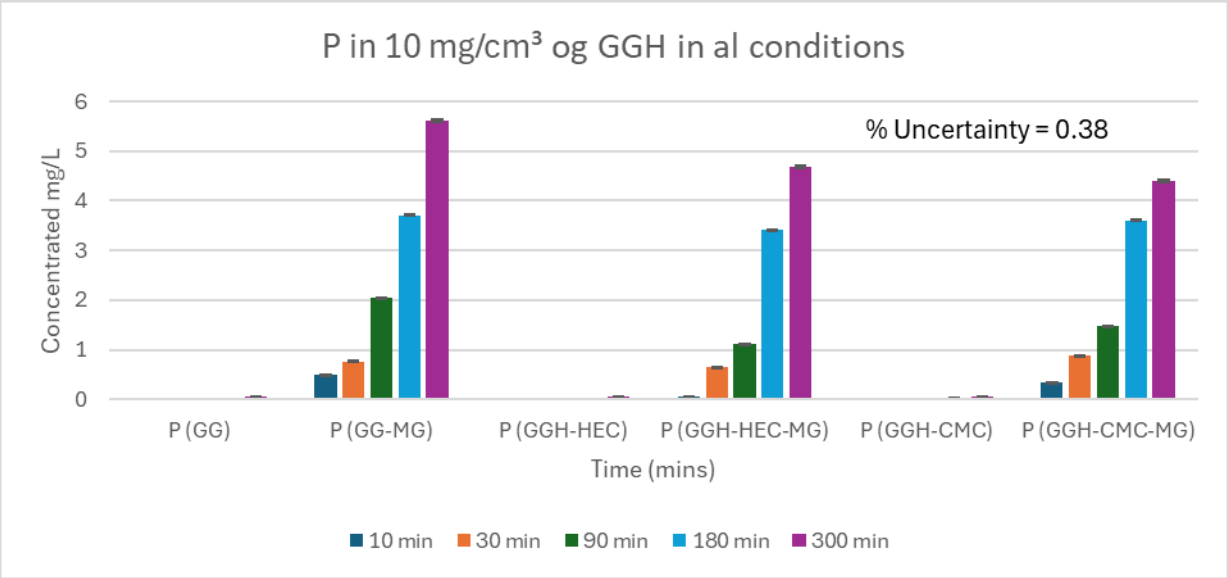

Figure 4.8: The image is a bar graph titled "P in 10 mg/cm³ GGH at all conditions", which presents the concentration of phosphorus (P) in mg/L over time across different sample conditions involving GGH.

The bar graph illustrates the phosphorus (P) concentrations over time in various 10 mg/cm³ GGH formulations under different conditions. Samples containing an added MG component specifically GGH-CMC-MG, GGH-HEC-MG, and GG-MG show a substantial and steady increase in phosphorus release, with GG-MG reaching the highest concentration of approximately 5.6 mg/L after 300 minutes. In comparison, the corresponding formulations without MG (GGH-CMC, GGH-HEC, and GG) exhibit minimal phosphorus release, with concentrations remaining near baseline even at extended time points. This trend clearly indicates that the addition of MG plays a critical role in enhancing phosphorus availability or mobilization from the GGH matrix over time.

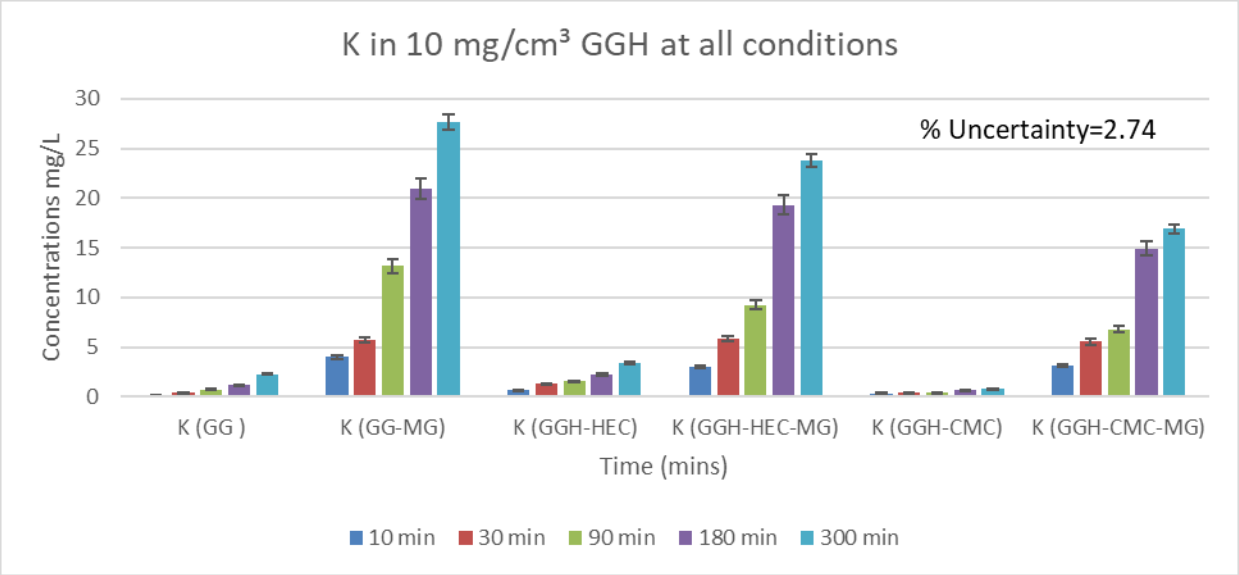

Figure 4.9: The image is a bar chart called "K in 10 mg/cm³ GGH at all conditions," showing the levels of potassium (K) in mg/L over time for different conditions of GGH samples.

The bar chart shows that GGH-based samples containing added MG (GGH-CMC-MG, GGH-HEC-MG, and GG-MG) exhibit significantly greater potassium release over time compared to their non-MG counterparts. Among them, GG-MG achieves the highest K concentration, nearing 28 mg/L at 300 minutes, followed by GGH-HEC-MG at approximately 24 mg/L, and GGH-CMC-MG at around 17 mg/L. In contrast, samples without MG release much lower amounts of potassium, all remaining well below 5 mg/L by the end of the observation period. All formulations demonstrate a gradual increase in K concentration over time, with the effect most pronounced in the MG groups. These findings highlight the critical role of added MG in facilitating or accelerating potassium mobilization from the GGH matrix, making it an essential component for enhancing nutrient delivery efficiency.

Figures 4.8 and 4.9 compare phosphorus (P) and potassium (K) release from various 10 mg/cm³ GGH-based formulations, emphasizing the effect of adding 1 mL of nutrient solution. The presence of the nutrient significantly enhances nutrient release, with GG-MG showing the highest levels of both P (~5.6 mg/L) and K (~27.6 mg/L) by 300 minutes. GGH-HEC-MGand GGH-CMC-MG also show strong performance, while formulations without MG release considerably lower amounts. Nutrient release in MG samples increase steadily over time, especially after 90 minutes, highlighting a time-dependent effect. Overall, the study shows that both the type of gel matrix and the presence of the nutrient solution are crucial for maximizing nutrient availability from GGH systems.

The differential release of elements from hydrogels, particularly the higher release of potassium (K) compared to phosphorus (P), can be attributed to several factors related to the

physicochemical properties of the elements and the structural characteristics of the hydrogels themselves. Firstly, the ionic nature of potassium allows it to interact more favourably with the hydrogel matrix. Potassium ions are generally smaller and more mobile than phosphate species (e.g. $H_2PO_4^-$ and HPO_4^{2-}), which are larger, multivalent ions, which tend to form larger, more complex structures, which are more capable of interacting with the hydrogel network. This mobility facilitates a higher diffusion rate of K through the hydrogel, leading to a more significant release compared to P. The release kinetics of ions from hydrogels are often governed by their size, charge, and the interactions they form with the polymer matrix. For instance, the swelling behaviour of hydrogels, which is crucial for drug release, is influenced by the ionic strength and the types of ions present. Potassium, being a monovalent cation, can effectively disrupt the hydrogen bonding and electrostatic interactions within the hydrogel, promoting swelling and enhancing the release rate of the encapsulated ions (110, 259).

Moreover, the structural characteristics of the hydrogel, such as pore size and crosslinking density, are likely to play a critical role in the release dynamics. Hydrogels with a higher crosslinking density may restrict the movement of larger ions like phosphorus, thereby limiting their release. Conversely, a lower crosslinking density can facilitate the release of smaller ions like potassium due to increased pore size and enhanced diffusion pathways (110, 260). The swelling ratio of the hydrogel also significantly affects the release profile; a higher swelling ratio generally correlates with increased release rates for smaller ions, as it allows for greater mobility within the hydrogel matrix (261). Additionally, the chemical interactions between the hydrogel and the released ions can further influence the release rates. For example, hydrogels that contain functional groups capable of forming specific interactions with potassium may enhance its release compared to phosphorus, which may not interact as favourably with the hydrogel matrix (262). The presence of water and the hydrophilicity of the hydrogel also contribute to the release mechanism, as water uptake can facilitate the dissolution and diffusion of ions from the hydrogel (263).

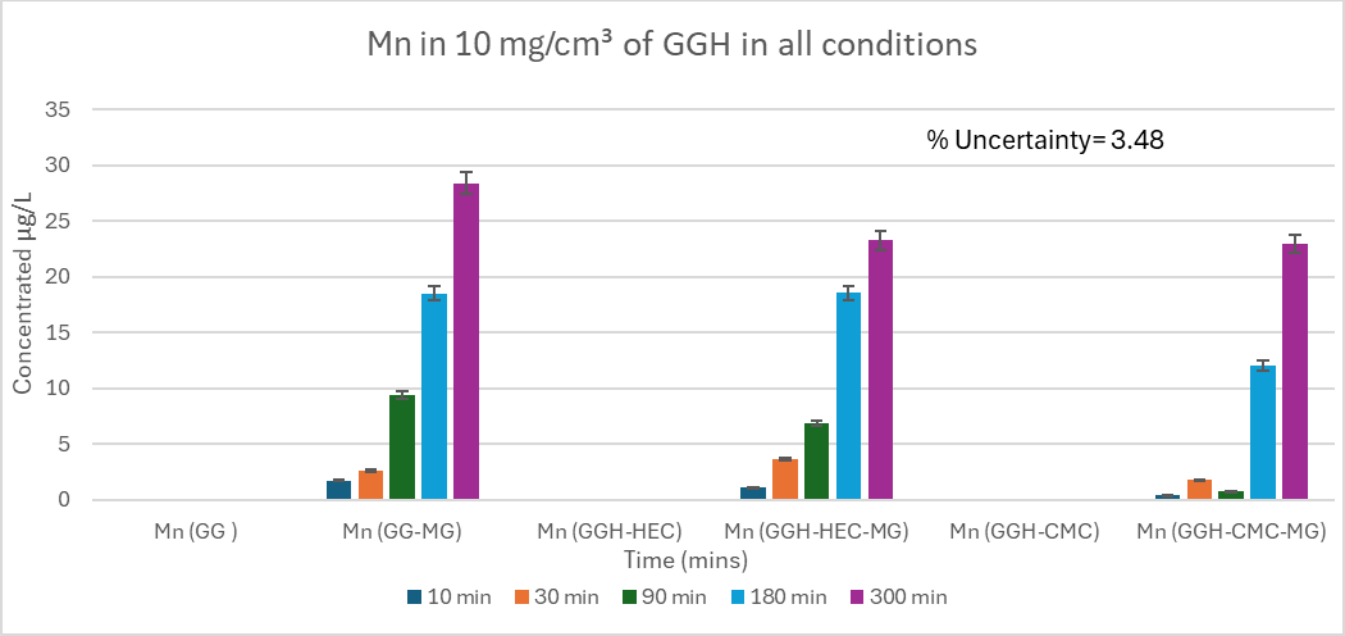

Figure 4.10: The image is a bar chart titled "Mn in 10 mg/cm³ of GGH in all conditions", which shows the concentration of manganese (Mn) over time for various GGH-based formulations under different treatments.

The chart shows that Mn (GG-MG) exhibits the highest manganese release, reaching around 28 mg/L at 300 minutes. This is followed by GGH-HEC-MG and GGH-CMC-MG, both of which exceed 20 mg/L by the same time point. In contrast, the non-N samples (GG, GGH-HEC, GGH-CMC) show significantly lower Mn release, remaining mostly below 6 mg/L throughout the duration. All MG samples display a strong upward trend in Mn concentration over time, with especially sharp increases observed between 90 and 300 minutes. Among all formulations, GGH-CMC without MG shows the lowest Mn release. These results clearly demonstrate that the addition of MG greatly enhances manganese mobilisation, with GG-MG being the most effective, highlighting the critical role of nutrient enhancers in improving Mn release from GGH systems.

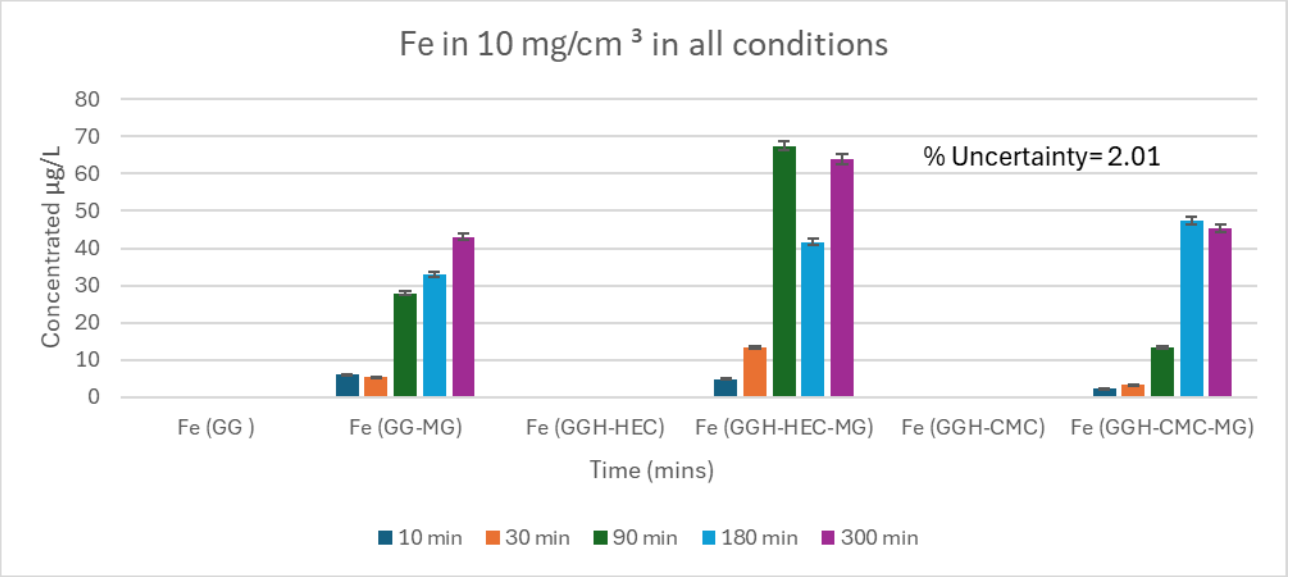

Figure 4.11: The image is a bar chart titled "Fe in 10 mg/cm³ of GGH in all conditions", showing the concentration of iron (Fe) in µg/L over time for various GGH-based formulations. The chart illustrates how Fe concentration changes at different time intervals and under different sample conditions.

The bar chart illustrates iron (Fe) release over time in various 10 mg/cm³ GGH-based formulations under different conditions. The highest Fe release is observed in the GGH-HEC - MG sample, peaking at around 66 µg/L at 90 minutes and maintaining a high concentration (~63 µg/L) at 300 minutes. GGH-CMC-MG and GG-MG also demonstrate substantial Fe release, reaching approximately 47 µg/L and 43 µg/L, respectively, by the end of the observation period. In contrast, non-N samples (GG, GGH-HEC, and GGH-CMC) show minimal Fe release, mostly remaining under 10 µg/L. A clear trend of increasing Fe concentration is evident in the MG samples, particularly between 90 and 180 minutes. These findings highlight the crucial role of nutrient enhancement in promoting effective Fe mobilisation from GGH systems, with GGH-HEC-MG proving to be the most effective matrix for iron delivery. Some inconsistent values were observed in the iron concentration, particularly in the GGH-CMC-MG sample at 300 minutes, which are likely due to analytical error during the ICP measurements. Nevertheless, the overall trend clearly confirms the significant role of nutrient addition in enhancing iron release from the hydrogel

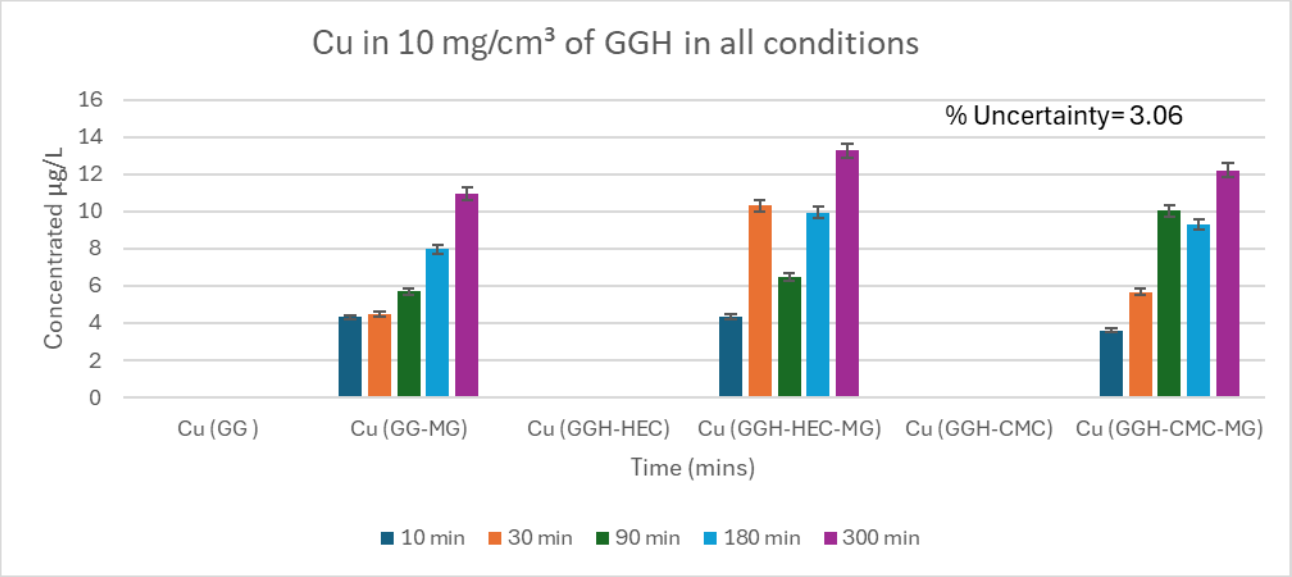

Figure 4.12: The image is a bar chart titled "Cu in 10 mg/cm³ of GGH in all conditions", which presents the copper (Cu) concentration in µg/L over time across different GGH-based formulations.

The chart shows that copper (Cu) release is highest in the GGH-HEC + N sample, reaching approximately 13 µg/L at 300 minutes. This is followed by GGH-CMC + N and GG + N, which reach just under 12 µg/L and around 11 µg/L, respectively. In contrast, samples without added nutrients—GG, GGH-HEC, and GGH-CMC—exhibit much lower Cu concentrations, typically between 3 and 6 µg/L, with little variation over time. A consistent upward trend in Cu release is observed in the +N formulations, especially after 90 minutes, while non-N samples show relatively flat profiles, indicating limited mobilization. These results highlight the significant role of nutrient enhancement in boosting copper release, with GGH-HEC-MG emerging as the most effective matrix. The release pattern also suggests a time-dependent behaviour, particularly in nutrient-enhanced systems.

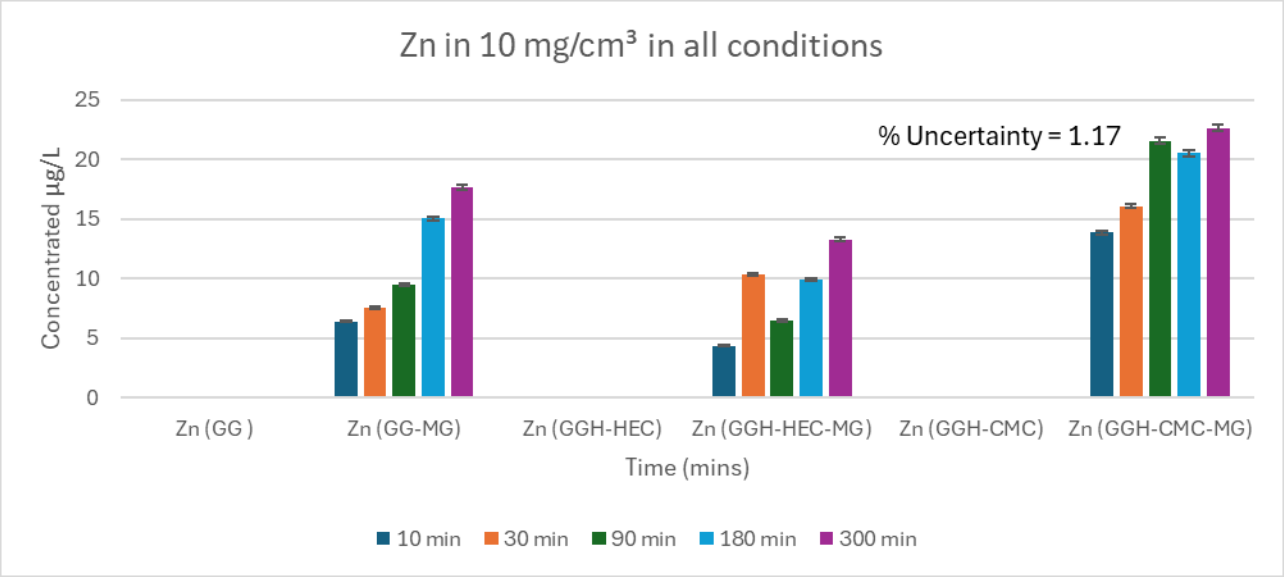

Figure 4.13: The image is a bar chart titled "Zn in 10 mg/cm³ of GGH in all conditions", which shows the zinc (Zn) concentration in µg/L over time for various GGH-based formulations.

The chart shows that zinc (Zn) release is highest in the GGH-CMC + N formulation, reaching approximately 23 µg/L at 300 minutes, with a steady, time-dependent increase. Zn (GG + N) and Zn (GGH-HEC + N) also demonstrate elevated levels, peaking at around 17 µg/L and 13 µg/L, respectively. In contrast, non-N samples (GG, GGH-HEC, and GGH-CMC) exhibit consistently lower Zn concentrations, generally staying below 10 µg/L, with Zn (GG) showing the least variation over time. All formulations with added nutrient solution (+N) show a clear and consistent upward trend in Zn release, highlighting the enhancing effect of the nutrient addition. Among all, GGH-CMC + N stands out as the most effective for sustained zinc release, underscoring the importance of both nutrient enhancement and formulation type in maximizing Zn availability.

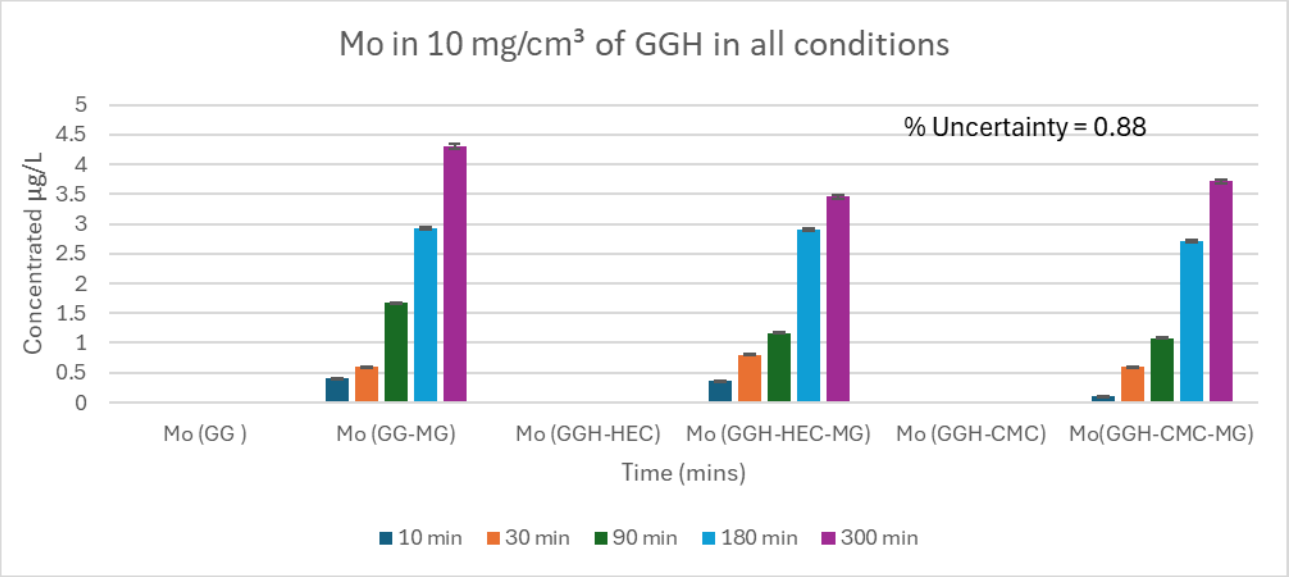

Figure 4.14: The image is a bar chart titled "Mo in 10 mg/cm³ of GGH in all conditions", which shows the (Mo) concentration in µg/L over time for various GGH-based formulations.

The chart demonstrates that the addition of a nutrient solution (MG) significantly boosts molybdenum (Mo) release across all GGH formulations. Mo (GG-MG) exhibits the highest release, reaching approximately 4.3 µg/L by 300 minutes, followed closely by Mo (GGH-HEC -MG) and Mo (GGH-CMC-MG), both exceeding 3.5 µg/L. In contrast, the non-MG samples (GG, GGH-HEC, and GGH-CMC) show minimal Mo release, consistently remaining below 1 µg/L throughout the duration. All MG formulations display a strong, time-dependent increase in Mo concentration, particularly between 90 and 300 minutes, while non-MG samples remain largely unchanged. These findings highlight the critical role of nutrient enhancement in facilitating effective Mo mobilisation in GGH systems.

4.2.2 Inductively coupled plasma studies on 12 mg/cm³ GGH in all conditions

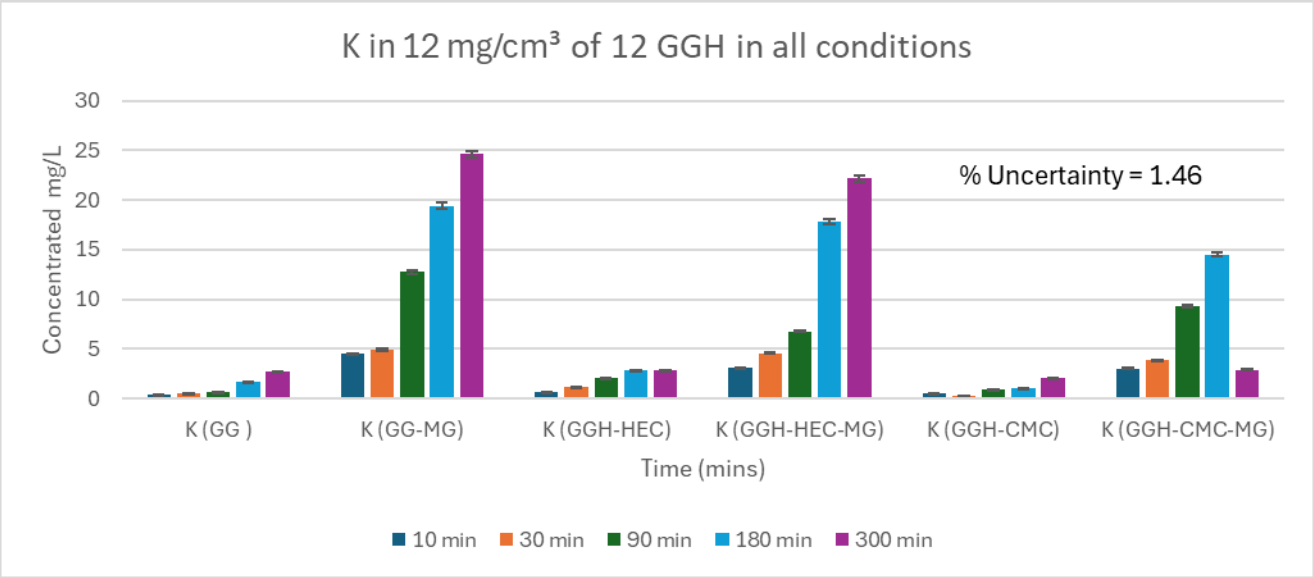

Figure 4.15: The image is a bar chart titled "K in 12 mg/cm³ GGH at all conditions", displaying the concentration of potassium (K) in mg/L across different sample conditions over various time intervals.

Figure 4.15 presents a bar chart showing potassium (K) release from various 12 mg/cm³ gellan gum hydrogel (GGH) formulations over time. Nutrient-loaded samples (MG) demonstrate significantly higher K concentrations compared to non-nutrient counterparts, with GG-MG reaching the highest level (~25 mg/L at 300 minutes), followed by GGH-HEC-MG and GGH-CMC-MG, both exhibiting strong sustained release. In contrast, nutrient-free samples such as GG, GGH-HEC, and GGH-CMC show minimal potassium release, generally remaining below 5 mg/L. Potassium concentration increases over time in all nutrient-loaded samples, highlighting the effectiveness of nutrient incorporation in promoting ion diffusion. Overall, the data indicate that nutrient addition, particularly at the 12 mg/cm³ concentration, significantly enhances potassium release, with GG-MG and GGH-HEC-MG formulations showing the most efficient performance. Some inconsistent values were observed in the K concentration, particularly in the GGH-CMC-MG sample at 300 minutes, which are likely due to analytical error during the ICP measurements. Nevertheless, the overall trend clearly confirms the significant role of nutrient addition in enhancing iron release from the hydrogel.

The data indicates that phosphorus (P) release is minimal in all samples lacking "N," with P (GG), P (GGH-HEC), and P (GGH-CMC) showing negligible to very low concentrations throughout the time points. In contrast, the addition of "N" significantly enhances P release across all material types. P (GG + N) exhibits the highest release, reaching approximately 5.2 mg/L at 300 minutes, followed by P (GGH-HEC + N) at around 4.3 mg/L. P (GGH-CMC + N) also shows a notable increase, peaking at about 3.6 mg/L at 180 minutes before slightly declining at 300 minutes. Overall, the presence of "N" plays a crucial role in improving phosphorus availability, with peak concentrations generally observed at 300 minutes, except for the GGH-CMC + N condition, which peaks earlier.

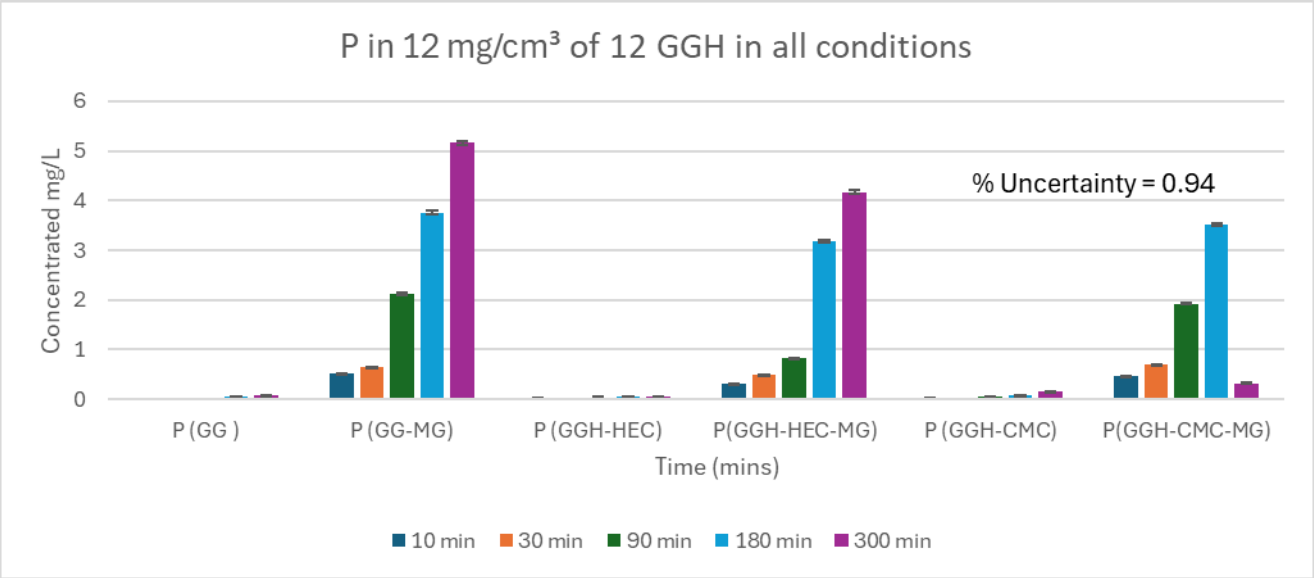

Figure 4.16: The image is a bar chart titled "P in 12 mg/cm³ GGH at all conditions", displaying the concentration of potassium (P) in mg/L across different sample conditions over various time intervals.

Figure 4.16 displays a bar chart showing phosphorus (P) release profiles from various gellan gum hydrogel (GGH) formulations at a concentration of 12 mg/cm³ across multiple time intervals. Nutrient-enriched samples (MG) show significantly higher phosphorus concentrations compared to non-nutrient variants. The GG-MG sample reaches the highest phosphorus level (~5.1 mg/L at 300 minutes), followed closely by GGH-HEC-MG (~4.2 mg/L) and GGH-CMC-MG (~3.8 mg/L), all showing a steady increase over time. In contrast,

non-nutrient samples (GG, GGH-HEC, GGH-CMC) exhibit very low phosphorus release, remaining below 0.5 mg/L. These results clearly demonstrate that nutrient loading greatly enhances phosphorus delivery, with GG-MGand GGH-HEC-MG offering the most efficient sustained release over time. Some inconsistent values were observed in the P concentration, particularly in the GGH-CMC-MG sample at 300 minutes, which are likely due to analytical error during the ICP measurements. Nevertheless, the overall trend clearly confirms the significant role of nutrient addition in enhancing iron release from the hydrogel.

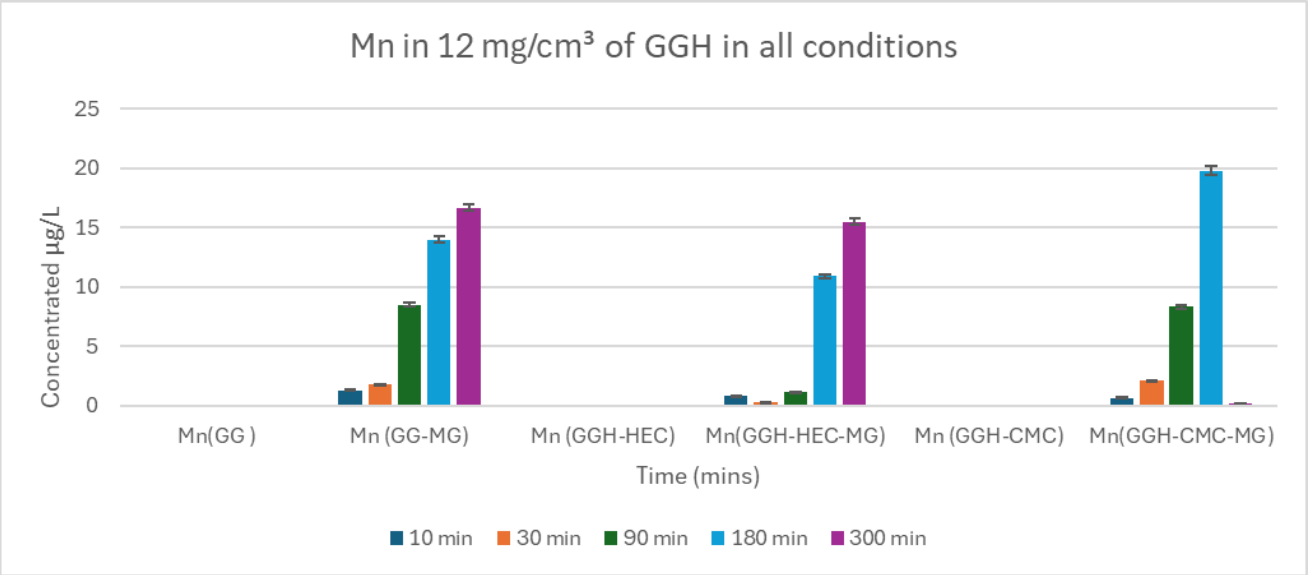

Figure 4.17: The bar chart titled "Mn in 12 mg/cm³ of GGH at all conditions" shows manganese (Mn) concentrations (in µg/L) across various material conditions and time intervals.

Mn release is minimal in Mn (GG), Mn (GGH-HEC), and Mn (GGH-CMC) conditions throughout the time range. However, the addition of MG significantly enhances Mn release. Mn (GG-MG) and Mn (GGH-HEC-MG) exhibit a steady time-dependent increase, peaking at around 17 µg/L and 16 µg/L respectively at 300 minutes. Notably, Mn (GGH-CMC-MG) shows a sharp rise, peaking at 20 µg/L at 180 minutes, then dropping at 300 minutes. Overall, the presence of MG greatly increases manganese availability, with peak values typically occurring at 300 minutes, except for GGH-CMC-MG, which peaks earlier. This unexpected decrease may reflect experimental or analytical variability, and therefore should be interpreted with caution.

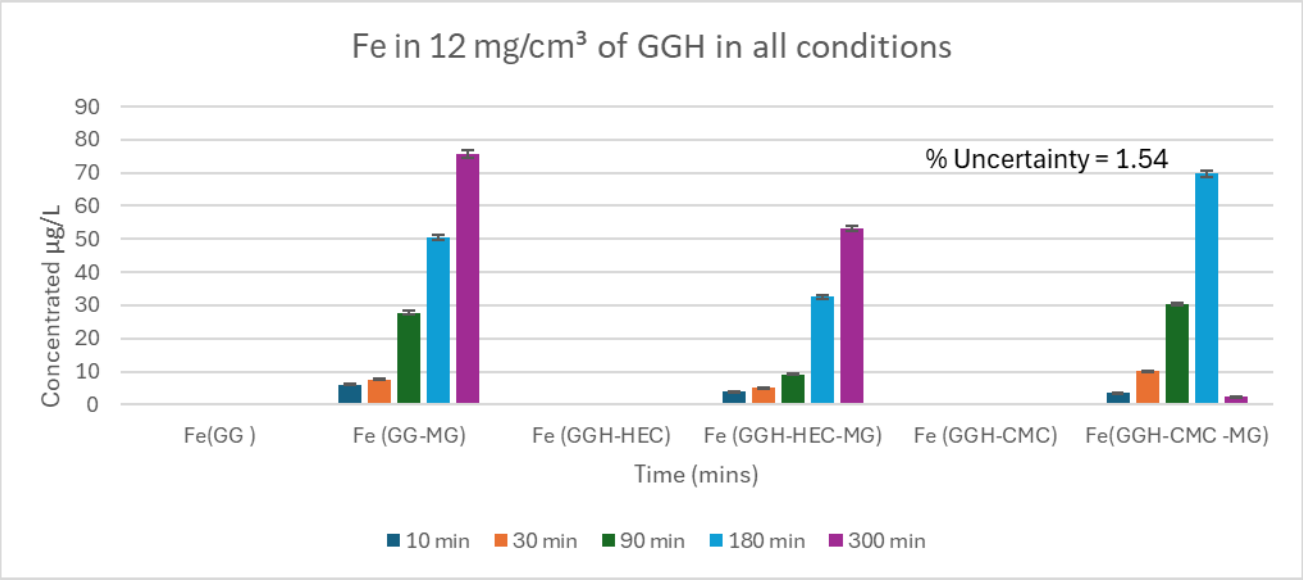

Figure 4.18: The bar chart titled "Fe in 12 mg/cm³ of GGH at all conditions" presents iron (Fe) concentrations (in µg/L) under different sample conditions across time intervals.

Iron release is minimal in Fe (GG), Fe (GGH-HEC), and Fe (GGH-CMC), with very low values throughout all time points. In contrast, the presence of "N" dramatically increases Fe release. Fe (GG-MG) shows a consistent rise, peaking at approximately 75 µg/L at 300 minutes, while Fe (GGH-HEC-MG) reaches around 53 µg/L at the same time. Fe (GGH-CMC-MG) displays a distinctive trend, with a sharp increase peaking at about 70 µg/L at 180 minutes, followed by a significant drop at 300 minutes. Overall, the addition of "MG" leads to a substantial increase in Fe availability, with peak levels generally observed at 300 minutes, except for GGH-CMC-MG, which peaks earlier at 180 minutes. Some inconsistent values were observed in the Fe concentration, particularly in the GGH-CMC-MG sample at 300 minutes, which are likely due to analytical error during the ICP measurements. Nevertheless, the overall trend clearly confirms the significant role of nutrient addition in enhancing iron release from the hydrogel.

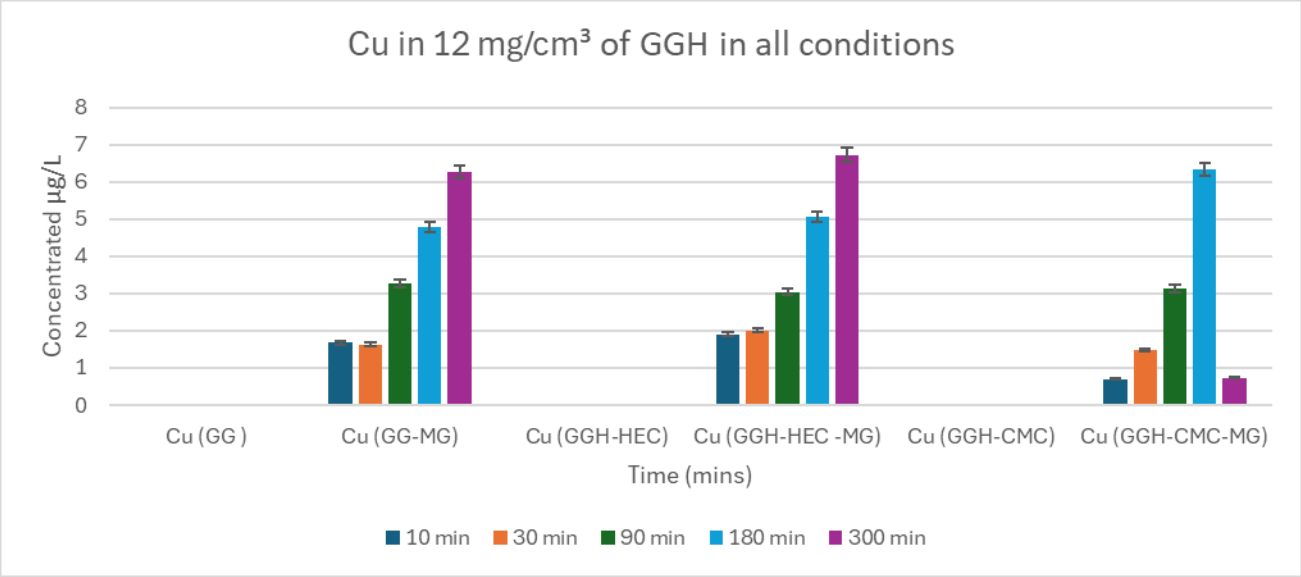

Figure 4.19: The bar chart titled "Cu in 12 mg/cm³ of GGH at all conditions" illustrates copper (Cu) concentrations (in µg/L) across various material conditions and time points.

The figure illustrates the time-dependent release of copper (Cu) from different GGH-based hydrogel formulations at a concentration of 12 mg/cm³. Hydrogels without MG (GG, GGH-HEC, and GGH-CMC) show negligible Cu release throughout the experiment, indicating strong metal retention within the matrix. In contrast, the inclusion of MG significantly enhances Cu release, with GG-MG and GGH-HEC-MG exhibiting a steady increase in Cu concentration over time, reaching their highest values at 300 minutes. The GGH-CMC-MG formulation shows increased release up to 180 minutes followed by a decrease at 300 minutes, which should be interpreted with caution as it may reflect experimental or analytical variability rather than true release behaviour. Overall, the results highlight the critical role of MG and hydrogel composition in controlling Cu release from GGH-based systems.

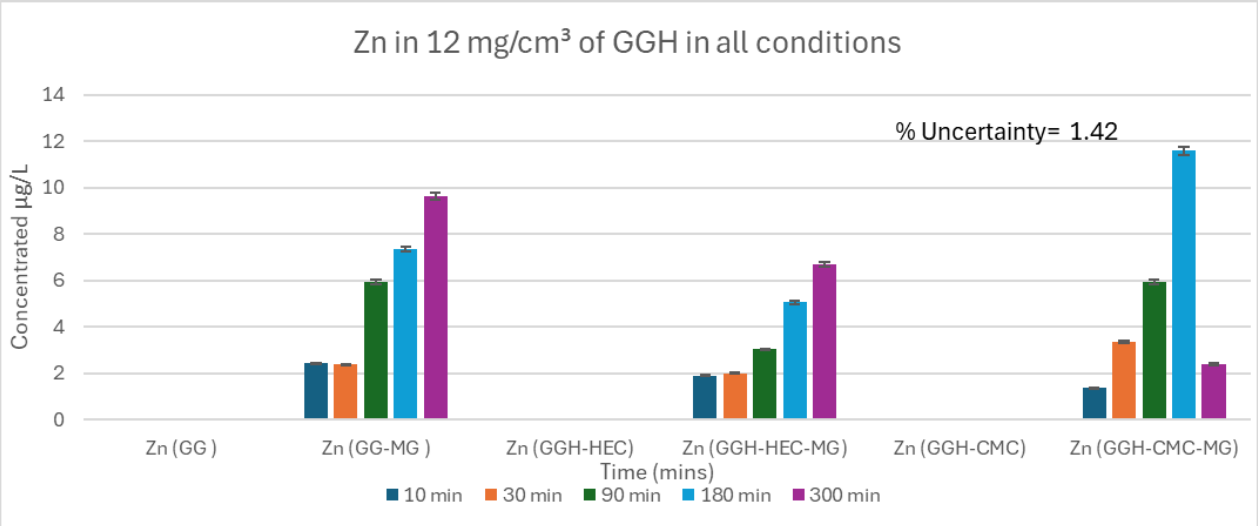

Figure 4.20: The bar chart titled "Zn in 12 mg/cm³ of GGH at all conditions" displays zinc (Zn) concentrations (in µg/L) across different material conditions over time.

Zn (GG), Zn (GGH-HEC), and Zn (GGH-CMC), which were formulated without MG and therefore do not contain Zn, exhibit negligible and nearly constant concentrations across all time points and should not be interpreted as Zn release. In contrast, the addition of "MG" substantially increases Zn release, as seen in Zn (GG-MG), which rises steadily to nearly 10 µg/L at 300 minutes. Similarly, Zn (GGH-HEC-MG) shows a progressive increase, reaching around 7 µg/L at 300 minutes. The most striking release occurs in Zn (GGH-CMC-MG), which peaks sharply at ~12 µg/L at 180 minutes before dropping significantly by 300 minutes. Overall, the presence of "MG" enhances Zn availability in all samples, with peak concentrations typically occurring between 180 and 300 minutes depending on the formulation. The observed decrease in zinc concentration of the GGH-CMC-MG sample at 300 minutes is likely due to experimental variation or analytical uncertainty, so this result should be interpreted with caution.

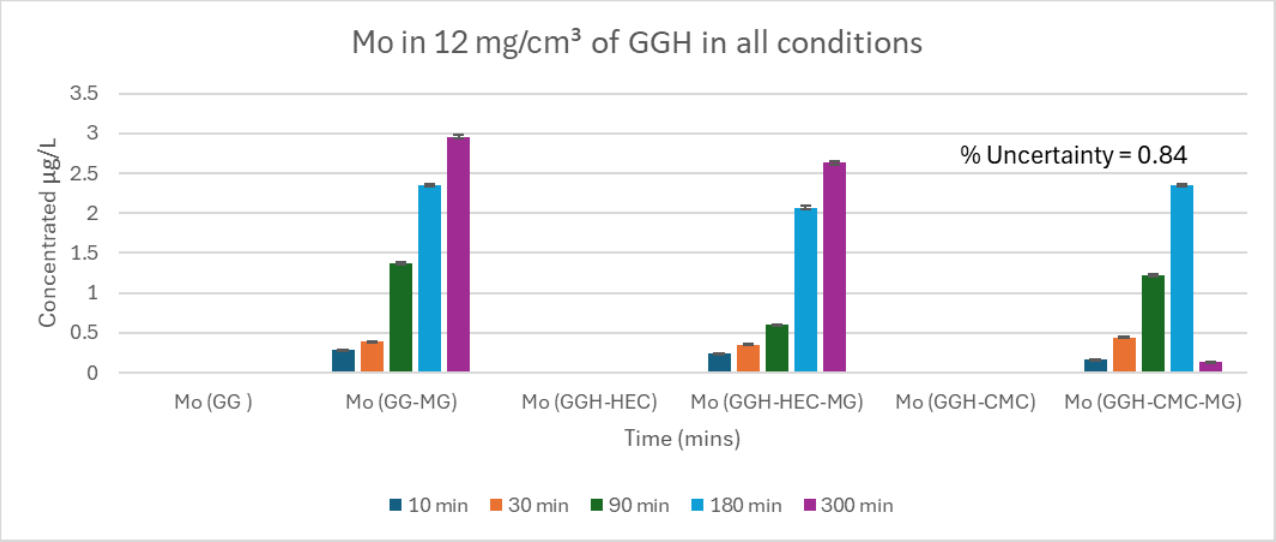

Figure 4.21: The bar chart titled "Mo in 12 mg/cm³ of GGH at all conditions" illustrates molybdenum (Mo) concentrations (in µg/L) across different sample types over a range of time intervals.

The figure illustrates the time-dependent release of molybdenum (Mo) from different GGH-based hydrogel formulations at a loading of 12 mg/cm³, with concentrations measured in µg/L.

Hydrogels without MG (Mo (GG), Mo (GGH-HEC), and Mo (GGH-CMC)) show negligible Mo concentrations at all time points, indicating minimal or no Mo release from these matrices. In contrast, formulations containing MG exhibit a clear increase in Mo concentration with time. Mo (GG-MG) shows the highest Mo release, increasing steadily and reaching approximately 3.0 µg/L at 300 minutes. Similarly, Mo (GGH-HEC-MG) demonstrates a time-dependent increase, though at slightly lower levels than GG-MG. Mo (GGH-CMC-MG) also shows increasing Mo concentration up to 180 minutes, followed by a marked decrease at 300 minutes. This late-stage decline should be interpreted with caution and is likely attributable to experimental or analytical variability rather than a true change in Mo release behaviour. Overall, the results indicate that MG plays a key role in enabling Mo release, while the specific polymer composition influences the magnitude and temporal profile of Mo availability.

4.2.3 Ionically coupled plasma studies on 14 mg/cm^3 GGH in all conditions.

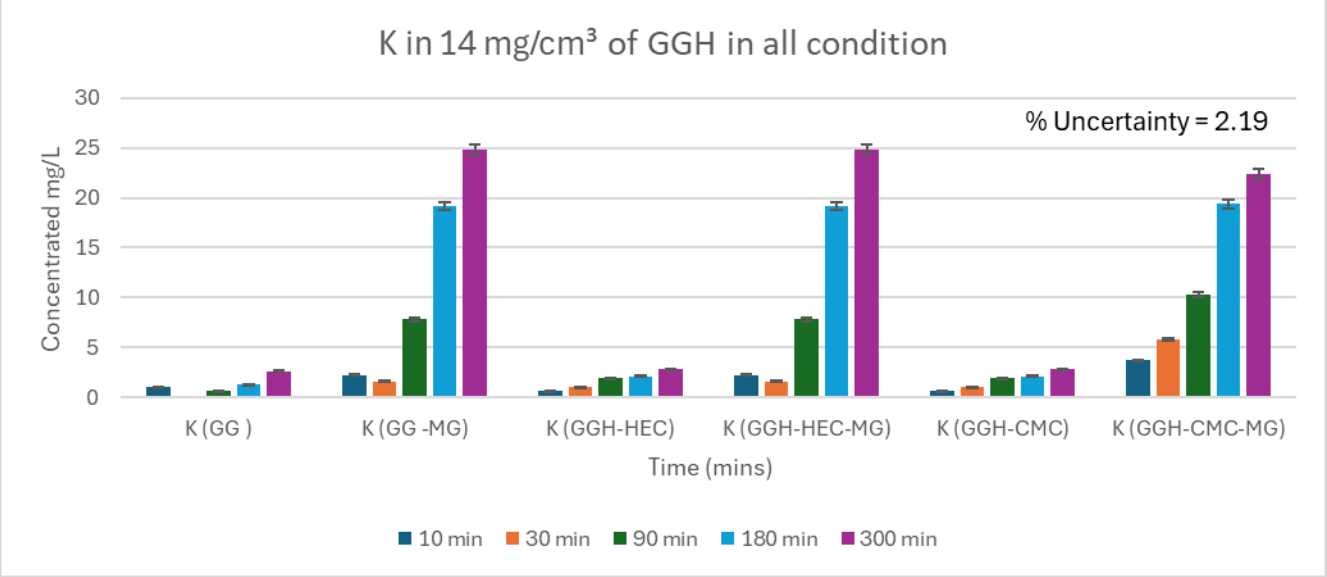

Figure 4.22: The bar chart titled "K in 14 mg/cm³ of GGH at all conditions" displays potassium (K) concentrations (in µg/L) across various material conditions and time intervals.

Potassium release is minimal in K (GG), remaining under 3 µg/L across all time points. The addition of "N" significantly increases K release in all formulations. K (GG-MG) and K (GGH-HEC-MG) both show strong time-dependent increases, peaking at 25 µg/L at 300 minutes. K (GGH-CMC-MG) follows a similar pattern, reaching about 23 µg/L at 300 minutes. Without "MG," K (GGH-HEC) and K (GGH-CMC) exhibit low to moderate release, never exceeding 6 µg/L. Overall, "MG" greatly enhances potassium availability, with all "MG" samples

showing steep increases and peaking at 300 minutes, indicating a clear time- and treatment-dependent release pattern.

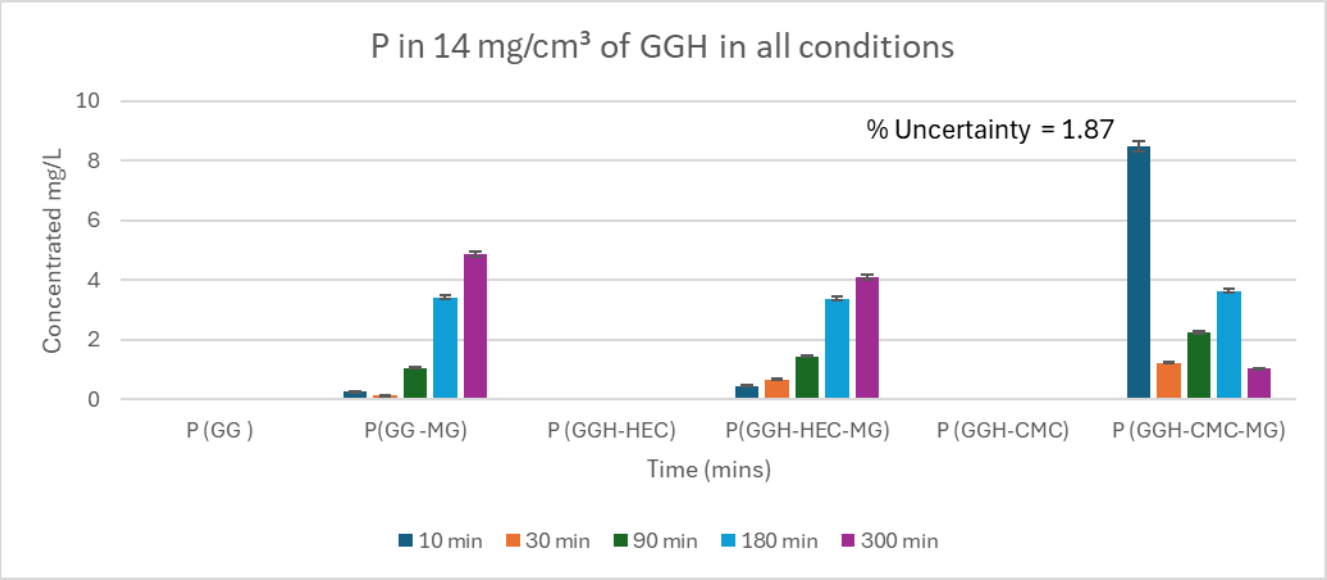

Figure 4.23: The bar chart titled "P in 14 mg/cm³ of GGH at all conditions" shows phosphorus (P) concentrations (in µg/L) across various material conditions and over time.

The figure presents the time-dependent release of phosphorus (P) from different GGH-based hydrogel formulations at a loading of 14 mg/cm³, with concentrations reported in mg/L. Formulations without MG (P (GG), P (GGH-HEC), and P (GGH-CMC)) show negligible phosphorus concentrations across all time points, indicating minimal or no P release from these hydrogels. In contrast, the incorporation of MG results in a pronounced increase in phosphorus release. P (GG-MG) and P (GGH-HEC-MG) exhibit steady, time-dependent increases, reaching approximately 4–5 mg/L by 300 minutes. The P (GGH-CMC-MG) formulation shows a distinct behaviour, with a very high concentration observed at 10 minutes, followed by lower values at later time points. This atypical early peak suggests rapid initial release and/or experimental variability and should be interpreted with caution. Overall, the data demonstrate that MG plays a critical role in enabling phosphorus release, while the polymer composition strongly influences the release profile and temporal behaviour.

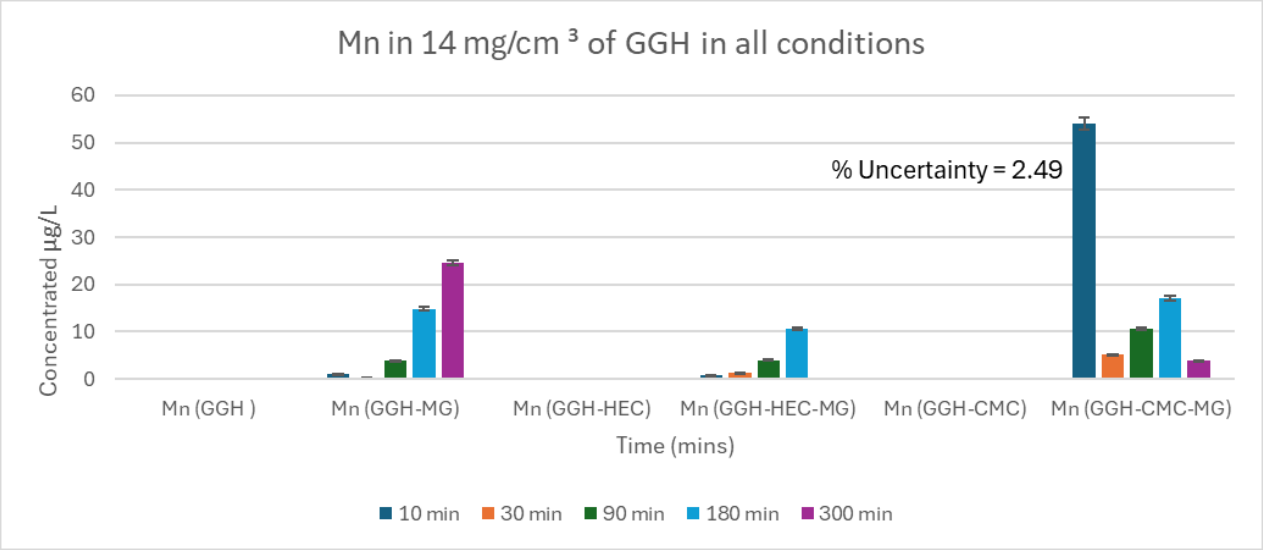

Figure 4.24: The bar chart titled "Mn in 14 mg/cm³ of GGH at all conditions" illustrates manganese (Mn) concentrations (in µg/L) across various material conditions over different time intervals.

The figure illustrates the time-dependent release of manganese (Mn) from different GGH-based hydrogel formulations at a loading of 14 mg/cm³, with Mn concentrations reported in µg/L. Formulations without MG (Mn (GGH), Mn (GGH-HEC), and Mn (GGH-CMC)) show negligible Mn concentrations across all time points, indicating minimal or no Mn release from these hydrogels. In contrast, the incorporation of MG leads to a substantial increase in Mn release. Mn (GGH-MG) exhibits a clear, time-dependent rise, reaching approximately 25 µg/L at 300 minutes, while Mn (GGH-HEC-MG) shows a more moderate increase, peaking at around 10 µg/L. The most pronounced release is observed for Mn (GGH-CMC-MG), which displays a very high initial concentration at 10 minutes, followed by decreasing values at later times; this atypical early peak should be interpreted with caution, as it may reflect rapid initial release and/or experimental variability rather than sustained release behaviour. Overall, the data highlight the critical role of MG in enabling Mn availability, with the polymer composition strongly influencing the magnitude and temporal profile of Mn release.

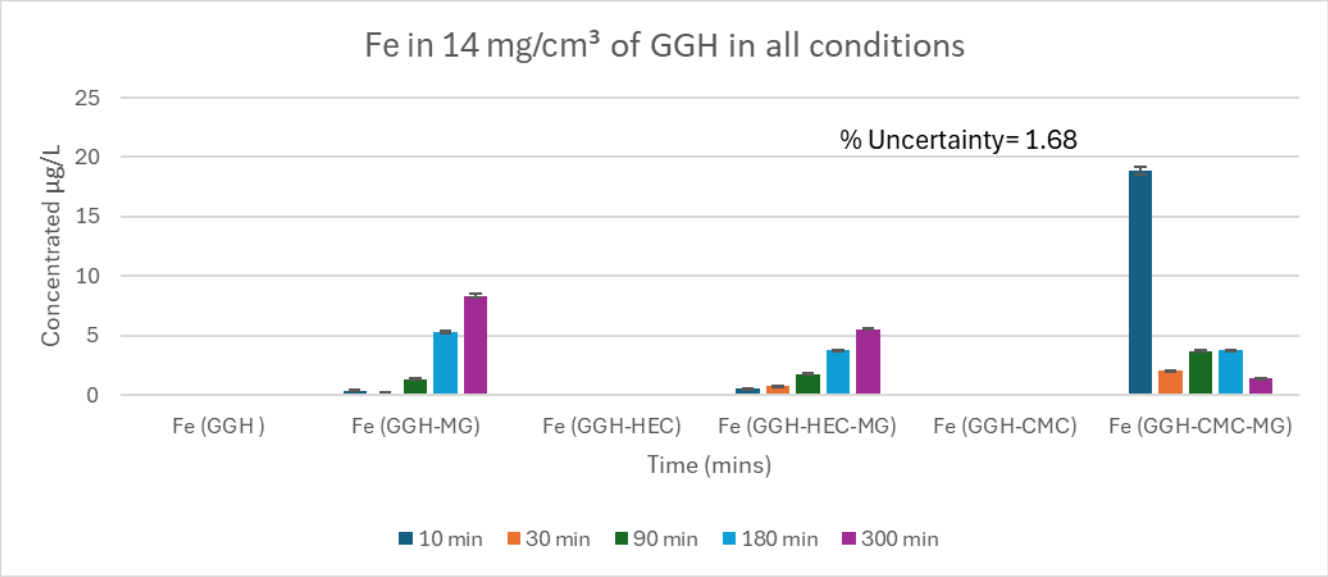

Figure 4.25: The bar chart titled "Fe in 14 mg/cm³ of GGH at all conditions" presents iron (Fe) concentrations (in µg/L) measured at different time points across various GGH formulations.

The figure shows the time-dependent release of iron (Fe) from different GGH-based hydrogel formulations at a loading of 14 mg/cm³, with Fe concentrations measured in µg/L.

Formulations without MG (Fe (GGH), Fe (GGH-HEC), and Fe (GGH-CMC)) exhibit negligible Fe concentrations across all time points, indicating minimal or no Fe release from these hydrogels. In contrast, the addition of MG results in a clear enhancement of Fe release. Fe (GGH-MG) shows a steady, time-dependent increase, reaching approximately 8–9 µg/L at 300 minutes, while Fe (GGH-HEC-MG) displays a more moderate increase, peaking at around 5–6 µg/L. The Fe (GGH-CMC-MG) formulation demonstrates a distinct behaviour, with a very high Fe concentration observed at 10 minutes, followed by lower concentrations at later time points. This pronounced early peak suggests rapid initial release and/or experimental variability and should therefore be interpreted with caution. Overall, the results indicate that MG plays a crucial role in enabling Fe availability, while the specific polymer composition significantly influences the magnitude and temporal profile of Fe release.

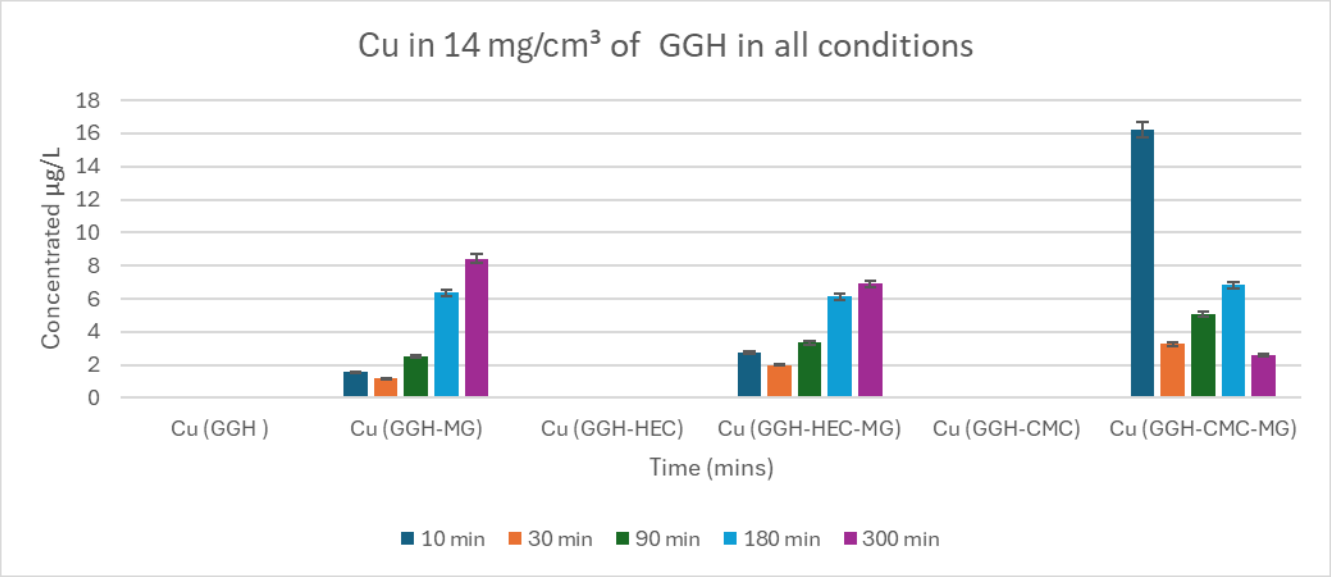

Figure 4.26: The bar chart titled "Cu in 14 mg/cm³ of GGH at all conditions" illustrates copper (Cu) concentrations (in µg/L) across different GGH formulations and time intervals.

Formulations without MG (Cu (GGH), Cu (GGH-HEC), and Cu (GGH-CMC)) exhibit negligible Cu concentrations across all time points, indicating minimal or no Cu release from these matrices. In contrast, the incorporation of MG markedly enhances Cu release. Cu (GGH-MG) and Cu (GGH-HEC-MG) display steady increases in Cu concentration with time, reaching approximately 8–9 µg/L and 6–7 µg/L at 300 minutes, respectively. The Cu (GGH-CMC-MG) formulation shows a distinct behaviour, with a very high initial Cu concentration at 10 minutes, followed by lower values at later times; this pronounced early peak suggests rapid initial release and/or experimental variability and should therefore be interpreted with caution. Overall, the results demonstrate that MG plays a critical role in enabling Cu availability, while the polymer composition strongly influences the magnitude and temporal profile of Cu release.

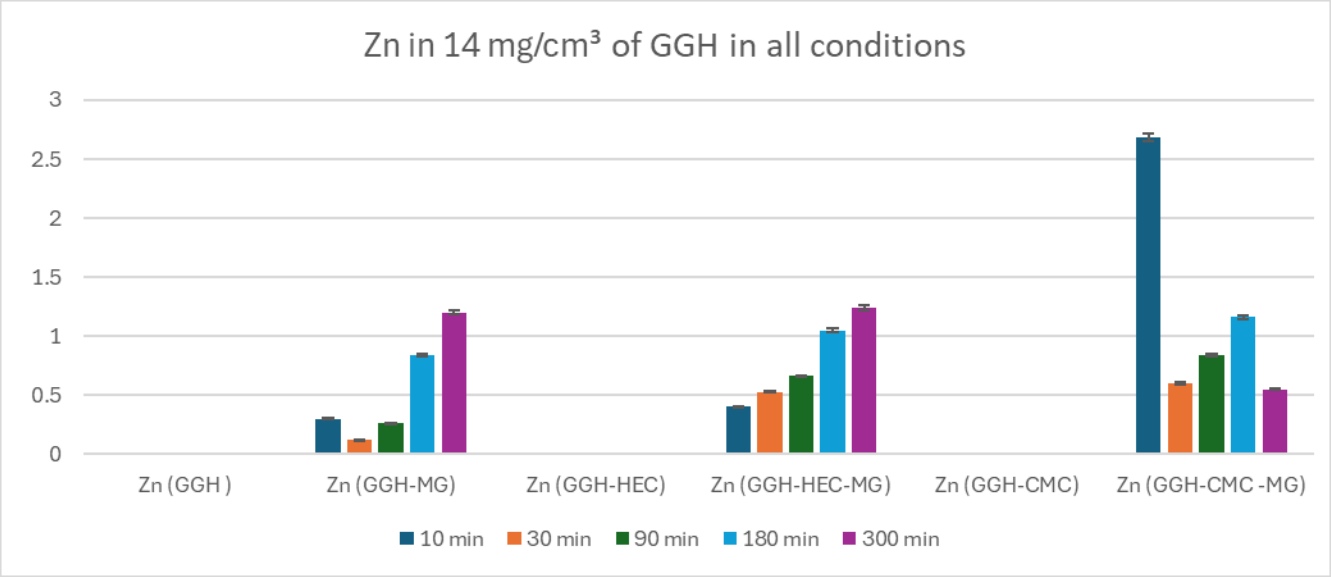

Figure 4.27: The bar chart titled "Zn in 14 mg/cm³ of GGH at all conditions" shows zinc (Zn) concentrations (in µg/L) across various GGH formulations over different time intervals.

Formulations without MG (Zn (GGH), Zn (GGH-HEC), and Zn (GGH-CMC)) exhibit negligible Zn concentrations across all time points, consistent with the fact that these samples do not contain Zn and therefore do not show true Zn release. In contrast, formulations containing MG display measurable Zn levels that increase with time. Zn (GGH-MG) and Zn (GGH-HEC-MG) show gradual, time-dependent increases, reaching approximately 1.2–1.3 µg/L at 300 minutes, indicating sustained Zn availability. The Zn (GGH-CMC-MG) formulation exhibits a distinct profile, with a high initial Zn concentration at 10 minutes, followed by lower values at later time points; this pronounced early peak likely reflects rapid initial release and/or experimental variability and should be interpreted with caution. Overall, the results indicate that Zn availability is strongly associated with the presence of MG, while polymer composition influences the magnitude and temporal pattern of the measured Zn concentrations.

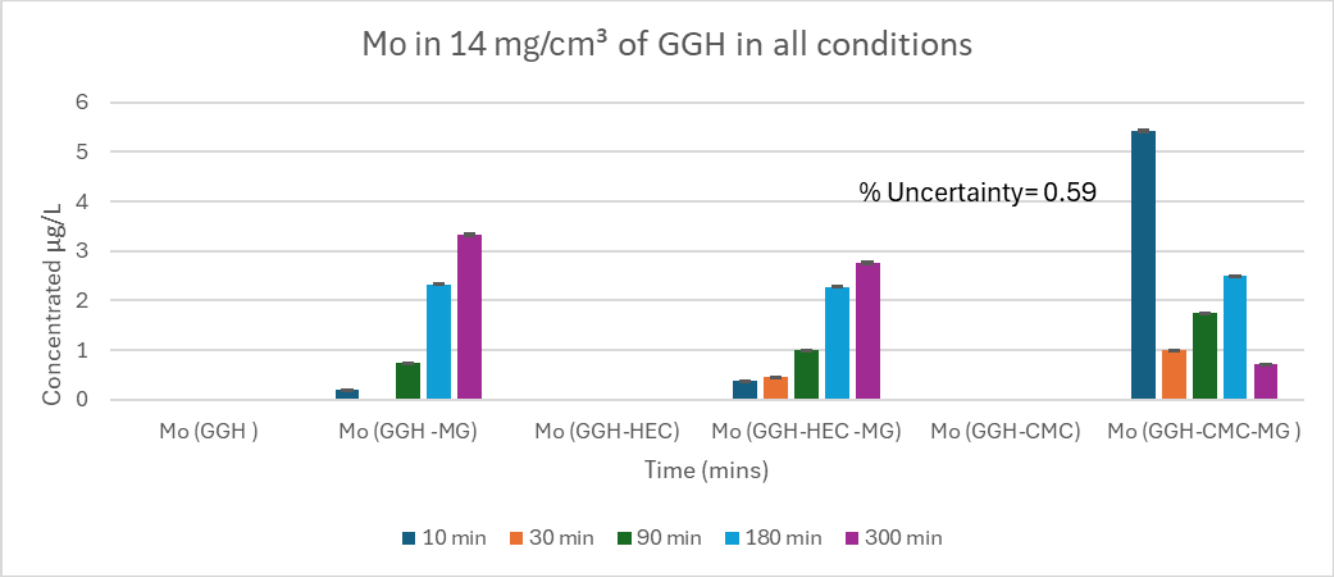

Figure 4.28: The bar chart titled "Mo in 14 mg/cm³ of GGH at all conditions" depicts molybdenum (Mo) concentrations (in µg/L) across various GGH formulations over five-time intervals.

Formulations without MG (Mo (GGH), Mo (GGH-HEC), and Mo (GGH-CMC)) exhibit negligible Mo concentrations across all time points, indicating no meaningful Mo release from these hydrogels. In contrast, the presence of MG leads to clear and measurable Mo availability. Mo (GGH-MG) and Mo (GGH-HEC-MG) show gradual, time-dependent increases, reaching approximately 3.3 µg/L and 2.8 µg/L at 300 minutes, respectively. The Mo (GGH-CMC-MG) formulation displays a distinct profile, with a very high initial Mo concentration at 10 minutes, followed by lower concentrations at later times; this pronounced early peak should be interpreted with caution and may reflect rapid initial release and/or experimental variability rather than sustained Mo release. Overall, the data demonstrate that Mo availability is strongly associated with the presence of MG, while the polymer composition significantly influences the magnitude and temporal profile of the measured Mo concentrations.

4.3 Summary and Conclusions

The conductivity values obtained suggest that higher gellan gum concentrations facilitate greater ion mobility or release. All samples followed a similar pattern, exhibiting an initial rapid increase in conductivity up to 10 hours, where the signal begins to plateau, indicating the samples are approaching ion release equilibrium. All the measured hydrogels exhibited the highest conductivity in the 12 mg/cm³ sample, suggesting optimal ion mobility, while the 10 mg/cm³ and 14 mg/cm³ samples showed reduced conductivity, likely due to lower ionic content and matrix density, respectively.

The nutrient release measurements showed that all non-nutrient loaded samples registered consistently negligible ion release across all concentrations, as would be expected, as most of the metal ion release should come from the additive. The broad trend was for all materials to show an increasing nutrient release concentration with time, with the native gellan gum hydrogel exhibiting the highest peak nutrient concentration. This agrees with the previous findings, as the composite materials had lower available surface area and substrate retention, therefore would be expected to adsorb a smaller quantity of nutrients, leading to a lower concentration released from the material over time. The release concentrations were observed to follow the trend Fe > K > Mn > Zn > P > Mo. However, this trend does not necessarily reflect intrinsic release behaviour related to ionic properties such as ionic radius. Instead, it is strongly influenced by the initial composition of the Miracle-Grow solution. For instance, Fe is present at a higher initial concentration compared to the other ions, which contributes to its higher measured release. To provide a more accurate assessment of release behaviour, the released concentrations should be considered relative to their initial amounts. When normalized in this way, the apparent trend may differ, offering a clearer understanding of the release efficiency of each ion. Also, The data for GGH-CMC-MG indicate an unexpected decrease in ion concentration between 180 and 300 minutes' - since it is only the case for this one sample. An apparent decrease in measured ion concentration was observed for the CMC composite between 180 and 300 minutes. As this behaviour is inconsistent with expected release kinetics, it is likely influenced by experimental variability and would require repeat measurements to confirm reproducibility.

Chapter 5: Rheological Investigations on Gellan Gum Hydrogels.

Hydrogels, both with and without added nutrients and incorporating carboxymethyl cellulose (CMC) and hydroxyethyl cellulose (HEC), are investigated. Rheological measurements were carried out using an Anton Paar Physica MCR 102 rheometer to evaluate and compare the viscoelastic and mechanical behaviour of the different hydrogel formulations. All hydrogels were prepared according to the protocol described in Chapter 2. To ensure complete gelation and structural stabilisation, rheological experiments were performed two days after hydrogel preparation. During this period, the samples were stored in sealed containers to minimise water evaporation and maintain consistent hydration prior to testing. It is acknowledged that variations in water content can influence the rheological properties of hydrogels; however, all samples were stored and tested under identical conditions, ensuring that any minor changes in water content would be systematic and would not affect the comparative analysis. The rheological characterisation included oscillatory measurements, frequency sweeps, and shear tests to assess viscoelastic behaviour and gel strength.

5.1 Standard Amplitude Sweep Test (SAST)

The Standard Amplitude Sweep Test (SAST) is an essential rheological evaluation employed to test the viscoelastic characteristics of materials, especially asphalt binders and other polymeric substances. The main goals of the test include: The main goal of the amplitude sweep test is to identify the linear viscoelastic region (LVER) of a material until the critical strain (γc). where G' and G" commence climbing or decrease. In this region, the material remains stable because its structure remains unchanged. This is a range of strain amplitudes that occur when the material exhibits elastic behaviour and the storage modulus (G') remains comparatively stable. The LVER allows researchers to conduct tests within a range that accurately reflects the material's elastic properties without causing structural disruption (264, 265) in addition, the SAST provides insights into the material's response to applied stress, enhancing the characterisation of its viscoelastic properties. This involves the analysis of both the storage modulus, which indicates the ability of the substance to retain energy, and the loss modulus, which denotes the energy wasted as heat. Knowing these features is crucial for forecasting material performance under various loading circumstances (266, 267). Furthermore, The SAST aids in identifying the transition from linear to non-linear viscoelastic (NLVE), where the

security of the samples has been damaged, behaviour, especially crucial for materials experiencing significant deformation under high-stress conditions. The SAST was conducted on every sample, to provide an insight into the viscoelastic properties of the hydrogels and providing data on the flow behaviour of a substrate using a parallel plate rheometer.

The viscoelastic behaviour of hydrogels, particularly their stability and functionality in providing water retention and nutrient release, is characterized by their linear viscoelastic region (LVER). Within this range, the materials exhibit both elastic and viscous properties, allowing them to efficiently absorb and hold water while also enabling controlled release. This characteristic is crucial for their applications in agriculture and various biotechnological fields. Research studies demonstrate that the LVER of hydrogels is essential for their performance. For example, Radvar and Azevedo discuss the rheological properties of hydrogels, highlighting that in all tested samples, the storage modulus (G') exceeded the loss modulus (G'') within the LVER, indicative of their stable gel structure (268). Similarly, Xuan *et al.* examined the viscoelastic characteristics of polyacrylamide hydrogel precursors and determined that knowing the LVER by strain amplitude scanning is essential for enhancing these materials for applications like 3D printing (269). Studies indicate that a well-defined LVER not only signifies stable gel formation but also plays a pivotal role in ensuring that the hydrogel can respond effectively to environmental changes while providing desired functionalities, including controlled hydration of surrounding soils or biological tissues (76, 270). The amplitude sweep tests can be broken down into three distinct phases that reflect the behaviour of gellan gum hydrogels:

1- **Linear Viscoelastic Region** (LVR):

   Gellan gum displays linear viscoelastic behaviour at low strain amplitudes, with constant storage and loss moduli. This makes it powerful for reversible deformation applications. The LVR provides a baseline for measuring elastic response without permanent structural changes, making it suitable for applications (271, 272).

2- **Transition Zone**

   Hydrogels undergo a transition zone after strain exceeds the linear limit, characterised by an increase in G'', indicating a shift from primarily elastic to a combination of elastic and viscous components. This zone is crucial for energy dissipation and viscoelastic properties, reflecting strain-induced molecular rearrangements (273). The gellan gum's coil-to-helix transition impacts its viscoelastic properties, with higher strain causing more significant molecular rearrangements (274).

3- **Non-Linear Viscoelastic Region** (Plastic State):

Gellan gum hydrogels transition into a non-linear viscoelastic state, known as the plastic state, at high strain amplitudes, exhibiting predominantly viscous behaviour and potentially undergoing permanent deformation (275). Zhao *et al.* emphasizes the importance of assessing materials for high mechanical stability, highlighting deformation thresholds beyond which they may not regain their original properties.(276)

The shear strain applied to composite hydrogel samples increased from 0.01 to 100%, with a constant frequency of ω = 10 rad/s, a temperature of T = 20 ◦C and hydrogels age 2 days. The graphics display dynamic moduli (Pa) on the Y-axis and shear strain (%) on the X-axis. The axis is on a logarithmic scale.

5.1.1 SAST for 10,12 and 14 GGH

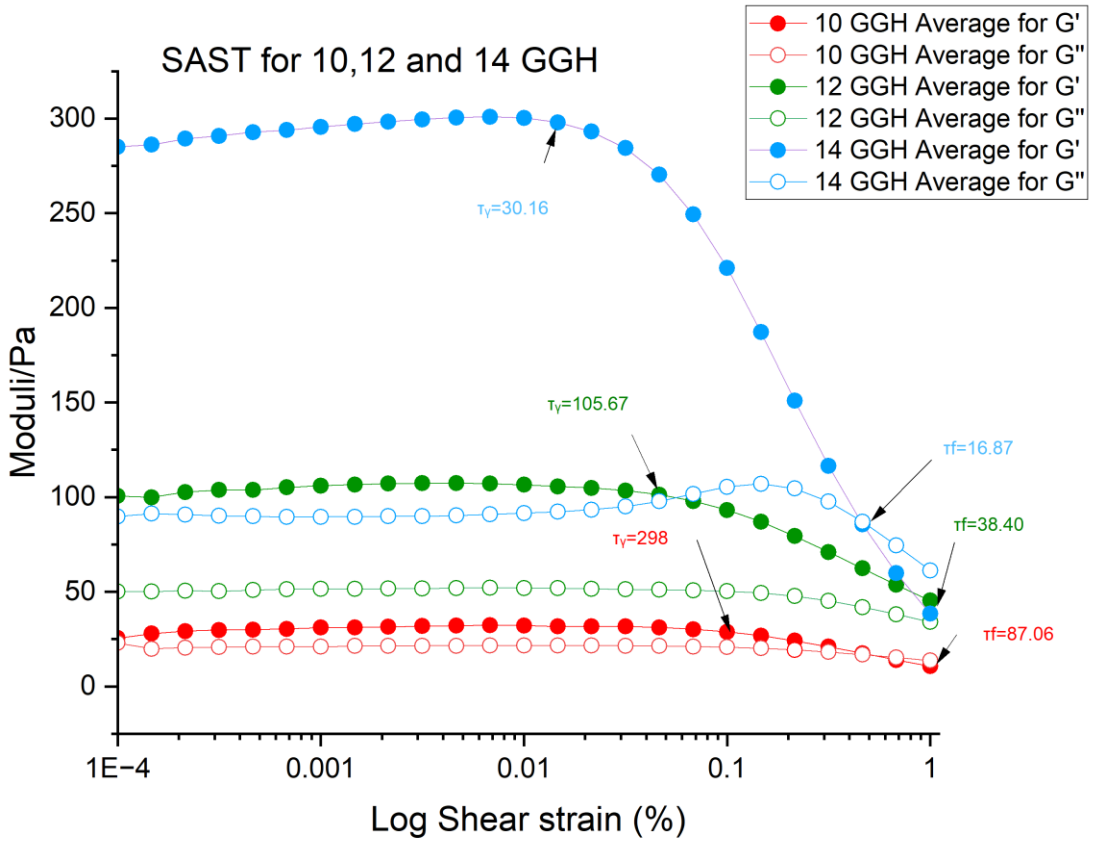

Fig*urea 5.1: Graph illustrating the results of the standard amplitude sweep test (SAST) for gellan gum hydrogels GGH at three different concentrations respectively (10,12 and 14 mg/cm^3) where illustrating the differences of storage (G') and loss (G") moduli. and 2 days of curing time. Strain varied from 0.01 to 100% on a logarithmic scale, with a constant frequency of ω=10 rad/s and a temperature of T=20 °C. The x-axis is log(10).*

In strain amplitude sweep tests, Gellan Gum Hydrogels (GGH) at concentrations of 10, 12, and 14 mg/cm³ exhibit a well-defined linear viscoelastic region (LVER) at low shear strains (approximately 0.0001% to 0.1%), where both the storage modulus (G′) and loss modulus (G″) remain relatively constant. This behaviour indicates a stable gel structure and is characteristic of viscoelastic materials in their LVER. As shear strain increases beyond this range, a significant decrease in G′ is observed, particularly in the 14 mg/cm³ concentration sample, signifying the onset of structural breakdown within the gel network. Concurrently, G″ also decreases, reflecting a loss of viscous behaviour. Higher GGH concentrations demonstrate increased modulus values, with the 14 mg/cm³ sample exhibiting G′ values exceeding 300 Pa, indicative of a stronger gel network. Conversely, the 10 mg/cm³ concentration sample shows lower G′ values (~30 Pa), suggesting a weaker gel structure, though it follows a similar mechanical behaviour pattern. τ(γ) is defined as the stress at the end of the linear viscoelastic region, whereas τ(f) corresponds to the stress required for complete flow of the hydrogel.

Table 5.1: Viscoelastic characteristic parameters for GGH at different concentrations. The flow transition index (FTI) is defined as the ratio of flow point stress to yield point stress (FTI = τf / τy).

GGH Conc. (mg/cm³)	**Yield Point (τ_γ, Pa) & Shear Strain (%)**	**Flow Point (τf, Pa) & Shear Strain (%)**	**Flow Transition Index (FTI) FTI = Flow Point Stress / Yield Point Stress**
10 GGH	30 (0.07 %)	17 (0.46%)	0.56
12 GGH `	106 (0.01 %)	38 (1%)	0.36
14 GGH	298 (0.01%)	87 (0.46%)	0.29

The table 5.1 presents a comparative analysis of the rheological behaviour of gellan gum hydrogels at three different concentrations: 10, 12, and 14 mg/cm³ (corresponding to 0.5 g, 0.6 g, and 0.7 g, respectively). For each concentration, the values for the yield point, flow point and flow transition index are shown. The table illustrates how increasing gellan gum concentration influences the mechanical strength and flow behaviour of hydrogels. The 10 mg/cm³ sample demonstrates moderate structural resistance (30.16 Pa) and a relatively brittle nature, as indicated by a FTI of 0.56 (FTI describes the nature of the solid–liquid transition, with lower values indicating enhanced structural robustness). At 12 mg/cm³, the gel exhibits a higher yield point (105.67 Pa) but flows at a proportionally lower stress (FTI = 0.36), suggesting a more fragile internal network. The 14 mg/cm³ sample has the highest yield point

(298.0 Pa) but the lowest FTI (0.29), indicating a robust yet brittle gel that fails rapidly once its structural threshold is exceeded. These findings are important for optimizing gellan gum formulations in applications across food, pharmaceutical, and biomedical industries, where tailored viscoelastic properties are essential.

5.1.2 SAST for 10,12 and 14 GGH-MG

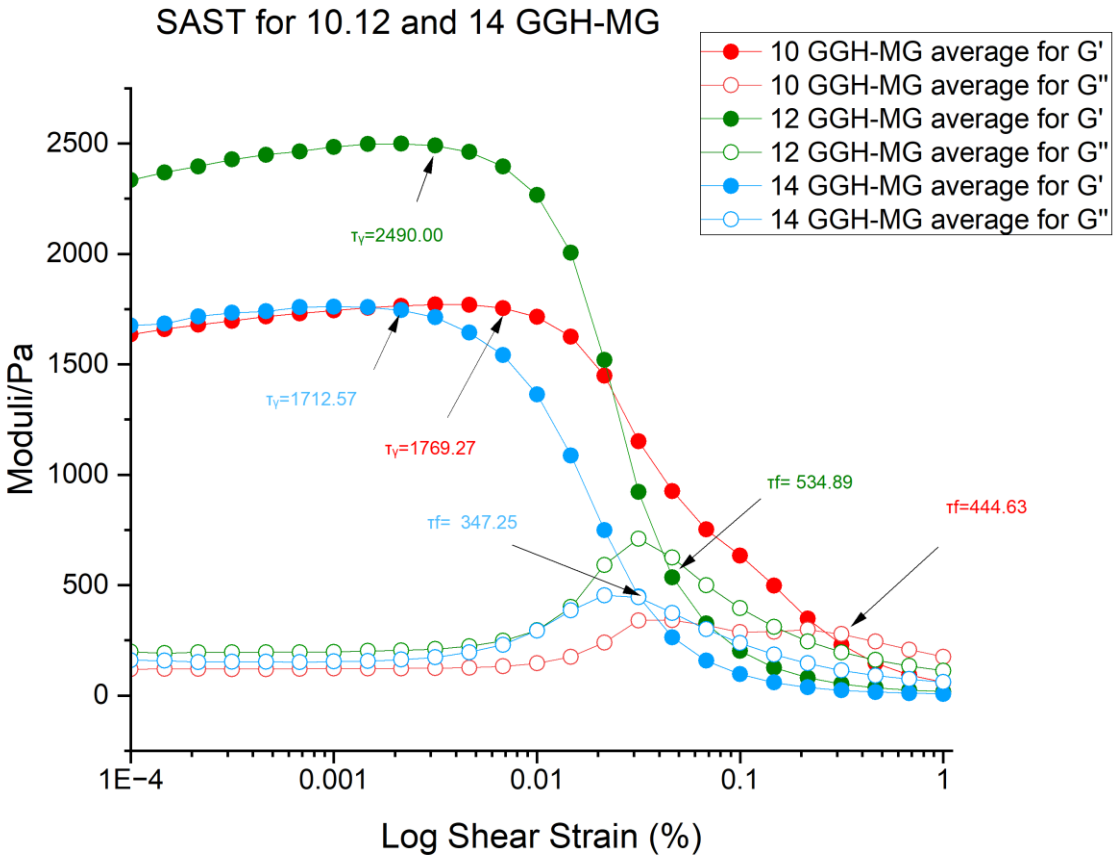

Figure 5.2: Graph illustrating the results of the standard amplitude sweep test (SAST) for gellan gum hydrogels GGH-MG at three different concentrations respectively (10,12 and 14 mg/cm^3) where illustrating the differences of storage (G') and loss (G") moduli. and 2 days of curing time. Strain varied from 0.01 to 100% on a logarithmic scale, with a constant frequency of ω=10 rad/s and a temperature of T=20 °C. The x-axis is log(10).

Figure 2.5 presents rheological data showing the relationship between shear strain (%) and modulus (Pa) for different gellan gum hydrogel samples. It displays both the storage modulus (G′), indicating elastic behaviour, and the loss model us (G″), indicating viscous behaviour. Data for three samples 10,12 and 14 mg/cm^3 with nutrients. At low shear strains, G′ is significantly higher than G″, suggesting a solid-like behaviour. As strain increases, G′ decreases and G″ increases, eventually crossing over, marking the gel–sol transition where the material becomes more liquid-like. Sample 12 mg/cm^3 exhibits the highest G′ values and the strongest

gel structure, while Sample 14mg/cm^3 shows a lower G′ and an earlier crossover point, indicating a weaker gel.

Table 5.2: Viscoelastic characteristic parameters for GGH-MG at different concentrations. The flow transition index (FTI) is defined as the ratio of flow point stress to yield point stress (FTI = τf / τy).

GGH Conc. (mg/cm³)	Yield Point (τ_γ, Pa) & Shear Strain (%)	Flow Point (τf, Pa) & Shear Strain (%)	Flow Transition Index (FTI) FTI = Flow Point Stress / Yield Point Stress
10 GG-MG	1769 (0.005%)	347 (0.22%)	0.20
12 GG-MG	2490 (0.003%)	535 (0.05%)	0.21
14 GG-MG	1713 (0.002%)	445 (0.03%)	0.26

The table 2.5 summarizes the rheological properties of gellan gum hydrogels supplemented with 1 mL of nutrients at three different concentrations: 10, 12, and 14 mg/cm³ (corresponding to 0.5 g, 0.6 g, and 0.7 g, respectively) 1 mL nutrients. The table illustrates how increasing gellan gum concentration 1 mL nutrients influence the mechanical strength and flow behaviour of hydrogels. The 10 mg/cm³ + nutrients hydrogel exhibits a high yield stress of 1769.27 Pa with a low FTI of 0.20, indicating a strong but brittle structure. The 12 mg/cm³ + nutrients sample demonstrates the highest yield stress at 2490 Pa and a similarly low FTI of 0.21, suggesting it possesses the greatest structural strength yet remains fragile under increasing stress. In contrast, the 14 mg/cm³ + nutrients formulation shows a slightly lower yield point (1712.57 Pa) but a modestly higher FTI of 0.26, indicating a marginally more ductile behaviour compared to the other concentrations.

In the above two graph Figures 5.1 and 5.2, although the general rheological trends are similar, the incorporation of MG leads to pronounced changes in the magnitudes of G′ and G″, reflecting significant modifications to the hydrogel network. Furthermore, comparing the impact of varying concentrations of gellan gum If alone or in the presence of nutrients on hydrogel structures revealed that an increase in concentration resulted in increased storage modulus (G') and loss modulus (G") indicating that the structure of the samples remains unchanged. In addition, it appears that an increase in concentration slightly reduced the LVER, critical yield point, and flow crossover point across all samples. Analysis of LVER has shown that the longer the LVER, the more stable the hydrogel (152). Consequently, at increasing concentrations, the stability of the hydrogel decreased. It was determined that high

concentrations exhibited reduced shear strain flow crossover points and diminished critical yield points. This indicated that increased concentrations of gellan gum resulted in decreased mechanical strength and stability (152).

Tables 5.1 and 5.2 present a comparative analysis of the rheological behaviour of gellan gum hydrogels at three concentrations (10, 12, and 14 mg/cm³), both without and with the addition of 1 mL of nutrients. Without nutrients, increasing gellan concentration enhances the yield point, with values rising from 30.2 Pa at 10 mg/cm³ to 298 Pa at 14 mg/cm³, while the FTI decreases, indicating a trend toward greater brittleness. With the addition of nutrients, the yield points significantly increase across all concentrations reaching up to 2490 Pa at 12 mg/cm³ yet all samples exhibit low FTIs (0.20–0.26), suggesting that while nutrient supplementation strengthens the gels, it also maintains or increases their brittleness. Notably, the 14 mg/cm³ + nutrients sample shows slightly more ductile behaviour compared to others. Overall, these findings highlight how both concentration and nutrient inclusion critically influence the mechanical strength and flow characteristics of gellan gum hydrogels, with implications for their formulation in food, pharmaceutical, and biomedical applications.

5.1.3 SAST for 10,12 and 14 GGH-HEC

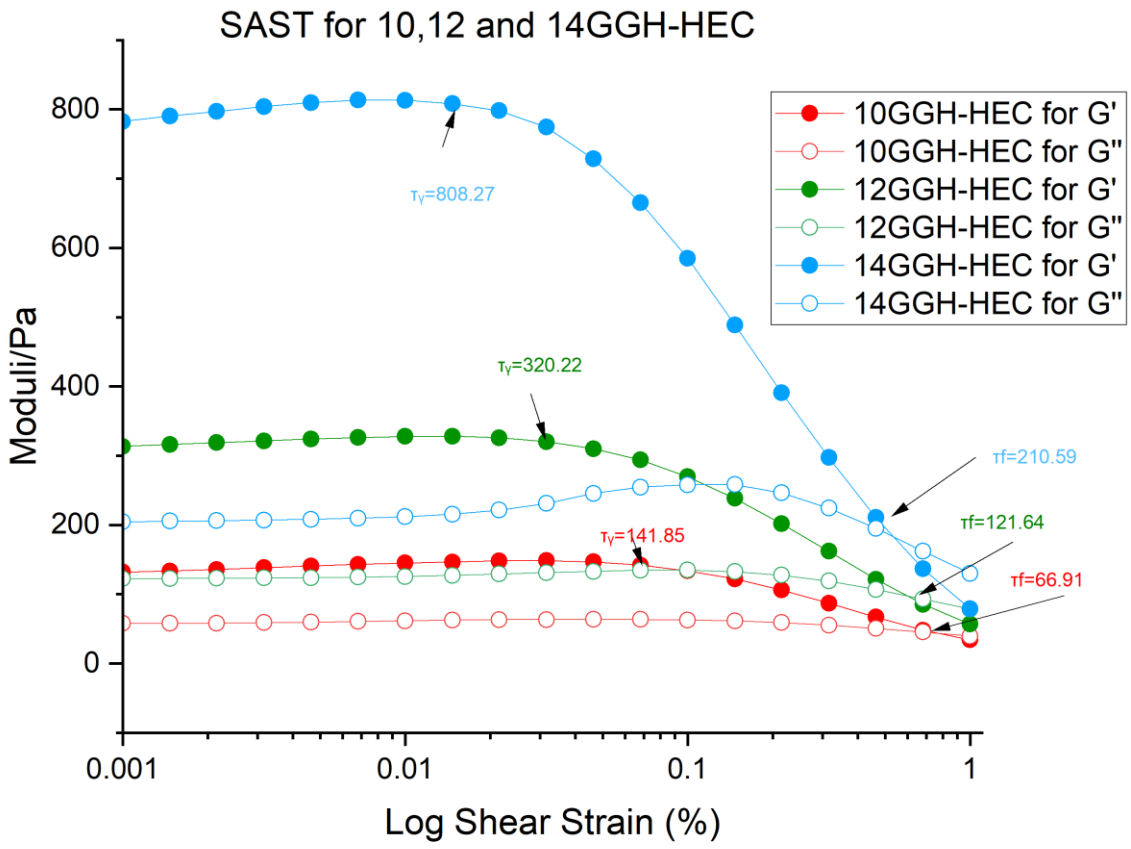

Figure 5.3: Graph illustrating the results of the standard amplitude sweep test (SAST) for gellan gum hydrogels GGH - HEC at three different concentrations respectively (10,12 and 14 mg/cm^3), where illustrating the differences of storage (G') and loss (G") moduli. and 2 days of curing time. Strain varied from 0.01 to 100% on a logarithmic scale, with a constant frequency of ω=10 rad/s and a temperature of T=20 °C. The x-axis is log (10).

Table 5.3: Viscoelastic characteristic parameters for GGH-HEC at different concentrations. . The flow transition index (FTI) is defined as the ratio of flow point stress to yield point stress (FTI = τf / τy).

GGH-HEC Conc. (mg/cm³)	Yield Point (τ_γ, Pa) & Shear Strain (%)	Flow Point (τf, Pa) & Shear Strain (%)	Flow Transition Index (FTI) FTI = Flow Point Stress / Yield Point Stress
10 (GGH-HEC)	142 (0.07%)	67.0 (0.46%)	0.47
12 (GGH-HEC)	320 (0.04%)	122 (0.46%)	0.38
14 (GGH-HEC)	808 (0.02%)	211 (0.46%)	0.26

Figure 5.3 and Table 5.3 collectively demonstrate that increasing the concentration of GGH-HEC hydrogels from 10 to 14 mg/cm³ markedly enhances their mechanical strength and structural stability. Within the linear viscoelastic region, all samples exhibited dominant elastic

behaviour (G′ > G″), confirming the formation of well-developed gel networks. A pronounced increase in yield stress (from 142 to 808 Pa) and flow stress (from 67 to 211 Pa) with increasing concentration indicates progressive reinforcement of the three-dimensional polymer network and greater resistance to deformation. However, the simultaneous decrease in the Flow Transition Index (from 0.47 to 0.26) suggests that although higher concentrations produce mechanically stronger gels, the transition from elastic to viscous behaviour becomes more abrupt after yielding, reflecting a denser and more rigid, yet relatively more brittle, network structure. These findings confirm that polymer concentration plays a critical role in governing both the strength and failure characteristics of GGH-HEC hydrogels.

5.1.4 SAST for 10,12 and 14 GGH-HEC-MG

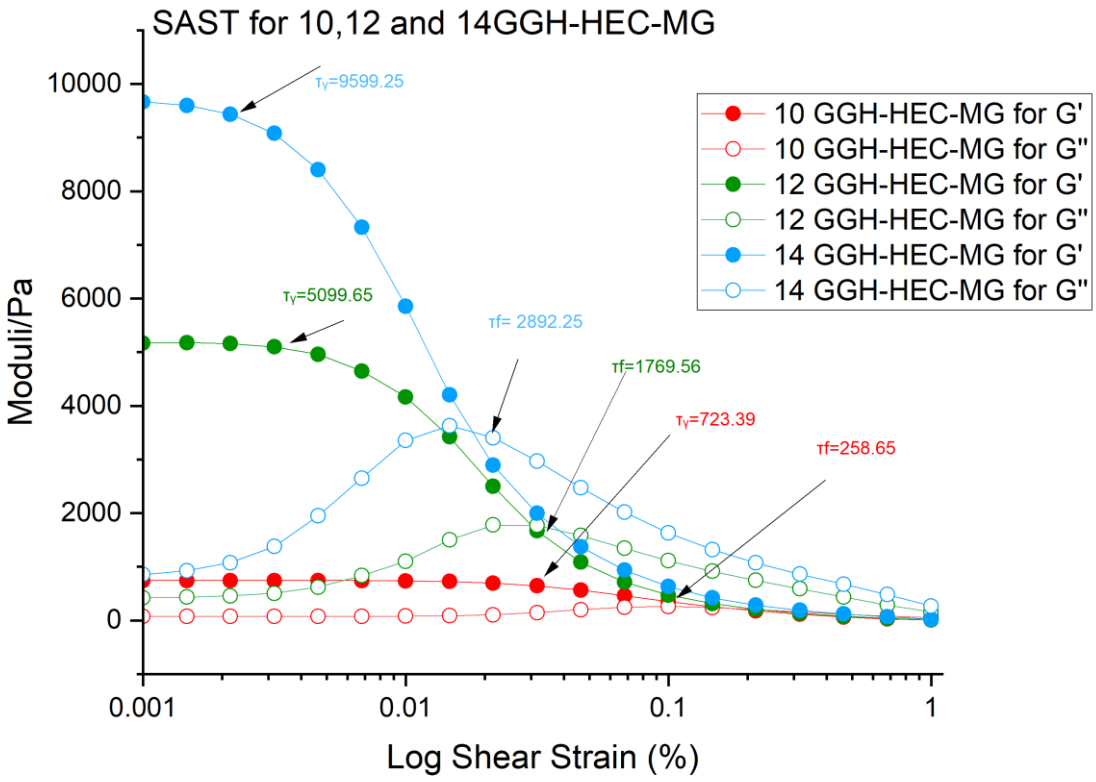

Figure 5.4: Graph illustrating the results of the standard amplitude sweep test (SAST) for gellan gum Hydrogels GGH-HEC-MG at three different concentrations respectively (10, 12 and 14 mg/cm^3) where illustrating the differences of storage (G') and loss (G") moduli. and 2 days of curing time. Strain varied from 0.01 to 100% on a logarithmic scale, with a constant frequency of ω=10 rad/s and a temperature of T=20 °C. The x-axis is log(10).

Table 5.4: Viscoelastic characteristic parameters for GGH-HEC-MG at different concentrations. . The flow transition index (FTI) is defined as the ratio of flow point stress to yield point stress (FTI = τf / τy).

GGH-HEC-MG Conc. (mg/cm³)	Yield Point (τ_γ, Pa) & Shear Strain (%)	Flow Point (τf, Pa) & Shear Strain (%)	Flow Transition Index (FTI) FTI = Flow Point Stress / Yield Point Stress
10 GGH-HEC-MG	723.39	258.65	0.36
12 GGH-HEC-MG	5099.65	1769.56	0.35
14 GGH-HEC-MG	9599.25	2892.25	0.30

Figure 5-4 and Table 5-4 collectively demonstrate a substantial enhancement in the viscoelastic and mechanical performance of GGH-HEC-MG hydrogels with increasing polymer concentration after two days of curing. Within the linear viscoelastic region (LVR), all formulations exhibited dominant elastic behaviour ($G' > G''$), confirming the formation of a highly structured and stable three-dimensional network. Notably, both the storage modulus and the critical stress parameters increased dramatically with concentration, indicating significant reinforcement of the hydrogel matrix upon MG incorporation.

The yield stress (τy) increased markedly from 723 Pa at 10 mg/cm³ to 5100 Pa at 12 mg/cm³ and further to 9599 Pa at 14 mg/cm³, reflecting a pronounced improvement in resistance to structural breakdown under applied strain. Similarly, the flow stress (τf) increased from 259 Pa to 1770 Pa and 2892 Pa with increasing concentration, confirming enhanced structural integrity prior to the elastic–viscous transition. These values are substantially higher than those observed for the non-MG system, indicating that MG contributes significantly to network densification and intermolecular interactions.

Although the Flow Transition Index (FTI) decreased slightly from 0.36 to 0.30 with increasing concentration, the reduction is moderate compared to the dramatic rise in strength parameters. This suggests that while the gels become considerably stronger and stiffer at higher concentrations, the elastic-to-viscous transition remains relatively controlled, indicating a robust yet structurally coherent network rather than a purely brittle system.

Overall, the combined analysis confirms that the incorporation of MG, together with increasing polymer concentration, leads to the formation of highly reinforced hydrogel networks characterized by exceptional mechanical strength, enhanced resistance to deformation, and improved structural stability, making the GGH-HEC-MG system mechanically superior to the corresponding GGH-HEC formulations.

5.1.5 SAST for 10,12 and 14 GGH-CMC

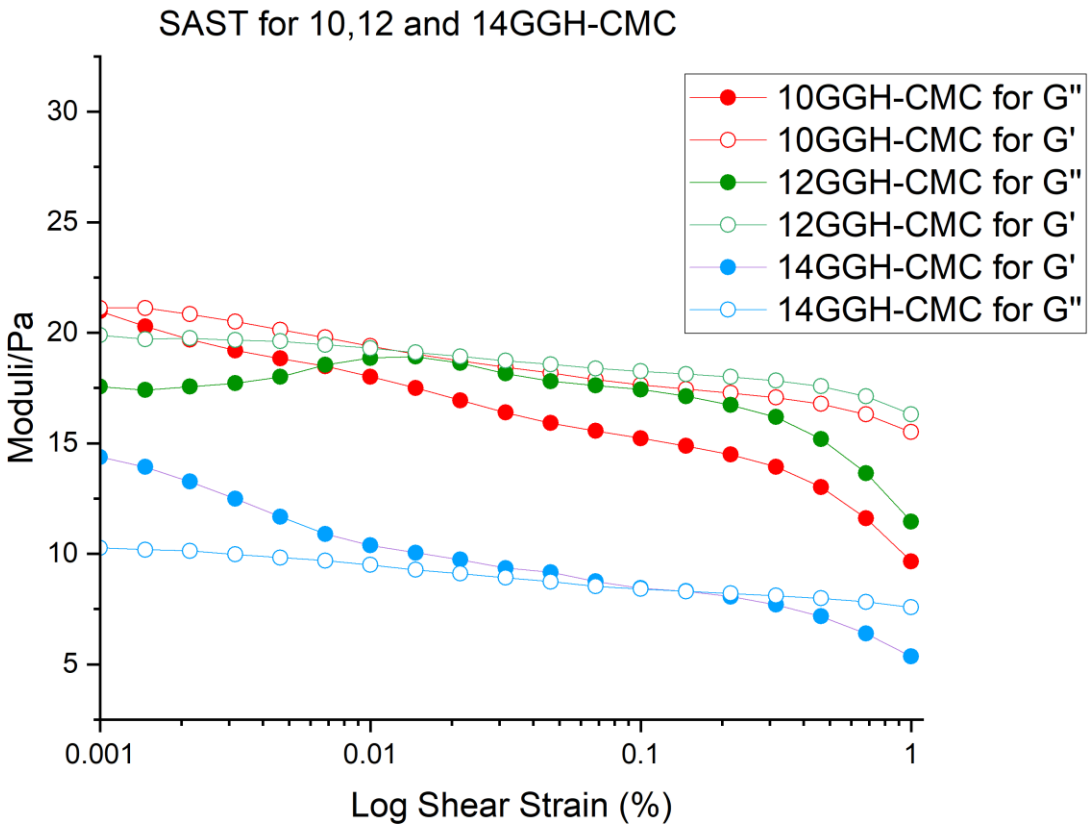

Figure 5.5: Graph illustrating the results of the standard amplitude sweep test (SAST) for gellan gum hydrogels GGH-CMC at three different concentrations respectively (10,12 and 14 mg/cm³) where illustrating the differences of storage (G') and loss (G") moduli. and 2 days of curing time. Strain varied from 0.01 to 100% on a logarithmic scale, with a constant frequency of ω=10 rad/s and a temperature of T=20 °C. The x-axis is log(10).

Table 5.5: Viscoelastic characteristic parameters for GGH-CMC at different concentrations. The flow transition index (FTI) is defined as the ratio of flow point stress to yield point stress (FTI = τf / τy). .

GGH-CMC Conc. (mg/cm³)	Yield Point (τ_γ, Pa) & Shear Strain (%)	Flow Point (τf, Pa) & Shear Strain (%)	Flow Transition Index (FTI) = Flow Point Stress / Yield Point Stress
10 GGH-CMC	30.0	20.1	1.5
12 GGH-CMC	20.0	17.8	1.1
14 GGH-CMC	14.8	10.0	1.5

Figure 5-5 and Table 5-5 present the amplitude sweep behaviour of GGH-CMC hydrogels at concentrations of 10, 12, and 14 mg/cm³ after two days of curing, evaluated at 20 °C and an angular frequency of 10 rad/s. Within the tested strain range, all samples exhibited viscoelastic

characteristics; however, unlike the previously studied systems, the mechanical response did not show a consistent reinforcement with increasing concentration. The yield stress decreased from 30.0 Pa at 10 mg/cm³ to 14.8 Pa at 14 mg/cm³, while the flow stress similarly declined from 20.1 Pa to 10.0 Pa, indicating a progressive reduction in resistance to structural deformation at higher concentrations. This trend suggests that increasing CMC content does not strengthen the three-dimensional network but may instead interfere with effective chain interactions or network cohesion. Furthermore, the Flow Transition Index (FTI) values (1.5, 1.1, and 1.5) remain comparatively high and irregular, implying a more gradual and less well-defined elastic–viscous transition relative to the GGH-HEC and GGH-HEC-MG systems. Overall, the combined results indicate that the GGH-CMC hydrogels form comparatively weaker and less mechanically stable networks, with concentration exerting a non-monotonic and potentially destabilizing influence on gel integrity.

5.1.6 SAST for 10,12 and 14 GGH-CMC-MG

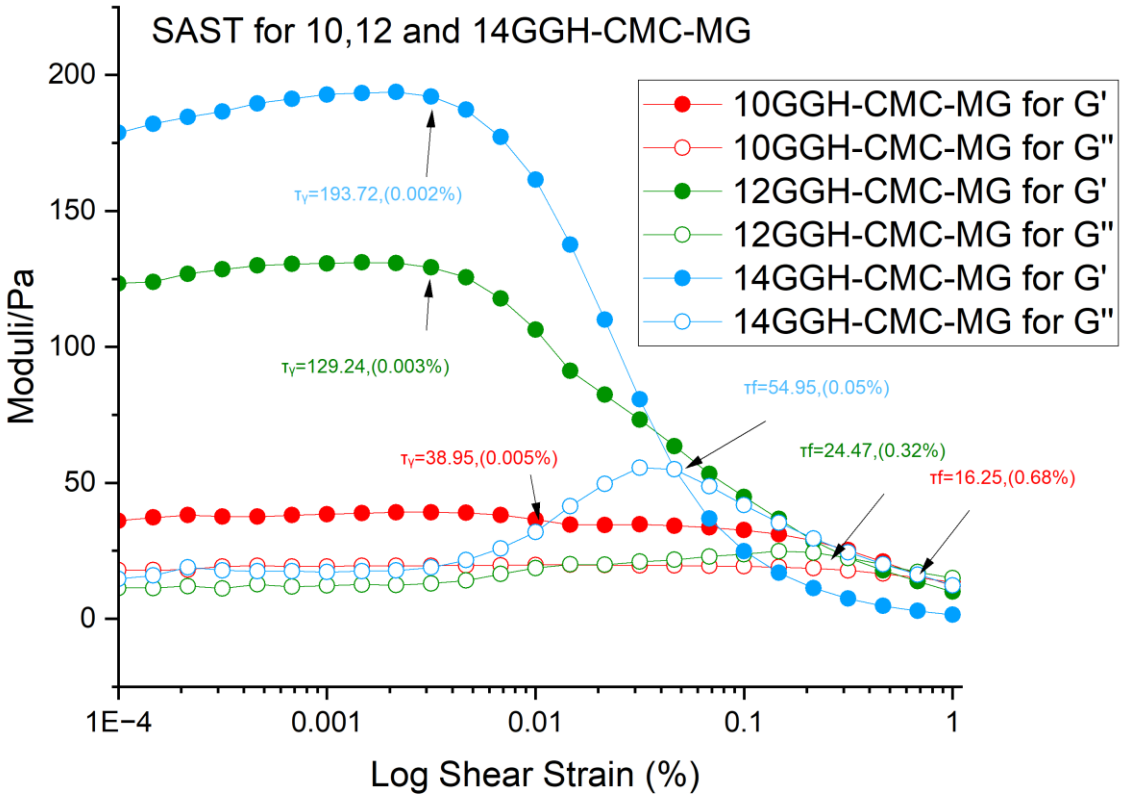

Figure 5.6: Graph illustrating the results of the standard amplitude sweep test (SAST) for gellan gum Hydrogels GGH-CMC-MG at three different concentrations respectively (10,12 and 14 mg/cm^3) where illustrating the differences of storage (G') and loss (G") moduli. and 2

days of curing time. Strain varied from 0.01 to 100% on a logarithmic scale, with a constant frequency of ω=10 rad/s and a temperature of T=20 °C. The x-axis is log(10).

Table 5.6: Viscoelastic characteristic parameters for GGH-CMC MG at different concentrations. . The flow transition index (FTI) is defined as the ratio of flow point stress to yield point stress (FTI = τf / τy).

GGH-HEC-MG Conc. (mg/cm³)	**Yield Point (τ_γ, Pa) & Shear Strain (%)**	**Flow Point (τf, Pa) & Shear Strain (%)**	**Flow Transition Index (FTI) = Flow Point Stress / Yield Point Stress**
10 GGH-CMC-MG	194	16.3	0.1
12 GGH-CMC-MG	129	24.5	0.2
14 GGH-CMC-MG	39.0	55.0	1.4

Figure 5-6 and Table 5-6 illustrate the amplitude sweep response of GGH-CMC-MG hydrogels at concentrations of 10, 12, and 14 mg/cm³ after two days of curing, evaluated at 20 °C and an angular frequency of 10 rad/s. All formulations initially exhibited dominant elastic behaviour (G′ > G″) within the linear viscoelastic region, confirming the formation of structured gel networks. However, unlike the GGH-HEC-MG system, the mechanical response of GGH-CMC-MG did not increase monotonically with concentration. The yield stress decreased significantly from 194 Pa at 10 mg/cm³ to 39 Pa at 14 mg/cm³, indicating a progressive reduction in resistance to structural breakdown as concentration increased. In contrast, the flow stress showed a non-monotonic trend, rising from 16.3 Pa (10 mg/cm³) to 55.0 Pa (14 mg/cm³), suggesting differences in post-yield structural rearrangement. The Flow Transition Index (FTI) increased markedly from 0.1 to 1.4 with increasing concentration, reflecting a transition from a sharply defined elastic failure at low concentration to a more gradual and extended elastic–viscous transition at higher concentration. Collectively, these results indicate that, in the GGH-CMC-MG system, increasing concentration does not simply reinforce the gel network but alters its failure mechanism, leading to a weaker initial structure yet a more progressive flow transition behaviour at elevated concentrations.

5.2 Frequency sweep test

5.2.1 Frequency sweep

5.2.1.1 Frequency sweep test for 10,12 and 14 GGH

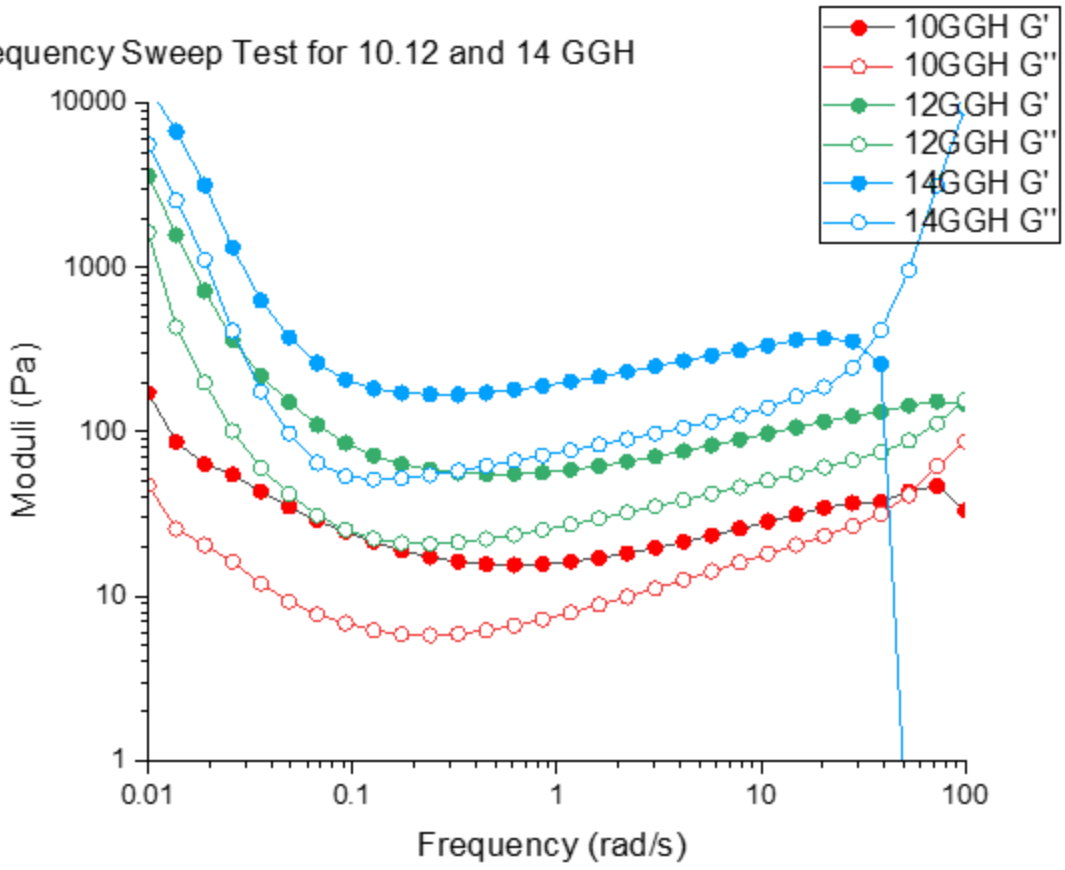

Figure 5.7: The graph displays the frequency sweep test results for gellan gum hydrogels modified with hydroxyethyl cellulose (GGH) at concentrations of 10, 12, and 14 mg/cm³, measured within the Linear Viscoelastic (LVE) region after 3 days of aging at 20°C. The test evaluates the storage modulus (G') and loss modulus (G") across a frequency range of 0.01 to 100 rad/s, providing insight into the viscoelastic behaviour of the hydrogels.

The frequency sweep test reveals several key trends in the viscoelastic behaviour of GGH hydrogels. Firstly, across all concentrations and frequencies, G′ remains greater than G″, indicating a consistently elastic-dominated, solid-like behaviour. Moreover, both G′ and G″ increase with frequency above approximately 0.1 rad/s , which is typical of gel-like or weakly crosslinked networks, as these materials tend to stiffen under faster deformations. In addition, as the GGH concentration increases, the overall modulus values rise, demonstrating that higher polymer content enhances gel strength and elasticity. Specifically, the 0.7 g sample (blue) exhibits the highest G′ and G″ values, indicating the strongest gel network, whereas the 0.5 g sample (red) shows the lowest moduli, reflecting a weaker structure. Furthermore, at low frequencies (0.01 to 1 rad/s), both moduli either decrease slightly or level off, which

corresponds to the gel's response under slower deformations or longer timescales. Conversely, at higher frequencies (10 to 100 rad/s), a more pronounced increase in moduli is observed, particularly in higher concentrations, suggesting that these gels become stiffer and more resistant to rapid mechanical stress.

5.2.1.2 Frequency sweep test for 10,12 and 14 GGH-MG

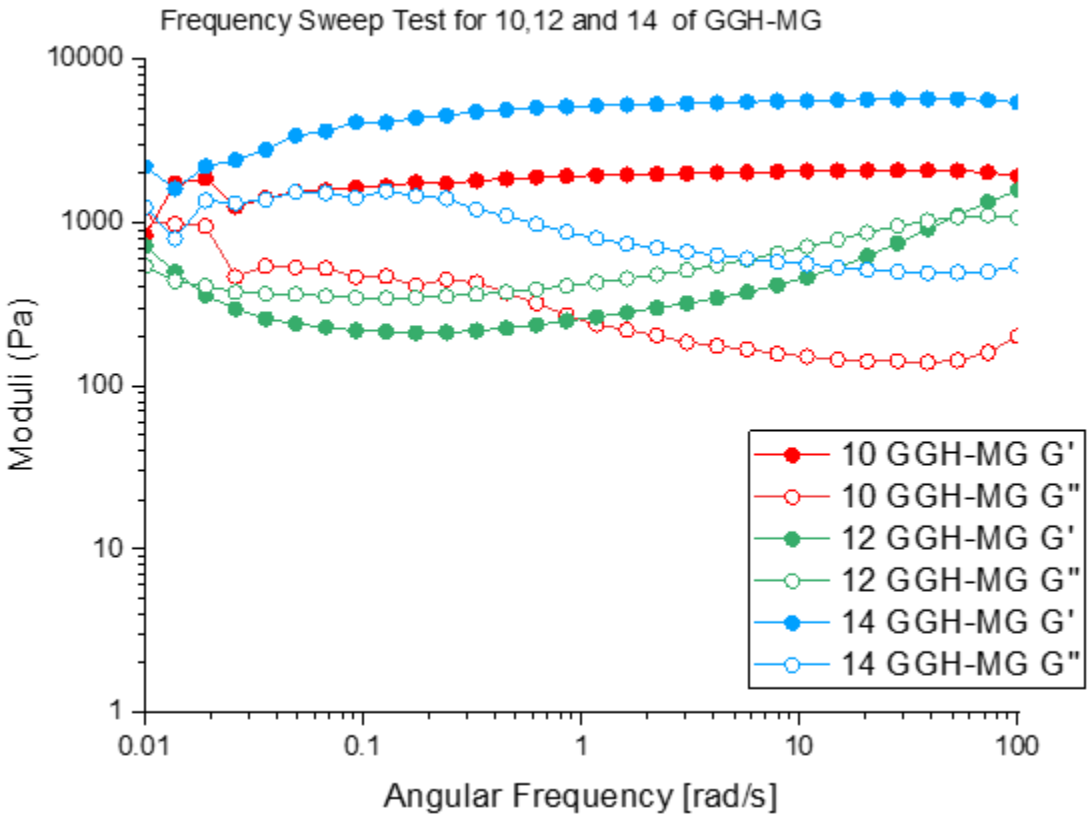

Figure 5.8: The graph displays the frequency sweep test results for gellan gum hydrogels modified with hydroxyethyl cellulose (GGH 1 mL of nutrient) at concentrations of 10, 12, and 14 mg/cm³, measured within the Linear Viscoelastic (LVE) region after 3 days of aging at 20°C. The test evaluates the storage modulus (G') and loss modulus (G") across a frequency range of 0.01 to 100 rad/s, providing insight into the viscoelastic behaviour of the hydrogels.

The frequency sweep graph shows the viscoelastic behaviour of gellan gum hydrogels (GGH) at concentrations of 10, 12, and 14 mg/cm³, each supplemented with 1 mL of nutrient, measured within the linear viscoelastic (LVE) region at 20 °C after 3 days of aging. Across all samples and throughout the investigated frequency range (0.01–100 rad/s), the storage modulus (G′) remains consistently higher than the loss modulus (G″), indicating predominantly elastic, solid-like behaviour. Both moduli exhibit only limited frequency dependence, particularly at intermediate and high frequencies, suggesting the formation of relatively stable gel networks.

In terms of concentration effects, higher GGH concentrations generally lead to increased viscoelastic moduli, although the trend is not strictly monotonic across all samples. Notably, the 10 mg/cm³ sample exhibits G′ values comparable to, and in some frequency ranges slightly higher than, those of the 12 mg/cm³ sample. Nevertheless, the highest concentration (14 mg/cm³; 0.7 g, blue) consistently shows the largest G′ and G″ values across the frequency range, indicating the formation of the strongest and most elastic gel network. Conversely, the 10 mg/cm³ sample (0.5 g, red) displays the lowest moduli overall, reflecting a comparatively weaker network structure. All samples exhibit a broad plateau in G′ within the LVE region, particularly at higher concentrations, indicating stable gel formation without pronounced structural transitions across the tested frequencies. The absence of abrupt increases or decreases in either modulus suggests that the addition of nutrient contributes to maintaining mechanical stability and reinforces the gel matrix over a wide range of deformation rates.

A comparison between Graph 5.7 (GGH without nutrient) and Graph 5.8 (GGH with 1 mL nutrient) highlights the influence of nutrient incorporation on the rheological response. In the absence of nutrient (Graph 5.7), the gels display lower elastic moduli, stronger frequency dependence, and a more pronounced U-shaped modulus profile at lower concentrations, indicative of moderate to weaker gel structures and reduced resistance to dynamic deformation. In contrast, nutrient-containing gels (Graph 5.8) exhibit enhanced elasticity and reduced viscous contributions, as evidenced by flatter and more stable G′ and G″ curves. This behaviour reflects the formation of more robust and mechanically stable networks, particularly at higher polymer concentrations, improving resistance to deformation under oscillatory loading.

5.2.1.3 Frequency sweep test for 10,12 and 14 GGH-HEC

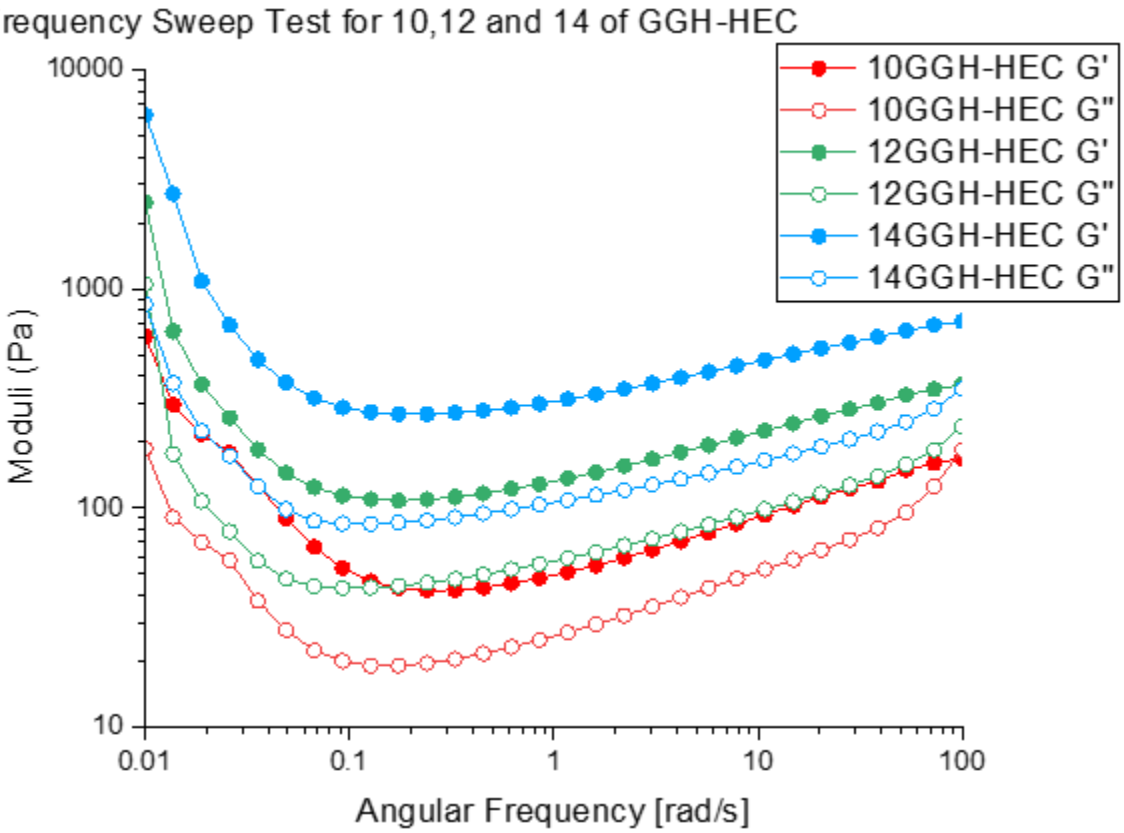

Figure 5.9: The graph displays the frequency sweep test results for gellan gum hydrogels modified with hydroxyethyl cellulose (GGH-HEC) at concentrations of 10, 12, and 14 mg/cm³, measured within the Linear Viscoelastic (LVE) region after 3 days of aging at 20°C. The test evaluates the storage modulus (G') and loss modulus (G") across a frequency range of 0.01 to 100 rad/s, providing insight into the viscoelastic behaviour of the hydrogels.

The frequency sweep test results for GGH-HEC hydrogels show that G′ remains consistently higher than G″ across all frequencies and concentrations, indicating a predominantly elastic, solid-like behaviour. Both moduli exhibit a characteristic U-shaped trend, particularly evident in G″, where values decrease at low frequencies due to structural relaxation, then rise at higher frequencies as elastic recovery becomes dominant. With increasing GGH-HEC concentration, G′ and G″ increase, most notably in the 0.7 g sample (blue), which demonstrates the strongest gel network. In contrast, the 0.5 g sample (red) shows the lowest moduli, indicating a weaker and more frequency-sensitive structure. Additionally, a plateau observed in the mid-frequency range, followed by a distinct rise in moduli, suggests that the gels possess good resilience and resistance to deformation under dynamic conditions. This graph demonstrates that the incorporation of HEC enhances the mechanical strength and elasticity of gellan gum hydrogels in a concentration-dependent manner. The observed frequency sensitivity and viscoelastic

response suggest that GGH-HEC formulations can maintain elastic dominance while adapting to a broad range of mechanical stimuli, making them suitable for applications requiring both flexibility and structural integrity, such as biomedical scaffolds or food gels.

5.2.1.4 Frequency sweep test for 10,12 and 14 GGH-HEC-MG

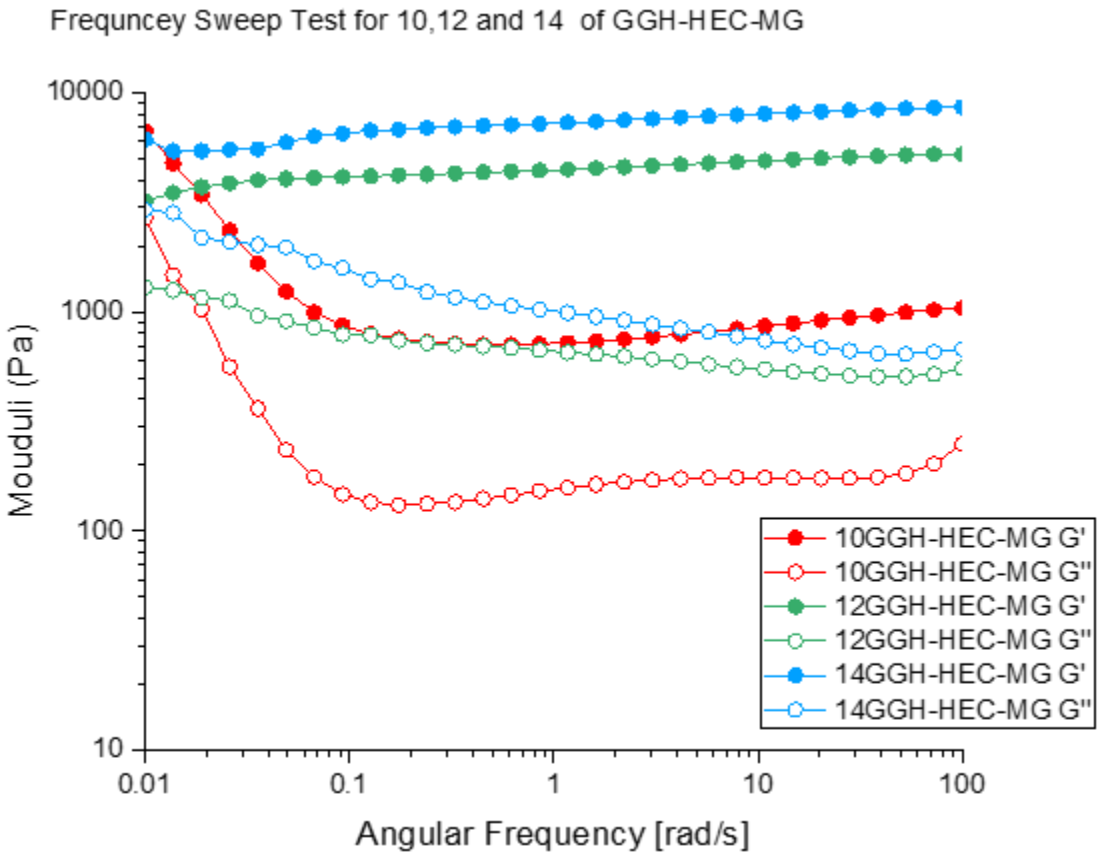

Figure 5.10: The graph displays the frequency sweep test results for gellan gum hydrogels modified with hydroxyethyl cellulose (GGH-HEC + 1 mL of nutrient) at concentrations of 10, 12, and 14 mg/cm³, measured within the Linear Viscoelastic (LVE) region after 3 days of aging at 20°C. The test evaluates the storage modulus (G') and loss modulus (G") across a frequency range of 0.01 to 100 rad/s, providing insight into the viscoelastic behaviour of the hydrogels.

The frequency sweep graph demonstrates that G′ consistently exceeds G″ across all GGH-HEC samples supplemented with 1 mL of nutrient, confirming their predominantly elastic (solid-like) behaviour. Both moduli exhibit a U-shaped trend, most evident in the 0.5 g sample (red), where a decline at low frequencies due to structural relaxation is followed by an increase at higher frequencies, indicating elastic recovery. As the GGH-HEC concentration increases, the moduli significantly rise, particularly in the 0.7 g sample (blue), which maintains high, stable G′ values across the frequency range, reflecting a strong, well-structured gel network. In

contrast, the 0.5 g sample shows lower moduli and greater frequency sensitivity, suggesting a weaker, less crosslinked structure. The plateau observed at mid frequencies and the upward trend at higher frequencies highlight the gel's resilience under dynamic conditions. Overall, the combined effect of HEC and nutrient addition enhances the viscoelastic properties of GGH hydrogels in a concentration-dependent manner, making higher concentration formulations especially suitable for applications requiring consistent elasticity and structural integrity, such as in biomedical, food, or pharmaceutical systems.

The two graphs (5.9 and 5.10) present frequency sweep test results for GGH-HEC hydrogels at concentrations of 10, 12, and 14 mg/cm³, with the first figure showing samples without nutrient supplementation and the second including 1 mL of nutrient. In both graphs, the storage modulus (G′) is consistently higher than the loss modulus (G″), indicating dominant elastic (solid-like) behaviour across all concentrations and frequencies. Both sets of data exhibit a characteristic U-shaped trend in G′ and G″, especially at lower concentrations, where moduli decrease at low frequencies due to structural relaxation and rise again at higher frequencies as elastic recovery takes over. However, a key difference is that the nutrient-supplemented samples (second graph) show significantly higher G′ and G″ values across all concentrations, particularly at 0.6 and 0.7 g, along with flatter curves that suggest reduced frequency sensitivity and enhanced gel stability. The 0.7 g nutrient-enhanced sample demonstrates the most robust and stable network, while the 0.5 g sample in both graphs remains the weakest, although the nutrient addition still improves its structural performance. Overall, the inclusion of nutrients strengthens the hydrogel matrix and enhances its resilience under dynamic stress, making it more suitable for applications demanding consistent mechanical properties.

5.2.1.5 Frequency sweep test for 10,12 and 14 GGH-CMC

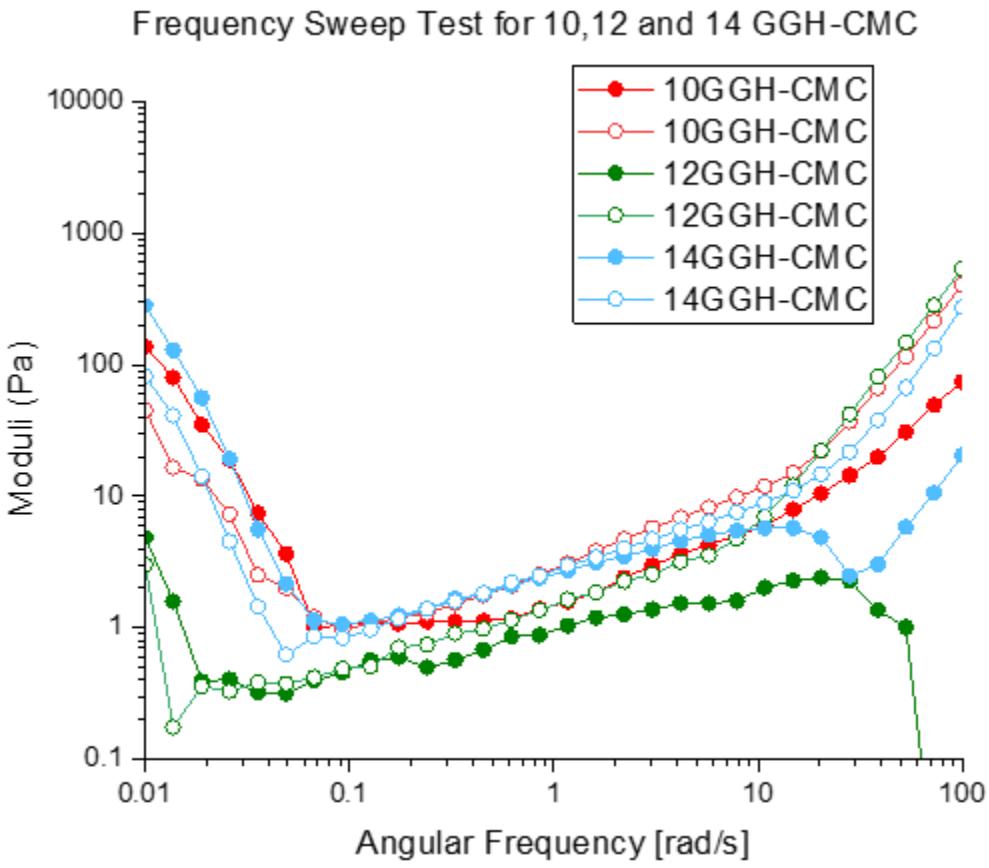

Figure 5.11: Graph showing the standard frequency sweep test results for 10,12 and 14 mg/cm3 of GGH-CMC. in the LVE domain with change in frequency from 100 $s^{-1}$to 0.1 s^{-1} (gels age =3 days, T = 20 ◦C).

Figure 5.11 displays the frequency sweep test results for gellan gum–carboxymethyl cellulose (GGH-CMC) hydrogels at concentrations of 10, 12, and 14 mg/cm³, conducted within the Linear Viscoelastic (LVE) region at 20°C after 3 days of aging. The graph plots both storage modulus (G′) and loss modulus (G″) over a frequency range of 0.01 to 100 rad/s. Across all concentrations, a characteristic V-shaped trend is observed in both G′ and G″: moduli initially decrease with decreasing frequency due to structural relaxation, reach a minimum at intermediate frequencies, and then increase again at higher frequencies, indicating elastic recovery. Notably, none of the samples display G′ consistently above G″ across the full frequency range, suggesting that these hydrogels have a more viscous-dominated response compared to their HEC or nutrient-enriched counterparts. The 0.6 g sample (green) again shows the lowest overall moduli and irregularities at higher frequencies, indicating weaker gel formation or potential instability. In contrast, the 0.5 g and 0.7 g samples maintain relatively stronger responses, although still exhibiting frequency-sensitive viscoelasticity. Overall, these

results suggest that GGH-CMC hydrogels, without nutrient addition, form weaker and more frequency-dependent gel structures.

5.2.1.6 Frequency sweep test for 10,12 and 14 GGH-CMC-MG

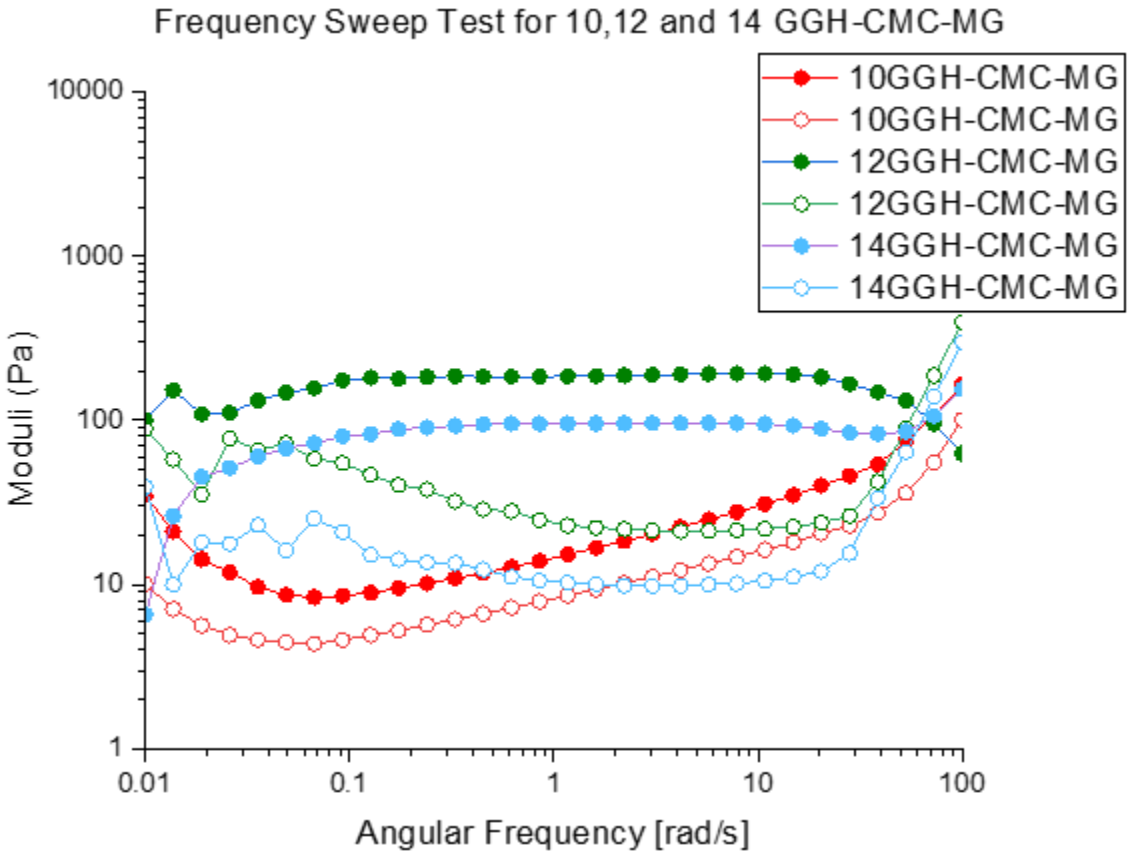

Figure 5.12: Graph showing the standard frequency sweep test results for 10,12 and 14 mg/cm3 of GGH-CMC-MG. in the LVE domain with change in frequency from 100 s^{-1} to 0.1 s^{-1} (gels age =3 days, T = 20 ◦C).

Figure 5.12 presents the frequency sweep test results for GGH-CMC hydrogels at concentrations of 10, 12, and 14 mg/cm³, each supplemented with 1 mL of nutrient, tested in the Linear Viscoelastic (LVE) domain at 20°C after 3 days of aging. The graph shows storage modulus (G′) and loss modulus (G″) as functions of angular frequency (0.01 to 100 rad/s). The curves reveal distinct viscoelastic behaviour, with moduli displaying a generally non-monotonic trend. The 0.6 g sample (green) exhibits the highest and most stable G′ values, indicating the strongest gel structure, particularly at low and mid frequencies, followed by a decrease at high frequencies. In contrast, the 0.5 g (red) and 0.7 g (blue) samples demonstrate lower and more variable G′ and G″ values, with pronounced frequency sensitivity. The data suggest that nutrient addition significantly influences gel behaviour, enhancing network

strength and stability in the 0.6 g formulation, while the other concentrations show less consistent performance. This implies an optimal gellan-CMC-to-nutrient ratio near 12 mg/cm³ for achieving the most resilient and elastic hydrogel structure under dynamic conditions.

5.2.2 Complex viscosity

Complex viscosity (η*) is a rheological parameter that describes how a viscoelastic material (like a hydrogel) resists deformation when subjected to oscillatory (dynamic) shear. It reflects a combination of elastic (solid-like) and viscous (liquid-like) behaviour (277). η* is derived from oscillatory tests, where the material is deformed in a back-and-forth motion (not a continuous flow).

During an oscillatory frequency sweep test, the material is subjected to a constant small strain ensuring it remains within the Linear Viscoelastic (LVE) range, while the angular frequency is systematically varied. This test measures how the storage modulus (G′), loss modulus (G″), and phase angle respond to these changes in frequency. Using the recorded values of G′ and G″ at each frequency, the complex viscosity (η*) can then be calculated, providing insight into the material's resistance to deformation under oscillatory shear conditions.

The following equation shows the ratio of the complex shear modulus G* to the frequency, which is

$$\eta^* = G^* / \omega \qquad \textit{Equation 1.8}$$

The values of (η*) for GGH, GGH + 1mL of nutrient, GGH-HEC, GGH-HEC I mL of nutrient, GGH-CMC and GGH-CMC 1mL of nutrient composite hydrogels for all samples obtained from frequency sweep test are presented in figures 5.13 to 5-18. It is a graph that displays complex viscosity (Pa) on the Y-axis and angular frequency (rad/s) on the X-axis, with both axes presented on a logarithmic scale.

5.2.2.1 Complex viscosity for 10,12 and 14 GGH

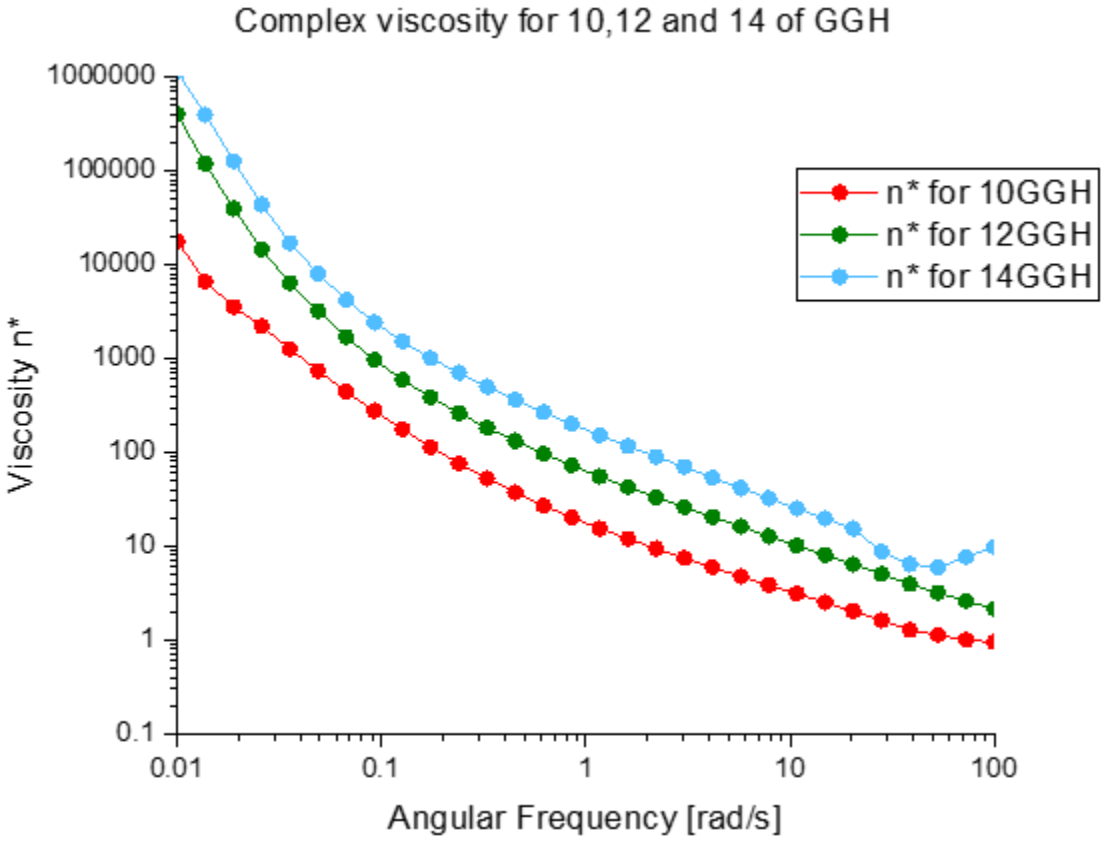

Figure 5.13: Shows how complex viscosity (η) changes with angular frequency (ω) from 100 to 0.01 rad/s for GGH composite hydrogels at concentrations of 10, 12, and 14 GGH. We set the treatment time at 3 days. The graph shows information for three amounts of GGH: 10, 12, and 14, with both axes using a logarithmic scale (base 10), a steady shear strain of γ = 1%, and a temperature of T = 20°C.*

Across all samples, complex viscosity decreases with increasing frequency, showing the typical shear-thinning behaviour characteristic of viscoelastic materials. The 0.7 g sample exhibits the highest viscosity across the entire frequency range, indicating a denser, more structured gel network, while the 0.5 g sample has the lowest viscosity, suggesting a weaker internal structure. The curves remain smooth and well-separated, highlighting a clear concentration-dependent effect, where increased GGH content leads to greater resistance to deformation. This result confirms that higher GGH concentrations enhance the mechanical strength and viscoelastic resistance of the hydrogel, making them more suitable for applications requiring structural integrity under dynamic conditions.

5.2.2.2 Complex viscosity for 10,12 and 14 GGH-MG

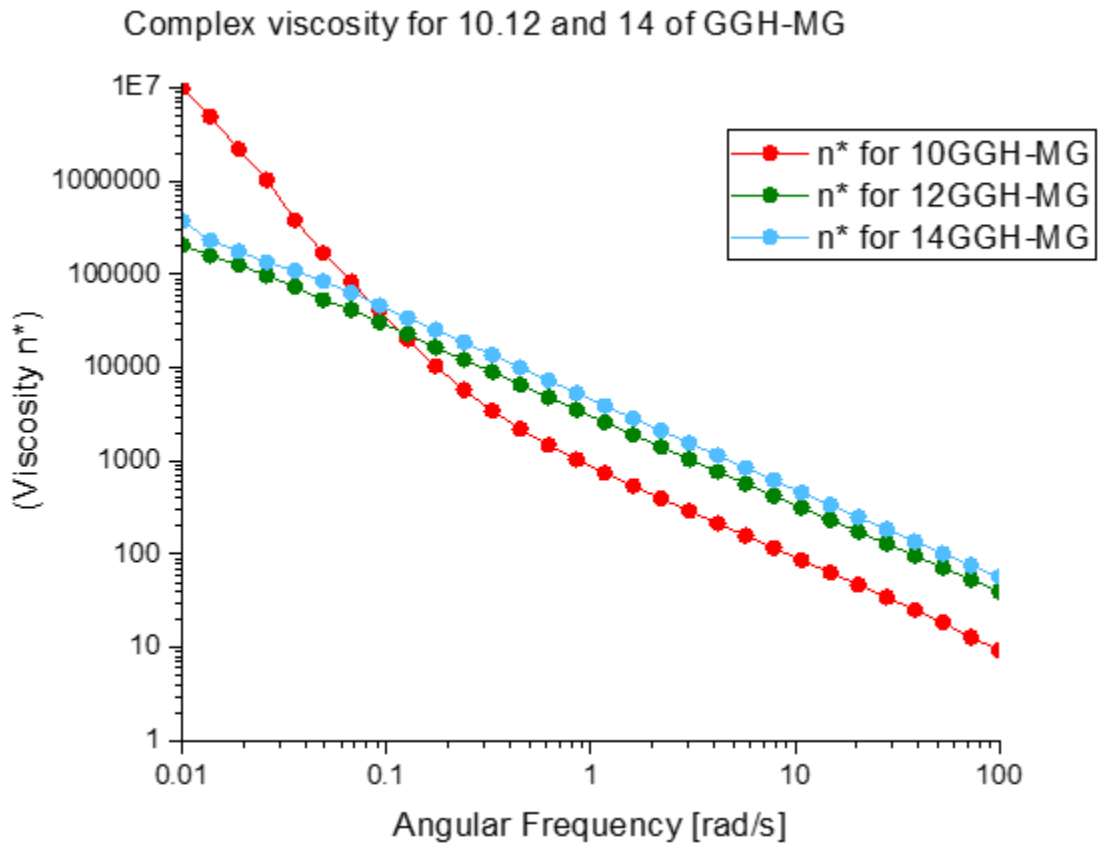

Figure 5.14: Shows how complex viscosity (η) changes with angular frequency (ω) from 100 to 0.01 rad/s for GGH-MG composite hydrogels at concentrations of 10, 12, and 14 GGH. We set the treatment time at 3 days. The graph shows information for three amounts of GGH: 10, 12, and 14, with both axes using a logarithmic scale (base 10), a steady shear strain of γ = 1%, and a temperature of T = 20°C.*

In both cases, the curves display typical shear-thinning behaviour, where viscosity decreases as angular frequency increases, indicating that the material becomes less resistant to deformation under faster oscillatory stress. However, a clear distinction is observed between the two graphs. In the nutrient-free system, viscosity values are lower across all concentrations (0.5, 0.6, 0.7 g), with broader separation between curves, especially at low frequencies. Higher GGH concentrations generally lead to increased complex viscosity, with the 0.7 g sample showing the highest values over most of the frequency range, while a deviation is observed for the 10 mg/cm³ sample at low frequencies.Conversely, the nutrient-enhanced system (Figure 5.13 with nutrients) shows dramatically increased complex viscosity, particularly at low frequencies. The curves are more closely aligned, suggesting that the presence of nutrients reduces the concentration dependence, likely by promoting additional interactions or crosslinking that enhance the uniformity of the gel structure. Interestingly, the 0.5 g sample

with nutrients surpasses even the 0.7 g sample without nutrients in viscosity at low frequencies, highlighting the significant reinforcing effect of nutrient inclusion.

5.2.2.3 Complex viscosity for 10,12 and 14 GGH-HEC

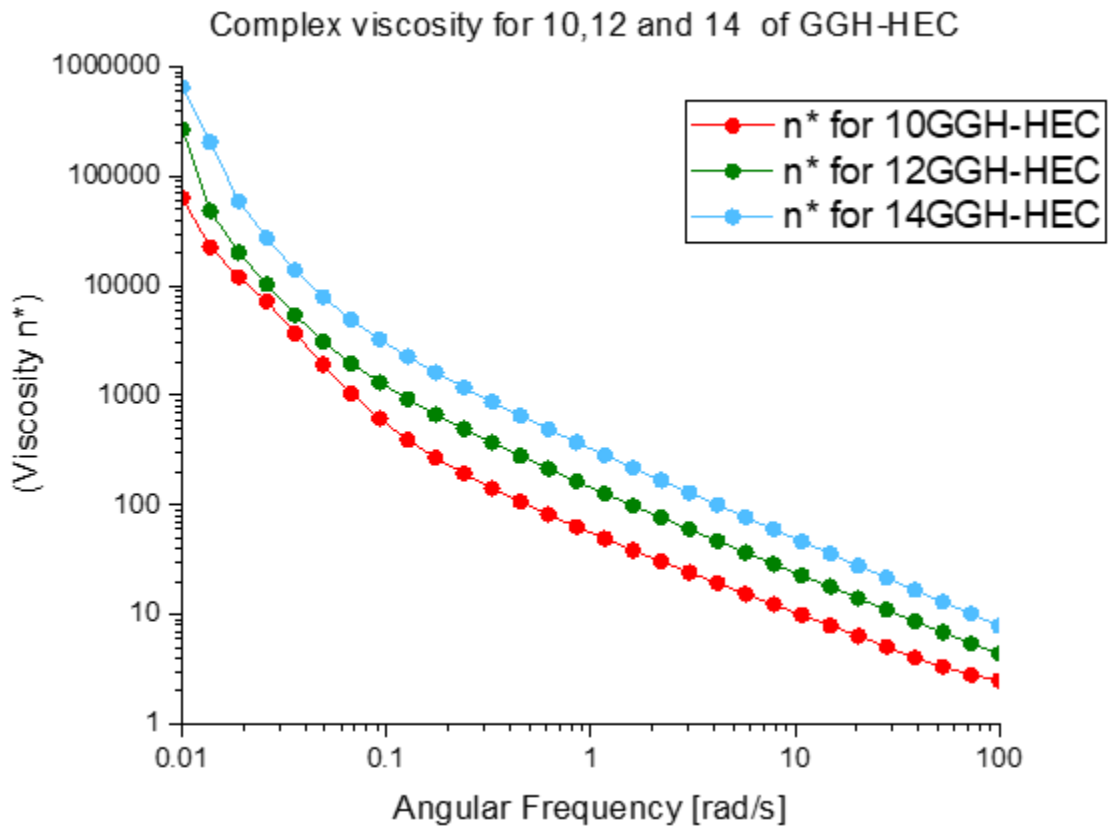

Figure 5.15: Shows how complex viscosity (η) changes with angular frequency (ω) from 100 to 0.01 rad/s for GGH-HEC composite hydrogels at concentrations of 10, 12, and 14 GGH-HEC. We set the treatment time at 3 days. The graph shows information for three amounts of GGH: 10, 12, and 14, with both axes using a logarithmic scale (base 10), a steady shear strain of γ = 1%, and a temperature of T = 20°C.*

All three curves representing 10,12 and 14 mg/cm^3 concentrations exhibit a shear-thinning behaviour, where complex viscosity decreases consistently with increasing frequency. This indicates that GGH-HEC gels become less resistant to deformation under faster oscillatory conditions. The 0.7 g sample consistently shows the highest viscosity across the entire frequency range, suggesting a stronger, more cohesive gel network, while the 0.5 g sample exhibits the lowest viscosity, pointing to a less structured material. The moderate spacing between the curves reflects a clear concentration-dependent effect, with complex viscosity increasing in parallel with GGH-HEC content. These findings demonstrate that incorporating HEC into gellan gum enhances the viscoelastic structure and flow resistance of the hydrogel,

making it more suitable for applications requiring both mechanical strength and dynamic stability.

5.2.2.4 Complex viscosity for 10,12 and 14 GGH-HEC-MG

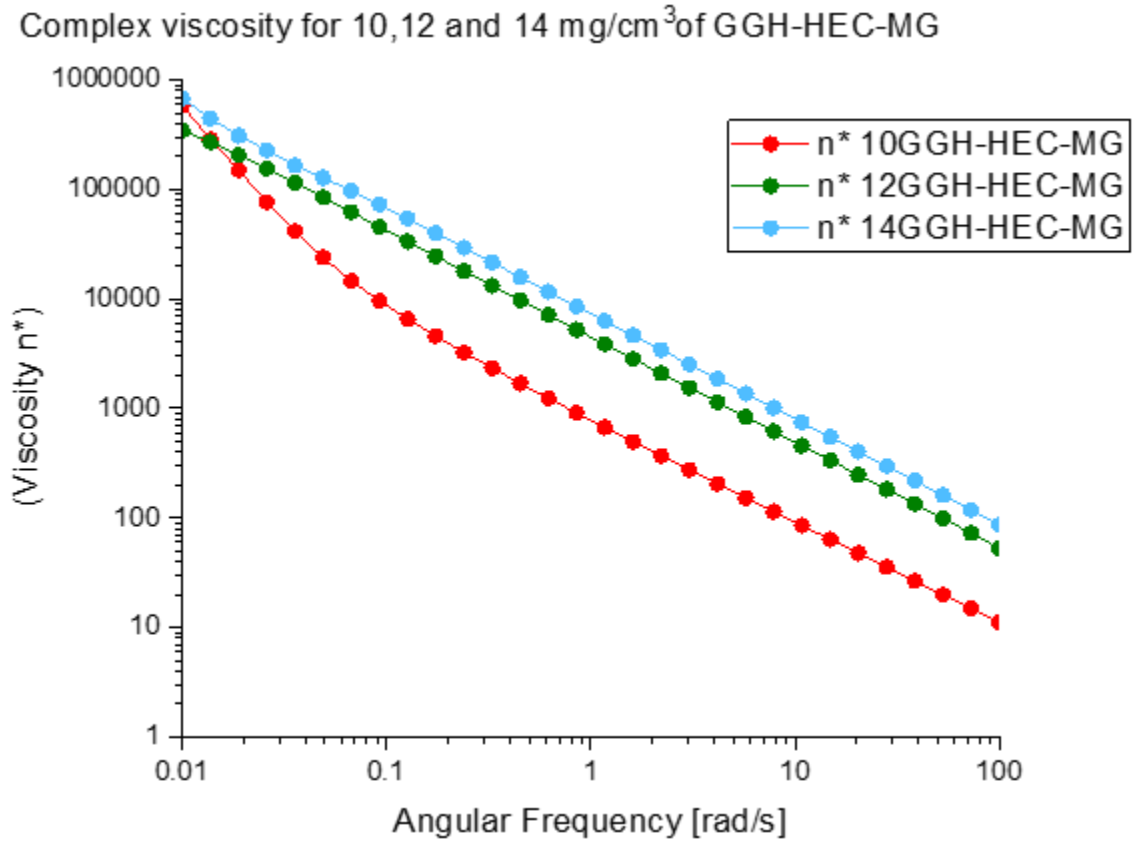

Figure 5.16: Shows how complex viscosity (η) changes with angular frequency (ω) from 100 to 0.01 rad/s for GGH -HEC-MG composite hydrogels at concentrations of 10, 12, and 14 GGH. We set the treatment time at 3 days. The graph shows information for three amounts of GGH: 10, 12, and 14, with both axes using a logarithmic scale (base 10), a steady shear strain of γ = 1%, and a temperature of T = 20°C.*

All samples exhibit shear-thinning behaviour, characterised by a steady decrease in viscosity with increasing frequency. Notably, the curves are smoother and more parallel compared to non-supplemented samples, indicating that the addition of nutrients enhances structural uniformity and flow stability. The 0.7 g sample shows the highest viscosity across all frequencies, reflecting a more resistant and cohesive gel network, while the 0.5 g sample consistently demonstrates the lowest values. These results highlight the combined role of HEC and nutrient enrichment in significantly reinforcing the hydrogel structure, improving its mechanical strength and resistance to deformation under dynamic conditions.

5.2.2.5 Complex viscosity for 10,12 and 14 GGH-CMC

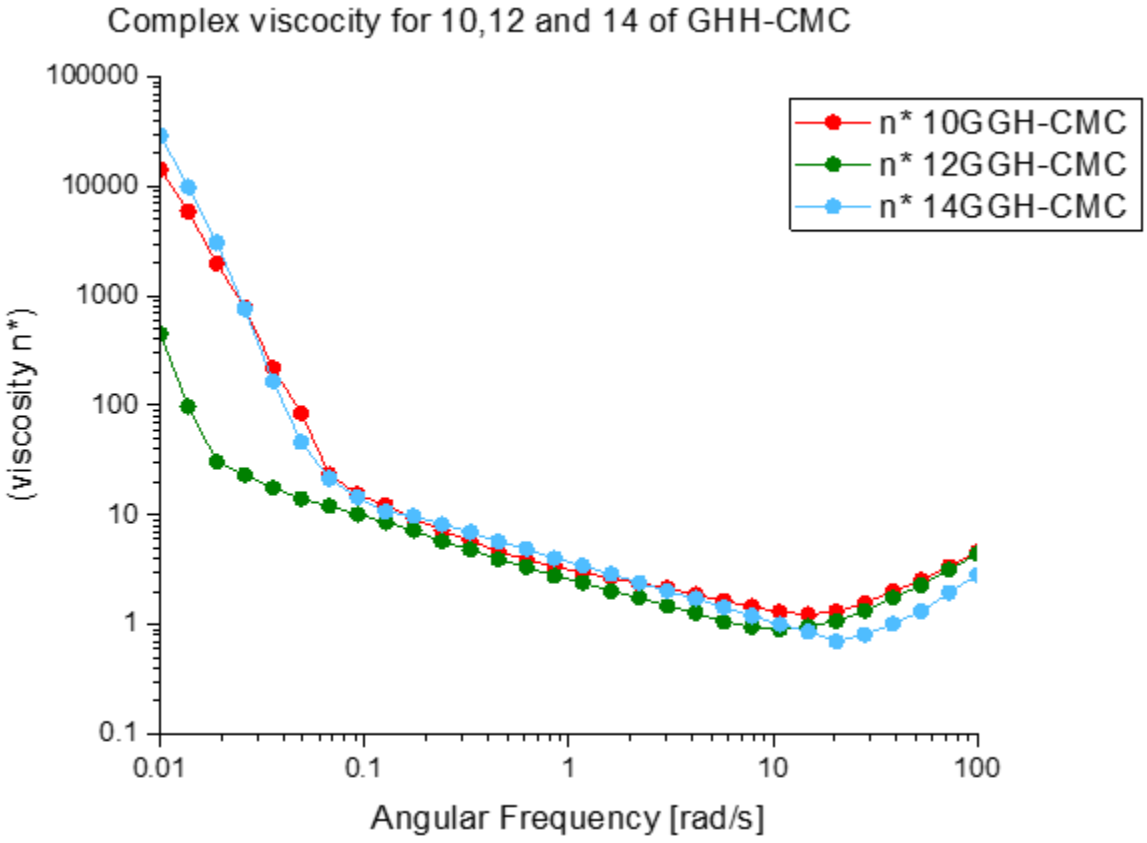

Figure 5.17: Shows how complex viscosity (η) changes with angular frequency (ω) from 100 to 0.01 rad/s for GGH -CMC composite hydrogels at concentrations of 10, 12, and 14 GGH. We set the treatment time at 3 days. The graph shows information for three amounts of GGH: 10, 12, and 14, with both axes using a logarithmic scale (base 10), a steady shear strain of γ = 1%, and a temperature of T = 20°C.*

The viscosity curves exhibit nonlinear shear-thinning behaviour, with complex viscosity (η*) decreasing with increasing angular frequency across all concentrations. Overall, the curves display very similar trends, indicating comparable viscoelastic behaviour among the different GGH–CMC formulations. A slight deviation is observed for the 0.6 g sample (green) at low frequencies, where a shallow minimum in viscosity appears; however, this behaviour is confined to a narrow frequency range and may reflect experimental variability or increased sensitivity at low frequencies rather than a fundamental difference in gel structure. Consequently, while all samples demonstrate frequency-dependent behaviour, the present data do not support strong conclusions regarding systematic differences in gel strength or network cohesion as a function of concentration under these conditions.

5.2.2.6 Complex viscosity for 10,12 and 14 GGH-CMC-MG

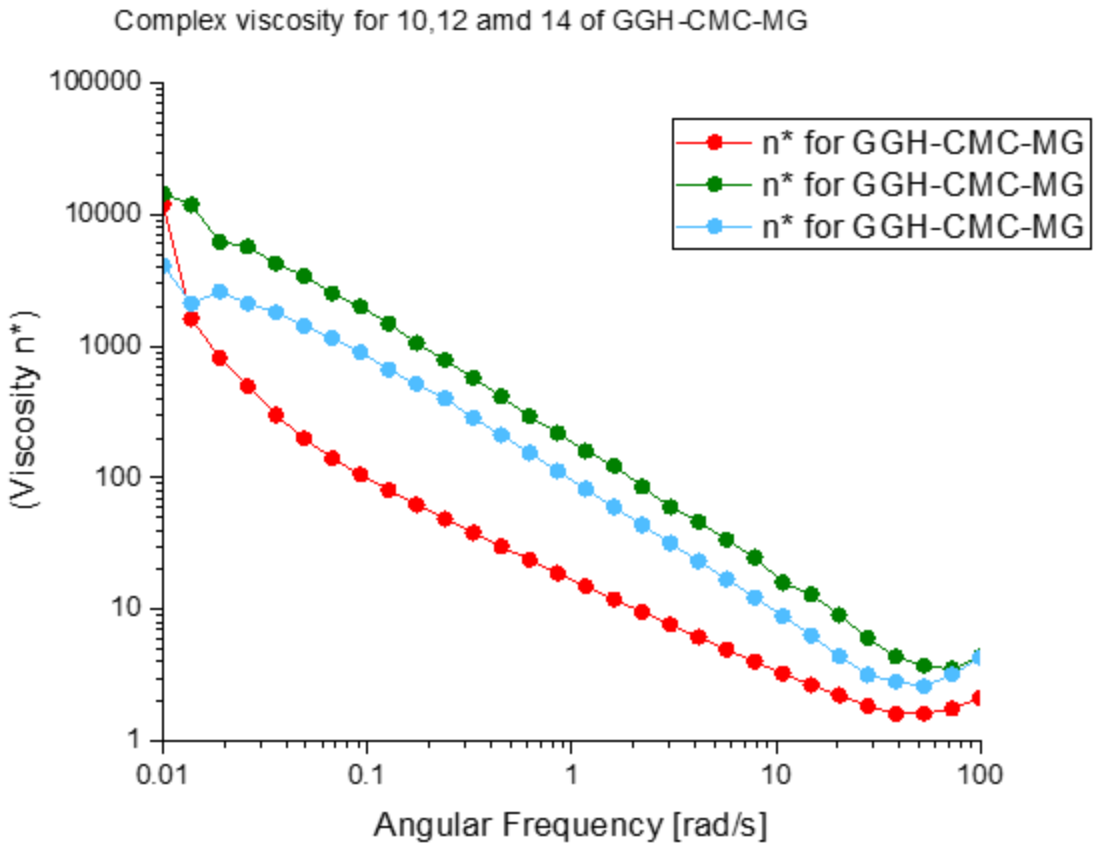

Figure 5.18: Shows how complex viscosity (η) changes with angular frequency (ω) from 100 to 0.01 rad/s for GGH CMC-MG composite hydrogels at concentrations of 10, 12, and 14 GGH-. We set the treatment time at 3 days. The graph shows information for three amounts of GGH: 10, 12, and 14, with both axes using a logarithmic scale (base 10), a steady shear strain of γ = 1%, and a temperature of T = 20°C.*

The viscosity curves exhibit nonlinear shear-thinning behaviour, characterised by a decrease in complex viscosity (η*) with increasing angular frequency, followed by a broad plateau at intermediate frequencies. Overall, the curves for different concentrations are very similar, indicating comparable viscoelastic behaviour across the formulations. While the 0.6 g sample (green) shows a slightly more pronounced minimum in viscosity at low frequencies, this deviation is limited to a narrow frequency range and may reflect experimental variability rather than a fundamental difference in gel structure. Consequently, although all GGH–CMC formulations exhibit frequency-sensitive behaviour, the available data do not support a strong or systematic dependence of gel strength on concentration under these conditions.

5.2.3 Complex shear modulus (G*) and complex Young's modulus (E*)

In material science and engineering, understanding the mechanical properties of materials is crucial for predicting their behaviour under various stress and strain conditions. Two important parameters in this context are the complex shear modulus (G*) and the complex Young's modulus (E*). These moduli incorporate both the elastic (storage) and viscous (loss) components of material behaviour, providing a comprehensive view of the material's dynamic mechanical characteristics under oscillatory loading conditions. The complex shear modulus (G*) and complex Young's modulus (E*) are fundamental parameters for characterizing the viscoelastic behaviour of materials under oscillatory loading. These moduli incorporate both elastic (storage) and viscous (loss) components, offering a comprehensive view of how materials deform and dissipate energy.

The Complex Shear Modulus (G*) is a fundamental rheological parameter used to describe how a viscoelastic material responds to oscillatory shear deformation. It combines both the elastic (energy-storing) and viscous (energy-dissipating) components of a material's mechanical behaviour.

The complex shear modulus (G*) is employed to characterise the behaviour of viscoelastic materials. G* is derived from G' and G'' as illustrated in the equation 2 below. The complex shear modulus is defined as:

$$G^* = G' + i\,G'' \qquad \textit{Equation 5.1}$$

Where G' is the storage modulus representing energy stored elastically, and G'' is the loss modulus representing energy dissipated as heat. The complex shear modulus is defined as:

$$G^* = \sqrt{G'^2 + G''^2} \qquad \textit{Equation 5.2}$$

Similarly, the complex Young's modulus is given by:

$$E^* = 2G^*(1 + \nu\ ) \qquad \textit{Equation 5.3}$$

where ν is Poisson's ratio. These relationships are crucial in fields such as polymer processing, biomedical engineering, and asphalt mechanics, enabling engineers and scientists to assess a material's stiffness, damping ability, and mechanical performance under real-world dynamic conditions. The Poisson's ratio (ν) of gellan gum (GG) hydrogels depends on their concentration, crosslinking, and hydration level, but for most practical and modelling purposes, it is commonly assumed to be close to that of incompressible soft hydrated materials. This

range reflects the near-incompressible nature of gellan gum hydrogels due to their high-water content (typically >95%). A value of ν = 0.5 is often used in rheological or mechanical modelling to simplify analysis, as it represents a perfectly incompressible material (common in gels and soft biological tissues) (278, 279). For hydrated, soft gellan gum hydrogels, assuming ν ≈ 0.5 is appropriate and widely accepted in the literature.

The reported values were obtained from oscillatory rheological measurements within the linear viscoelastic region. G′ and G″ values correspond to representative values extracted at a fixed angular frequency within the plateau region, and G* was calculated using the standard relation as the above equation

The Young's modulus (E*) was subsequently estimated assuming isotropic elastic behaviour.

Table 5.7: The results of complex shear moduli (G) and Young's shear moduli (E*) for both GGH and modified GGH-MG composite hydrogels at concentrations of 10, 12, and 14 mg/cm³.*

Hydrogel	G' (Pa)	G'' (Pa)	G* (Pa)	E* (Pa)
10 GGH	35.6	19.5	40.5	121.5
12 GHH	293.1	119.9	316.7	950.0
14 GGH	859.4	305.8	912.1	2736.4
10 GGH-MG	1825.0	357.8	1859.8	5579.3
12 GHH-MG	464.5	566.3	732.5	2197.4
14 GGH-MG	4579.1	930.1	4672.6	14017.7

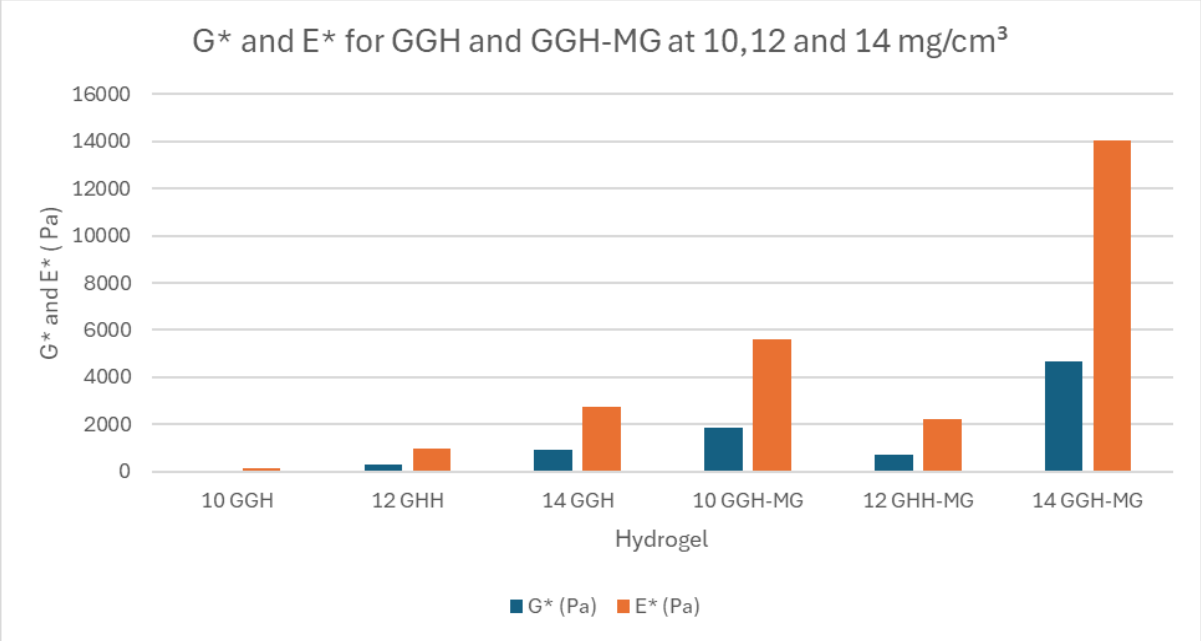

Figure 5.19: shows the calculated complex shear moduli (G) and Young's shear moduli (E*) for both GGH and modified GGH-MG composite hydrogels at concentrations of 10, 12, and 14 mg/cm³.*

Figure 5.19 and Table 5.7 compare the mechanical properties of GGH and GGH-MG hydrogels through their complex shear modulus (G*) and Young's shear modulus (E*) at concentrations of 10, 12, and 14 mg/cm³. For the native GGH system, both G* and E* increase monotonically with concentration, indicating progressive stiffening of the gel network with increasing polymer content. In contrast, the GGH-MG system does not exhibit a strictly monotonic trend between 10 and 12 mg/cm³, where a reduction in both G* and E* is observed at 12 mg/cm³ compared to 10 mg/cm³. However, a pronounced increase in both moduli occurs at 14 mg/cm³, yielding the highest stiffness values overall. Despite this non-linear concentration dependence, GGH-MG hydrogels consistently exhibit substantially higher G* and E* values than their GGH counterparts at equivalent concentrations, demonstrating the reinforcing effect of MG incorporation. Notably, at 14 mg/cm³, GGH-MG reaches a G* of approximately 4673 Pa and an E* of approximately 14,018 Pa, far exceeding the corresponding GGH values (~912 Pa and ~2736 Pa). These results indicate that MG significantly enhances the elastic and structural integrity of gellan gum hydrogels, particularly at higher polymer concentrations, while intermediate compositions may be influenced by competing network interactions or structural heterogeneity.

Table 5.8: The results of complex shear moduli (G) and Young's shear moduli (E*) for both GGH-HEC and modified GGH-HEC-MG composite hydrogels at concentrations of 10, 12, and 14 mg/cm³.*

Hydrogel	G' (Pa)	G'' (Pa)	G* (Pa)	E* (Pa)
10 GGH-HEC	114.9	54.9	127.3	381.9
12 GHH-HEC	289.0	120.9	313.3	939.8
14 GGH-HEC	715.7	240.3	754.9	2264.8
10 GGH-HEC-MG	1341.1	344.1	1384.6	4153.7
12 GHH-HEC-MG	4474.5	727.0	4533.2	13599.6
14 GGH-HEC-MG	7204.7	1243.7	7311.3	21933.9

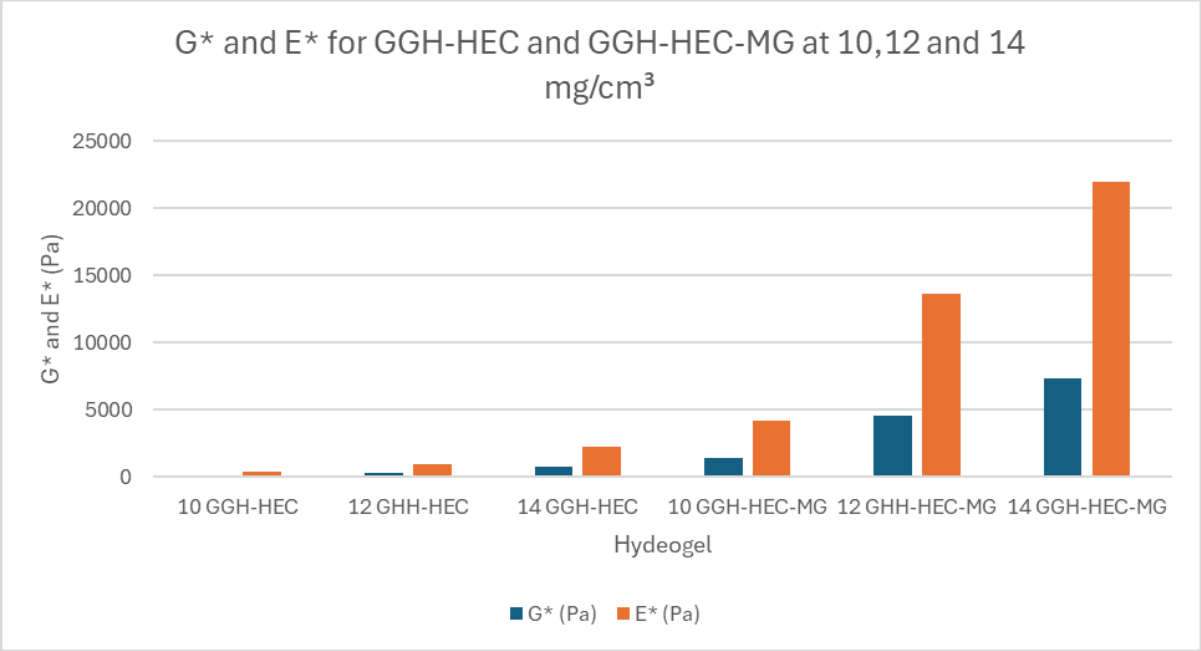

Figure 5.20: Shows the calculated complex shear moduli (G) and Young's shear moduli (E*) for both GGH-HEC and modified GGH-HEC-MG composite hydrogels at concentrations of 10, 12, and 14 mg/cm³.*

Figure 5.20 and Table 5.8 compare the mechanical properties of GGH-HEC and GGH-HEC-MG hydrogels across increasing concentrations, focusing on complex shear modulus (G*) and Young's modulus (E*). Both G* and E* increase with concentration for all samples, with GGH-HEC-MG hydrogels showing significantly higher values than their GGH-HEC counterparts. At 14 mg/cm³, GGH-HEC-MG reaches a G* of ~7311 Pa and an E* of ~21,934 Pa, nearly ten times the corresponding GGH-HEC values (~755 Pa and ~2265 Pa, respectively). These results clearly demonstrate that the incorporation of MG into GGH-HEC substantially enhances the gel's stiffness and mechanical integrity, particularly at higher concentrations, making them potentially more suitable for applications requiring high strength and stability.

Table 5.9: The results of complex shear moduli (G) and Young's shear moduli (E*) for both GGH-CMC and modified GGH-CMC-MG composite hydrogels at concentrations of 10, 12, and 14 mg/cm³.*

Hydrogel	G' (Pa)	G'' (Pa)	G* (Pa)	E* (Pa)
10 GGH-CMC	17.6	34.5	38.7	116.0
12 GHH-CMC	1.1	38.9	38.9	116.7
14 GGH-CMC	19.8	165.6	166.8	500.3
10 GGH-CMC-MG	29.8	15.6	33.7	101.0
12 GHH-CMC-MG	162.5	57.0	172.2	516.5
14 GGH-CMC-MG	83.8	30.6	89.2	267.5

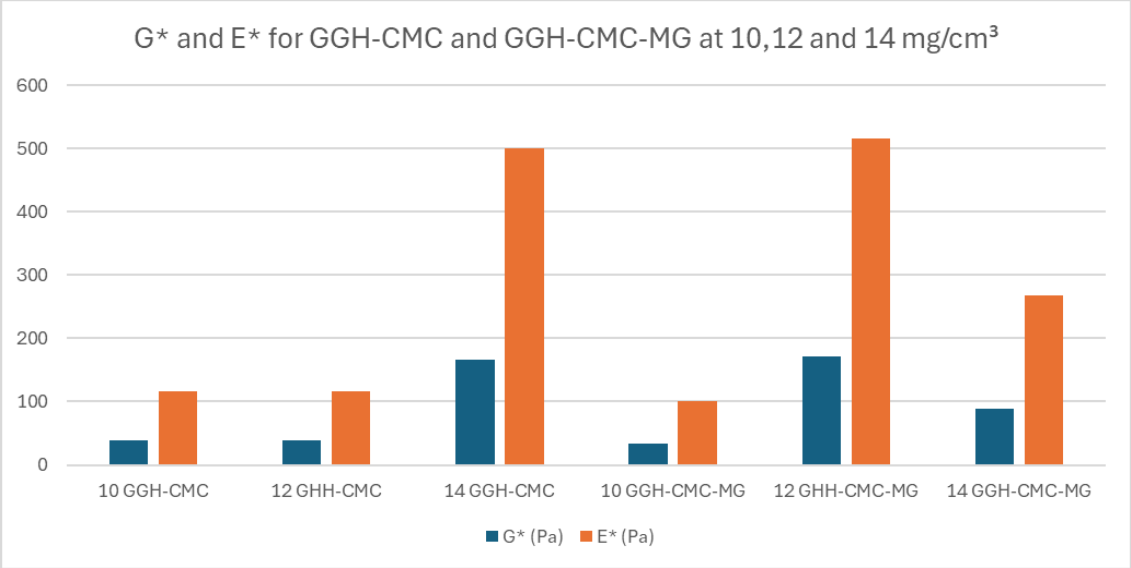

Figure 5.21: Shows the calculated complex shear moduli (G) and Young's shear moduli (E*) for both GGH-CMC and modified GGH-CMC-MG composite hydrogels at concentrations of 10, 12, and 14 mg/cm³.*

Figure 5.21 and Table 5.9 illustrate the mechanical properties of GGH-CMC and GGH-CMC-MG hydrogels, revealing non-monotonic trends in the complex shear modulus (G*) and Young's modulus (E*) with concentration. For GGH-CMC, the moduli at 10 and 12 mg/cm³ are very similar (G* ≈ 39 Pa, E* ≈ 116 Pa), indicating that increasing concentration within this range has a negligible effect on stiffness. A marked increase is observed at 14 mg/cm³ (G* ≈ 167 Pa, E* ≈ 500 Pa), suggesting enhanced network rigidity only at higher polymer content. For GGH-CMC-MG, the highest G* (~172 Pa) and E* (~517 Pa) values occur at 12 mg/cm³, while the 14 mg/cm³ sample exhibits lower moduli. This non-monotonic behaviour may indicate either a reduction in effective network connectivity at higher MG loading or an anomalous experimental result. Given the limited number of concentrations examined, this decrease cannot be conclusively attributed to structural instability. Overall, MG incorporation enhances stiffness at moderate concentrations; however, its reinforcing effect does not scale linearly with polymer concentration, highlighting the importance of concentration optimisation in GGH-CMC-MG hydrogel formulation

5.3 Rotational Shear Strength

The third test conducted was the rotational shear strength test, designed to evaluate the shear strength of the composite hydrogels: GGH, GGH-MG, GGH-HEC, GGH-HEC-MG, GGH-CMC, and GGH-CMC-MG. During this assessment, samples were subjected to shear deformation with a strain amplitude of up to 500%, applied at a constant shear rate of $\dot{\gamma}$=0.1 s^{-1}

The temperature was maintained at a constant T = 20 ˚C throughout the experiment. Shear stress was recorded as a function of shear strain to characterize the mechanical response of the materials. The results of this test are illustrated in Figures 5.22 to 5.27, where shear stress (Pa) is plotted against shear strain (%). Shear stress (in Pascals) is plotted on the Y-axis, while shear strain (expressed as a percentage) is shown on the X-axis

5.3.1 Rotational Shear Strength test for 10,12 and 14 mg/cm^3 of GGH

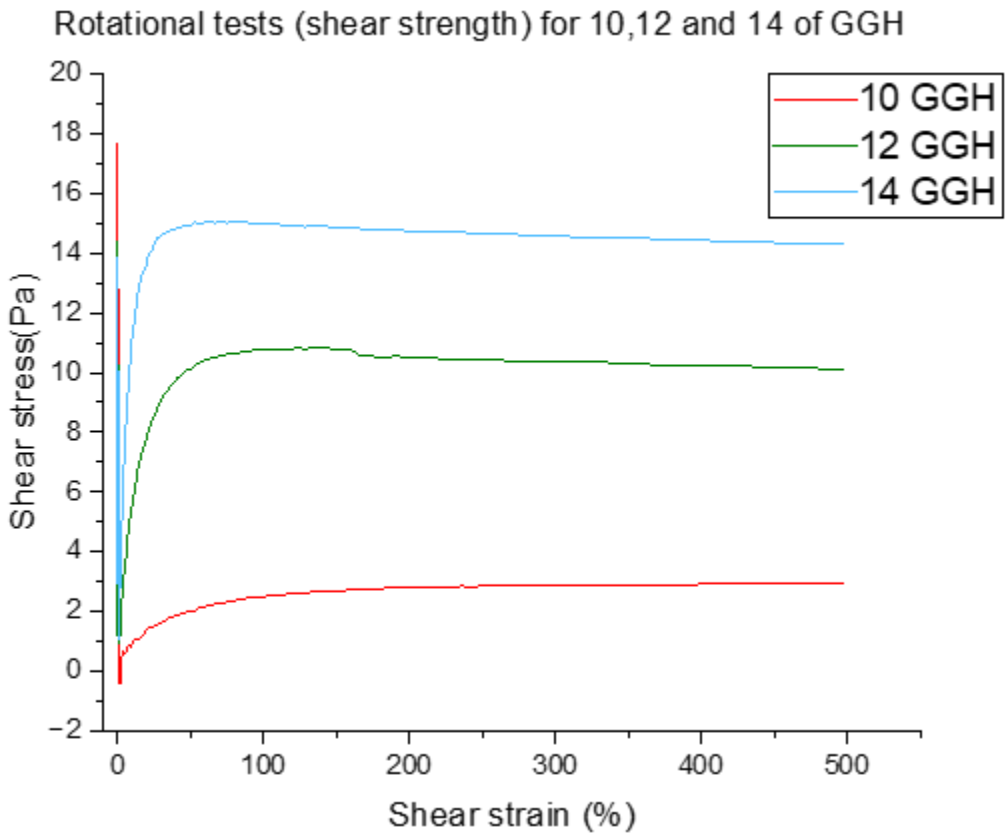

Figure 5.22: Rotational Shear Strength of GGH at 10, 12, and 14 mg/cm³ with a Constant Strain Rate of 0.1 s^{-1} and Temperature of 20°C.

Figure 5.22 shows the shear stress–shear strain relationship for GGH at concentrations of 10, 12, and 14 mg/cm³, tested at a constant strain rate of 0.1 s^{-1} and temperature of 20°C. All samples exhibit an initial sharp increase in shear stress followed by a plateau, indicating yielding and steady flow under shear. Higher GGH concentrations result in greater shear stress responses, with the 14 mg/cm³ sample showing the highest resistance to deformation and the 10 mg/cm³ sample the lowest. This suggests that increasing GGH concentration enhances the gel's structural integrity and shear strength.

5.3.2 Rotational Shear Strength test for 10,12 and 14 mg/cm³ of GGH-MG

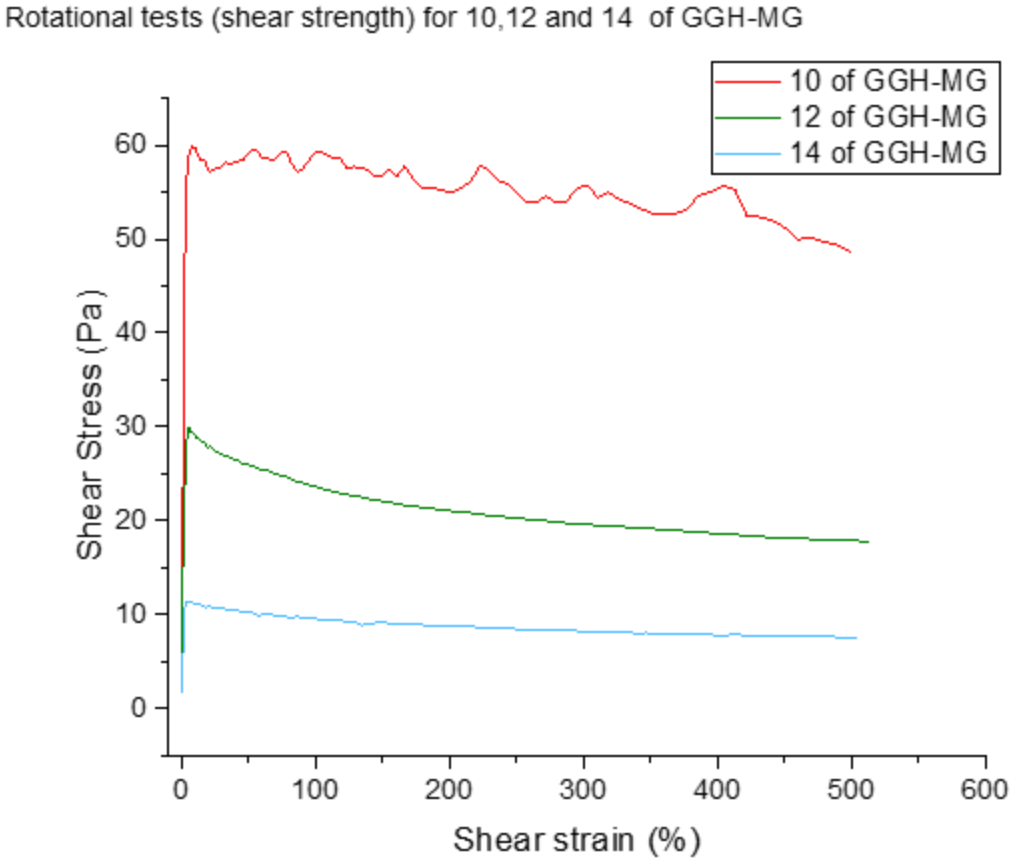

Figure 5.23: Rotational Shear Strength of GGH-MG at 10, 12, and 14 mg/cm³ with a Constant Strain Rate of 0.1 s^{-1} and Temperature of 20°C.

Figure 5.23 presents the shear stress–shear strain behaviour of GGH-MG at concentrations of 10, 12, and 14 mg/cm³, tested at a constant strain rate of 0.1 s^{-1} and temperature of 20°C. All samples show an initial sharp increase in shear stress, followed by different stress responses based on concentration. Interestingly, the 10 mg/cm³ sample exhibits the highest and most sustained shear stress, while higher concentrations (12 and 14 mg/cm³) show progressively lower stress values. This inverse trend suggests that increasing the concentration of GGH-MG may weaken the gel structure, possibly due to altered cross-linking or phase separation, indicating that the addition of MG modifies the mechanical response compared to pure GGH.

5.3.3 Rotational Shear Strength test for 10,12 and 14 mg/cm^3 of GGH-HEC

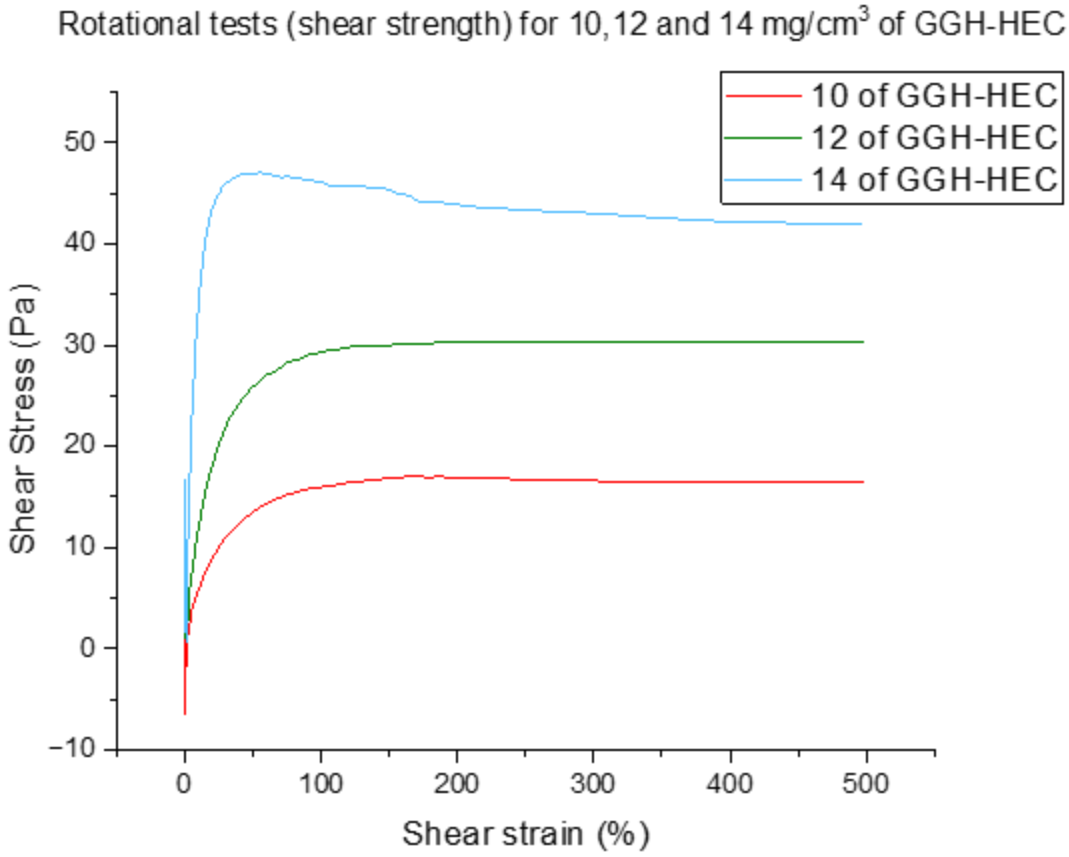

Figure 5.24: Rotational Shear Strength of GGH-HEC at 10, 12, and 14 mg/cm³ with a Constant Strain Rate of 0.1 s^{-1} and Temperature of 20°C.

Figure 5.24 displays the shear stress–shear strain behaviour of GGH-HEC at concentrations of 10, 12, and 14 mg/cm³, tested at a constant strain rate of 0.1 s^{-1} and temperature of 20°C. All samples show a sharp initial rise in shear stress followed by a plateau, indicating yielding and stable flow. As concentration increases, shear stress also increases, with the 14 mg/cm³ sample showing the highest resistance to deformation, followed by 12 mg/cm³ and then 10 mg/cm³. This suggests that higher GGH-HEC concentrations form stronger, more structurally stable gels, enhancing their shear strength under deformation.

5.3.4 Rotational Shear Strength test for 10,12 and 14 mg/cm^3 of GGH-HEC-MG

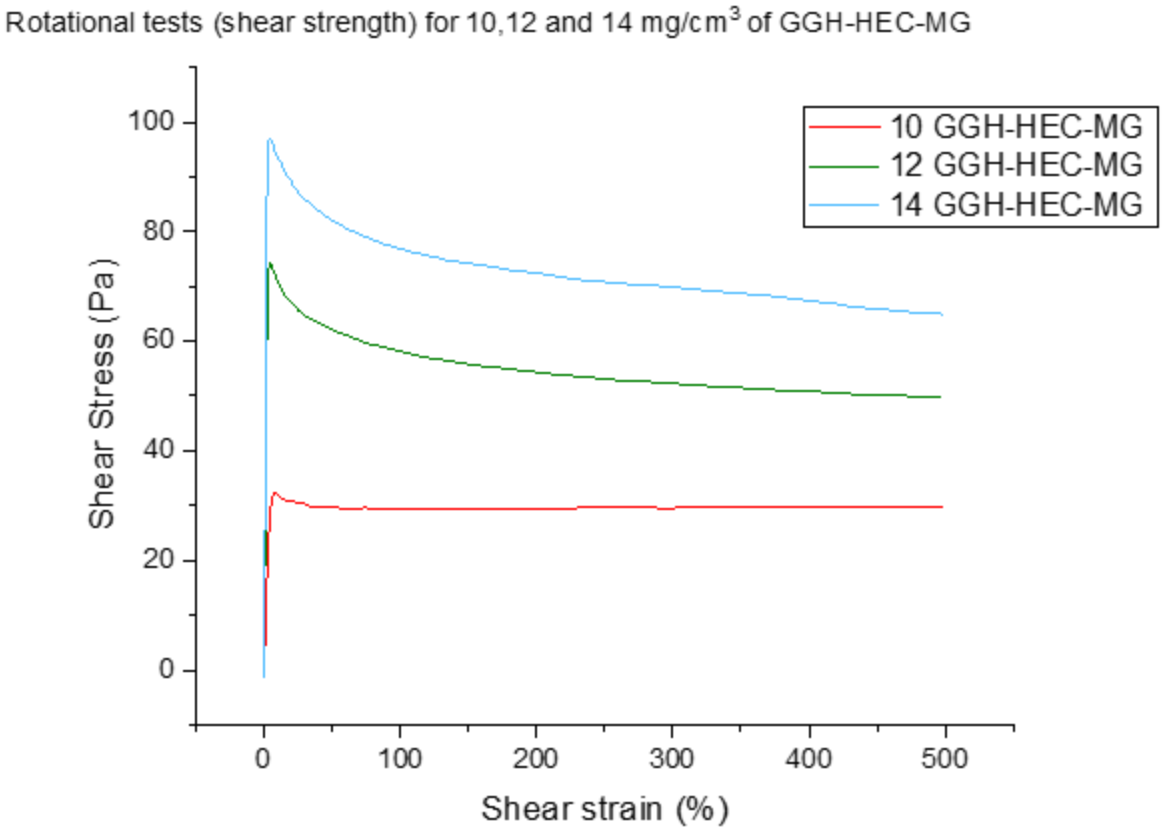

Figure 5.25: Rotational Shear Strength of GGH-HEC-MG at 10, 12, and 14 mg/cm³ with a constant strain rate of 0.1 s⁻¹ and Temperature of 20°C.

Figure 5.25 shows the shear stress–shear strain behaviour of GGH-HEC-MG at concentrations of 10, 12, and 14 mg/cm³, tested at a constant strain rate of 0.1 s^{-1} and temperature of 20°C. All samples exhibit a sharp initial peak in shear stress followed by a gradual decline to a stable plateau, indicating strong initial resistance and steady flow behaviour. The 14 mg/cm³ sample shows the highest shear strength, followed by 12 and then 10 mg/cm³, demonstrating that higher concentrations enhance both initial and sustained resistance to deformation. This suggests that GGH-HEC-MG forms a robust network suitable for applications requiring high yield strength and mechanical stability.

5.3.5 Rotational Shear Strength test for 10,12 and 14 mg/cm^3 of GGH-CMC

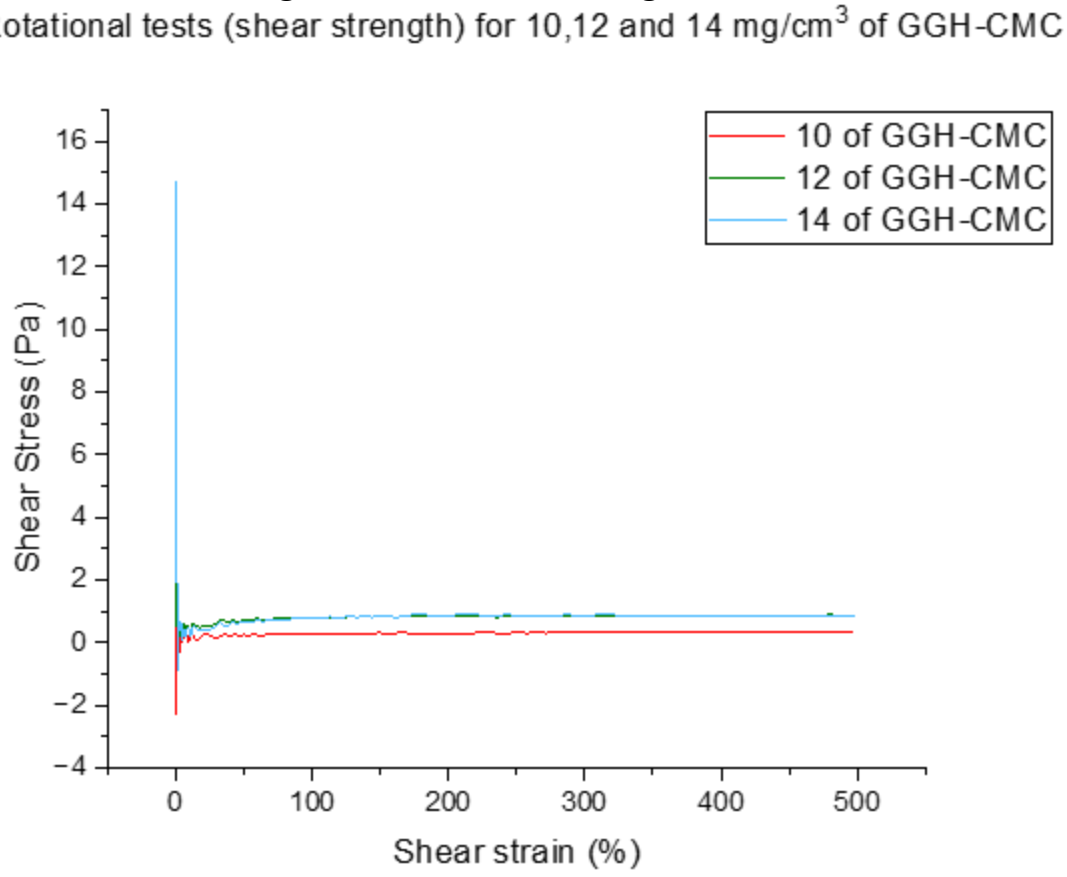

Figure 5.26: Rotational Shear Strength of GGH-CMC at 10, 12, and 14 mg/cm³ with a constant strain rate of 0.1 s^{-1} and Temperature of 20 °C.

Figure 5.26 illustrates the shear stress–shear strain behaviour of GGH-CMC at concentrations of 10, 12, and 14 mg/cm³, tested at a constant strain rate of 0.1 s^{-1} and temperature of 20 °C. All samples exhibit very low shear stress values, with a sharp initial spike followed by an immediate drop and a flat, low-stress response throughout the strain range. This indicates weak structural integrity and minimal resistance to shear. Additionally, increasing concentration has little effect on improving shear strength, suggesting that GGH-CMC forms a poorly cross-linked or unstable gel network, making it unsuitable for applications requiring mechanical stability under deformation.

5.3.6 Rotational Shear Strength test for 10,12 and 14 mg/cm^3 of GGH-CMC-MG

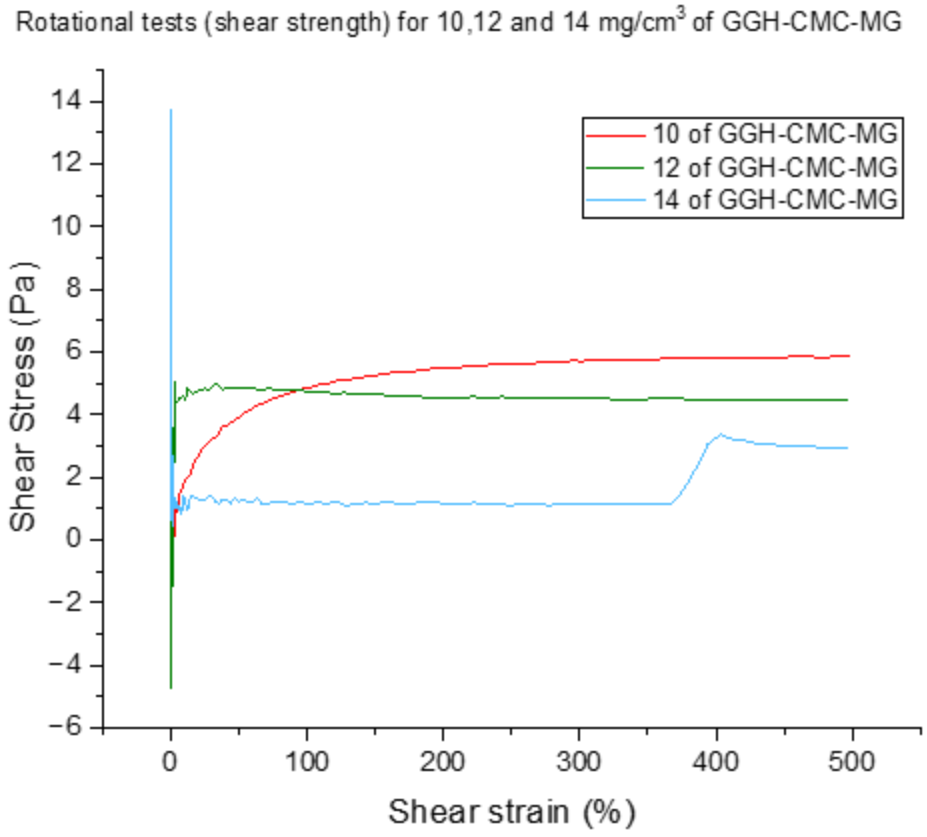

Figure 5.27: Rotational Shear Strength of GGH-CMC-MG at 10, 12, and 14 mg/cm³ with a constant strain rate of 0.1 s^{-1} and Temperature of 20 °C.

Figure 5.27 shows the shear stress–shear strain behaviour of GGH-CMC-MG at concentrations of 10, 12, and 14 mg/cm³, tested at a constant strain rate of 0.1 s^{-1} and temperature of 20°C. The results reveal irregular initial responses, followed by distinct stress patterns across concentrations. Surprisingly, the 10 mg/cm³ sample exhibits the highest and most stable shear stress (~6 Pa), while the 12 and 14 mg/cm³ samples display lower and less consistent stress values. The 14 mg/cm³ sample shows a sudden jump at higher strain, suggesting instability. Overall, the data indicate that increasing concentration does not enhance shear strength in GGH-CMC-MG and may instead disrupt the gel network, with 10 mg/cm³ offering the most stable mechanical performance.

5.4 Conclusion

Rheological testing demonstrates that all gellan gum–based hydrogels exhibit typical gel-like behaviour, with elastic dominance ($G' > G''$), shear-thinning characteristics, and strain-dependent yielding. Increasing gellan gum concentration generally enhances stiffness and mechanical strength, although this effect is formulation-dependent.

The incorporation of Miracle-Gro (MG) consistently increases storage modulus, complex viscosity, and yield stress across all systems, confirming its strong reinforcing effect through additional ionic interactions. However, this reinforcement is frequently accompanied by reduced strain tolerance and increased brittleness, particularly at higher concentrations. Among all formulations, GGH-MG and GGH-HEC-MG exhibit the most pronounced improvements in elastic behaviour, frequency stability, and overall mechanical robustness.

Hydrogels modified with HEC display a favourable balance between strength and deformability, showing smooth, stable rheological responses across amplitude, frequency, and rotational sweep tests. In contrast, CMC-based hydrogels consistently show weaker mechanical performance, higher variability, and signs of structural instability, especially when combined with MG at elevated concentrations.

Overall, these results demonstrate that mechanical performance is governed by the combined effects of polymer chemistry, additive compatibility, and concentration. GGH-HEC-MG at 12–14 mg/cm³ provides the most mechanically stable and tunable system within the tested formulations, whereas GGH-CMC systems require careful optimisation due to their limited structural integrity.

Chapter 6: Experimental procedure

6.1 Materials and instruments

6.1.1 Chemicals

Table 6.1: The table above provides a summary of the reagents used in this study.

Chemicals	Supplier	Purity
Water	In school of chemistry- university of Leeds	Water purifying system; Purite Select Analyst deioni-sation system
GGH	Alfa Aesar	
HEC	Bioserv	Physical Description: White to light-yellow or faint beige powder pH (1% in water): 6.0 – 8.5 Water: ≤ 10.0% Viscosity: 4500 – 6500 cps (2%, LVT, 60 rpm, sp. 4)
CMC	Thermo scientific	Carboxymethyl cellulose, sodium salt, average M.W. 250000 (DS = 1.2) Carboxymethylcellulose, Natriumsalz, M.W. ca. 250000 (DS = 1.2)
Miracle-gro		All-purpose concentrated plant food
Liquid Nitrogen	In school of chemistry – university of Leeds	
KCl	Sigma- Aldrich	
KH_2PO_4	Sigma- Aldrich	
C TMP	Sigma- Aldrich	≥95%
STPP	Sigma- Aldrich	
Sodium Hydroxide	Fisher chemical	≥97.0%
Hydrochloride Acid	Fisher chemical	37%

6.1.2 Technical instrumentation

Table 6.2: The table above outlines the technical equipment employed in this study.

Instrument	Supplier	Purpose & instrumental settings
Lyophilization	SciQuip	Freeze drying of samples
Mass balance	Ohaus	Wight the solid sample in my experiments
Heating Magnetic Stirrer (with thermocouple T-control)	VELP Scientifica	Magnetic stirring and heating
PH meter	Jenway	Measures PH
Conductivity meter	JENWAY 4510	to measure the ionic conductivity of solutions, gels, or hydrogels.
BROOKFIELD DV-I PRIME Digital Viscometer		Viscosity measurement of sample
SEM	Hitachi SU8230	visualise and analyse the surface morphology and microstructure of materials at high magnification and resolution
EDX	Hitachi SU8230	Identify each element in the sample and percentage.
BET	Hitachi SU8230	measure the specific surface area of materials by adsorption of gas molecules (usually nitrogen) onto the material's surface.
NMR Spectroscopy	BROOKFIELD DV-I PRIME	Viscosity measurement for samples
UV-visible spectrum	Agilent technology cray series	Gelation time
ICP-MS	Thermo Scientific iCAPQc ICP-MS	The following elements were analysed using ICP-MS: manganese (Mn), iron (Fe), copper (Cu), zinc (Zn), and molybdenum (Mo).
ICP-OES	Thermo Scientific iCAP7400 radial ICP-OES	The elements potassium (K) and phosphorus (P) were analysed using ICP-OES.
TGA	A Mettler Toledo TGA/DSC 3+.	Weight loss profile against T
DSC	A Mettler Toledo TGA/DSC 3+.	Thermal transmissions across samples as a function of T.
rheometer.	The instrument is an Anton Paar MCR 302 stress-controlled rheometer	to characterize the rheological (flow and deformation) properties of materials.

6.2 Preparation of Gellan Gums

6.2.1 Preparation of Gellan Gum Hydrogel (GGH) with and without Nutrients

Three concentrations (10, 12, and 14 mg/ mL) of GGH hydrogels were prepared by adding 0.5, 0.6, and 0.7 g of gellan gum powder, respectively, to 50 mL of deionised water in a 50 mL round-bottom flask. The mixture was stirred continuously at 7500 rpm using a magnetic stirrer for 4 hours at 80 °C, while the gellan gum was gradually added to ensure uniform dispersion. To prepare three concentrations (10, 12, and 14 mg/ mL) of the modified hydrogels (GGH-MG), the same procedure used for the unmodified GGH hydrogels was followed, with one key modification: the volume of distilled water was reduced from 50 mL to 49 mL, and 1 mL of Miracle-Gro solution was added to the mixture. The table below show all Chemical for Miracle-Gro.

Table 6.3: Percentage concentrations of key elements and compounds used as crop nutrients in Miracle-Gro.

Chemical	**Element/ compound measured**	**Concentration (%)**
Urea	N	3.5
Nitric	N	1.7
Ammoniacal	N	1.8
Phosphorus pentoxide	P2O5	3
Potassium oxide	K2O	5
Copper (Cu)**	Cu	0.002
Iron (Fe)***	Fe	0.03
Mn**	Mn	0.01
Mo	Mo	0.001
Zn**	Zn	0.002

6.2.2 Modified Gellan Gum Hydrogels by HEC with and without Nutrients

GGH hydrogels at concentrations of 10, 12, and 14 mg/ mL were prepared by dissolving 0.5, 0.6, and 0.7 g of gellan gum powder, respectively, in 25 mL of deionised water using a 50 mL round-bottom flask. At the same time, Hydroxyethyl Cellulose (HEC) was introduced into a separate 50 mL beaker containing 25 mL of distilled water. The mixture was heated to 80 °C

and stirred under identical conditions for four hours to achieve full dispersion. Following the initial preparation, the GG and HEC solutions were mixed and stirred at 80 °C for another four hours to ensure a uniform and homogeneous blend. HEC was consistently used at 0.25 g (equivalent to 5.00 mg/cm³) in all formulations. As for the other three samples to which nutrients were added, 10, 12 and 14 GGH-HEC-MG the same procedure used for the unmodified GGH-HEC hydrogels was followed, with one key modification: the volume of distilled water was reduced from 50 mL to 49 mL, and 1 mL of Miracle-Gro solution was added to the mixture.

6.2.3 Modified Gellan Gum Hydrogels by CMC with and without Nutrients

GGH hydrogels at concentrations of 10, 12, and 14 mg/ mL were prepared by dissolving 5, 6, and 7 mg of gellan gum powder, respectively, in 25 mL of deionised water using a 50 mL round-bottom flask. After three hours of GGH preparation we started to prepare CMC solution. CMC was dissolved in a separate 50 mL beaker containing another 25 mL of distilled water, also heated to 80°C and stirred continuously for 4 hours until a uniform solution formed. Once both polymers were completely dissolved, the GG and CMC solutions were combined into a single beaker. The combined mixture was stirred at 80°C for an additional 4 hours to ensure complete homogenisation. For samples 10,12 and 14 GGH-CMC-MG which nutrient-loaded samples, 1 mL of nutrient solution was prepared in advance.

The same method used for preparing the unmodified GGH-CMC hydrogels was applied, with one main adjustment: 1 mL of Miracle-Gro solution was added by reducing the amount of distilled water from 50 mL to 49 mL to maintain the total volume.

6.3 Experiment procedures for SEM, EDX, EDX map and BET

All GGH and modified GGH samples (50 mL) were left for 48 hours following preparation prior to any analysis, to ensure a degree of consistency in gelation. After this period, the hydrogels were lyophilised to eliminate moisture. Subsequently, they were analysed using scanning electron microscopy (SEM), energy-dispersive X-ray spectroscopy (EDX), and surface area determination via the BET method.

6.3.1 Freeze-drying

All the samples of the hydrogel and the modified hydrogel were frozen in two stages. In the first stage, they 50mL were placed in liquid nitrogen for 30 minutes while inside Falcon tubes 50mL. Then, they were transferred to freeze-dryer device (50mL and kept there for five days.

The samples were placed in a Virtis BenchTop Pro freeze-dryer, operating with a condenser temperature of −100.8 °C. Lyophilisation was carried out at a pressure of 0.12 mbar over a period of 120 hours 5 days.

6.3.2 SEM-EDX and BET Analysis of GGH and Modified GGH

The dried and frozen samples were submitted to Dr Alexander Kulak Materials Characterisn Istrmn Speclst at the School of Chemistry, University of Leeds, for analysis using SEM, EDX, EDX mapping, and BET surface area measurements. SEM images were taken using a field emission SEM FEI Nova 450. Samples were dispersed using ethanol onto a silicon wafer and attached to a stub. Images were prepared without coating and using a CBS detector (secondary electron detector). The typical voltage used was 3 kV, and EDX spectra were taken using EDAX TEAM software and a voltage of 18 kV.

The surface area of material was measured using nitrogen gas absorption with a Micromeritics ASAP2020 instrument, after degassing for 3 h the crystals at 120 °C.

6.4 Experiments procedure Thermogravimetric and Differential scanning calorimetry Analysis

Chapter 3 shows experiments done on six specially made hydrogel samples:12GGH, 12GGH-GM, 12GGH-HEC, 12GGH-HEC-MG, 12GGH-CMC, and 12GGH-CMC-MG. All these samples were dried and then frozen. The concentration of GGH was consistently maintained at 12 mg/cm³ (0.6 mg), while the concentrations of HEC and CMC were fixed at 5 mg/cm³ (0.25 mg). In the nutrient-enhanced samples, 1 mL of nutrient solution was incorporated. The detailed preparation process is outlined in chapter 2 section 2.2.1, 2.2.2 and 2.2.3. After formulation, all six samples were transferred into Falcon tubes (50 mL) and allowed to rest for two days to ensure complete gel formation. Following this, the samples underwent a cooling and drying process, as described in Section 7.3.1.

In this study, six polymer fibre-form samples comprising GGH and GGH-based compositions with and without nutrient additives were prepared and analysed at a fixed concentration of 12 mg/cm³. The thermal behaviour of the samples was investigated using Thermogravimetric Analysis (TGA) and Differential Scanning Calorimetry (DSC), in collaboration with Dr. A.M. Cunliffe (CSci MRSC), Analytical Laboratory Manager at the School of Chemical and Process Engineering, The Energy Building. The TGA procedure involved three steps: an initial heating phase from 30 °C to 100 °C at a rate of 10 K/min under an air flow of 50.0 mL/min; an isothermal hold at 100 °C for 10 minutes; and a final heating phase from 100 °C to 600 °C, maintaining the same heating rate and airflow. This method allowed for a detailed assessment

of the decomposition profile and thermal stability of the hydrogel formulations. All thermal analyses were carried out using a Mettler Toledo TGA/DSC 3+ instrument with sample robot (auto-sampler) and the purge gas was air at 50mL min^{-1}. The crucible (Al_2O_3, 70 µL) was weighed, tared, then 10mg sample was weighed in. A removable aluminium lid was added to prevent sample loss or moisture gain while waiting to be run. The robot removed the lid after the crucible was placed on the sensor beam.

6.5 Experiments procedure for ionic conductivity and Experiments procedure ICP.

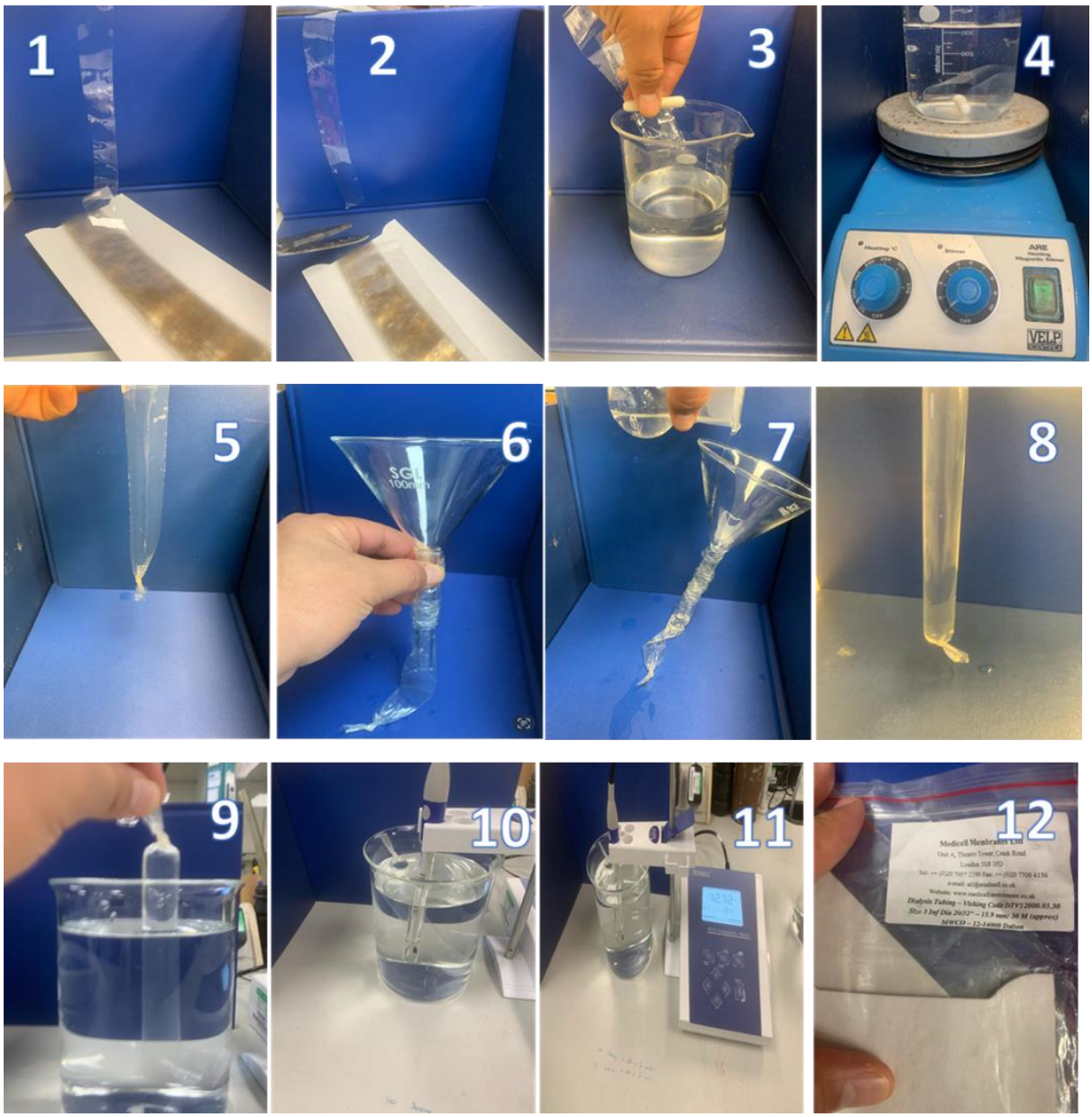

Figure 6.1: The sequence of images illustrates the complete procedure for conducting an ion conductivity experiment with a hydrogel sample.

In this experiment, dialysis tubing made from regenerated cellulose a cellulose-based, semi-permeable material was used due to its excellent biocompatibility and chemical stability. The material was sourced from Scientific Laboratory Supplies (SLS). This material features a porous structure that permits the diffusion of small molecules and ions while effectively containing larger macromolecules or hydrogels within the tubing. Its defined molecular weight cut-off (MWCO) ensures selective permeability, making it particularly suitable for investigating the release of ions from hydrogel matrices. Dialysis Tubing - Visking Code DTV12000.03.30 Size 3 InfDia 20/32" - 15.9 mm: 30 M (approx) MWCO - 12-14000 Dalton. Next, we followed the necessary procedure to prepare the dialysis tubing for the introduction of the hydrogel samples. Firstly, Soften and Clean the Tubing To prepare the dialysis tubing, it was first cut to the desired length (typically around 30 cm, depending on the sample size). The tubing was then thoroughly rinsed with cold deionised water to eliminate any residual preservatives, such as glycerol. Following this, it was soaked in warm (but not boiling) deionised water for 10 to 30 minutes to soften the material and ensure the pores were fully opened, allowing for optimal diffusion during the experiment. See 1 to 4 in Figure 6.1 Then tying the analysis tube from the bottom side in another side place Dropping funnels: Also used for controlled addition of gels solution inter analysis tube then start adding hydrogel solution in the other side. Here using a fixed volume of 30 mL in all experiments. Then tying in the top in preparation for conducting the ionic conductivity tests and ICP.

6.5.1 Experiments procedure for ionic conductivity

These experiments were carried out on all GGH samples and their modified hydrogel counterparts, both with and without nutrient additives, in the laboratory. I personally conducted all these experimental procedures. For each sample, three measurements were recorded to obtain an average value. These values were documented in a dedicated table and subsequently used for data plotting and analysis. The values were monitored continuously over a period of six hours. The device was used is 4510 conductivity metre. 4510 conductivity metre supplied with glass conductivity probe with ATC (K=1) (027 013), electrode holder (903 300) and UK power supply (021 030). Following synthesis or formulation, around 30 mL of the hydrogel sample was transferred into a clean, dry analytical tube, with one end sealed to prevent leakage. The tube was then immersed in a 1000 mL beaker containing distilled water to establish a stable environment for ionic conductivity testing. Electrodes commonly made of platinum, stainless steel, or graphite were inserted into the sample to ensure effective electrical contact. Prior to

measurement, the conductivity meter was calibrated using standard solutions like potassium chloride (KCl), if required, to ensure measurement accuracy or Calibration by cell constant. The temperature was maintained consistently between 20–25 °C throughout the test. Ionic conductivity values were recorded using a conductivity meter, with readings taken at regular intervals, such as every 30 minutes or hourly. For data analysis, the results were plotted against time or concentration to observe trends such as stabilisation behaviour, diffusion dynamics, or ionic release profiles.

6.5.2 Experiments procedure for ICP

Preparation of samples for the ICP experiments followed the same procedure as that used for the ionic conductivity tests. Hydrogel samples were placed in analytical tubes and submerged in a 1000 mL beaker filled with distilled water. At specific time intervals 10 minutes, 30 minutes, 90 minutes, 3 hours, and 6 hours 5 mL aliquots were withdrawn from the beaker and transferred into 10 mL Falcon tubes for analysis. These prepared samples were then submitted to Mr. Stephen Reid, Aqueous Analytical Experimental Officer at the School of Earth and Environment, University of Leeds. His areas of expertise include inductively coupled plasma (ICP), mass spectrometry (ICP-MS), optical emission spectroscopy (ICP-OES), and atomic absorption spectroscopy (AAS).

The instrumentation used for elemental analysis included the Thermo Scientific iCAP Qc ICP-MS and the Thermo Scientific iCAP 7400 Radial ICP-OES. A combination of these techniques was employed depending on the target element. Specifically, the elements Mn, Fe, Cu, Zn, Mo, K, and P were analysed using ICP-MS, while ICP-OES was also utilized where appropriate to support multi-element detection and quantification.

Samples were all analysed undiluted. Appropriate internal standard was added to each sample (outline below).

6.5.2.1 ICP-OES

The elements potassium (K) and phosphorus (P) were analysed using ICP-OES. ICP-OES analysis was used in radial mode. No Internal Standard was required. The table below summarises what wavelength as used for each element. Where possible two wavelengths were observed to provide further data verification.

Table 6.4: This table summarises the specific wavelengths used during ICP-OES analysis for potassium and phosphorus.

Element	Wavelength / nm
Potassium	766.5
Phosphorus	178.3

Calibrations

Direct calibration was used for the analysis using 2% HNO_3 as diluent.
Calibrations were performed in the range of 0.1-10 mg L^{-1}.

Limit of Detection

Limit of Detection was estimated as 3 times the standard deviation of 5 blank measurements.

$$LOD = 3\sigma_{5\ Blanks} \qquad \textit{Equation 6.1}$$

Limit of Quantification

Limit of Detection was estimated as 10 times the standard deviation of 5 blank measurements.

$$LOD = 10\sigma_{5\ Blanks} \qquad \textit{Equation 6.2}$$

Precision

Precision was estimated by calculating the 95% confidence interval of 5 repeated sample measurements.

$$\bar{x} \pm \frac{t_{n-1}s}{\sqrt{n}} \qquad \textit{Equation 6.3}$$

Where n = number of measurements
n-1 = degrees of freedom (5)
t = t value (2.78 for 4 degrees of freedom)
s = calculated standard deviation of 5 measurements
x = calculated mean of 5 measurements

6.5.2.2 ICP-MS

The following elements were analysed using ICP-MS: manganese (Mn), iron (Fe), copper (Cu), zinc (Zn), and molybdenum (Mo).

ICP-MS Analysis

ICP-MS analysis was used in "Kinetic Energy Discrimination (KED) mode. The table below summarises what mass and mode was used for each element.

Table 6.5: ICP-MS Analysis Parameters for Selected Elements (KED Mode).

Element	Mass (*m/z*)
Manganese	55
Iron	56
Copper	65
Zinc	66
Molybdenum	96

Calibrations

Direct calibration was used for the analysis using 2% HNO_3 as diluent.

Calibrations were performed in the range of 0.1-10 µg L^{-1} for Mn, Cu and Zn and 1 – 100 µg L^{-1} for Fe and Zn.

Internal Standardisation

Scandium (*m/z* 45) Rhodium (*m/z* 103) and iridium (*m/z* 193) at a concentration of 1 µg L^{-1} was added to all standards and samples for use as an internal standard.

Limit of Detection

Limit of Detection was estimated as 3 times the standard deviation of 5 blank measurements.

$$LOD = 3\sigma_{6\ Blanks} \qquad \textit{Equation 6.4}$$

Limit of Quantification

Limit of Detection was estimated as 10 times the standard deviation of 5 blank measurements.#

$$LOD = 10\sigma_{6\ Blanks} \qquad \textit{Equation 6.5}$$

Precision

Precision was estimated by calculating the 95% confidence interval of 5 repeated plant extract sample measurements.

$$\bar{x} \pm \frac{t_{n-1}s}{\sqrt{n}} \qquad \textit{Equation 6.6}$$

Where n = number of measurements

n-1 = degrees of freedom (5)

t = t value (2.78 for 4 degrees of freedom)

s = calculated standard deviation of 5 measurements

x = calculated mean of 5 measurements

6.6 Experiments procedure for rheology measurements.

Samples of GGH and modified GGH hydrogels with and without Miracle-Gro were prepared using the procedure described in Sections 2.2.1, 2.2.2 and 2.2.3. Subsequently, a series of rheological tests were conducted on the samples to evaluate their viscoelastic characteristics using an Anton Paar Physica MCR 301 rheometer. Each sample was subjected to three types of rheological tests: the Standard Amplitude Sweep Test, the Standard Frequency Sweep Test, and the Rotational Test. Each test was performed in triplicate to ensure repeatability and accuracy of the results. The device was equipped with a flat parallel plate configuration and a 1 mm gap. The sample (a small spoon 490.87 mm^3 = 0.491 mL) was then positioned on the lower plate of the rheometer, and the upper plate was gradually lowered until it made contact. I cleaned the sample from the edges after the parallel plate geometry came down. To control the sample's temperature and evaporation during measurements, we attached a closed Peltier hood to the parallel plate measuring device. We use oscillation and rotational testing techniques to determine the dynamic moduli and shear strength of the material by applying shear stresses, strains, and strain rates through both oscillatory and rotational testing methods. All tests were performed using the upper plate while maintaining a constant normal force of zero throughout the measurements. The shear strain and shear strain rate were controlled by adjusting the angular displacement (amplitude), Displacement (angular strain) usually ranges from 0.01% to 1000% shear strain to identify the linear viscoelastic region (LVR). A common starting point is around 0.1% to 10% strain depending on material sensitivity. In oscillatory testing, the shear strain rate is controlled by varying the oscillation frequency. The angular displacement is kept

constant (within the LVR, e.g., 1% strain), and frequency is varied (usually 0.1 to 100 rad/s). This approach also helps evaluate the reproducibility of the measurements and detect any potential slip effects at the rheometer plates. Each sample concentration was tested three times independently, with careful observation for any signs of detachment from the parallel plates following each measurement.

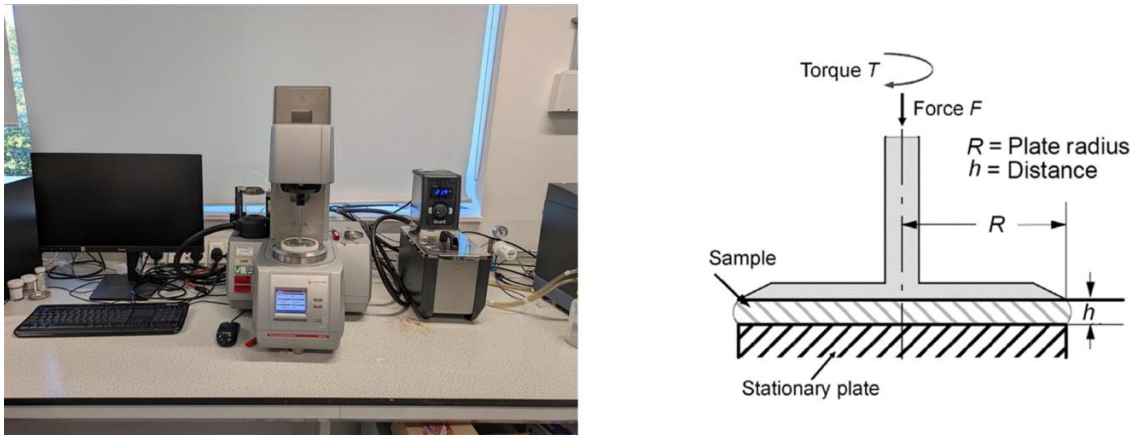

Figure 6.2: Parallel plate flow configuration, adapted from Schramm (280, 281).

Steps to run Rheology Experiments

1- Open all three instruments (temperature controller + Rheometer + PC) from the lift.
2- Wait for 30 mins.
3- Open the Program. (the control software for the rheometer is RheoCompass).
4- Initialize.
5- Put the geometry.
6- Click Set to zero.
7- Select Verification and Adjustment (follow the picture wait for report (this step in each work on the device)
8- Select The test
9- Put sample.
10- Revise the sitting.
11- Select Start.

6.6.1 Oscillatory Tests

Oscillatory amplitude sweep experiments were conducted to identify the linear viscoelastic (LVE) range of the gel samples. During these tests, the shear strain was gradually increased from 0.01% to 100%, while maintaining a constant oscillation frequency of 0.1 s^{-1} and a temperature of 25°C. The measurements were performed on gels that had been aged for 2 days.

6.6.2 Frequency Sweep Tests

Frequency sweep tests were conducted to assess the dependence of the gel's properties on frequency or shear strain rate. In these experiments, the oscillation frequency was varied from 100 to 0.01 s^{-1}, while keeping the shear strain constant at 1% and the temperature fixed at 25 °C.

6.6.3 Rotational Tests

We determined the shear strength of samples using rotating shear strength tests, in which samples were deformed by applying a shear strain of up to 500% at a constant strain rate and temperature (0.1 s^{-1} and 25 ◦C). The material's shear. We measured the stress as a function of strain. Here, the maximum shear stress defines the shear strength or maximum shear strength of the material

Chapter 7: Conclusion and future work

7.1 Chapter 1 summary

This chapter highlights the growing challenges in global agriculture including climate change, resource scarcity, and increasing food demand and the need for sustainable solutions, especially in water-stressed regions. Hydrogels, particularly superabsorbent polymer hydrogels, are presented as a promising tool to improve soil moisture retention, reduce irrigation and nutrient loss, and support crop growth.

Hydrogels are categorized into synthetic, semi-synthetic, and natural types. While synthetic hydrogels offer high durability, they often lack biodegradability. In contrast, natural polysaccharide-based hydrogels such as those made from cellulose, gellan gum, and guar gum are biodegradable and eco-friendly, though generally weaker in mechanical strength.

A focus of the study is on gellan gum cellulose composite hydrogels, which combine the beneficial properties of both materials and are further enhanced with additives like nanoparticles and biochar. These composite hydrogels offer improved water retention, nutrient delivery, and mechanical stability, making them ideal for sustainable agricultural applications. Additionally, hydrogels can act as carriers for nutrients and soil amendments, including macronutrients, micronutrients, pH regulators, and organic additives. Ultimately, hydrogel composites represent a versatile, environmentally friendly technology that can help ensure long-term agricultural resilience in the face of climate and resource challenges.

7.2 Chapter 2 summary SEM,EDX , EDXmap and BET

SEM analysis reveals that pure GG forms a rough, fibrous, and highly entangled network, reflecting its rigid double-helix aggregation and limited chain flexibility. Incorporation of HEC produces a smoother, more folded and continuous microstructure, attributable to the non-ionic, flexible cellulose backbone of HEC, which promotes hydrogen bonding and enhanced chain entanglement with gellan gum. In contrast, GG–CMC exhibits a more corrugated, plate-like, and rigid morphology due to electrostatic interactions introduced by carboxymethyl groups, leading to increased stiffness but reduced structural homogeneity. Addition of MG generally reduces network order across all systems, likely by partially disrupting polymer–polymer interactions, with GG–HEC retaining the most coherent microstructure, consistent with its more adaptable chemical architecture.

EDX analysis confirms that all hydrogels are primarily composed of carbon and oxygen, consistent with their polysaccharide-based nature. The incorporation of nutrients (MG)

introduces additional mineral elements such as K, P, Na, S (and trace Cu in some formulations), confirming successful nutrient integration within the hydrogel matrix rather than surface adsorption. EDX elemental mapping reveals a more homogeneous distribution of these elements in GGH-HEC-MG compared to GGH-CMC-MG, indicating stronger and more uniform nutrient–polymer interactions. Overall, the non-ionic and flexible structure of HEC promotes more even mineral dispersion, whereas the ionic nature of CMC leads to more localized elemental distribution and reduced homogeneity.

BET analysis shows that all hydrogel formulations exhibit very low and comparable specific surface areas (≈3–10 m^2/g), indicating dense, non-porous structures. Incorporation of MG generally increases or maintains surface area in GGH and GGH-CMC systems, while a noticeable decrease is observed for GGH-HEC-MG, suggesting pore blocking or structural densification due to stronger polymer–nutrient interactions. Overall, the small variations fall within experimental uncertainty, indicating that BET surface area is not the dominant factor controlling the observed differences in mechanical or release behaviour, which are more strongly governed by polymer chemistry and network structure.

7.3 Chapter 3 summary (thermal analysis)

Thermogravimetric analysis (TGA) shows that the incorporation of Miracle-Gro generally enhances the thermal stability of all hydrogel systems, as evidenced by reduced mass loss and higher residual mass at elevated temperatures due to the presence of inorganic salts. Among the formulations, GGH-HEC exhibits superior thermal stability compared with GGH and GGH-CMC, which can be attributed to the non-ionic and flexible chemical structure of HEC that promotes strong hydrogen bonding and a more cohesive polymer network, slowing thermal degradation. In contrast, GGH-CMC displays faster decomposition, particularly after nutrient addition, due to the ionic carboxymethyl groups that facilitate chain scission at high temperatures. Overall, GGH-HEC-MG is identified as the best-performing material in terms of thermal stability, combining improved resistance to degradation with enhanced inorganic residue retention.

DSC Summary (linked to chemical composition):

DSC analysis shows that polymer chemistry strongly governs the thermal transitions of the hydrogels. Incorporation of CMC significantly increases Tg, reflecting reduced chain mobility due to its ionic carboxymethyl groups, which produce a more rigid and constrained network. HEC-containing systems exhibit higher crystallisation temperatures (Tc), consistent with enhanced hydrogen bonding and better chain packing arising from the flexible, non-ionic

cellulose backbone. Addition of Miracle-Gro (MG) generally lowers Tc but slightly raises Tm, indicating improved local packing alongside simplified thermal decomposition pathways due to inorganic nutrient salts. Overall, GG–HEC formulations show the most balanced thermal behaviour, combining stability with structural flexibility, whereas GG–CMC systems are thermally rigid but more brittle, confirming the dominant role of chemical functionality in controlling thermal response.

7.4 Chapter 4 summary (Ionic conductivity and ICP)

Ionic conductivity increases markedly with the incorporation and concentration of Miracle-Gro, confirming progressive ion release from the hydrogel matrices. GGH-MG shows the highest conductivity, reflecting limited ionic binding in pure gellan gum and rapid diffusion of dissolved salts. In contrast, GGH-HEC-MG exhibits lower but more controlled conductivity, consistent with hydrogen bonding and chain entanglement in the non-ionic HEC network that partially restricts ion mobility. GGH-CMC-MG displays higher conductivity than GGH-HEC-MG, due to the presence of charged carboxymethyl groups in CMC that facilitate ion transport. Across all systems, conductivity rises rapidly within the first 5–10 hours before reaching equilibrium, indicating fast initial ion release followed by diffusion-controlled stabilisation.

The nutrient release results show a clear time-dependent increase in ion concentration for all MG-loaded hydrogels, with rapid release during the first 90–180 minutes followed by a slower approach to equilibrium. GG-MG consistently exhibits the highest release levels for all nutrients, reflecting weaker ion–polymer interactions and a more open network. GG-HEC-MG shows moderated and more controlled release, attributable to strong hydrogen bonding and chain entanglement from the non-ionic HEC, which improves ion retention. In contrast, GG-CMC-MG displays the slowest and most restricted release, as electrostatic interactions between CMC carboxylate groups and metal ions limit ion mobility, indicating superior nutrient retention but reduced release efficiency.

7.5 Chapter 5 summary (Rheological Investigations)

Summary of viscoelastic behaviour (Amplitude sweep)

Amplitude sweeps tests show that viscoelastic behaviour strongly depends on polymer chemistry and network interactions. GG–HEC–MG exhibits the highest storage modulus (G′), the widest linear viscoelastic region (LVR), and the highest yield strain, indicating a strong, elastic, and deformation-resistant network. This behaviour arises from the flexible, non-ionic HEC chains, which enhance hydrogen bonding and chain entanglement with gellan gum, while MG ions further reinforce the network. GG–MG shows moderate strength with a narrower

LVR, suggesting partial disruption of the GG network by salts. In contrast, GG–CMC–MG displays the lowest G′ and the narrowest LVR, reflecting a weak and easily deformed structure due to electrostatic repulsion from CMC's carboxylate groups, which limits effective chain packing.

Summary of frequency sweep rheology to composition and chemical structure:

The frequency sweep results show that adding Miracle-Gro (MG) consistently increases the elastic modulus (G′) and reduces frequency dependence, indicating the formation of stronger and more stable gel networks. GG-HEC-MG exhibits the highest and most frequency-independent G′, reflecting the flexible, non-ionic HEC chains that promote effective chain entanglement and hydrogen bonding, further reinforced by ionic crosslinking from MG. GG-CMC-MG also shows enhanced elasticity compared to GG-CMC, but the rigid, anionic CMC structure limits molecular mobility, leading to a stiffer yet less adaptable network. Overall, GG-HEC-MG demonstrates the best viscoelastic performance due to the synergistic combination of flexible polymer chemistry and MG-induced crosslinking, resulting in a strong, elastic, and stable hydrogel.

Summary of mechanical results (G*, E*) to composition and chemistry:

The complex modulus (G*) and Young's modulus (E*) clearly show that polymer chemistry and nutrient incorporation strongly control gel stiffness. GG-HEC-MG exhibits the highest G* and E*, indicating the strongest and most elastic network, which arises from the flexible, non-ionic HEC chains that enhance chain entanglement and hydrogen bonding, further reinforced by ionic interactions introduced by MG. In contrast, GG-CMC and GG-CMC-MG display the lowest moduli, reflecting the rigid and charged CMC structure that limits effective network formation. Overall, MG addition consistently improves mechanical strength across all systems, but the GG-HEC-MG formulation provides the best mechanical performance due to its optimal balance of polymer flexibility and crosslinking density.

Summary of rotational rheology results to composition and chemistry, without repetition:

All GG-based hydrogels exhibit clear shear-thinning behaviour, consistent with physically crosslinked polymer networks. GG-HEC-MG shows the highest shear stress over the full strain range, indicating the strongest and most stable structure, which arises from enhanced chain entanglement of flexible HEC combined with additional ionic crosslinking from MG. In contrast, GG-CMC and GG-CMC-MG display much lower shear stress, reflecting weaker, more brittle networks caused by the rigid and charged CMC backbone. Overall, MG addition increases shear resistance in all formulations, but the GG-HEC-MG system provides the most robust and deformation-resistant gel.

7.6 Future studies

.

This project aims to develop hydrogel systems using organic gelators like gellan gum to promote controlled release of nutrient sources like nitrates, phosphates, and key metal ions like potassium, calcium, zinc, and iron, essential for plant growth, metabolism, and structural integrity. It is proposed that the development of Gellan Gum hydrogels serves as a feasible mechanism to achieve this objective. This study investigates the structural and mechanical behaviour of polysaccharide-based hydrogels, specifically HEC- and CMC-modified systems, using a range of analytical techniques to evaluate their viscoelastic and stability responses under different conditions. This investigation employed multiple techniques to assess the hydrogels' responses to different environmental conditions. Future phases of the project will concentrate on the following areas:

1. Structured Seed Germination and Plant Growth Trials

While preliminary results suggest that these hydrogels improve moisture retention and nutrient availability, future studies should adopt a more systematic approach to evaluating plant responses. Key objectives include:

- Quantifying germination rates, seedling vigor, and biomass under different hydrogel formulations (e.g., GG, GG-HEC, GG-CMC, and nutrient-loaded variants).
- Testing performance across multiple plant species such as basil, radish, and lettuce.
- Examining growth under controlled environmental conditions—varying temperature, humidity, and light cycles.

These trials will help establish the biological effectiveness and compatibility of the hydrogels across plant types and conditions.

2. Field Trials and Soil Interaction Studies

To validate laboratory findings in real-world scenarios, it is essential to transition toward greenhouse and field-level experimentation. Proposed activities include:

- Long-term nutrient leaching studies using soil columns.
- Monitoring soil parameters such as pH, moisture content, and microbial activity with and without hydrogel amendment.
- Assessing biodegradability and environmental persistence of different hydrogel systems in soil.

This work will provide crucial insights into environmental impact and agricultural scalability.

3. Mechanical Reinforcement of Hydrogel Networks

Enhancing the structural and functional stability refers to the ability of the hydrogel to maintain controlled nutrient release while preserving its structural integrity and viscoelastic response under mechanical and environmental stresses.. Future work can focus on:

- Metal ion cross-linking (e.g., Ca^{2+}, Zn^{2+}) to reinforce the polymer matrix and regulate nutrient diffusion.
- Incorporation of synthetic polymers such as polyacrylate or polyvinyl alcohol to develop hybrid or interpenetrating networks.
- Exploring self-healing or thermoresponsive hydrogels for adaptive nutrient delivery in fluctuating environmental conditions.

Such modifications could optimize both durability and performance across different crop cycles.

4. Multi-Nutrient and Micronutrient Delivery Platforms

While the current study emphasizes macronutrients (N, P, K), future systems should accommodate comprehensive nutrient profiles. This includes:

- Co-loading macronutrients and micronutrients (e.g., Fe, Zn, Cu, Mn, Mo) into a single hydrogel system.
- Using chelated or nano-formulated micronutrients to improve nutrient bioavailability.
- Synchronizing nutrient release with specific plant developmental stages and uptake rates.

This integrated approach would enhance fertilizer efficiency and reduce environmental nutrient runoff.

5. Development of Smart and Responsive Hydrogel Systems

An innovative future direction involves designing hydrogels that respond to real-time environmental conditions. Stimuli-responsive systems could trigger nutrient release based on:

- Changes in soil moisture levels.
- Temperature or pH fluctuations.
- Root exudates or microbial signals in the rhizosphere.

Such intelligent systems would allow precise, need-based nutrient delivery, reducing waste and maximizing crop productivity.

Chapter 8: Appendices

Chapter 2

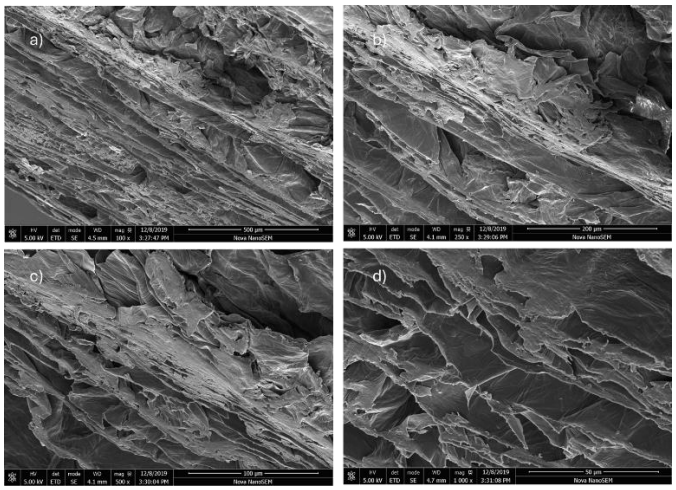

Figure 8.1: SEM micrographs of 16 GGH and various magnifications. scale bar: a) 500 µM b) 200 µM c) 100 µM d) 50 µM.

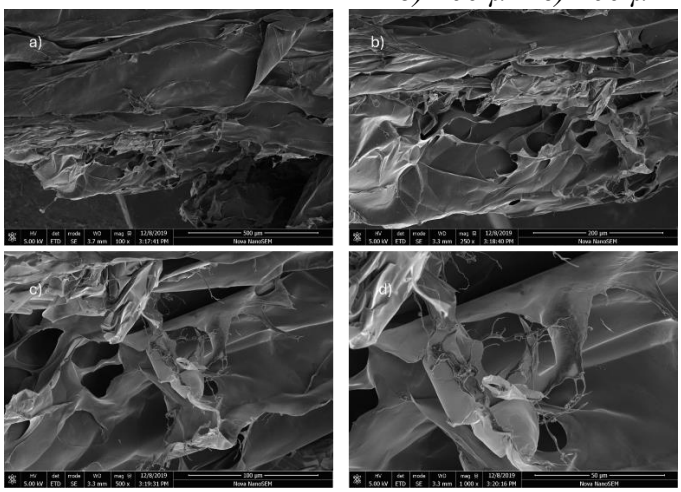

Figure 8.2: SEM micrographs of 18 GGH and various magnifications. scale bar: a) 500 µM b) 200 µM c) 100 µM d) 50 µM.

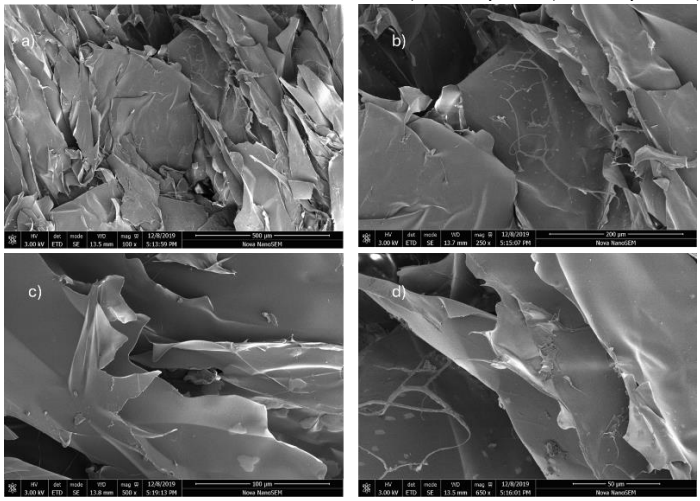

Figure 8.3: SEM micrographs of 20 GGH and various magnifications. scale bar: a) 500 µM b) 200 µM c) 100 µM d) 50 µM.

cyclic trimetaphosphate

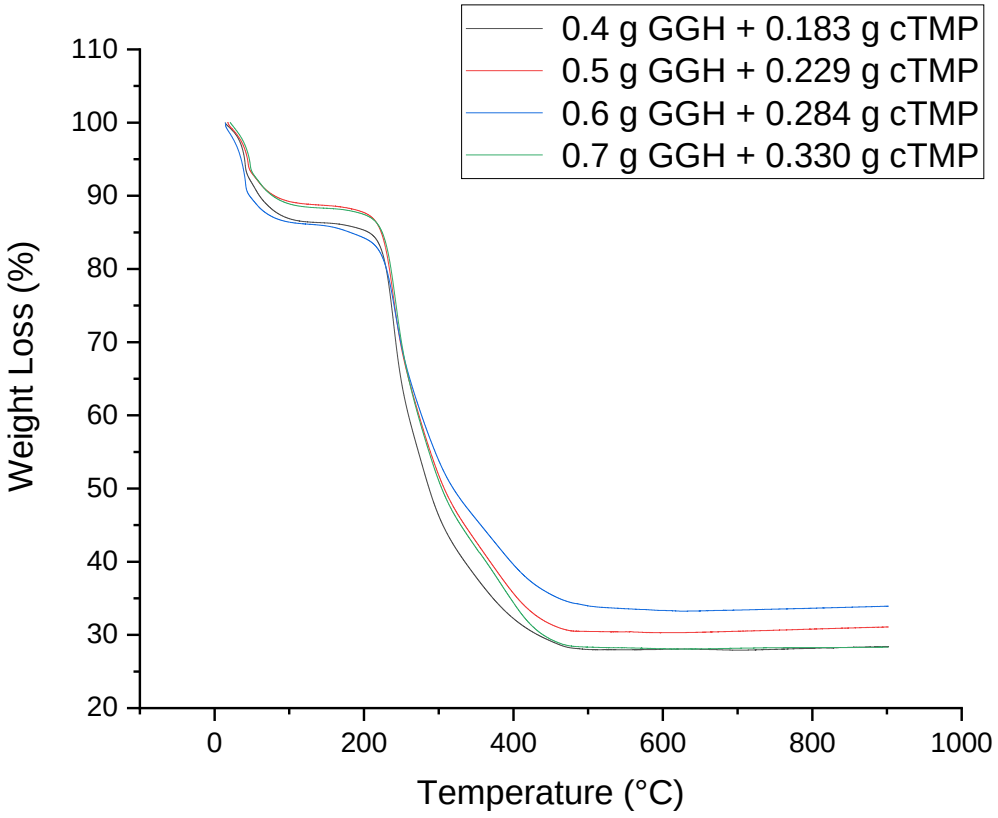

Figure 8.4: Thermogravimetric Analysis (TGA) Curves of GGH-cTMP Hydrogels with Varying GGH and cTMP Ratios.

a)

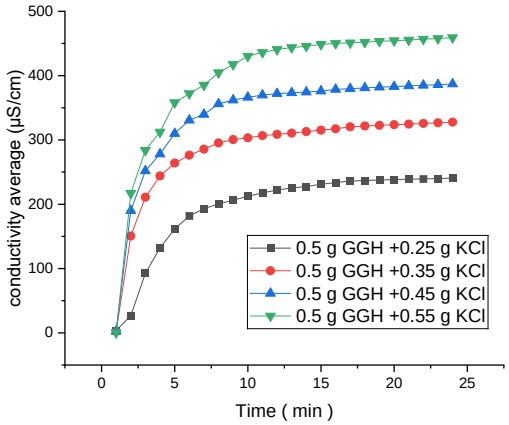

b)

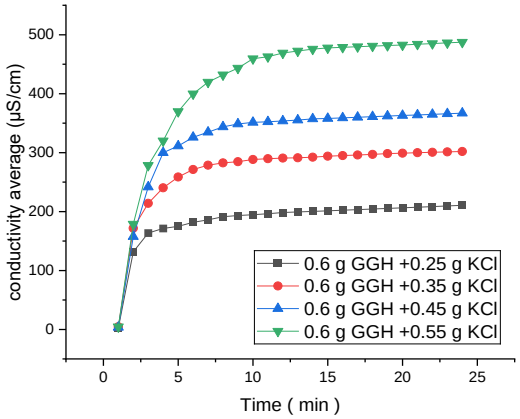

c)

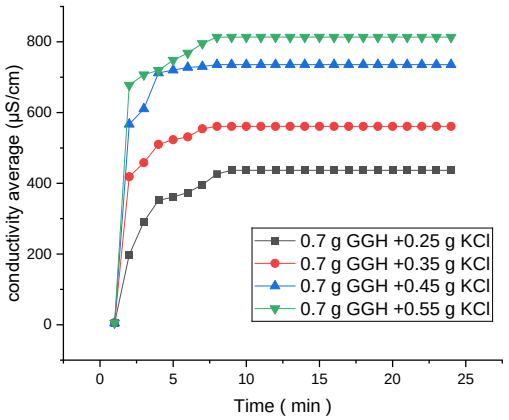

Figure 8.5: Ionic Conductivity Profiles of GGH Hydrogels with Varying KCl Concentrations over Time. a) 0.5 g GGH b) 0.6 g GGH and 0.7 GGH.

a)

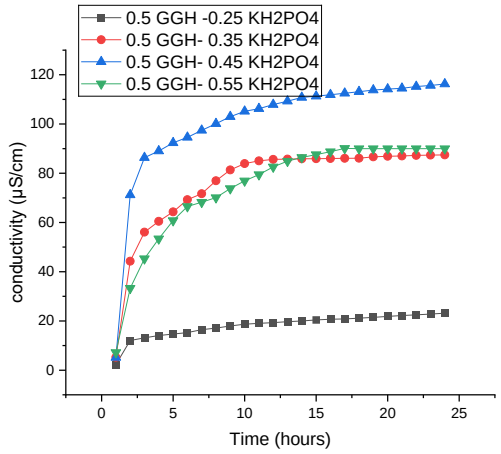

b)

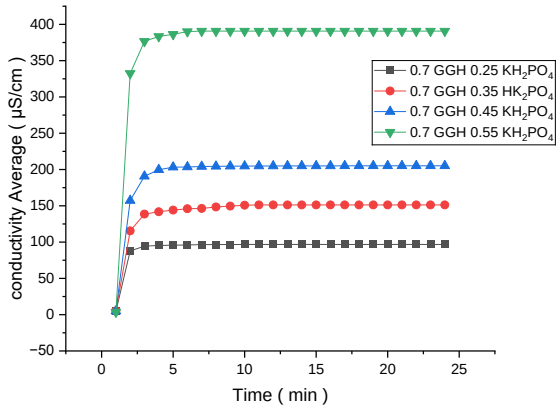

Figure 8.6: Ionic Conductivity Profiles of GGH Hydrogels with Varying KH_2PO_4 $^{-2}$ Concentrations over Time. a) 0.5 g GGH b) 0.7 g GGH .

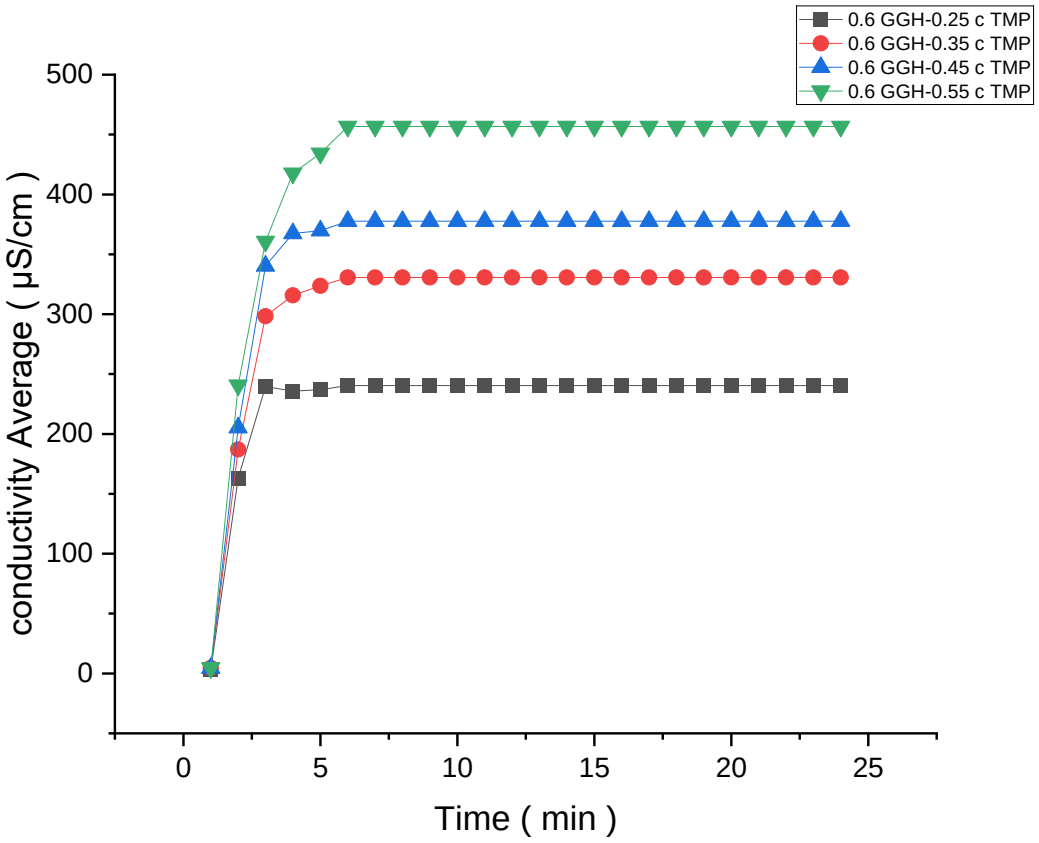

Figure 8.7: Ionic Conductivity Profiles of GGH Hydrogels with Varying c TMP Concentrations over Time.

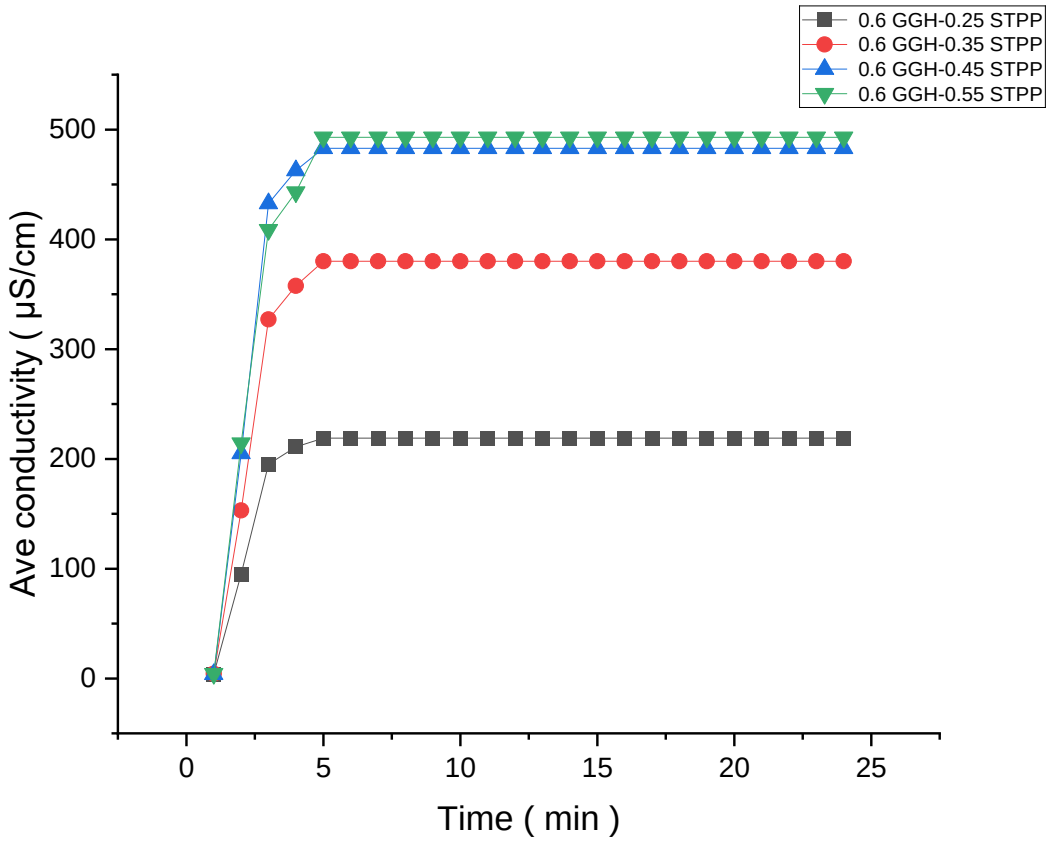

Figure 8.8: Ionic Conductivity Profiles of GGH Hydrogels with Varying STPP Concentrations over Time.

Table 8.1: Effect of Salt Type and Concentration on Ionic Conductivity of Functionalized Hydrogels

Weight, Salts	Conductivity KH_2PO_4 **Potassium dihydrogen phosphate**	Conductivity C_STMP Sodium trimetaphosphate	Conductivity STPP sodium tripolyphosphate	Conductivity KCl Potassium chloride
0.25 g	458µS	658µS	710 µS	1317 µS
0.35 g	655µS	820µS	950 µS	1717 µS
0.45 g	904µS	1058µS	1200 µS	2040 µS
0.55 g	1082µS	1291µS	1580 µS	2570 µS

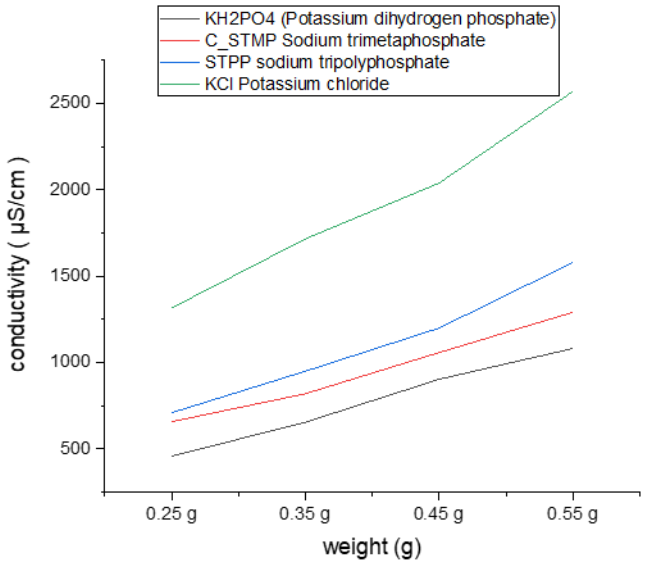

Figure 8.9: Comparison of Ionic Conductivity for Different Salts at Varying Concentrations in Gellan Gum Hydrogels

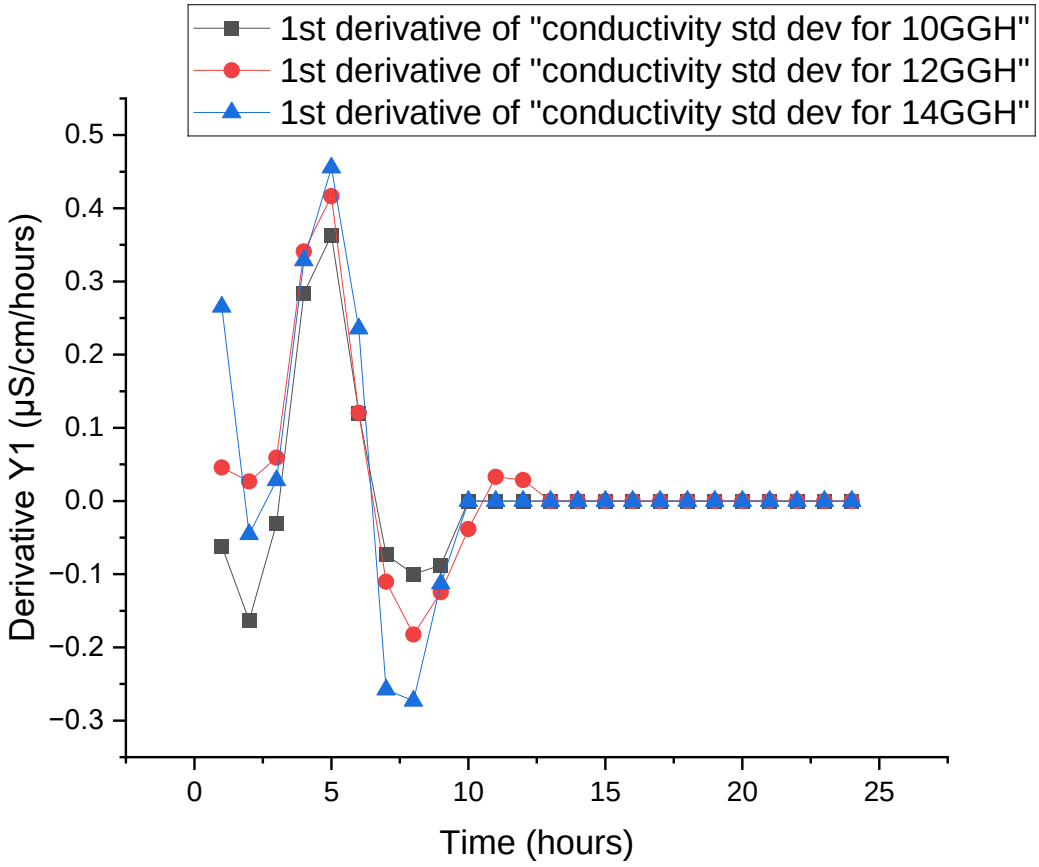

Figure 8.10: First Derivative of Conductivity Standard Deviation Over Time for GGH Hydrogels at 10, 12, and 14 mg/cm³

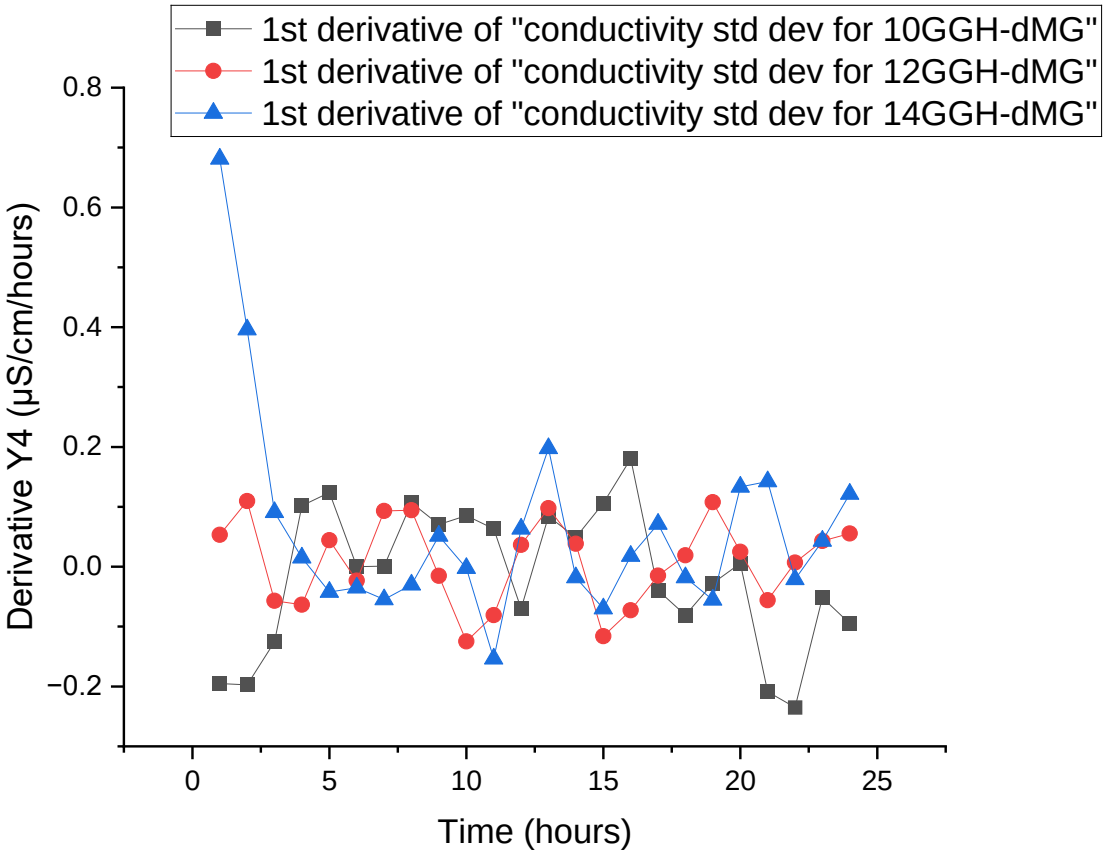

Figure 8.11: First Derivative of Conductivity Standard Deviation Over Time for GG-d MG Hydrogels at 10, 12, and 14 mg/cm³

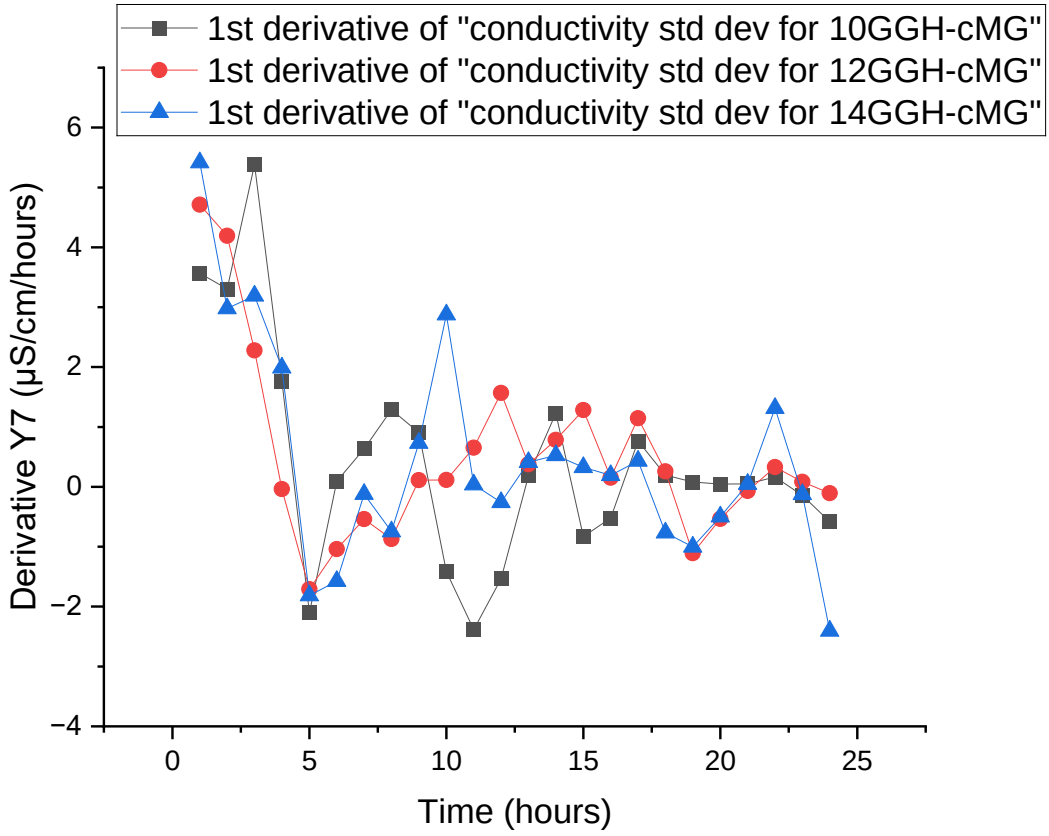

Figure 8.12: First Derivative of Conductivity Standard Deviation Over Time for GGH-cMG Hydrogels at 10, 12, and 14 mg/cm³

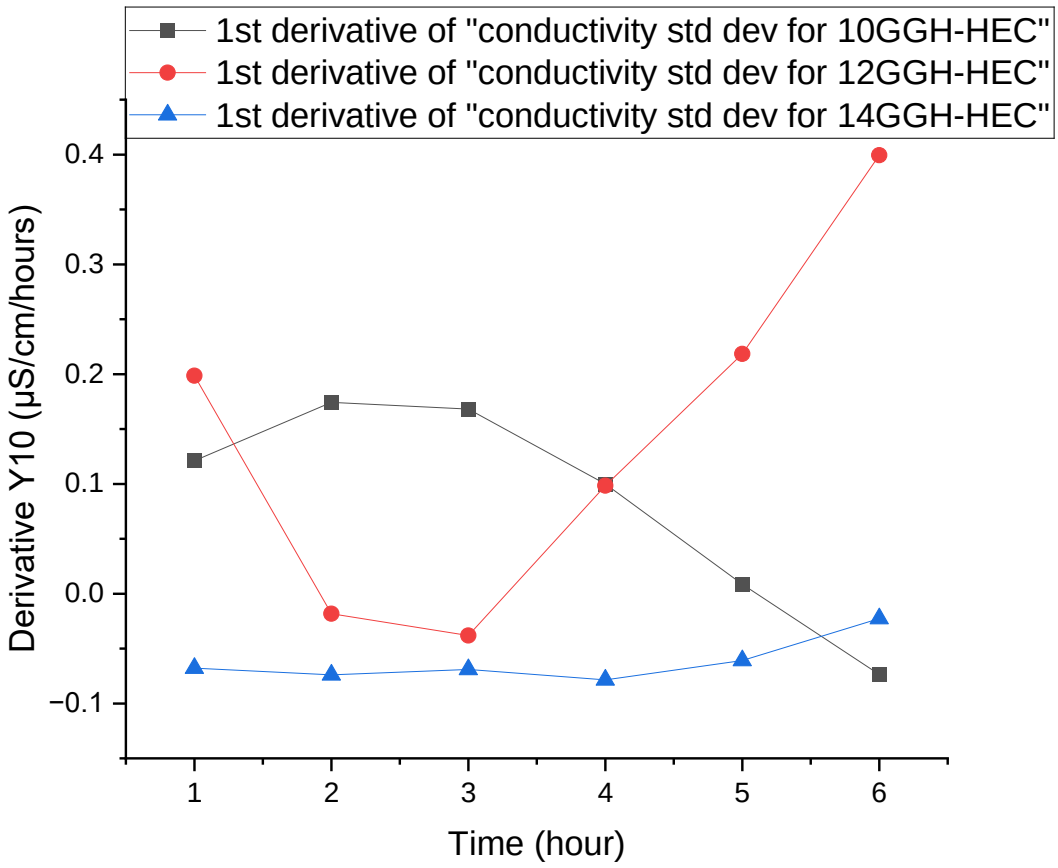

Figure 8.13: First Derivative of Conductivity Standard Deviation Over Time for GGH-HEC Hydrogels at 10, 12, and 14 mg/cm³

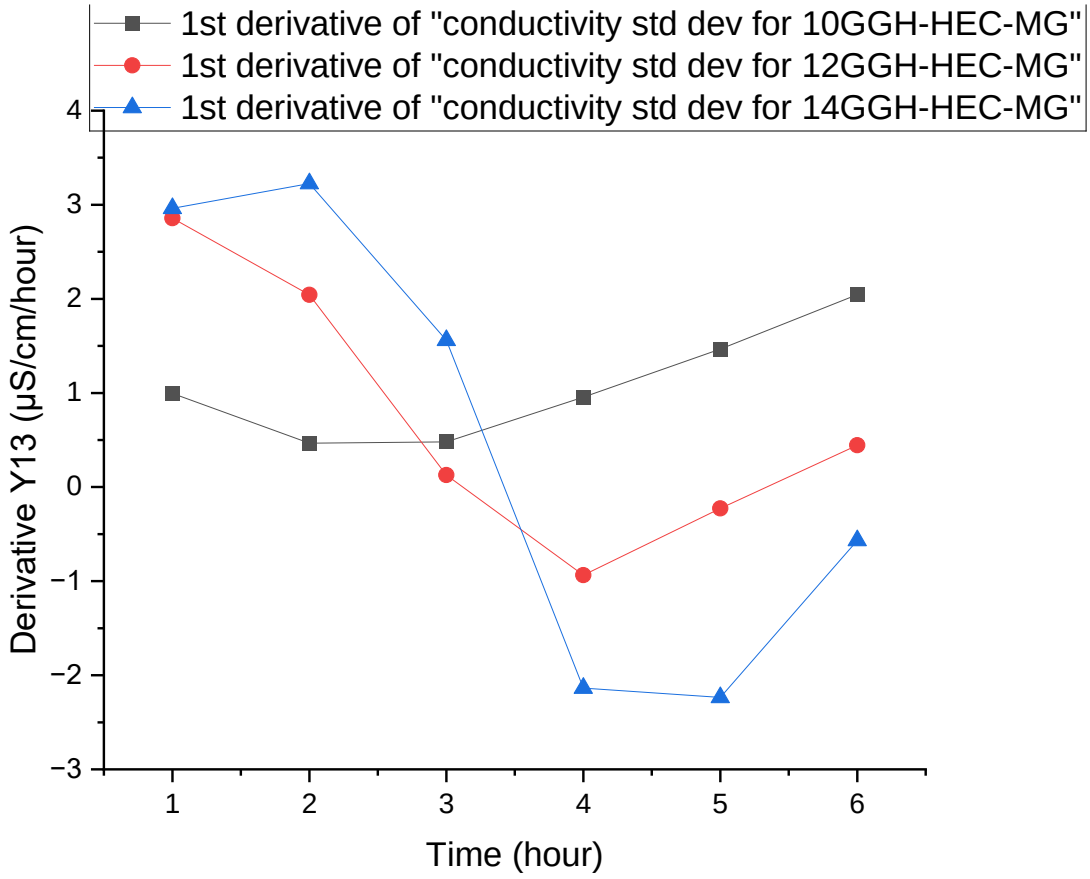

Figure 8.14: First Derivative of Conductivity Standard Deviation Over Time for GGH-HEC-MG Hydrogels at 10, 12, and 14 mg/cm³

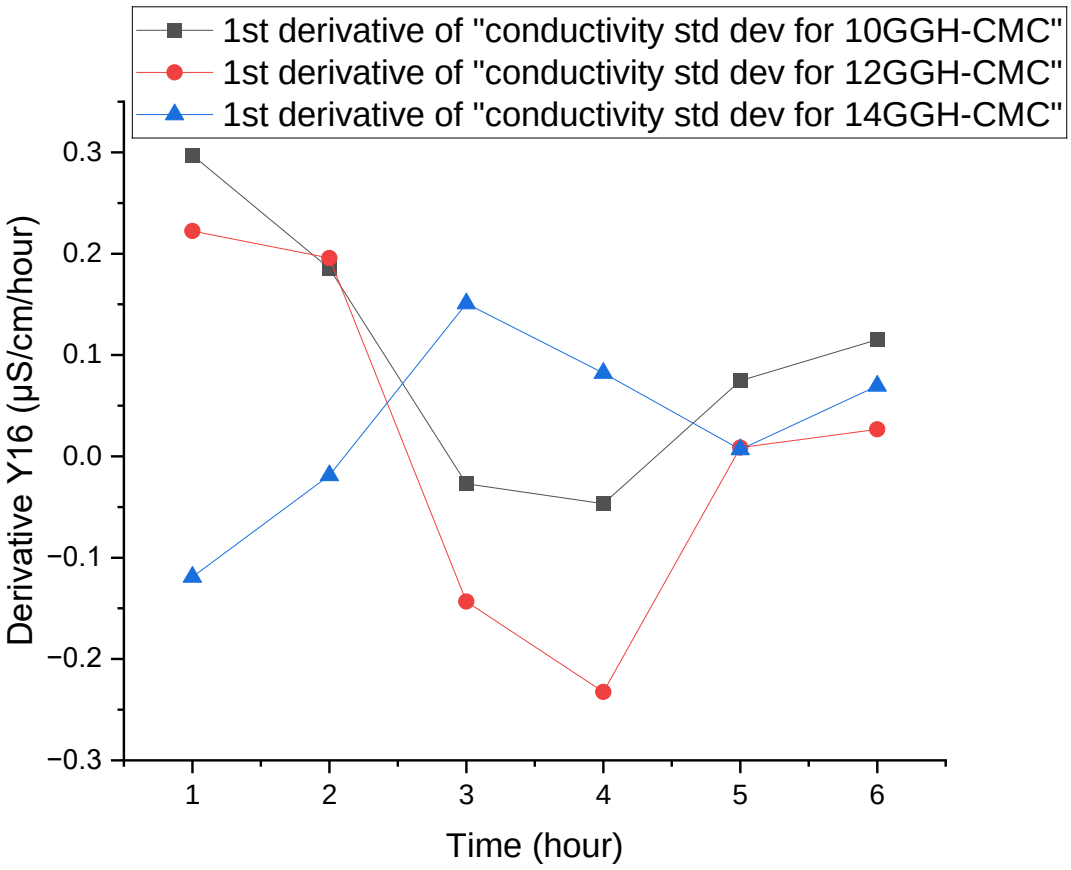

Figure 8.15: First Derivative of Conductivity Standard Deviation Over Time for GGH-CMC-MG Hydrogels at 10, 12, and 14 mg/cm³

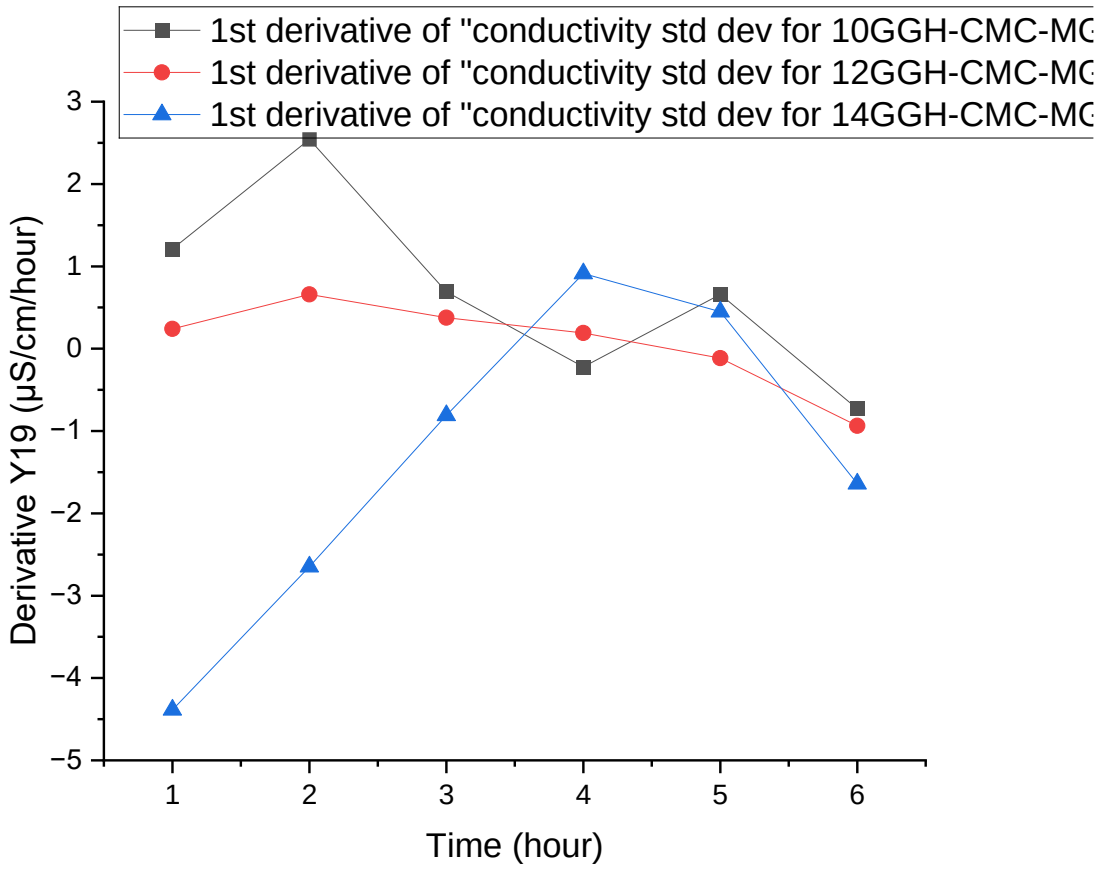

Figure 8.16: First Derivative of Conductivity Standard Deviation Over Time for GGH-CMC-MG Hydrogels at 10, 12, and 14 mg/cm³

Table 8.2: Turbidity Measurements Over Time for 10 mg/cm³ Hydrogel Samples (Mean ± Standard Deviation)

Time (mins)	Turbidity (MTU) of 10 mg/cm3 (sample 1)	Turbidity (MTU) of 10 mg/cm3 (sample 2)	Turbidity (MTU) of 10 mg/cm3 (sample 3)	Average	STDEV
0	3.36	3.57	5.46	4.13	1.15659
10	3.6	4.1	3.99	3.896667	0.262742
20	3.96	4.34	4.23	4.176667	0.195533
30	4.12	4.66	4.39	4.39	0.27
40	12.42	9.1	5.93	9.15	3.245289
50	19.2	17.43	17.67	18.1	0.960156
60	21.6	18.8	19	19.8	1.56205
70	22.7	20.1	20.3	21.03333	1.446836
80	23.9	21.3	22.2	22.46667	1.320353
90	24.5	22.3	22.6	23.13333	1.193035
100	26.2	22.9	22.9	24	1.905256
110	27.4	23.4	23.6	24.8	2.253886
120	27.9	24	24.6	25.5	2.1
130	28.1	27.7	24.6	26.8	1.915724
140	28.7	25.1	25	26.26667	2.107922
150	28.9	25.4	25.2	26.5	2.080865
160	29.1	25.7	25.7	26.83333	1.962991
170	29.5	26.1	25.7	27.1	2.088061
180	29.7	26.9	26.6	27.73333	1.709776
190	30	27.3	26.7	28	1.75784
200	31.2	27.9	27.8	28.96667	1.93477
210	33	28.3	28.2	29.83333	2.74287
220	33.3	28.4	28.6	30.1	2.773085
230	33.8	28.5	28.7	30.33333	3.003886
240	35.3	28.6	28.9	30.93333	3.784618
250	35.5	28.7	29.2	31.13333	3.789899
260	35.9	28.8	29.4	31.36667	3.937427
270	36	29.6	29.5	31.7	3.724245
280	36.2	29.4	30.3	31.96667	3.693688
290	36.4	29.5	30.3	32.06667	3.774034
300	36.3	30	30.4	32.23333	3.527511

Table 8.3: Turbidity Measurements Over Time for 12 mg/cm³ Hydrogel Samples (Mean ± Standard Deviation)

Time (min)	Turbidity (MTU) of 12 mg/cm3 (sample 1)	Turbidity (MTU) of 12 mg/cm3 (sample 2)	Turbidity (MTU) of 12 mg/cm3 (sample 3)	Average	STDEV
0	4.71	5.89	5.53	5.376667	0.604759
10	4.55	5.29	6.73	5.523333	1.108573
20	4.96	5.32	5.45	5.243333	0.253837
30	5.37	20.7	7.68	11.25	8.265041
40	9.49	26.6	25	20.36333	9.450504
50	26	26.5	28.3	26.93333	1.209683
60	28.6	28.5	29.9	29	0.781025
70	30.2	28.9	30.9	30	1.014889
80	31.4	29.8	31.6	30.93333	0.986577
90	31.5	30.3	32.5	31.43333	1.101514
100	31.8	31.1	32.9	31.93333	0.907377
110	32.2	31.6	33.6	32.46667	1.02632
120	32.4	31.9	33.9	32.73333	1.040833
130	32.8	32.2	34.2	33.06667	1.02632
140	33.5	32.5	34.5	33.5	1
150	33.1	33.2	34.9	33.73333	1.011599
160	33.5	33.8	35	34.1	0.793725
170	33.9	33.9	35.3	34.36667	0.80829
180	34.5	34	35.5	34.66667	0.763763
190	34.6	34.1	35.6	34.76667	0.763763
200	34.9	34.3	35.7	34.96667	0.702377
210	35.1	34.5	35.8	35.13333	0.650641
220	35.5	34.7	35.8	35.33333	0.568624
230	35.5	34.8	35.9	35.4	0.556776
240	35.8	35	36	35.6	0.52915
250	36.1	35.2	36.2	35.83333	0.550757
260	36.1	35.3	36.3	35.9	0.52915
270	36.3	35.3	36.5	36.03333	0.64291
280	36.5	35.3	36.4	36.06667	0.665833
290	35.6	35.4	36.7	35.9	0.7
300	36.7	35.9	36.7	36.43333	0.46188

Table 8.4: Turbidity Measurements Over Time for 14 mg/cm³ Hydrogel Samples (Mean ± Standard Deviation)

Time (mins)	Turbidity (MTU) of 14 mg/cm3 (sample 1)	Turbidity (MTU) of 14 mg/cm3 (sample 2)	Turbidity (MTU) of 14 mg/cm3 (sample 3)	Average	STDEV
0	5.05	6.21	5.48	5.58	0.58643
10	5.07	5.89	4.07	5.01	0.911482
20	6.44	5.98	7.46	6.626667	0.757452
30	14.67	5.97	14.05	11.56333	4.853878
40	27.3	24.9	27.6	26.6	1.479865
50	29.4	29.7	29.5	29.53333	0.152753
60	29.4	30.8	30.9	30.36667	0.83865
70	30	31.6	30.9	30.83333	0.802081
80	30.5	32.7	31.6	31.6	1.1
90	31.9	33.2	31.9	32.33333	0.750555
100	32.1	33.9	32.1	32.7	1.03923
110	30	34.2	32.3	32.16667	2.103172
120	29.5	34.7	32.5	32.23333	2.610236
130	29.5	34.9	32.6	32.33333	2.709859
140	29.5	35.1	32.7	32.43333	2.809508
150	32.4	35.2	32.8	33.46667	1.514376
160	33.5	35.4	33.1	34	1.228821
170	33.9	35.6	33.2	34.23333	1.234234
180	33.95	35.7	33.3	34.31667	1.241303
190	34.5	35.8	33.3	34.53333	1.250333
200	34.8	35.9	33.5	34.73333	1.201388
210	35	35.9	35.9	35.6	0.519615
220	35.2	35.9	35.9	35.66667	0.404145
230	35.4	36	36	35.8	0.34641
240	35.6	36	36	35.86667	0.23094
250	35.5	36	36	35.83333	0.288675
260	35.6	36	36	35.86667	0.23094
270	35.7	36	36	35.9	0.173205
280	35.9	36	36	35.96667	0.057735
290	36	36.2	36	36.06667	0.11547
300	36	36.2	36	36.06667	0.11547

Table 8.5: Turbidity Measurements Over Time for 10 mg/cm³ GGH Hydrogel Containing 0.229 g cTMP (Mean ± Standard Deviation)

Time (min)	(MA01 10 mg/cm³ GGH + 0.229 g cTMP)	(MA02 10 mg/cm³ GGH + 0.229 g cTMP)	(MA03 10 mg/cm³ GGH + 0.229 g cTMP)	Average	STDEV
0	5.57	5.17	4.84	5.193333	0.365559
10	5.8	5.39	4.92	5.37	0.440341
20	6.22	6.15	6.23	6.2	0.043589
30	6.45	6.39	7.47	6.77	0.60696
40	7.27	7.3	8.1	7.556667	0.470779
50	7.52	7.4	8.41	7.776667	0.551755
60	7.76	7.65	8.67	8.026667	0.559851
70	7.95	7.93	8.86	8.246667	0.531256
80	8.03	8.12	8.96	8.37	0.512933
90	8.13	8.16	9.1	8.463333	0.551574
100	8.2	8.4	9.2	8.6	0.52915
110	8.3	8.45	9.25	8.666667	0.510718
120	8.4	8.73	9.41	8.846667	0.515008
130	8.52	9.1	9.48	9.033333	0.48346
140	8.6	9.33	9.55	9.16	0.497293
150	8.69	9.49	9.69	9.29	0.52915
160	8.71	9.59	9.67	9.323333	0.532666
170	8.8	9.6	9.7	9.366667	0.493288
180	8.8	9.85	9.8	9.483333	0.592312
190	8.84	10.37	10.15	9.786667	0.827184
200	8.86	10.53	10.3	9.896667	0.905115
210	8.92	10.62	10.35	9.963333	0.913583
220	8.94	10.8	10.43	10.05667	0.984598
230	8.94	10.96	10.56	10.15333	1.069642
240	8.96	11	10.69	10.21667	1.099288
250	9.1	11.12	10.75	10.32333	1.075469
260	9.1	11.19	10.87	10.38667	1.125715
270	9.12	11.22	10.9	10.41333	1.13143
280	9.2	11.35	10.97	10.50667	1.147446
290	9.3	11.74	11.08	10.70667	1.262115
300	9..40	11.8	11.15	11.475	0.459619

Table 8.6: Turbidity Measurements Over Time for 12 mg/cm³ GGH Hydrogel Containing 0.275 g cTMP (Mean ± Standard Deviation)

Time (mins)	(MA01 12 mg/cm³+ 0.275g cTMP)	(MA02 12 mg/cm³+ 0.275g cTMP)	(MA03 12 mg/cm³+ 0.275g cTMP)	Avreage	STDEV
0	9.29	7.18	6.23	7.566667	1.566216
10	9.31	7.59	6.54	7.813333	1.39844
20	16.69	15.77	12.88	15.11333	1.988073
30	19.4	18.15	17.21	18.25333	1.098651
40	20.5	19	18.15	19.21667	1.189888
50	21.3	19.6	18.7	19.86667	1.320353
60	21.7	20.4	19.2	20.43333	1.250333
70	22.2	20.6	19.7	20.83333	1.266228
80	22.7	20.8	20.2	21.23333	1.305118
90	22.9	20.9	20.3	21.36667	1.361372
100	23	21	20.6	21.53333	1.28582
110	23.1	21.2	20.7	21.66667	1.266228
120	23.2	21.2	20.8	21.73333	1.28582
130	23.2	21.2	21	21.8	1.216553
140	23.2	21.3	21.1	21.86667	1.159023
150	23.2	21.4	21.2	21.93333	1.101514
160	23.2	21.5	21.2	21.96667	1.078579
170	23.2	21.5	21.2	21.96667	1.078579
180	23.3	21.6	21.2	22.03333	1.115049
190	23.1	21.5	21.1	21.9	1.058301
200	23.3	21.5	21.1	21.96667	1.171893
210	23.4	21.5	21.2	22.03333	1.193035
220	23.4	21.4	21.2	22	1.216553
230	23.4	21.4	21.2	22	1.216553
240	23.3	21.4	21.2	21.96667	1.159023
250	23.2	21.4	21.2	21.93333	1.101514
260	23.2	21.4	21.2	21.93333	1.101514
270	23.2	21.4	21.2	21.93333	1.101514
280	23.4	21.4	21.2	22	1.216553
290	23.4	21.4	21.2	22	1.216553
300	23.4	21.4	21.2	22	1.216553

Table 8.7: Turbidity Measurements Over Time for 14 mg/cm³ GGH Hydrogel Containing 0.330 g cTMP (Mean ± Standard Deviation)

Time (min)	(MA01 14 mg/cm³+ 0.330g cTMP)	(MA02 14 mg/cm³+ 0.330g cTMP)	(MA03 14 mg/cm³+ 0.330g cTMP)	Average	STDEV
0	12.82	13.20	13.02	13.01333	0.190088
10	12.99	14.30	14.84	14.04333	0.951332
20	24.60	24.30	25.10	24.66667	0.404145
30	27.80	26.60	27.80	27.4	0.69282
40	29.50	27.1	29.90	28.83333	1.514376
50	30.50	27.6	30.60	29.56667	1.703917
60	31.1	28.2	31.40	30.23333	1.767295
70	31.5	28.4	31.80	30.56667	1.882374
80	32.00	28.4	32.00	30.8	2.078461
90	32.3	28.3	32.40	31	2.338803
100	32.5	28.3	32.90	31.23333	2.548202
110	32.5	28.3	33.0	31.26667	2.581343
120	32.6	28.3	33.20	31.36667	2.672702
130	32.9	28.3	33.30	31.5	2.778489
140	33.1	28.3	33.40	31.6	2.861818
150	33.2	28.3	33.50	31.66667	2.919475
160	33.2	28.3	33.60	31.7	2.951271
170	33.1	28.3	33.70	31.7	2.95973
180	33.0	28.3	33.80	31.7	2.971532
190	33.0	28.3	33.80	31.7	2.971532
200	33.0	28.3	33.80	31.7	2.971532
210	33.0	28.3	33.90	31.73333	3.007214
220	33.0	28.3	33.90	31.73333	3.007214
230	33.0	28.3	33.90	31.73333	3.007214
240	33.0	28.3	33.90	31.73333	3.007214
250	33.0	28.3	33.90	31.73333	3.007214
260	33.0	28.3	33.90	31.73333	3.007214
270	33.0	28.3	33.90	31.73333	3.007214
280	33.0	28.3	33.90	31.73333	3.007214
290	33.0	28.3	33.90	31.73333	3.007214
300	33.0	28.3	33.90	31.73333	3.007214

Chapter 9: References

1. Akrofi-Atitianti, F., Ifejika Speranza, C., Bockel, L. and Asare, R. Assessing climate smart agriculture and its determinants of practice in Ghana: A case of the cocoa production system. *Land.* [Online]. 2018, **7**(1), p.30.
2. Saltiel, J., Bauder, J.W. and Palakovich, S. Adoption of sustainable agricultural practices: Diffusion, farm structure, and Profitability 1. *Rural sociology.* [Online]. 1994, **59**(2), pp.333-349.
3. Abrol, I. and Sangar, S. Sustaining Indian agriculture–conservation agriculture the way forward. *Current Science.* [Online]. 2006, pp.1020-1025.
4. *World population by nation.* [Online]. 2025. [Accessed October 2025]. Available from: https://worldpopulationreview.com/countries
5. Pimentel, D. and Burgess, M. Soil erosion threatens food production. *Agriculture.* [Online]. 2013, **3**(3), pp.443-463.
6. Waldron, A., Garrity, D., Malhi, Y., Girardin, C., Miller, D. and Seddon, N. Agroforestry can enhance food security while meeting other sustainable development goals. *Tropical Conservation Science.* [Online]. 2017, **10**, p.1940082917720667.
7. Shiraishi, H., Shiraishi, H., Sakaki, T. and Iwamura, M. Development of Load-lifting-assist Mechanism Using Lower Limbs. *Sensors & Materials.* [Online]. 2024, **36**.
8. Matygov, M., Pshikova, O. and Shaov, M. Transforming agriculture in response to modern emerging challenges: A close look at the late shifts in farming practices. In: *E3S Web of Conferences*: EDP Sciences, 2023, p.02004.
9. Islam, S. Evaluation of low-carbon sustainable technologies in agriculture sector through grey ordinal priority approach. *International Journal of Grey Systems.* [Online]. 2021, **1**(1), pp.5-26.
10. Acharya Balkrishna, A.K., Arya, V., Sharma, G., Srivastava, D., Sharma, A. and Khan, N. Situational Analysis of Government Initiatives for the Welfare of Farmers in India: Impact and Futuristic Insights. *Indian Journal of Ecology.* [Online]. 2022, **49**(3), pp.1023-1035.
11. Ali, Z. and Gillani, S.U.A. Assessing the Challenges and Impact of Access to Agricultural Credit in Southern Punjab (Pakistan): A Qualitative Study. *Pakistan Journal of Humanities and Social Sciences.* [Online]. 2023, **11**(3), pp.3242–3254-3242–3254.
12. Nurhadi, I., Rozikin, M. and Nuh, M. Implementation of Smart Farming-based Agricultural Policy in Trenggalek Regency (Study on the Department of Agriculture and Food in Trenggalek Regency). *Journal of Law and Sustainable Development.* [Online]. 2024, **12**(1), pp.e2650-e2650.
13. Tokgoz, S., Allen, S., Majeed, F., Paris, B., Adeola, O. and Osabuohien, E. Distortions to agricultural incentives: Evidence from Nigerian value chains. *Review of Development Economics.* [Online]. 2020, **24**(3), pp.1027-1045.
14. Fishman, R.M., Siegfried, T., Raj, P., Modi, V. and Lall, U. Over-extraction from shallow bedrock versus deep alluvial aquifers: Reliability versus sustainability considerations for India's groundwater irrigation. *Water Resources Research.* [Online]. 2011, **47**(6).
15. Shidiq, M.R. Determinants of agripreneurial career intentions: evidence from agriculture students. *Jurnal Manajemen & Agribisnis.* [Online]. 2020, **17**(2), pp.128-128.
16. Oladosu, Y., Rafii, M.Y., Arolu, F., Chukwu, S.C., Salisu, M.A., Fagbohun, I.K., Muftaudeen, T.K., Swaray, S. and Haliru, B.S. Superabsorbent polymer hydrogels for sustainable agriculture: A review. *Horticulturae.* [Online]. 2022, **8**(7), p.605.
17. Zhang, J., Li, A. and Wang, A. Study on superabsorbent composite. VI. Preparation, characterization and swelling behaviors of starch phosphate-graft-acrylamide/attapulgite superabsorbent composite. *Carbohydrate Polymers.* [Online]. 2006, **65**(2), pp.150-158.
18. Ahmed, E.M. Hydrogel: Preparation, characterization, and applications: A review. *Journal of advanced research.* [Online]. 2015, **6**(2), pp.105-121.
19. Ovalesha, M., Yadav, B. and Rai, P.K. Effects of polymer seed coating and seed treatment on plant growth, seed yield and quality of Cowpea (Vigna unguiculata). *Journal of Pharmacognosy and Phytochemistry.* [Online]. 2017, **6**(4), pp.106-109.
20. Dehkordi, D.K. and Seyyedboveir, S. Evaluation of super AB A 200 Superabsorbent on water use efficiency and yield response factor of SCKaroun701 corn under deficit irrigation. *Advances in Environmental Biology.* [Online]. 2013, pp.4615-4623.

21. Abobatta, W. Impact of hydrogel polymer in agricultural sector. *Adv. Agric. Environ. Sci. Open Access.* [Online]. 2018, **1**(2), pp.59-64.
22. Montesano, F.F., Parente, A., Santamaria, P., Sannino, A. and Serio, F. Biodegradable superabsorbent hydrogel increaseswater retention properties of growing media and plant growth. *Agriculture and Agricultural Science Procedia.* [Online]. 2015, **4**, pp.451-458.
23. Abdel-raouf, M.E.-S., Sayed, A. and Mostafa, M. Application of Guar Gum and Its Derivatives in Agriculture. In: *Gums, Resins and Latexes of Plant Origin: Chemistry, Biological Activities and Uses*. Springer, 2021, pp.1-17.
24. Maleki, B., Kargar, P.G., Ashrafi, S.S. and Ghani, M. Perspective Chapter: Introduction to Hydrogels–Definition, Classifications, Applications and Methods of Preparation. [Online]. 2024.
25. Dodda, J.M., Deshmukh, K., Bezuidenhout, D. and Yeh, Y.-C. Hydrogels: definition, history, classifications, formation, constitutive characteristics, and applications. [Online]. 2023.
26. Lu, J., Li, Y.Y., Li, B., Xu, Z. and Liu, J. *Mineral hydrogels from inorganic salts*. Google Patents. 2023.
27. Wichterle, O. and Lim, D. Hydrophilic gels for biological use. *Nature.* [Online]. 1960, **185**(4706), pp.117-118.
28. Ermiş, N. Drug delivery application of poly (2-hydroxyethyl methacrylate)/ethylene glycol dimethacrylate composite hydrogel. *Gazi University Journal of Science.* [Online]. 2022, **35**(4), pp.1318-1331.
29. Maldonado-Codina, C. and Efron, N. Impact of manufacturing technology and material composition on the mechanical properties of hydrogel contact lenses. *Ophthalmic and Physiological Optics.* [Online]. 2004, **24**(6), pp.551-561.
30. Updike, S.J. and Hicks, G.P. The enzyme electrode. *Nature.* [Online]. 1967, **214**(5092), pp.986-988.
31. Tanaka, T. Collapse of gels and the critical endpoint. *Physical review letters.* [Online]. 1978, **40**(12), p.820.
32. Yue, S., He, H., Li, B. and Hou, T. Hydrogel as a biomaterial for bone tissue engineering: A review. *Nanomaterials.* [Online]. 2020, **10**(8), p.1511.
33. Bahram, M., Mohseni, N. and Moghtader, M. An introduction to hydrogels and some recent applications. In: *Emerging concepts in analysis and applications of hydrogels*. IntechOpen, 2016.
34. Okay, O. General properties of hydrogels. *Hydrogel sensors and actuators: engineering and technology.* [Online]. 2010, pp.1-14.
35. Saini, K. Preparation method, Properties and Crosslinking of hydrogel: a review. *PharmaTutor.* [Online]. 2017, **5**(1), pp.27-36.
36. Zhang, Y.S. and Khademhosseini, A. Advances in engineering hydrogels. *Science.* [Online]. 2017, **356**(6337), p.eaaf3627.
37. Wang, C., Zhao, N., Huang, Y., He, R., Xu, S. and Yuan, W. Coordination of injectable self-healing hydrogel with Mn-Zn ferrite@ mesoporous silica nanospheres for tumor MR imaging and efficient synergistic magnetothermal-chemo-chemodynamic therapy. *Chemical Engineering Journal.* [Online]. 2020, **401**, p.126100.
38. Li, L., Zeng, Z., Chen, Z., Gao, R., Pan, L., Deng, J., Ye, X., Zhang, J., Zhang, S. and Mei, C. Microenvironment-triggered degradable hydrogel for imaging diagnosis and combined treatment of intraocular choroidal melanoma. *ACS nano.* [Online]. 2020, **14**(11), pp.15403-15416.
39. Li, Z., Yu, C., Kumar, H., He, X., Lu, Q., Bai, H., Kim, K. and Hu, J. The effect of crosslinking degree of hydrogels on hydrogel adhesion. *Gels.* [Online]. 2022, **8**(10), p.682.
40. Zhou, K., Yang, S., Zhao, G., Ning, Y. and Xu, C. Self-assembly of the sodium salts of fatty acids into limpid hydrogels through non-covalent interactions with peptides. *RSC Advances.* [Online]. 2015, **5**(76), pp.61719-61724.
41. Ghobril, C., Charoen, K., Rodriguez, E.K., Nazarian, A. and Grinstaff, M.W. A dendritic thioester hydrogel based on thiol-thioester exchange as a dissolvable sealant system for wound closure. *Angewandte Chemie (International ed. in English).* [Online]. 2013, **52**(52), p.14070.
42. Huang, L.-C., Wang, H.-C., Chen, L.-H., Ho, C.-Y., Hsieh, P.-H., Huang, M.-Y., Wu, H.-C. and Wang, T.-W. Bioinspired self-assembling peptide hydrogel with proteoglycan-assisted growth factor delivery for therapeutic angiogenesis. *Theranostics.* [Online]. 2019, **9**(23), p.7072.
43. Duin, S., Schütz, K., Ahlfeld, T., Lehmann, S., Lode, A., Ludwig, B. and Gelinsky, M. 3D bioprinting of functional islets of langerhans in an alginate/methylcellulose hydrogel blend. *Advanced healthcare materials.* [Online]. 2019, **8**(7), p.1801631.
44. Byun, E. and Lee, H. Enhanced loading efficiency and sustained release of doxorubicin from hyaluronic acid/graphene oxide composite hydrogels by a mussel-inspired catecholamine. *Journal of nanoscience and nanotechnology.* [Online]. 2014, **14**(10), pp.7395-7401.

45. Breger, J.C., Yoon, C., Xiao, R., Kwag, H.R., Wang, M.O., Fisher, J.P., Nguyen, T.D. and Gracias, D.H. Self-folding thermo-magnetically responsive soft microgrippers. *ACS applied materials & interfaces.* [Online]. 2015, **7**(5), pp.3398-3405.
46. Krüger, M., Oosterhoff, L.A., van Wolferen, M.E., Schiele, S.A., Walther, A., Geijsen, N., De Laporte, L., van der Laan, L.J., Kock, L.M. and Spee, B. Cellulose nanofibril hydrogel promotes hepatic differentiation of human liver organoids. *Advanced healthcare materials.* [Online]. 2020, **9**(6), p.1901658.
47. Zhang, X., Guan, Y. and Zhang, Y. Ultrathin hydrogel films for rapid optical biosensing. *Biomacromolecules.* [Online]. 2012, **13**(1), pp.92-97.
48. You, Z., Behl, M., Grage, S.L., Bürck, J., Zhao, Q., Ulrich, A.S. and Lendlein, A. Shape-memory effect by sequential coupling of functions over different length scales in an architectured hydrogel. *Biomacromolecules.* [Online]. 2019, **21**(2), pp.680-687.
49. Chen, C., Wang, Y., Zhang, H., Zhang, H., Dong, W., Sun, W. and Zhao, Y. Responsive and self-healing structural color supramolecular hydrogel patch for diabetic wound treatment. *Bioactive Materials.* [Online]. 2022, **15**, pp.194-202.
50. Choe, A., Yeom, J., Shanker, R., Kim, M.P., Kang, S. and Ko, H. Stretchable and wearable colorimetric patches based on thermoresponsive plasmonic microgels embedded in a hydrogel film. *NPG Asia Materials.* [Online]. 2018, **10**(9), pp.912-922.
51. Jing, Z., Ni, R., Wang, J., Lin, X., Fan, D., Wei, Q., Zhang, T., Zheng, Y., Cai, H. and Liu, Z. Practical strategy to construct anti-osteosarcoma bone substitutes by loading cisplatin into 3D-printed titanium alloy implants using a thermosensitive hydrogel. *Bioactive Materials.* [Online]. 2021, **6**(12), pp.4542-4557.
52. Yang, R., Li, G., Zhuang, C., Yu, P., Ye, T., Zhang, Y., Shang, P., Huang, J., Cai, M. and Wang, L. Gradient bimetallic ion–based hydrogels for tissue microstructure reconstruction of tendon-to-bone insertion. *Science Advances.* [Online]. 2021, **7**(26), p.eabg3816.
53. Obra, J., Maranan, J.Q., Lensoco, D.F. and Tumolva, T. Synthesis and Characterization of NaCMC/HEC/Activated Carbon Hydrogel Composites for the Desalination of Seawater. [Online]. 2022.
54. Gong, F., Jiang, L., Gao, Y., Xu, J. and Wang, T. Delivery of soluble ethinylestradiol complex by pH-responsive core-shell composite hydrogel capsules. *Journal of Applied Polymer Science.* [Online]. 2023, **140**(31), p.e54225.
55. Zu, S., Zhang, Z., Liu, Q., Wang, Z., Song, Z., Guo, Y., Xin, Y. and Zhang, S. 4D printing of core–shell hydrogel capsules for smart controlled drug release. *Bio-Design and Manufacturing.* [Online]. 2022, **5**(2), pp.294-304.
56. Asy-Syifa, N., Waresindo, W.X., Edikresnha, D., Suciati, T. and Khairurrijal, K. The Study of the Swelling Degree of the PVA Hydrogel with varying concentrations of PVA. In: *Journal of Physics: Conference Series*: IOP Publishing, 2022, p.012053.
57. Hoffman, A.S. Hydrogels for biomedical applications. *Advanced drug delivery reviews.* [Online]. 2012, **64**, pp.18-23.
58. Budai, L., Budai, M., Fülöpné Pápay, Z.E., Vilimi, Z. and Antal, I. Rheological considerations of pharmaceutical formulations: Focus on viscoelasticity. *Gels.* [Online]. 2023, **9**(6), p.469.
59. Guilherme, M.R., Aouada, F.A., Fajardo, A.R., Martins, A.F., Paulino, A.T., Davi, M.F., Rubira, A.F. and Muniz, E.C. Superabsorbent hydrogels based on polysaccharides for application in agriculture as soil conditioner and nutrient carrier: A review. *European Polymer Journal.* [Online]. 2015, **72**, pp.365-385.
60. Reddy, N. and Yang, Y. Properties and potential applications of natural cellulose fibers from cornhusks. *Green Chemistry.* [Online]. 2005, **7**(4), pp.190-195.
61. Demitri, C., Scalera, F., Madaghiele, M., Sannino, A. and Maffezzoli, A. Potential of cellulose-based superabsorbent hydrogels as water reservoir in agriculture. *International Journal of Polymer Science.* [Online]. 2013, **2013**(1), p.435073.
62. Morris, E.R., Nishinari, K. and Rinaudo, M. Gelation of gellan–a review. *Food Hydrocolloids.* [Online]. 2012, **28**(2), pp.373-411.
63. Vedovello, P., Sanches, L.V., da Silva Teodoro, G., Majaron, V.F., Bortoletto-Santos, R., Ribeiro, C. and Putti, F.F. An Overview of Polymeric Hydrogel Applications for Sustainable Agriculture. *Agriculture.* [Online]. 2024, **14**(6), p.840.
64. Butnariu, M. and Flavius, A.I. General information about cellulose. *J. Biotechnol. Bioprocess.* [Online]. 2022, **3**(3), pp.1-5.
65. Miao, C. and Hamad, W.Y. Cellulose reinforced polymer composites and nanocomposites: a critical review. *Cellulose.* [Online]. 2013, **20**(5), pp.2221-2262.
66. Chang, C., Duan, B., Cai, J. and Zhang, L. Superabsorbent hydrogels based on cellulose for smart swelling and controllable delivery. *European Polymer Journal.* [Online]. 2010, **46**(1), pp.92-100.

67. Criado, P., Fraschini, C., Salmieri, S., Becher, D., Safrany, A. and Lacroix, M. Evaluation of antioxidant cellulose nanocrystals and applications in gellan gum films. *Industrial Biotechnology.* [Online]. 2015, **11**(1), pp.59-68.
68. Thakur, V., Guleria, A., Kumar, S., Sharma, S. and Singh, K. Recent advances in nanocellulose processing, functionalization and applications: A review. *Materials Advances.* [Online]. 2021, **2**(6), pp.1872-1895.
69. Zhang, L.M. New water-soluble cellulosic polymers: a review. *Macromolecular Materials and Engineering.* [Online]. 2001, **286**(5), pp.267-275.
70. Karthika, J. and Vishalakshi, B. pH responsive gels of gellan gum and carboxymethyl cellulose: Matrix for ketoprofen delivery. *Int. J. ChemTech Res.* [Online]. 2014, **6**, pp.1055-1069.
71. Tavagnacco, L., Chiessi, E., Severini, L., Franco, S., Buratti, E., Capocefalo, A., Brasili, F., Mosca Conte, A., Missori, M. and Angelini, R. Molecular origin of the two-step mechanism of gellan aggregation. *Science Advances.* [Online]. 2023, **9**(10), p.eadg4392.
72. Rebelo, R.C., Fonseca, A.C., Coelho, J.F. and Serra, A.C. A sustainable synthesis of cellulose hydrogels for agriculture with repurpose of solvent as fertilizer. *Carbohydrate Polymers.* [Online]. 2025, p.124156.
73. Guo, B., Finne-Wistrand, A. and Albertsson, A.-C. Facile synthesis of degradable and electrically conductive polysaccharide hydrogels. *Biomacromolecules.* [Online]. 2011, **12**(7), pp.2601-2609.
74. Ibrahim, M.M., Abd-Eladl, M. and Abou-Baker, N.H. Lignocellulosic biomass for the preparation of cellulose-based hydrogel and its use for optimizing water resources in agriculture. *Journal of Applied Polymer Science.* [Online]. 2015, **132**(42).
75. Kaur, P., Agrawal, R., Pfeffer, F.M., Williams, R. and Bohidar, H.B. Hydrogels in agriculture: Prospects and challenges. *Journal of Polymers and the Environment.* [Online]. 2023, **31**(9), pp.3701-3718.
76. Shahid, S.A., Qidwai, A.A., Anwar, F., Ullah, I. and Rashid, U. Improvement in the water retention characteristics of sandy loam soil using a newly synthesized poly (acrylamide-co-acrylic acid)/AlZnFe2O4 superabsorbent hydrogel nanocomposite material. *Molecules.* [Online]. 2012, **17**(8), pp.9397-9412.
77. Zhang, W., Mu, X., Xu, Y., Ma, G. and Lei, Z. Research progress of environment-responsive hydrogel applications in agriculture. *Express Polymer Letters.* [Online]. 2024, **18**(2), pp.193-213.
78. Park, J., Guan, W., Lei, C. and Yu, G. Self-irrigation and slow-release fertilizer hydrogels for sustainable agriculture. *ACS Materials Letters.* [Online]. 2024, **6**(8), pp.3471-3477.
79. Kabir, S.F., Sikdar, P.P., Haque, B., Bhuiyan, M.R., Ali, A. and Islam, M. Cellulose-based hydrogel materials: Chemistry, properties and their prospective applications. *Progress in biomaterials.* [Online]. 2018, **7**, pp.153-174.
80. Liu, X., Feng, T., Ding, W., Zeng, W., Wang, N., Yang, F., Yang, C., Yang, S., Kong, Y. and Lei, Z. Synthesis of tamarind seed gum-based semi-IPN hydrogels with integration of fertilizer retention and anti-evaporation. *Journal of Applied Polymer Science.* [Online]. 2023, **140**(3), p.e53325.
81. Mazloom, N., Khorassani, R., Zohuri, G.H., Emami, H. and Whalen, J. Development and characterization of lignin-based hydrogel for use in agricultural soils: preliminary evidence. *CLEAN–Soil, Air, Water.* [Online]. 2019, **47**(11), p.1900101.
82. Reidy, E., Leonard, N., Treacy, O. and Ryan, A. A 3D View of Colorectal Cancer Models in Predicting Therapeutic Responses and Resistance. *Cancers.* [Online]. 2021, **13**, p.227. Available from: https://doi.org/10.3390/cancers13020227
83. Buwalda, S.J., Vermonden, T. and Hennink, W.E. Hydrogels for therapeutic delivery: current developments and future directions. *Biomacromolecules.* [Online]. 2017, **18**(2), pp.316-330.
84. Chirani, N., Yahia, L., Gritsch, L., Motta, F.L., Chirani, S. and Farè, S. History and applications of hydrogels. *Journal of biomedical sciences.* [Online]. 2015, **4**(02), pp.1-23.
85. Macdougall, L.J., Truong, V.X. and Dove, A.P. Efficient in situ nucleophilic thiol-yne click chemistry for the synthesis of strong hydrogel materials with tunable properties. *ACS Macro Letters.* [Online]. 2017, **6**(2), pp.93-97.
86. Hunt, J.N., Feldman, K.E., Lynd, N.A., Deek, J., Campos, L.M., Spruell, J.M., Hernandez, B.M., Kramer, E.J. and Hawker, C.J. Tunable, high modulus hydrogels driven by ionic coacervation. *Advanced Materials.* [Online]. 2011, **23**(20), pp.2327-2331.
87. Bryant, S.J. and Vernerey, F.J. Programmable hydrogels for cell encapsulation and neo-tissue growth to enable personalized tissue engineering. *Advanced healthcare materials.* [Online]. 2018, **7**(1), p.1700605.
88. Alves, T.F., Morsink, M., Batain, F., Chaud, M.V., Almeida, T., Fernandes, D.A., da Silva, C.F., Souto, E.B. and Severino, P. Applications of natural, semi-synthetic, and synthetic polymers in cosmetic formulations. *Cosmetics.* [Online]. 2020, **7**(4), p.75.

89. Catoira, M.C., Fusaro, L., Di Francesco, D., Ramella, M. and Boccafoschi, F. Overview of natural hydrogels for regenerative medicine applications. *Journal of Materials Science: Materials in Medicine.* [Online]. 2019, **30**, pp.1-10.
90. Rajanna, G., Manna, S., Singh, A., Babu, S., Singh, V., Dass, A., Chakraborty, D., Patanjali, N., Chopra, I. and Banerjee, T. Biopolymeric superabsorbent hydrogels: impact on soil moisture release pattern, crop and water productivity of soybean–wheat under different irrigation regimes in Indo-Gangetic plains of India. [Online]. 2021.
91. Adjuik, T.A., Nokes, S.E., Montross, M.D. and Wendroth, O. The impacts of bio-based and synthetic hydrogels on soil hydraulic properties: A review. *Polymers.* [Online]. 2022, **14**(21), p.4721.
92. Xu, L., Zhang, X., Zhu, C., Zhang, Y., Fu, C., Yang, B., Tao, L. and Wei, Y. Nonionic polymer cross-linked chitosan hydrogel: preparation and bioevaluation. *Journal of Biomaterials Science, Polymer Edition.* [Online]. 2013, **24**(13), pp.1564-1574.
93. Shelke, N.B., James, R., Laurencin, C.T. and Kumbar, S.G. Polysaccharide biomaterials for drug delivery and regenerative engineering. *Polymers for Advanced Technologies.* [Online]. 2014, **25**(5), pp.448-460.
94. McArthur, S.L., McLean, K.M., Kingshott, P., St John, H.A.W., Chatelier, R.C. and Griesser, H.J. Effect of polysaccharide structure on protein adsorption. *Colloids and Surfaces B: Biointerfaces.* [Online]. 2000, **17**(1), pp.37-48. Available from: https://doi.org/https://doi.org/10.1016/S0927-7765(99)00086-7
95. Aguilar-Arevalo, A., Bazarko, A., Brice, S., Brown, B., Bugel, L., Cao, J., Coney, L., Conrad, J., Cox, D. and Curioni, A. Measurement of muon neutrino quasielastic scattering on carbon. *Physical review letters.* [Online]. 2008, **100**(3), p.032301.
96. Mizrahy, S. and Peer, D. Polysaccharides as building blocks for nanotherapeutics. *Chemical Society Reviews.* [Online]. 2012, **41**(7), pp.2623-2640.
97. Sinha, V.R. and Kumria, R. Polysaccharides in colon-specific drug delivery. *International journal of pharmaceutics.* [Online]. 2001, **224**(1-2), pp.19-38.
98. Doublier, J.-L., Garnier, C., Renard, D. and Sanchez, C. Protein–polysaccharide interactions. *Current opinion in Colloid & interface Science.* [Online]. 2000, **5**(3-4), pp.202-214.
99. Li, X., Jiang, F., Liu, M., Qu, Y., Lan, Z., Dai, X., Huang, C., Yue, X., Zhao, S. and Pan, X. Synthesis, characterization, and bioactivities of polysaccharide metal complexes: a review. *Journal of Agricultural and Food Chemistry.* [Online]. 2022, **70**(23), pp.6922-6942.
100. Silva, A.K.A., Letourneur, D. and Chauvierre, C. Polysaccharide nanosystems for future progress in cardiovascular pathologies. *Theranostics.* [Online]. 2014, **4**(6), p.579.
101. Visakh, P., Mathew, A.P., Oksman, K. and Thomas, S. Starch-Based Bionanocomposites: Processing and Properties. *Polysaccharide building blocks: A sustainable approach to the development of renewable biomaterials.* [Online]. 2012, pp.287-306.
102. Herrick, F.W., Casebier, R.L., Hamilton, J.K. and Sandberg, K.R. Microfibrillated cellulose: morphology and accessibility. In: *J. Appl. Polym. Sci.: Appl. Polym. Symp.;(United States)*: ITT Rayonier Inc., Shelton, WA, 1983.
103. Nevell, T.P. and Zeronian, S.H. Cellulose chemistry and its applications. [Online]. 1985.
104. O'sullivan, A.C. Cellulose: the structure slowly unravels. *Cellulose.* [Online]. 1997, **4**(3), pp.173-207.
105. Abdl Aali, R.A.K. and Al-Sahlany, S.T.G. Gellan Gum as a Unique Microbial Polysaccharide: Its Characteristics, Synthesis, and Current Application Trends. *Gels.* [Online]. 2024, **10**(3), p.183.
106. Raghunandan, K., Kumar, A., Kumar, S., Permaul, K. and Singh, S. Production of gellan gum, an exopolysaccharide, from biodiesel-derived waste glycerol by Sphingomonas spp. *3 Biotech.* [Online]. 2018, **8**, pp.1-13.
107. Lau, M., Tang, J. and Paulson, A. Effect of polymer ratio and calcium concentration on gelation properties of gellan/gelatin mixed gels. *Food research international.* [Online]. 2001, **34**(10), pp.879-886.
108. McGuffey, J.C., Leon, D., Dhanji, E.Z., Mishler, D.M. and Barrick, J.E. Bacterial production of gellan gum as a Do-It-Yourself alternative to Agar. *Journal of Microbiology & Biology Education.* [Online]. 2018, **19**(2), p.10.1128/jmbe. v1119i1122. 1530.
109. Ichimura, K., Niki, T., Kato, M., Shimizu-Yumoto, H. and Norikoshi, R. Effect of Gellan Gum and MS Inorganic Salt Gel Formulations on the Vase Life of Cut Roses and Physical Properties of Gel. *Journal of the Japanese Society for Horticultural Science.* [Online]. 2009, **78**(4), pp.443-449.
110. Abd El-Mohdy, H., Hegazy, E., El-Nesr, E. and El-Wahab, M.A. Control release of some pesticides from starch/(ethylene glycol-co-methacrylic acid) copolymers prepared by γ-irradiation. *Journal of Polymer Research.* [Online]. 2011, **18**, pp.1605-1615.
111. Mao, R., Tang, J. and Swanson, B. Texture properties of high and low acyl mixed gellan gels. *Carbohydrate Polymers.* [Online]. 2000, **41**(4), pp.331-338.

112. Kang, K.S., Veeder, G.T., Mirrasoul, P.J., Kaneko, T. and Cottrell, I.W. Agar-like polysaccharide produced by a Pseudomonas species: production and basic properties. *Applied and environmental microbiology.* [Online]. 1982, **43**(5), pp.1086-1091.
113. Osmałek, T., Froelich, A. and Tasarek, S. Application of gellan gum in pharmacy and medicine. *International journal of pharmaceutics.* [Online]. 2014, **466**(1-2), pp.328-340.
114. Mudgil, D., Barak, S. and Khatkar, B.S. Guar gum: processing, properties and food applications—a review. *Journal of food science and technology.* [Online]. 2014, **51**, pp.409-418.
115. O'connor, N., Tredger, J. and Morgan, L. Viscosity differences between various guar gums. *Diabetologia.* [Online]. 1981, **20**, pp.612-615.
116. Gupta, S. and Variyar, P.S. Guar gum: a versatile polymer for the food industry. In: *Biopolymers for food design*. Elsevier, 2018, pp.383-407.
117. Rodge, A., Sonkamble, S., Salve, R. and Hashmi, S.I. Effect of hydrocolloid (guar gum) incorporation on the quality characteristics of bread. [Online]. 2012.
118. Omidian, H., Akhzarmehr, A. and Dey Chowdhury, S. Hydrogel Composites for Multifunctional Biomedical Applications. *Journal of Composites Science.* [Online]. 2024, **8**(4), p.154.
119. Bashir, S., Hina, M., Iqbal, J., Rajpar, A., Mujtaba, M., Alghamdi, N., Wageh, S., Ramesh, K. and Ramesh, S. Fundamental concepts of hydrogels: Synthesis, properties, and their applications. *Polymers.* [Online]. 2020, **12**(11), p.2702.
120. Zaragoza, J., Fukuoka, S., Kraus, M., Thomin, J. and Asuri, P. Exploring the role of nanoparticles in enhancing mechanical properties of hydrogel nanocomposites. *Nanomaterials.* [Online]. 2018, **8**(11), p.882.
121. Jin, Y., Liu, C., Chai, W., Compaan, A. and Huang, Y. Self-supporting nanoclay as internal scaffold material for direct printing of soft hydrogel composite structures in air. *ACS applied materials & interfaces.* [Online]. 2017, **9**(20), pp.17456-17465.
122. Xiang, X., Li, H., Zhu, Y., Xia, S. and He, Q. The composite hydrogel with “2D flexible crosslinking point” of reduced graphene oxide for strain sensor. *Journal of Applied Polymer Science.* [Online]. 2021, **138**(32), p.50801.
123. Wang, C., Liu, X., Wulf, V., Vázquez-González, M., Fadeev, M. and Willner, I. DNA-based hydrogels loaded with Au nanoparticles or Au nanorods: thermoresponsive plasmonic matrices for shape-memory, self-healing, controlled release, and mechanical applications. *ACS nano.* [Online]. 2019, **13**(3), pp.3424-3433.
124. Rumon, M.M.H., Akib, A.A., Sultana, F., Moniruzzaman, M., Niloy, M.S., Shakil, M.S. and Roy, C.K. Self-healing hydrogels: Development, biomedical applications, and challenges. *Polymers.* [Online]. 2022, **14**(21), p.4539.
125. Chen, X., Yan, H., Bao, C., Zhu, Q., Liu, Z., Wen, Y., Li, Z., Zhang, T. and Lin, Q. Fabrication and evaluation of homogeneous alginate/polyacrylamide–chitosan–gelatin composite hydrogel scaffolds based on the interpenetrating networks for tissue engineering. *Polymer Engineering & Science.* [Online]. 2022, **62**(1), pp.116-128.
126. Jiang, L., Gentile, C., Lauto, A., Cui, C., Song, Y., Romeo, T., Silva, S.M., Tang, O., Sharma, P. and Figtree, G. Versatile fabrication approach of conductive hydrogels via copolymerization with vinyl monomers. *ACS applied materials & interfaces.* [Online]. 2017, **9**(50), pp.44124-44133.
127. Xia, Y. and Zhu, H. Polyaniline nanofiber-reinforced conducting hydrogel with unique pH-sensitivity. *Soft matter.* [Online]. 2011, **7**(19), pp.9388-9393.
128. Omar, H. and Alsharaeh, E. Improving Water Retention in Sandy Soils with High-Performance Superabsorbents Hydrogel Polymer. *ACS omega.* [Online]. 2024.
129. Canton, H. Food and agriculture organization of the United Nations—FAO. In: *The Europa directory of international organizations 2021*. Routledge, 2021, pp.297-305.
130. Abdelghafar, R., Abdelfattah, A. and Mostafa, H. Effect of super absorbent hydrogel on hydro-physical properties of soil under deficit irrigation. *Scientific Reports.* [Online]. 2024, **14**(1), p.7655.
131. Heidari, H. and Hosseini, A. Hydrogel polymer improves plant biomass and leaf relative water content in dill and fenugreek. *Ratarstvo i povrtarstvo.* [Online]. 2024.
132. Thombare, N., Mishra, S., Shinde, R., Siddiqui, M. and Jha, U. Guar gum based hydrogel as controlled micronutrient delivery system: Mechanism and kinetics of boron release for agricultural applications. *Biopolymers.* [Online]. 2021, **112**(3), p.e23418.
133. Chaudhary, J., Thakur, S., Sharma, M., Gupta, V.K. and Thakur, V.K. Development of biodegradable agar-agar/gelatin-based superabsorbent hydrogel as an efficient moisture-retaining agent. *Biomolecules.* [Online]. 2020, **10**(6), p.939.

134. Barrientos-Sanhueza, C., Cargnino-Cisternas, D., Díaz-Barrera, A. and Cuneo, I.F. Bacterial alginate-based hydrogel reduces hydro-mechanical soil-related problems in agriculture facing climate change. *Polymers.* [Online]. 2022, **14**(5), p.922.
135. Huang, Y., Chang, Y., Ni, Z. and Wang, L. Environmental parameters factors exploration on lettuce seed germination with hydrogel. *Frontiers in Plant Science.* [Online]. 2024, **15**, p.1308553.
136. Peyrusson, F. Hydrogels improve plant growth in Mars analog conditions. *Frontiers in Astronomy and Space Sciences.* [Online]. 2021, **8**, p.729278.
137. Partheeban, C., Chandrasekhar, C., Jeyakumar, P., Ravikesavan, R. and Gnanam, R. Effect of PEG induced drought stress on seed germination and seedling characters of maize (Zea mays L.) genotypes. *International Journal of Current Microbiology and Applied Sciences.* [Online]. 2017, **6**(5), pp.1095-1104.
138. Samarah, N. and Alqudah, A. Effects of late-terminal drought stress on seed germination and vigor of barley (Hordeum vulgare L.). *Archives of Agronomy and Soil Science.* [Online]. 2011, **57**(1), pp.27-32.
139. Kintl, A., Huňady, I., Vymyslický, T., Ondrisková, V., Hammerschmiedt, T., Brtnický, M. and Elbl, J. Effect of seed coating and PEG-induced drought on the germination capacity of five clover crops. *Plants.* [Online]. 2021, **10**(4), p.724.
140. Azeem, B., KuShaari, K., Man, Z.B., Basit, A. and Thanh, T.H. Review on materials & methods to produce controlled release coated urea fertilizer. *Journal of controlled release.* [Online]. 2014, **181**, pp.11-21.
141. Uysal, Y., Doğaroğlu, Z.G., Makas, M.N. and Çaylali, Z. Boosting Water Retention in Agriculture: Vine Biochar-Doped Hydrogels' Swelling and Germination Effects. *Global Challenges.* [Online]. 2024, **8**(5), p.2300254.
142. Omirova, R.Z., Bolysbek, A.A., Shirinov, S.D. and Dzhalilov, A.T. Development of complex fertilizer technology with improved agrochemical properties using hydrogel. *Rasayan Journal of Chemistry.* [Online]. 2020, **13**(1), pp.733-738.
143. *Secondary Nutrients.* [Online]. [Accessed 21 Octoper]. Available from: https://www.cropnutrition.com/nutrient-management/secondary-nutrients/
144. Shukla, A.K., Sinha, N.K., Tiwari, P.K., Prakash, C., Behera, S.K., Surendra Babu, P., Patnaik, M., Somasundaram, J., Singh, P. and Dwivedi, B.S. Evaluation of spatial distribution and regional zone delineation for micronutrients in a semiarid Deccan Plateau Region of India. *Land Degradation & Development.* [Online]. 2018, **29**(8), pp.2449-2459.
145. Deng, Y. and Dixon, J.B. Soil organic matter and organic-mineral interactions. *Soil mineralogy with environmental applications.* [Online]. 2002, **7**, pp.69-107.
146. Čechmánková, J., Skála, J., Sedlařík, V., Duřpeková, S., Drbohlav, J., Šalaková, A. and Vácha, R. The synergic effect of whey-based hydrogel amendment on soil water holding capacity and availability of nutrients for more efficient valorization of dairy by-products. *Sustainability.* [Online]. 2021, **13**(19), p.10701.
147. Janani, N. and Rajeswari, M. Effects of Organic and Inorganic Soil Conditioners on Soil Moisture in Drylands. [Online]. 2023.
148. Kareem, S.A., Dere, I., Gungula, D.T., Andrew, F.P., Saddiq, A.M., Adebayo, E.F., Tame, V.T., Kefas, H.M., Joseph, J. and Patrick, D.O. Synthesis and characterization of slow-release fertilizer hydrogel based on hydroxy propyl methyl cellulose, polyvinyl alcohol, glycerol and blended paper. *Gels.* [Online]. 2021, **7**(4), p.262.
149. Naushabayev, A.K., Vassilina, T.K., Rsymbetov, B.A., Seitkali, N., Balgabayev, A.M. and Bakenova, Z.B. Effects of different polymer hydrogels on moisture capacity of sandy soil. *Eurasian Journal of Soil Science.* [Online]. 2022, **11**(3), pp.241-247.
150. Lee, S.S., Chang, S.X., Chang, Y.-Y. and Ok, Y.S. Commercial versus synthesized polymers for soil erosion control and growth of Chinese cabbage. *SpringerPlus.* [Online]. 2013, **2**, pp.1-10.
151. Alberts, B. Molecular biology of the cell 4th edition. *(No Title).* [Online]. 2002.
152. Andrew, S.M., Titus, J.A. and Zumstein, L. Dialysis and concentration of protein solutions. *Current protocols in toxicology.* [Online]. 2001, **10**(1), pp.A. 3H. 1-A. 3H. 5.
153. Hwang, S.-T. Fundamentals of membrane transport. *Korean Journal of Chemical Engineering.* [Online]. 2011, **28**(1), pp.1-15. Available from: https://doi.org/10.1007/s11814-010-0493-z
154. Zhang, W., Zhao, X., Zhang, Z., Xu, Y. and Wang, X. Preparation of poly (vinyl alcohol)-based membranes with controllable surface composition and bulk structures and their pervaporation performance. *Journal of Membrane Science.* [Online]. 2012, **415**, pp.504-512.
155. Emmanuel, K., Cheng, C., Erigene, B., Mondal, A.N., Hossain, M.M., Khan, M.I., Afsar, N.U., Liang, G., Wu, L. and Xu, T. Imidazolium functionalized anion exchange membrane blended with PVA for acid recovery via diffusion dialysis process. *Journal of Membrane Science.* [Online]. 2016, **497**, pp.209-215.

156. Prosapio, V., Norton, I. and De Marco, I. Optimization of freeze-drying using a Life Cycle Assessment approach: Strawberries' case study. *Journal of cleaner production.* [Online]. 2017, **168**, pp.1171-1179.
157. Remington, J.P. *Remington: the science and practice of pharmacy.* Lippincott Williams & Wilkins, 2006.
158. Ratti, C. Hot air and freeze-drying of high-value foods: a review. *Journal of food engineering.* [Online]. 2001, **49**(4), pp.311-319.
159. Franks, F. Freeze-drying of bioproducts: putting principles into practice. *European journal of Pharmaceutics and BioPharmaceutics.* [Online]. 1998, **45**(3), pp.221-229.
160. Ratti, C. *Advances in food dehydration.* CRC Press, 2008.
161. do Vale Morais, A.R., do Nascimento Alencar, É., Júnior, F.H.X., De Oliveira, C.M., Marcelino, H.R., Barratt, G., Fessi, H., Do Egito, E.S.T. and Elaissari, A. Freeze-drying of emulsified systems: A review. *International journal of pharmaceutics.* [Online]. 2016, **503**(1-2), pp.102-114.
162. Keskintepe, L. and Eroglu, A. Freeze-drying of mammalian sperm. *Cryopreservation and freeze-drying protocols.* [Online]. 2014, pp.489-497.
163. Stokes, D. *Principles and practice of variable pressure/environmental scanning electron microscopy (VP-ESEM).* John Wiley & Sons, 2008.
164. Goldstein, J.I., Newbury, D.E., Michael, J.R., Ritchie, N.W., Scott, J.H.J. and Joy, D.C. *Scanning electron microscopy and X-ray microanalysis.* springer, 2017.
165. Jöns, N., Kahl, W.-A. and Bach, W. Reaction-induced porosity and onset of low-temperature carbonation in abyssal peridotites: Insights from 3D high-resolution microtomography. *Lithos.* [Online]. 2017, **268**, pp.274-284.
166. Akelah, A. Polymers in plantation and plants protection. In: *Functionalized Polymeric Materials in Agriculture and the Food Industry*. Springer, 2013, pp.65-131.
167. Goldstein, J.I., Newbury, D.E., Echlin, P., Joy, D.C., Romig, A., Lyman, C.E., Fiori, C., Lifshin, E., Goldstein, J.I. and Newbury, D.E. Electron optics. *Scanning Electron Microscopy and X-Ray Microanalysis: A Text for Biologists, Materials Scientists, and Geologists.* [Online]. 1992, pp.21-68.
168. CHOUDHARY, O., Kalita, P., Doley, P. and Kalita, A. 1. Scanning Electron Microscope-Advantages and Disadvantages in Imaging Components by OP Choudhary, PC Kalita, PJ Doley and A. Kalita. *LIFE SCIENCES LEAFLETS.* [Online]. 2017, **85**, pp.1 to 7-1 to 7.
169. Nakanishi, A., Yamamoto, N., Sakihama, Y., Okino, T. and Matoba, N. Development of Targeted Protein-Displaying Technology with a Novel Carbon Material. *BioTech.* [Online]. 2022, **12**(1), p.2.
170. Brunauer, S., Emmett, P.H. and Teller, E. Adsorption of gases in multimolecular layers. *Journal of the American chemical society.* [Online]. 1938, **60**(2), pp.309-319.
171. Antoniono, E. *Design of prototype-biotech devices for anticancer drugs targeting*. thesis, Politecnico di Torino, 2023.
172. Lee, C.-J., Wu, H., Hu, Y., Young, M., Wang, H., Lynch, D., Xu, F., Cong, H. and Cheng, G. Ionic conductivity of polyelectrolyte hydrogels. *ACS applied materials & interfaces.* [Online]. 2018, **10**(6), pp.5845-5852.
173. Wang, S.-C. and Tsao, H.-K. Ion migration through a polymer solution: Microviscosity. *Macromolecules.* [Online]. 2003, **36**(24), pp.9128-9134.
174. Ugata, Y., Hasegawa, G., Kuwata, N., Ueno, K., Watanabe, M. and Dokko, K. Temperature dependency of ion transport in highly concentrated Li salt/sulfolane electrolyte solutions. *The Journal of Physical Chemistry C.* [Online]. 2022, **126**(45), pp.19084-19090.
175. Xu, W., Belieres, J.-P. and Angell, C.A. Ionic conductivity and electrochemical stability of poly [oligo (ethylene glycol) oxalate]− lithium salt complexes. *Chemistry of materials.* [Online]. 2001, **13**(2), pp.575-580.
176. John, P., Johnson, F. and Sutcliffe, P. A conductivity flow meter. *Journal of Hydraulic Research.* [Online]. 1976, **14**(1), pp.37-44.
177. Cookey, G. and Iboroma, D. CONDUCTIVITY STUDY OF SODIUM BROMIDE AND SODIUM CHLORIDE SALTS IN BINARY MIXTURES OFAQUEOUS AND ORGANIC SOLVENTS. *Journal of Chemical Society of Nigeria.* [Online]. 2023, **48**(2).
178. Pourhoseini, S., Ramezani-Aval, H. and Naghizadeh, N. FHD and MHD effects of Fe3O4-water magnetic nanofluid on the enhancement of overall heat transfer coefficient of a heat exchanger. *Physica Scripta.* [Online]. 2020, **95**(4), p.045705.
179. Hasan, M.Z., Mahbub, S., Hoque, M.A., Rub, M.A. and Kumar, D. Investigation of mixed micellization study of sodium dodecyl sulfate and tetradecyltrimethylammonium bromide mixtures at different compositions: Effect of electrolytes and temperatures. *Journal of Physical Organic Chemistry.* [Online]. 2020, **33**(5), p.e4047.

180. Amin, M.R., Alissa, S.A., Molla, M.R., Rub, M.A., Wabaidur, S.M., Hoque, M.A. and Kabir, S.E. Influence of the effect of different electrolytes on the interaction of promethazine hydrochloride drug with tetradecyltrimethylammonium bromide at different temperatures. *Journal of Physical Organic Chemistry.* [Online]. 2020, **33**(7), p.e4057.
181. Mohammadi, M.H., Khataar, M. and Shekari, F. Effect of soil salinity on the wheat and bean root respiration rate at low matric suctions. *Paddy and Water Environment.* [Online]. 2017, **15**, pp.639-648.
182. Yeboue, A.K., Kabran, M.R.G., Sorokina, A.E., Adou, A.D., Kouassi, C.K., Mamyrbekova-Bekro, A.J. and Bekro, Y.-A. Physical, physicochemical and nutritional profile of honey produced in nine localities in Côte d'Ivoire. *International Journal of Biological and Chemical Sciences.* [Online]. 2021, **15**(2), pp.846-859.
183. Guizani, A., Askri, H., Amenta, M.L., Defez, R., Babay, E., Bianco, C., Rapaná, N., Finetti-Sialer, M. and Gharbi, F. Drought responsiveness in six wheat genotypes: identification of stress resistance indicators. *Frontiers in Plant Science.* [Online]. 2023, **14**, p.1232583.
184. Abbas, M.T., Wadaan, M.A., Ullah, H., Farooq, M., Fozia, F., Ahmad, I., Khan, M.F., Baabbad, A. and Ullah, Z. Bioaccumulation and Mobility of Heavy Metals in the Soil-Plant System and Health Risk Assessment of Vegetables Irrigated by Wastewater. *Sustainability.* [Online]. 2023, **15**(21), p.15321.
185. Ma, C., Li, J. and Yu, S. Method of soil electrical conductivity measurement based on multi-sensor data fusion. In: *2011 International Conference on Mechatronic Science, Electric Engineering and Computer (MEC)*: IEEE, 2011, pp.1219-1221.
186. Lide, D.R. *A century of excellence in measurements, standards, and technology.* CRC Press, 2018.
187. Linge, K.L. and Jarvis, K.E. Quadrupole ICP-MS: Introduction to instrumentation, measurement techniques and analytical capabilities. *Geostandards and geoanalytical research.* [Online]. 2009, **33**(4), pp.445-467.
188. von der Au, M., Karbach, H., Bell, A.M., Bauer, O.B., Karst, U. and Meermann, B. Determination of metal uptake in single organisms, Corophium volutator, via complementary electrothermal vaporization/inductively coupled plasma mass spectrometry and laser ablation/inductively coupled plasma mass spectrometry. *Rapid communications in mass spectrometry.* [Online]. 2021, **35**(2), p.e8953.
189. Martínez-Sierra, J.G., San Blas, O.G., Gayón, J.M. and Alonso, J.G. Sulfur analysis by inductively coupled plasma-mass spectrometry: A review. *Spectrochimica Acta Part B: Atomic Spectroscopy.* [Online]. 2015, **108**, pp.35-52.
190. Wilschefski, S.C. and Baxter, M.R. Inductively coupled plasma mass spectrometry: introduction to analytical aspects. *The Clinical Biochemist Reviews.* [Online]. 2019, **40**(3), p.115.
191. Mazarakioti, E.C., Zotos, A., Thomatou, A.-A., Kontogeorgos, A., Patakas, A. and Ladavos, A. Inductively coupled plasma-mass spectrometry (ICP-MS), a useful tool in authenticity of agricultural products' and foods' origin. *Foods.* [Online]. 2022, **11**(22), p.3705.
192. Khan, S.R., Sharma, B., Chawla, P.A. and Bhatia, R. Inductively coupled plasma optical emission spectrometry (ICP-OES): a powerful analytical technique for elemental analysis. *Food Analytical Methods.* [Online]. 2022, pp.1-23.
193. Herman, M., Golasik, M., Piekoszewski, W., Walas, S., Napierala, M., Wyganowska-Swiatkowska, M., Kurhanska-Flisykowska, A., Wozniak, A. and Florek, E. Essential and toxic metals in oral fluid–a potential role in the diagnosis of periodontal diseases. *Biological trace element research.* [Online]. 2016, **173**, pp.275-282.
194. Mitić, S.S., Stojanović, B.T., Mitić, M.N., Pavlović, A.N., Arsić, B. and Stankov-Jovanović, V. Multi-element analysis of methanol apple peel extracts by inductively coupled plasma-optical emission spectrometry. [Online].
195. Losev, V.N., Parfenova, V.V., Elsuf'ev, E.V., Borodina, E.V., Metelitsa, S.I. and Trofimchuk, A.K. Separation and preconcentration followed by ICP-OES and ICP-MS determination of precious metals using silica gel chemically modified with dithiocarbamate groups. *Separation Science and Technology.* [Online]. 2020, **55**(15), pp.2659-2669.
196. Coats, A. and Redfern, J. Thermogravimetric analysis. A review. *Analyst.* [Online]. 1963, **88**(1053), pp.906-924.
197. Company, M.-H.B. *McGraw-Hill Encyclopedia of Science and Technology: An International Reference Work.* McGraw-Hill, 1960.
198. Saadatkhah, N., Carillo Garcia, A., Ackermann, S., Leclerc, P., Latifi, M., Samih, S., Patience, G.S. and Chaouki, J. Experimental methods in chemical engineering: Thermogravimetric analysis—TGA. *The Canadian Journal of Chemical Engineering.* [Online]. 2020, **98**(1), pp.34-43.

199. Plante, A.F., Fernández, J.M. and Leifeld, J. Application of thermal analysis techniques in soil science. *Geoderma.* [Online]. 2009, **153**(1-2), pp.1-10.
200. Hatakeyama, T. and Quinn, F. *Thermal analysis: fundamentals and applications to polymer science.* [sl], 1999.
201. Mackenzie, R. and Mitchell, B. Differential thermal analysis. A review. *Analyst.* [Online]. 1962, **87**(1035), pp.420-434.
202. Balasundram, V., Alias, N., Ibrahim, N., Kasmani, R.M., Isha, R., Hamid, M.K.A. and Hasbullah, H. Thermal characterization of Malaysian biomass via thermogravimetric analysis. *Journal of Energy and Safety Technology (JEST).* [Online]. 2018, **1**(1).
203. Lázaro, I.A. A Comprehensive Thermogravimetric Analysis Multifaceted Method for the Exact Determination of the Composition of Multifunctional Metal-Organic Framework Materials. *European Journal of Inorganic Chemistry.* [Online]. 2020, **2020**(45), pp.4284-4294.
204. Scalet, V., da Róz, A.L., Santos, L.R.O., Hansted, A.L.S., Pires, A.A.F., Nakashima, G.T., Tomeleri, J.O.P. and Yamaju, F.M. Waste of the Licuri (syagrus coronata) nut shells: an alternative energy source. *Revista Brasileira de Energias Renováveis.* [Online]. 2019, **8**(3), pp.583-597.
205. Mansfield, E., Tyner, K.M., Poling, C.M. and Blacklock, J.L. Determination of nanoparticle surface coatings and nanoparticle purity using microscale thermogravimetric analysis. *Analytical chemistry.* [Online]. 2014, **86**(3), pp.1478-1484.
206. Moliner, C., Aguilar, K., Bosio, B., Arato, E. and Ribes, A. Thermo-oxidative characterisation of the residues from persimmon harvest for its use in energy recovery processes. *Fuel Processing Technology.* [Online]. 2016, **152**, pp.421-429.
207. Bredin, A., Larcher, A.V. and Mullins, B.J. Thermogravimetric analysis of carbon black and engine soot—Towards a more robust oil analysis method. *Tribology international.* [Online]. 2011, **44**(12), pp.1642-1650.
208. Sun, N., Liang, Y., Xu, Z., Li, H., Shaohua, J. and Yibiao, L. The thermal degradation behavior of meta-and para-hetero-amide fibers by TGA-FTIR. *Journal of Polymer Engineering.* [Online]. 2013, **33**(4), pp.337-344.
209. Serapiglia, M.J., Cameron, K.D., Stipanovic, A.J. and Smart, L.B. Analysis of biomass composition using high-resolution thermogravimetric analysis and percent bark content for the selection of shrub willow bioenergy crop varieties. *Bioenergy research.* [Online]. 2009, **2**, pp.1-9.
210. MISSAK, P. INFILTRATION GROWTH PROCESSING OF YBCO NANO-COMPOSITES: SHAPE FORMING, MICROSTRUCTURAL AND MAGNETIC STUDIES. [Online].
211. Rojek, B. and Wesolowski, M. A combined differential scanning calorimetry and thermogravimetry approach for the effective assessment of drug substance-excipient compatibility. *Journal of Thermal Analysis and Calorimetry.* [Online]. 2023, **148**(3), pp.845-858.
212. Sharma, D., MacDonald, J.C. and Iannacchione, G.S. Thermodynamics of activated phase transitions of 8CB: DSC and MC calorimetry. *The Journal of Physical Chemistry B.* [Online]. 2006, **110**(33), pp.16679-16684.
213. Leyva-Porras, C., Cruz-Alcantar, P., Espinosa-Solís, V., Martínez-Guerra, E., Piñón-Balderrama, C.I., Compean Martínez, I. and Saavedra-Leos, M.Z. Application of differential scanning calorimetry (DSC) and modulated differential scanning calorimetry (MDSC) in food and drug industries. *Polymers.* [Online]. 2019, **12**(1), p.5.
214. Zabarnick, S. and Widmor, N. Studies of jet fuel freezing by differential scanning calorimetry. *Energy & fuels.* [Online]. 2001, **15**(6), pp.1447-1453.
215. Feeney, A. and Lucas, M. Differential scanning calorimetry of superelastic Nitinol for tunable cymbal transducers. *Journal of Intelligent Material Systems and Structures.* [Online]. 2016, **27**(10), pp.1376-1387.
216. Teh, J.S., Teoh, Y.H., How, H.G. and Sher, F. Thermal analysis technologies for biomass feedstocks: a state-of-the-art review. *Processes.* [Online]. 2021, **9**(9), p.1610.
217. De Kee, D. and Wissbrun, K.F. Polymer rheology. *Physics Today.* [Online]. 1998, **51**(6), pp.24-29.
218. Chen, D.T., Wen, Q., Janmey, P.A., Crocker, J.C. and Yodh, A.G. Rheology of soft materials. *Annu. Rev. Condens. Matter Phys.* [Online]. 2010, **1**(1), pp.301-322.
219. Li, S., Ma, Y., Fu, T., Zhu, C. and Li, H. The viscosity distribution around a rising bubble in shear-thinning non-newtonian fluids. *Brazilian Journal of Chemical Engineering.* [Online]. 2012, **29**, pp.265-274.
220. Ault, J.T., Shin, S., Garcia, A., Perazzo, A. and Stone, H.A. Viscosity measurements of glycerol in a parallel-plate rheometer exposed to atmosphere. *Journal of Fluid Mechanics.* [Online]. 2023, **968**, p.A2.

221. Coussot, P. Rheometry of pastes, suspensions, and granular materials: applications in industry and environment. [Online]. 2005.
222. Malkin, A.Y. and Isayev, A. Concepts, methods and applications. *Appl Rheol.* [Online]. 2006, **16**(5), pp.240-241.
223. Diryak, R., Kontogiorgos, V., Ghori, M.U., Bills, P., Tawfik, A., Morris, G.A. and Smith, A.M. Behavior of In Situ Cross-Linked Hydrogels with Rapid Gelation Kinetics on Contact with Physiological Fluids. *Macromolecular Chemistry and Physics.* [Online]. 2018, **219**(8), p.1700584.
224. Chen, X., McClements, D.J., Zhu, Y., Zou, L., Li, Z., Liu, W., Cheng, C., Gao, H. and Liu, C. Gastrointestinal fate of fluid and gelled nutraceutical emulsions: Impact on proteolysis, lipolysis, and quercetin bioaccessibility. *Journal of agricultural and food chemistry.* [Online]. 2018, **66**(34), pp.9087-9096.
225. Gigante, V., Aliotta, L., Coltelli, M.B., Cinelli, P., Botta, L., La Mantia, F.P. and Lazzeri, A. Fracture behavior and mechanical, thermal, and rheological properties of biodegradable films extruded by flat die and calender. *Journal of Polymer Science.* [Online]. 2020, **58**(23), pp.3264-3282.
226. Li, S., Kong, Y., Wang, X., Zhang, G., Long, S. and Yang, J. The influence of processing aids on the melt stability and mobility of poly (arylene sulfide sulfone). *High Performance Polymers.* [Online]. 2016, **28**(7), pp.784-792.
227. Laskar, A.I. and Talukdar, S. Correlation between Compressive Strength and Rheological Parameters of High-Performance Concrete. *Advances in Materials Science and Engineering.* [Online]. 2007, **2007**(1), p.045869.
228. Li, H., Yu, J., Wu, S., Liu, Q., Li, Y., Wu, Y. and Xu, H. Investigation of the effect of induction heating on asphalt binder aging in steel fibers modified asphalt concrete. *Materials.* [Online]. 2019, **12**(7), p.1067.
229. Falchetto, A.C., Alisov, A., Goeke, M. and Wistuba, M. Identification of structural changes in bitumen due to aging and fatigue. In: *Proceedings of the 6th Eurasphalt & Eurobitume Congress, Prague, Czech Republic*, 2016, pp.1-3.
230. Clasen, C. High shear rheometry using hydrodynamic lubrication flows. *Journal of Rheology.* [Online]. 2013, **57**(1), pp.197-221.
231. Desprat, N., Guiroy, A. and Asnacios, A. Microplates-based rheometer for a single living cell. *Review of scientific instruments.* [Online]. 2006, **77**(5).
232. Nawab, Y., Shahid, S., Boyard, N. and Jacquemin, F. Chemical shrinkage characterization techniques for thermoset resins and associated composites. *Journal of Materials Science.* [Online]. 2013, **48**, pp.5387-5409.
233. Kirchmajer, D.M., Steinhoff, B., Warren, H., Clark, R. and in het Panhuis, M. Enhanced gelation properties of purified gellan gum. *Carbohydrate Research.* [Online]. 2014, **388**, pp.125-129. Available from: https://doi.org/https://doi.org/10.1016/j.carres.2014.02.018
234. Li, A., Khan, I.N., Khan, I.U., Yousaf, A.M. and Shahzad, Y. Gellan Gum-Based Bilayer Mucoadhesive Films Loaded with Moxifloxacin Hydrochloride and Clove Oil for Possible Treatment of Periodontitis. *Drug Des Devel Ther.* [Online]. 2021, **15**, pp.3937-3952. Available from: https://doi.org/10.2147/dddt.S328722
235. Ahearne, M. and Kelly, D.J. A comparison of fibrin, agarose and gellan gum hydrogels as carriers of stem cells and growth factor delivery microspheres for cartilage regeneration. *Biomed Mater.* [Online]. 2013, **8**(3), p.035004. Available from: https://doi.org/10.1088/1748-6041/8/3/035004
236. Silva, N.A., Moreira, J., Ribeiro-Samy, S., Gomes, E.D., Tam, R.Y., Shoichet, M.S., Reis, R.L., Sousa, N. and Salgado, A.J. Modulation of bone marrow mesenchymal stem cell secretome by ECM-like hydrogels. *Biochimie.* [Online]. 2013, **95**(12), pp.2314-2319. Available from: https://doi.org/https://doi.org/10.1016/j.biochi.2013.08.016
237. Douglas, T.E., Dokupil, A., Reczyńska, K., Brackman, G., Krok-Borkowicz, M., Keppler, J.K., Božič, M., Van Der Voort, P., Pietryga, K., Samal, S.K., Balcaen, L., van den Bulcke, J., Van Acker, J., Vanhaecke, F., Schwarz, K., Coenye, T. and Pamuła, E. Enrichment of enzymatically mineralized gellan gum hydrogels with phlorotannin-rich Ecklonia cava extract Seanol(®) to endow antibacterial properties and promote mineralization. *Biomed Mater.* [Online]. 2016, **11**(4), p.045015. Available from: https://doi.org/10.1088/1748-6041/11/4/045015
238. Douglas, T.E., Wlodarczyk, M., Pamula, E., Declercq, H.A., de Mulder, E.L., Bucko, M.M., Balcaen, L., Vanhaecke, F., Cornelissen, R., Dubruel, P., Jansen, J.A. and Leeuwenburgh, S.C. Enzymatic mineralization of gellan gum hydrogel for bone tissue-engineering applications and its enhancement by polydopamine. *J Tissue Eng Regen Med.* [Online]. 2014, **8**(11), pp.906-918. Available from: https://doi.org/10.1002/term.1616
239. Chen, H., Zhang, Y., Ding, P., Zhang, T., Zan, Y., Ni, T., Lin, R., Liu, M. and Pei, R. Bone Marrow-Derived Mesenchymal Stem Cells Encapsulated in Functionalized Gellan Gum/Collagen Hydrogel for Effective

Vascularization. *ACS Applied Bio Materials.* [Online]. 2018, **1**(5), pp.1408-1415. Available from: https://doi.org/10.1021/acsabm.8b00361

240. Mouser, V.H., Melchels, F.P., Visser, J., Dhert, W.J., Gawlitta, D. and Malda, J. Yield stress determines bioprintability of hydrogels based on gelatin-methacryloyl and gellan gum for cartilage bioprinting. *Biofabrication.* [Online]. 2016, **8**(3), p.035003. Available from: https://doi.org/10.1088/1758-5090/8/3/035003
241. Destruel, P.-L., Zeng, N., Seguin, J., Douat, S., Rosa, F., Brignole-Baudouin, F., Dufaÿ, S., Dufaÿ-Wojcicki, A., Maury, M., Mignet, N. and Boudy, V. Novel in situ gelling ophthalmic drug delivery system based on gellan gum and hydroxyethylcellulose: Innovative rheological characterization, in vitro and in vivo evidence of a sustained precorneal retention time. *International Journal of Pharmaceutics.* [Online]. 2020, **574**, p.118734. Available from: https://doi.org/https://doi.org/10.1016/j.ijpharm.2019.118734
242. Johndel Obra, J.Q.M., Denise Faye Lensoco, Terence Tumolva. Synthesis and Characterization of NaCMC/HEC/ Activated Carbon Hydrogel Composites for the Desalination of Seawater. *Smart Environmental Science Technology and Management.* [Online]. 2022, **1**. Available from: https://doi.org/doi.org/10.36647/978-93-92106-02-6.16
243. Panday, A., Yadav, H., Patel, J., Paliwal, R. and Maiti, S. Calcium silicate-reinforced pH-sensitive alginate-gellan gum composite hydrogels for prolonged drug delivery. *Journal of Applied Polymer Science.* [Online]. 2023, **140**(37), p.e54392.
244. Iijima, M., Hatakeyama, T. and Hatakeyama, H. DSC and TMA Studies of Polysaccharide Physical Hydrogels. *Analytical Sciences.* [Online]. 2021, **37**(1), pp.211-219. Available from: https://doi.org/10.2116/analsci.20SAR10
245. Zhou, J., Lin, S., Zeng, H., Liu, J., Li, B., Xu, Y., Zhao, X. and Chen, G. Dynamic intermolecular interactions through hydrogen bonding of water promote heat conduction in hydrogels. *Materials Horizons.* [Online]. 2020, **7**(11), pp.2936-2943. Available from: https://doi.org/10.1039/D0MH00735H
246. Wu, J., Wu, Z., Sun, X., Yuan, S., Zhang, R., Lu, Q. and Yu, Y. Effect of Sodium Alginate on the Properties of Thermosensitive Hydrogels. *Journal of the Chinese Chemical Society.* [Online]. 2017, **64**(2), pp.231-238. Available from: https://doi.org/https://doi.org/10.1002/jccs.201600152
247. Yamada, M. and Kametani, Y. Preparation of Gellan Gum-Inorganic Composite Film and Its Metal Ion Accumulation Property. *Journal of Composites Science.* [Online]. 2022, **6**(2), p.42. Available from: https://www.mdpi.com/2504-477X/6/2/42
248. Balasubramanian, R., Srinivasan, R. and Lee, J. Barrier, rheological, and antimicrobial properties of sustainable nanocomposites based on gellan gum/polyacrylamide/zinc oxide. *Polymer Engineering & Science.* [Online]. 2021, **61**(10), pp.2477-2486. Available from: https://doi.org/https://doi.org/10.1002/pen.25773
249. Kanesaka, S., Watanabe, T. and Matsukawa, S. Binding Effect of Cu2+ as a Trigger on the Sol-to-Gel and the Coil-to-Helix Transition Processes of Polysaccharide, Gellan Gum. *Biomacromolecules.* [Online]. 2004, **5**(3), pp.863-868. Available from: https://doi.org/10.1021/bm030072t
250. Liu, X., Tian, Y., Wu, Y., Chen, F., Mu, Y., Minus, M.L. and Zheng, Y. Fully Biomass-Based Hybrid Hydrogel for Efficient Solar Desalination with Salt Self-Cleaning Property. *ACS Applied Materials & Interfaces.* [Online]. 2021, **13**(36), pp.42832-42842. Available from: https://doi.org/10.1021/acsami.1c11636
251. Silva-Correia, J., Zavan, B., Vindigni, V., Silva, T.H., Oliveira, J.M., Abatangelo, G. and Reis, R.L. Biocompatibility Evaluation of Ionic- and Photo-Crosslinked Methacrylated Gellan Gum Hydrogels: In Vitro and In Vivo Study. *Advanced Healthcare Materials.* [Online]. 2013, **2**(4), pp.568-575. Available from: https://doi.org/https://doi.org/10.1002/adhm.201200256
252. Astanina, A., Koivisto, J.T., Hannula, M., Salminen, T., Kellomäki, M. and Massera, J. Chemical interactions in composites of gellan gum and bioactive glass: self-crosslinking and in vitro dissolution. *Front Chem.* [Online]. 2023, **11**, p.1133374. Available from: https://doi.org/10.3389/fchem.2023.1133374
253. Vyazovkin, S., Burnham, A.K., Criado, J.M., Pérez-Maqueda, L.A., Popescu, C. and Sbirrazzuoli, N. ICTAC Kinetics Committee recommendations for performing kinetic computations on thermal analysis data. *Thermochimica Acta.* [Online]. 2011, **520**(1), pp.1-19. Available from: https://doi.org/https://doi.org/10.1016/j.tca.2011.03.034
254. Rouquerol, J., Rouquerol, F., Llewellyn, P., Maurin, G. and Sing, K. *Adsorption by Powders and Porous Solids: Principles, Methodology and Applications.* Academic Press, 2013.
255. Brown, M.E. *Introduction to Thermal Analysis: Techniques and Applications.* Springer Netherlands, 2001.
256. Laye, P.G., Warrington, S.B., Group, T.M., Heal, G.R., Price, D.M. and Wilson, R. *Principles of Thermal Analysis and Calorimetry.* The Royal Society of Chemistry, 2002.

257. Kolgesiz, S., Ozcelik, N., Erdemir, N.E. and Unal, H. Hybrid Pectin/Polydopamine Hydrogels with Photothermal Properties. *ACS Omega.* [Online]. 2025, **10**(21), pp.21994-22004. Available from: https://doi.org/10.1021/acsomega.5c02084
258. Zhao, M., Wang, D., Fan, Z., Lu, J., Li, Y., Zhang, Y., Lv, M., Sun, M. and Wang, W. Algae Biomass Hydrogels for Enhanced Removal of Heavy Metal Ions. *Gels.* [Online]. 2025, **11**(3), p.150. Available from: https://www.mdpi.com/2310-2861/11/3/150
259. Paukkonen, H., Kunnari, M., Laurén, P., Hakkarainen, T., Auvinen, V.-V., Oksanen, T., Koivuniemi, R., Yliperttula, M. and Laaksonen, T. Nanofibrillar cellulose hydrogels and reconstructed hydrogels as matrices for controlled drug release. *International Journal of Pharmaceutics.* [Online]. 2017, **532**(1), pp.269-280. Available from: https://doi.org/https://doi.org/10.1016/j.ijpharm.2017.09.002
260. Mikac, U. and Kristl, J. Magnetic Resonance Methods as a Prognostic Tool for the Biorelevant Behavior of Xanthan Tablets. *Molecules.* [Online]. 2020, **25**(24). Available from: https://doi.org/10.3390/molecules25245871
261. Anderson, T.R., Marquart, M.E. and Janorkar, A.V. Effective release of a broad spectrum antibiotic from elastin-like polypeptide-collagen composite. *J Biomed Mater Res A.* [Online]. 2015, **103**(2), pp.782-790. Available from: https://doi.org/10.1002/jbm.a.35219
262. García-Villén, F., Sánchez-Espejo, R., Borrego-Sánchez, A., Cerezo, P., Cucca, L., Sandri, G. and Viseras, C. Correlation between Elemental Composition/Mobility and Skin Cell Proliferation of Fibrous Nanoclay/Spring Water Hydrogels. *Pharmaceutics.* [Online]. 2020, **12**(9). Available from: https://doi.org/10.3390/pharmaceutics12090891
263. Soontornworajit, B., Zhou, J., Zhang, Z. and Wang, Y. Aptamer-Functionalized In Situ Injectable Hydrogel for Controlled Protein Release. *Biomacromolecules.* [Online]. 2010, **11**(10), pp.2724-2730. Available from: https://doi.org/10.1021/bm100774t
264. Bilek Jr, V. and Pazour, M. Structural build-up and breakdown of sodium hydroxide-activated slag paste assessed using oscillatory rheology. *Journal of Physics: Conference Series.* [Online]. 2022, **2341**(1), p.012001. Available from: https://doi.org/10.1088/1742-6596/2341/1/012001
265. Avila Torrado, M., Constantinescu, A., Johlitz, M. and Lion, A. Viscoelastic behavior of filled silicone elastomers and influence of aging in inert and hermetic environment. *Continuum Mechanics and Thermodynamics.* [Online]. 2024, **36**(2), pp.333-350. Available from: https://doi.org/10.1007/s00161-022-01112-9
266. Foroutan Mirhosseini, A., Kavussi, A., Jalal Kamali, M.H., Khabiri, M.M. and Hassani, A. Evaluating fatigue behavior of asphalt binders and mixes containing Date Seed Ash. *Journal of Civil Engineering and Management.* [Online]. 2017, **23**(8), pp.1164-1175. Available from: https://doi.org/10.3846/13923730.2017.1396560
267. Shakeel, A., Zander, F., Gebert, J., Chassagne, C. and Kirichek, A. Influence of Anaerobic Degradation of Organic Matter on the Rheological Properties of Cohesive Mud from Different European Ports. *Journal of Marine Science and Engineering.* [Online]. 2022, **10**(3), p.446. Available from: https://www.mdpi.com/2077-1312/10/3/446
268. Radvar, E. and Azevedo, H.S. Supramolecular Nanofibrous Peptide/Polymer Hydrogels for the Multiplexing of Bioactive Signals. *ACS Biomaterials Science & Engineering.* [Online]. 2019, **5**(9), pp.4646-4656. Available from: https://doi.org/10.1021/acsbiomaterials.9b00941
269. Xuan, X., Zhang, H., Xu, X., Pan, Z., Luo, Y., Li, Y. and Sun, L. Tuning Polyacrylamide Precursor Viscoelasticity Using Nanoclay for Extrusion-Based 3D Printing of Hydrogels. *Journal of Polymer Science.* [Online]. 2025, **63**(8), pp.1924-1937. Available from: https://doi.org/https://doi.org/10.1002/pol.20250147
270. Rana, V.K., Karami, P., Nasrollahzadeh, N. and Pioletti, D.P. Nano Surface-Heterogeneities of Particles Modulate the Macroscopic Properties of Hydrogels. *Advanced Materials Interfaces.* [Online]. 2023, **10**(14), p.2202248. Available from: https://doi.org/https://doi.org/10.1002/admi.202202248
271. Israkarn, K., Buathongjan, C., Gamonpilas, C., Methacanon, P. and Wisetsuwannaphum, S. Effects of gellan gum and calcium fortification on the rheological properties of mung bean protein and gellan gum mixtures. *J Food Sci.* [Online]. 2022, **87**(11), pp.5001-5016. Available from: https://doi.org/10.1111/1750-3841.16337
272. Bacelar, A.H., Silva-Correia, J., Oliveira, J.M. and Reis, R.L. Recent progress in gellan gum hydrogels provided by functionalization strategies. *J Mater Chem B.* [Online]. 2016, **4**(37), pp.6164-6174. Available from: https://doi.org/10.1039/c6tb01488g
273. Kudaibergenov, S.E., Tatykhanova, G.S., Sigitov, V.B., Nurakhmetova, Z.A., Blagikh, E.V., Gussenov, I.S. and Seilkhanov, T.M. Physico-Chemical and Rheological Properties of Gellan in Aqueous-Salt Solutions

and Oilfield Saline Water. *Macromolecular Symposia.* [Online]. 2016, **363**(1), pp.20-35. Available from: https://doi.org/https://doi.org/10.1002/masy.201500139

274. Bradbeer, J.F., Hancocks, R., Spyropoulos, F. and Norton, I.T. Self-structuring foods based on acid-sensitive low and high acyl mixed gellan systems to impact on satiety. *Food Hydrocolloids.* [Online]. 2014, **35**, pp.522-530. Available from: https://doi.org/https://doi.org/10.1016/j.foodhyd.2013.07.014
275. He, W., Wu, Y., Luo, Z., Yang, G., Ye, W., Chen, X., Ren, J., Liang, T., Liao, Z., Jiang, S. and Wang, K. Injectable Decorin/Gellan Gum Hydrogel Encapsulating Adipose-Derived Stem Cells Enhances Anti-Inflammatory Effect in Cartilage Injury via Autophagy Signaling. *Cell Transplantation.* [Online]. 2023, **32**, p.09636897231196493. Available from: https://doi.org/10.1177/09636897231196493
276. Zhao, X. Multi-scale multi-mechanism design of tough hydrogels: building dissipation into stretchy networks. *Soft matter.* [Online]. 2014, **10**(5), pp.672-687.
277. Mezger, T. *The Rheology Handbook: For users of rotational and oscillatory rheometers.* Vincentz Network, 2020.
278. Caló, E. and Khutoryanskiy, V.V. Biomedical applications of hydrogels: A review of patents and commercial products. *European Polymer Journal.* [Online]. 2015, **65**, pp.252-267. Available from: https://doi.org/https://doi.org/10.1016/j.eurpolymj.2014.11.024
279. Chaudhuri, O., Gu, L., Klumpers, D., Darnell, M., Bencherif, S.A., Weaver, J.C., Huebsch, N., Lee, H.-p., Lippens, E., Duda, G.N. and Mooney, D.J. Hydrogels with tunable stress relaxation regulate stem cell fate and activity. *Nature Materials.* [Online]. 2016, **15**(3), pp.326-334. Available from: https://doi.org/10.1038/nmat4489
280. Ghanbari, A., Mousavi, Z., Heuzey, M.-C., Patience, G.S. and Carreau, P.J. Experimental methods in chemical engineering: Rheometry. *The Canadian Journal of Chemical Engineering.* [Online]. 2020, **98**(7), pp.1456-1470. Available from: https://doi.org/https://doi.org/10.1002/cjce.23749
281. Schramm, G. and Haake, G. *A Practical Approach to Rheology and Rheometry.* Gebrueder Haake, 1994.